EPI International Journal of Engineering

Foreword

Natural disaster and mitigation has been a major problem in our society, especially in Asia, the densely-populated area in the world. Data has shown that the impact of disaster has been increasing within two decades. However, low awareness of people who live in natural disaster-prone areas makes the disaster is more likely to be more destructive. One of the key to reduce the risk of the disaster is to create a comprehensive mitigation scheme using the application of science and technology.

This current edition included a mini-special edition on Natural Disaster and Mitigation which is intended to increase the awareness on the natural disaster and mitigation issue. The issue covers a widespread of topic for the sake of disaster risk reduction campaign. The articles ranges from a laboratory scale study to a field work-based investigation in some natural disaster-prone areas in Indonesia and other places. The five articles in this issue were invited, submitted, and then reviewed thoroughly according to the usual and standard of the journal.

Maulana and his collaborator proposed a Landslide Disaster Risk Assessment Model in Soppeng Regency, South Sulawesi. Their study is based on a field-work based data collection combining with geographic information system analyses to design a model for risk assessment. A mitigation scenario for landslide disaster in Soppeng Regency is comprehensively proposed. Baeda and Namiruddin present a study on mitigation scheme for Banggae Future Tsunami, West Sulawesi, Indonesia. Such a study provides some data related to possibility in proposing mitigation scheme in the one of tsunami-prone areas in Sulawesi based on historical record.

Yoshida conduct an investigation on Massive fire incidents of multiple aboveground storage tanks due to vapor cloud explosion. He presents a type of combination between man-made and natural disaster that frequently happen in above storage tanks and prevention suggestion in the future. Two basic but technically important articles are provided by Nakazawa and his team. They studied the deformation evaluation of steel wire mesh for rational gabion structure design which is important in building a more resilience construction.

These five interesting articles cover a wide spectrum of topics, and demonstrate the combination of the typical natural disaster mitigation research and laboratory-based work. We thank all authors for submitting their articles to this special issue, and all referees for their time and efforts. We would also like to thank the editors for their constant support and making this special issue possible.

Warm regards,

Dr. Adi Maulana
Guest Editor of EPI-IJE,
Director, Research and Development Center for Disaster Study, UNHAS

TABLE OF CONTENTS

Landslide Disaster Risk Assessment Model in Soppeng Regency, South Sulawesi

Adi Maulana[a,b,*], Suharman Hamzah[c], Iswandi Utama[d], Jamal Rauf Husain[e]

[a]Research and Development Center for Disaster Study, Hasanuddin University, Makassar, Indonesia. E-mail: adi-maulana@unhas.ac.id
[b]Department of Geological Engineering, Faculty of Engineering, Hasanuddin University.
[c]Department of Civil Engineering, Faculty of Engineering, Hasanuddin University, Indonesia.
[d]Department of Geological Engineering, Faculty of Engineering, Hasanuddin University.
[e]Department of Geological Engineering, Faculty of Engineering, Hasanuddin University.

Abstract

Landslide disaster risk assessment model has been proposed for Soppeng Regency which is located in the central part of South Sulawesi Province. Some areas in this regency are classified as landslide prone area based on its geological condition. This study is aimed to assess the landslide vulnerability level and produce a landslide vulnerability map by using mapping method as a basis to model the risk reduction assessment. The component of disaster risk assessment consists of threats, vulnerabilities, and capacities. These components are used to obtain the level of disaster risk in an area by calculating the potential for exposed lives, loss of property and environmental damage. The result shows that Soppeng Regency region has some areas that are prone to landslides with low-high levels. The Vulnerability Assessment is classified as medium level whereas the result of landslide disaster capacity assessment is also shown as medium level. Based on these analyses, it was concluded that Soppeng Regency had a high landslide threat index, with a medium exposed population index and a medium capacity index. The study of landslide disaster risk assessment in Soppeng Regency has shown that Soppeng Regency has been classified as landslide prone area with the medium risk level, especially in mountainous and river bank area. It is recommended that disaster risk assessment model should be used as one of the references for providing disaster risk mitigation plan in disaster risk reduction program.

Keywords: Assessment; disaster; landslide; risk; Soppeng; South Sulawesi

1. Background

Disaster risk assessment is the basis for choosing a strategy that is considered capable of reducing disaster risk. This disaster risk assessment must be able to become an adequate basis for regions to develop disaster management policies [1]. Disasters occur due to the collectivity of the hazard components that affect nature and environmental conditions, as well as how the level of vulnerability and capacity of a community in managing threats [2]. The higher the value of threats and vulnerability, the higher the risk of disaster to occur. To reduce the risk of disaster, the needs to reduce the value of vulnerability and increase the capacity of the community is of paramount importance that is by strengthening the capacity within the community to manage the environment, recognize the threat and know the impact that can be caused by the factors that cause the disaster [3].

Corresponding author. Tel.: +62-821-9502-4779
Jalan Poros Malino km. 6, Bontomarannu, Gowa
South Sulawesi, Indonesia 90245

At the community level, the results of the assessment are expected to be a strong basis in planning disaster risk reduction efforts [4]. The value of disaster risk depends on the interaction between the magnitude of the threats and vulnerabilities. Hence, the interaction of threats, vulnerabilities, and external factors is the basis for conducting a disaster risk assessment of an area.

Soppeng Regency is one of the regencies in the province of South Sulawesi, Indonesia with the capital city located in Watansoppeng City. This regency has an area of about 1,500 km² and can be divided into three geomorphological units, namely plain, hills and mountainous units. The plain unit occupies the eastern and northern sections with an area of 700 km2 with an elevation of approximately 60 m above sea level. Mountains and hills morphology has an area of about 800 km2 at an average altitude of 200 m above sea level. The plain unit is generally located in Walanae depression which is partially filled by material alluvial forming Lake Tempe in the north and the Walanae River, flowing to the east and southeast [5].

Judging from the existing morphological conditions, especially in mountainous morphology, some areas in this regency can be classified as landslide disaster area [6]. The landslide in this area has caused enormous damage in road construction, bridge, irrigation canal and settlement area [6]. In addition, BNPB in 2018 also included the Soppeng Regency, especially those in mountainous and hilly areas as landslide-prone areas. The landslide also accounts for less physical loss and human life [5]. As an effort to reduce disaster risk, a study on landslide disaster risk assessment in Soppeng Regency is conducted to reduce the level of vulnerability of landslides. The component of disaster risk assessment consists of threats, vulnerabilities, and capacities. This component is used to obtain the level of disaster risk in an area by calculating the potential for exposed lives, loss of property and environmental damage. In addition to reduce the level of risk, the study is also expected to be able to produce a landslide vulnerability map in Soppeng Regency. This vulnerability study report and map will be an adequate basis for the local government to develop disaster management policies. At the community level the results of the assessment are expected to be a strong basis in planning disaster risk reduction efforts.

2. Regional Geology

Soppeng Regency is included in Regional Geological Map of Pangkajene and Western Part of Watampone Map [7]. Almost 80% of Soppeng region is located in the Walanae Depression which was formed by a major north northwest – south southeast trending fault system of the Walanae Zone in Late Neogene. The Late Neogene basin is filled by clastic sediments containing fossils of Late Miocene age. The clastic deposit is called as Walanae Formation showing Late Miocene to Holocene clastic sequences. In the Soppeng area, the West Sengkang Basin sediments are dominated by calcareous grey clay¬stone in the lower part of the Walanae Formation, known as the Burecing Member, after Burecing Village along the Cabenge –Pampanua road. Locally, small carbonate reefs of the Tacipi Member were formed in the East Sengkang Basin, where these shallow marine facies interfingered with or conformably overlaid marine claystones representing the base of Late Miocene Walanae Forma¬tion. The claystone accumulated in the down faulted Walanae depression and north of the Bone Mountains [8]. The western part of the regency, especially in the mountainous hill, is covered by a series of very thick volcanic sequence called Soppeng Volcanic [7] which is Miocene in age. The volcanic consist of tuff, breccia and lava flow with the present of feldspathoidal rich volcanic rocks. The geological map of Soppeng Regency can be seen in Fig. 1 below.
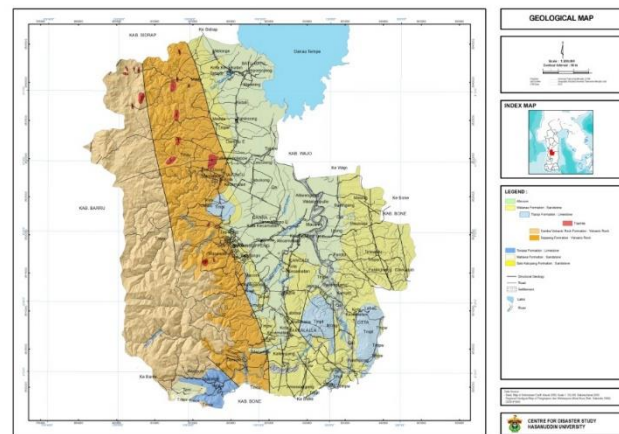
Figure 1. Geological map of Soppeng Regency [7]

3. Methodology

The method used in this study consists of 2 methods;
1) Mapping of landslide-prone areas in Soppeng Regency;
2) Risk reduction assessment method.

3.1. Mapping disaster-prone

General prerequisites for making a disaster-prone map are:
- Map scale with a scale of 1: 50,000
- Able to count the number of people exposed to disasters.
- Able to calculate the value of property loss and environmental damage (in rupiah).
- Using 3 risk level interval classes, i.e. high, medium and low risk levels.
- Using GIS with Grid Analysis (10 meters) in disaster risk mapping.

3.2. Risk reduction assessment method

- Threat assessment method
Determination of the level of disaster threat using a threat level matrix, by combining the landslide hazard index in the lane with the population index exposed in the column. The threat index scale is divided into 3 categories: low (0.0-0.3), moderate (> 0.3-0.6), and high (> 0.6-1.0).

The exposed population index scale is divided into 3 categories, namely low, medium and high, with each index value as follows:
- Low: 0.0 - 0.3, if the population density is exposed to less than 500 people/Km^2, and the population of vulnerable groups is less than 20%.
- Medium:> 0.3 - 0.6, if the population density is exposed to 500-1000 people/Km^2, and the population of vulnerable groups is 20% -40%.
- High:> 0.6 1.0, if the population density is exposed to more than 1000 people/Km^2, and the population of vulnerable groups is more than 40%.

- Vulnerability assessment method

Disaster vulnerability consists of socio-cultural, physical, economic and environmental components. Calculation of vulnerability of an area when exposed to a disaster threat consists of 3 vulnerability indices. The index is the Reported Population Index (in life units), Loss Index (in Rupiah units) and Environmental Damage Index (in hectares). Loss Levels can be prepared if the Threat Level in an area has been assessed. Loss Levels are obtained from combining Threat Level with Loss Indexes. Determination of Loss Levels is done using a matrix, determination is carried out by connecting the two index values in the matrix. The color of the meeting place symbolizes the level of loss that may be caused by a disaster in the area.

- Risk assessment method

Based on the identification of disasters described previously, the disaster index will be processed into a disaster risk assessment. In reviewing disaster risk studies, the guideline used is the General Guidelines for National Disaster Risk Assessment issued by BNPB in 2012. The guideline states that the disaster risk assessment will provide an overview of the regions related to the level of risk of a disaster in each region. Risk assessment consists of determining the level of threat, determining the level of loss and determining the level of capacity, especially in landslide disaster. This process is by reformulating the results of mapping and supplement maps in the form of a matrix into a predetermined value table. Figure 2 below illustrates the flow for the analysis of landslide disaster risk studies. From this figure, a level determination is made for each variable. Determination is made by connecting the two values described in accordance with the characteristics of the disaster.

4. Results and Discussions

Data processing in this study consist of several processes to obtain the parameters causing landslides. Rainfall, geology and land cover maps in the form of shapefiles are made of clips in the study area. Google earth image data processing is carried out by supervised classification which is classified into 10 classes of land cover namely Forests, Shrubs, Rivers, Gardens, Fields, Rice Fields, Open Land, Settlements, River Cliffs, Road Cliffs (Table 1). Then the results of the classification are tested with the field and IFSAR DEM processing is carried out to obtain the slope, the DEM is extracted into contours and slopes. The slope of the DEM is classified into 5 classes. The slope of the DEM data extraction is in the form of raster because it must be converted into shapefile data by reclassify to get the slope info table then convert raster to polygon. After the landslide parameters are obtained then a score is given for each class and the weights for each parameter are then overlaid. The processing flow is shown in Fig. 3 and Landslide vulnerability map can be shown in Fig. 4.

Figure 3. Flow diagram for Making Landslide Hazard Map Based on Soil Movement Vulnerability Zones [3]
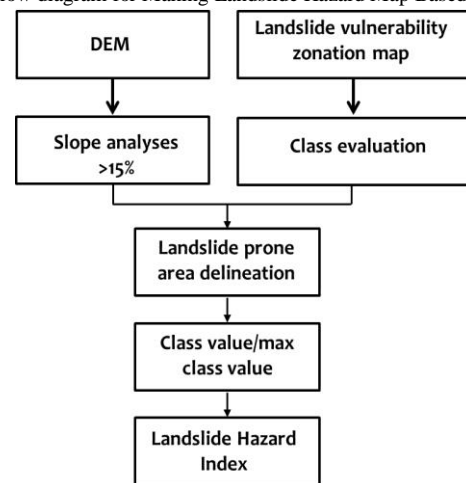
Figure 2. The flow diagram analysis of disaster risk studies [3]
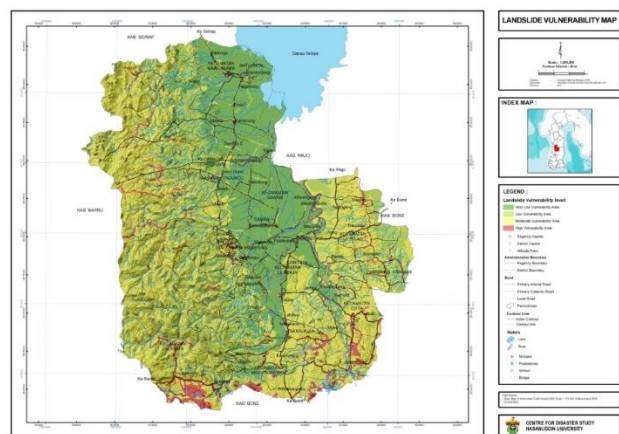
Figure 4. Landslide vulnerability map of Soppeng Regency

Table 1. Parameters that affect the occurrence of landslides in Soppeng Regency

Paramater	Unit	Score	Value	Percentage
Geology	Alluvium	3	2	20%
	Sandstone	3		
	Limestone	4		
	Volcanic Rock	4		
	Trakit	1		
Slope	> 40%	3	3	30%
	25-40%	2		
	15-25%	2		
	0-15%	1		
Rain fall	2000-2500 mm	2	1	10%
	1500-2000 mm	1		
Land Cover	Forest	1	3	30%
	Bush	1		
	Garden	1		
	Field	1		
	Open land	2		
	Settlement	2		
	River Bank	3		
	Road cliff	3		
Soil Weathering rate	Soil thickness >1 m	3	1	10%
	Soil thickness 0.3-1 m	2		
	Soil thickness <0.3 m	1		

Determination of the level of vulnerability of the landslide area in the study area is based on the estimation model of the landslide-prone area by being adjusted to the parameter conditions that triggered the landslide in Soppeng Regency using the following formula:

$$\text{Score} = (10\% \times \text{rainfall class factor}) + (20\% \times \text{geology}) + (10\% \times \text{weathering class factor}) + (30\% \times \text{land use}) + (30\% \times \text{slope class factor}) \tag{1}$$

4.1. Disaster threats assessment

Soppeng Regency region has some areas that are prone to landslides with low-high levels. The threat of landslides with high levels of landslides is in the southern part of Soppeng Regency, especially along Walanae River bank and several in the western part of Soppeng Regency. River bank landslides are the impact of high destructive power water flow during heavy rain which eroding river bank and river bed. Walanae River in Soppeng Regency is one of the locations that are affected and have river bank landslide vulnerability. The occurrence and vulnerability of river bank landslides can be analyzed through river morphometry and land use. The tendency of river morphometry to affect river bank landslide vulnerability can be analyzed through river bank landslide vulnerability maps which are validated by field checks.

Slopes from road sections are very susceptible to landslides, especially road slopes in the form of settlements and vacant land. Factors that cause landslides are caused by road cuts that are too steep, absence of talud on the road slopes, cuts in drainage and slopes left unused. Lithology of rocks on the slopes of the road which is volcanic rock is very vulnerable because the clay material from tuff is very easy to weathered and erode hence cause the path of water seepage that can be a trigger for landslides.

4.2. Landslide vulnerability assessment

Around 73 percent or 109,000 hectares of Soppeng Regency are in hilly areas with a slope of between 25-45% (10-23°) and more than 45% (> 23°). Technically, this area is very prone to landslides especially along the road slopes and settlements in hilly areas and triggering the mass movement. The mass movement can occur if rainfall is above normal, especially in areas bordering river valleys, cliffs, road cliffs or if slopes are disturbed.

Based on the Vulnerability Assessment, a landslide disaster in Soppeng Regency will affect 37,570 people who live and/or have activities in areas prone to landslides. For the Index of Losses, the results of the disaster risk assessment show that physical losses amounted to Rp.114,315,000,000 and economy due to landslide disasters amounting to Rp. 97,124,562,144. The threat of landslides also has the potential to damage the environment. The Environmental Damage Index due to landslides from a broad disaster risk assessment and threatened threat index is calculated around 2,698 Ha. The vulnerability factors of the landslide are mainly due to changes in land use to settlements, agriculture and plantations, roads, population density, and community behavior. Areas that were once forests then shifted into other functions, causing the area to be prone to landslides. Table 2 below shows the Soppeng Regency in various levels of landslide hazards.

4.3. Landslide disaster capacity assessment

Capacity for landslides covers various things such as facilities and infrastructure, information systems, human resources and community preparedness. The local government has been and is making various efforts to prevent landslides including construction such as gabions on slopes that have been opened for the benefit of building public facilities such as roads and settlements. The result of landslide disaster capacity assessment is shown in Table 3. For early information on landslides in Soppeng Regency, the following matters are needed to be considered;

- The existence of cracks in the land (agriculture, forest, gardens, and settlement) and/or roads that tend to get bigger in volume that can easily be seen visually.
- There are markings / subsidence on the asphalt road that can be seen visually.

- Installation of rainfall meter around areas prone to landslides. If the cumulative rainfall in a row for 2 days exceeds 200 mm while the 3rd day still seems to be raining, the community must be vigilant.
- The presence of water seepage at the foot of the slope, road cliffs, house yard cliffs (previously there has never been a renovation) or the flow of seepage (discharge) is greater than before.
- The existence of trees whose position is leaning towards the bottom of the hill.
- Changes in land cover (from forest to non-forest) on steep sloping land and moderate depth of soil.
- The existence of cliff cuts for roads and or housing on steep sloped land and deep soil layers.

4.4. Landslide risk assessment

Soppeng Regency has a high risk of landslides, especially on the slopes of road and river bank. The records of landslide events in Soppeng Regency both in terms of frequency and scale clearly show this threat is increasing. Figure 4 is a map of landslide-prone hazards in Soppeng Regency. Based on the study of disaster risk, it was concluded that Soppeng Regency had a HIGH landslide threat index, with a MEDIUM exposed population index and a MEDIUM capacity index (Table 5).

Table 2. Loss Level due to disaster in Soppeng Regency South Sulawesi Province

LOSS LEVEL		LOSS INDEX (IN RP)		
		LOW	MEDIUM	HIGH
HAZARD INDEX	LOW			
	MEDIUM			
	HIGH		Landslide	

Table 3. Capacity level of Soppeng Regency South Sulawesi Province

CAPACITY LEVEL		CAPACITY INDEX		
		LOW	MEDIUM	HIGH
HAZARD INDEX	LOW			
	MEDIUM			
	HIGH		Landslide	

Table 4. Landslide Risk Disaster Level of Soppeng Regency South Sulawesi Province

DISASTER THREAT LEVEL		CAPACITY INDEX		
		LOW	MEDIUM	HIGH
HAZARD INDEX	LOW			
	MEDIUM			
	HIGH		Landslide	

5. Conclusions

The study of landslide disaster risk assessment in Soppeng Regency has shown that Soppeng Regency has been classified as landslide prone area with the medium risk level. The landslide disaster risk assessment method can be used as a reference to provide disaster risk mitigation plan which is very important to reduce the risk of the disaster.

Acknowledgments

References

[1] Klinke, A., Renn, O., A new approach to risk evaluation and management: risk-based, precaution-based, and discourse-based strategies. Risk Analysis 22(6), 1071-1094, 2002.
[2] The Royal Society, Risk analysis, perception and management', UNISDR, 1992.
[3] BNPB, General Guidelines for National Disaster Risk Assessment. Jakarta, Indonesia, 2012.
[4] Djalante, R., Disaster risk reduction and climate change adaptation in Indonesia: Institutional challenges and opportunities for integration. International Journal of Disaster Resilience in the Built Environment 3(2), 166-180, 2012.
[5] BPBD Soppeng, Disaster Information Data of Soppeng Regency. Soppeng, Indonesia, 2018. [in Bahasa]
[6] Maulana, A., Geological constraints for disaster mitigation model in South Sulawesi. Journal of Physic, IOP Conference Proceeding Series, 2019.
[7] Sukamto, R., Geological Map of Pangkajene and Western Part of Watampone, Geological Research Centre, Bandung, Indonesia, 1982.
[8] Suyono., Kusnama, Stratigraphy and Tectonics of the Sengkang Basin, South Sulawesi. Jurnal Geologi Indonesia, 5, 1-11, 2010.

Mitigation Schemes for Banggae Future Tsunami, West Sulawesi Province, Indonesia

Achmad Yasir Baeda[a,*], Nurhidayani Namiruddin[b]

[a]Marine Disaster and Weather Anomalies Laboratory, Department of Ocean engineering, Universitas Hasanuddin, Makassar, Indonesia.
  E-mail: baeda@eng.unhas.ac.id
[b]Department of Ocean Engineering, Universitas Hasanuddin, Makassar, Indonesia.

Abstract

Geologically, Sulawesi Island is a complex area. It is caused by the convergence between three lithosphere plates, where the Australian Plate drifting to North, Pacific to West, and Eurasia from South to South-East respective. The future tsunami simulation was done by using SiTProS (Siam Tsunami Propagation Simulator) Version 1.5., which uses data such as earthquakes coordinate, magnitudes, focus depths, and propagation scheme, as the main input parameters in the simulations. Based on those future tsunami simulations results, the mitigation scheme chosen for Banggae District of Majene Region, West Sulawesi Province is the Vertical Tsunami Mitigation scheme. Due to its detailed parameters i.e. population details, evacuation time, distance and speed, the Vertical Tsunami Mitigation Scheme can determine the existence of shelters parameters and analyze the additional shelters needed in precise manner.

Keywords: Banggae; mitigation; sulawesi; tsunami

1. Introduction

Sulawesi Island has a development for tectonic activities since tertiary era. Due to this development, Sulawesi is included as one of active place in Indonesia which has geologically complex phenomenon. The tectonic manifestation formed fault and volcano in Sulawesi, such us; Walanae Fault in South Sulawesi, Palu Koro Fault expanded from Flores to Makassar Strait, Gorontalo Fault, Batui Fault in Central Sulawesi, Matano Fault, and Kolaka Fault (Southeast Sulawesi). The intersection areas of fault should be watched out and get more attention because these are the areas which generate earthquake causing geological problem.

Based on the historical data, it can be said that the earthquake and tsunami that happened in Majene in 1969 with 6.9 magnitude was caused by the movement of Saddang Fault and several small tectonic activities in South Sulawesi Province at that time. The movement of sea floor spreading in Makassar Strait that moved from West to East, can cause pressure impact to the region near by the Saddang Fault. Moreover, the activity of Saddang Fault is also caused by the movement of small plates such as Tempe Lake and Sidenreng (East side of Saddang Fault) which are moving from North-West to East respectively. Besides, the movement of sea floor spreading from East to West at Bone Bay was also actively contributed to tsunamigenic-earthquake event in 1969. The development of this mitigation schemes was based on future tsunami modelling for Banggae Beach, West Sulawesi Province.

Tsunami is a series of ocean waves typically caused by undersea earthquakes or volcano eruptions at tectonic plate boundaries. The surges of water may reach 100 feet and cause widespread destruction when they crash ashore. They race across the sea at a speed up to 500 miles per hour and cross the entire Pacific Ocean in less than a day. Their long wavelength means that they lose very little energy along the way.

*Corresponding author. Mobile:+62-851-4500-7300
Faculty of Engineering, UNHAS
Jl. Poros Marino, Bontomarannu, Gowa, South Sulawesi 92171
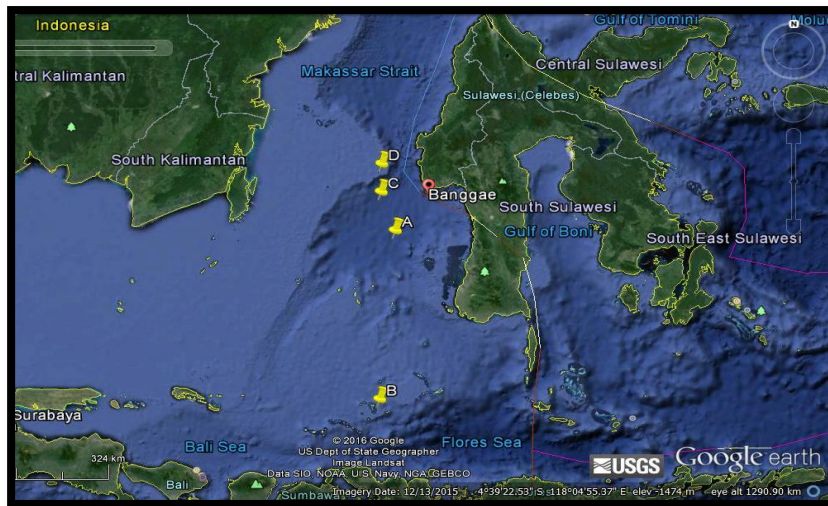
Figure 1. Territory restriction for tsunami simulation in Banggae (from Google Earth)

2. Research Methods

The data collected in this research are underwater earthquake direct observation in Banggae Beach, Majene Regency West Sulawesi. The underwater earthquake data were collected from Global Moment Tensor (Global CMT) and USGS which are has >5 magnitude. The territory restriction for this research was done in google earth as seen in figure 1, those data will be simulated in SiTProS version 1.5.

The results of this propagation modeling become the input of the preparation for developing a suitable mitigation schemes conducted by direct observation at Banggae Beach, Majene Regency, West Sulawesi Province.

3. Analysis and Discussion

Majene is a coastal city bordered by the Mandar bay and the strait of Makassar to the west, and it comfortably nestled in a semicircular valley against a backdrop of rolling, forested hills. The city covers a total area 55.19 square kilometers. Majene Regency consists of 8 districts; Banggae, West Banggae, Pamboang, Sendana, Rangas, Tubo Sendana, Malunda, and Ulumanda. The capital of Majene Regency is located in Banggae District. Geographically, Majene is located in 2'38'45''N - 3'38'15" N and 118'45'00" E – 119'4'45''E.

In 1969, an earthquake occurred in Majene and caused 64 people died, 97 people injured, and 1287 residences and public areas were damaged and destroyed. The pier broke along 50 meters and it raised 4 meters tsunami wave in Palatoang and 1.5 meters in Parasanga and Palili.

The tsunami was caused by the activity of Saddang Fault influencing another seismic activities in South Sulawesi.

Due to the historical tsunami accident, the government in Banggae has already prepared for future tsunami. They already put and point out several places as the evacuation areas. Generally, most of every districts in Banggae can reach the evacuation areas except Rangas district.

Modeling of tsunami propagation is done by Siam Tsunami Propagation Simulator (SiTProS) Version 1.5 which is based on a regional or global network with bathymetric and topographic dataset of ETOPO2. The basic term of determining the source of the tsunami in the form of underwater earthquakes are based on Sulawesi's Seismic Systems of faults that can generate tsunami [1, 2]

Figure 2. The city of Banggae (from Google Earth)
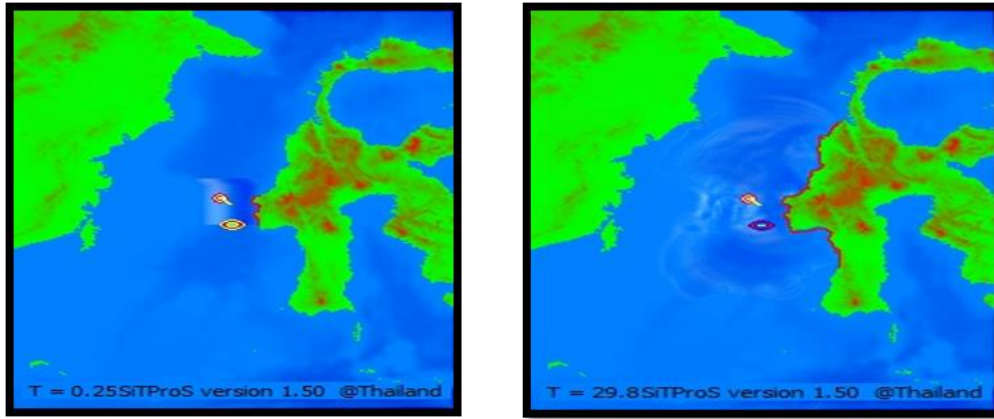
Figure 3. Tsunami Simulation in Banggae Beach with magnitude **6.9**, Majene Regency, West Sulawesi Province
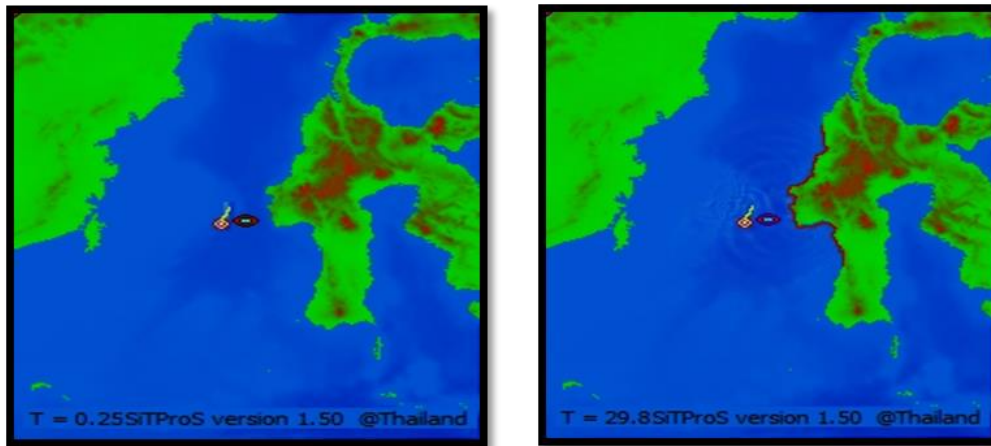
Figure 4. Tsunami Simulation in Banggae Beach with magnitude **5.8**, Majene Regency, West Sulawesi Province
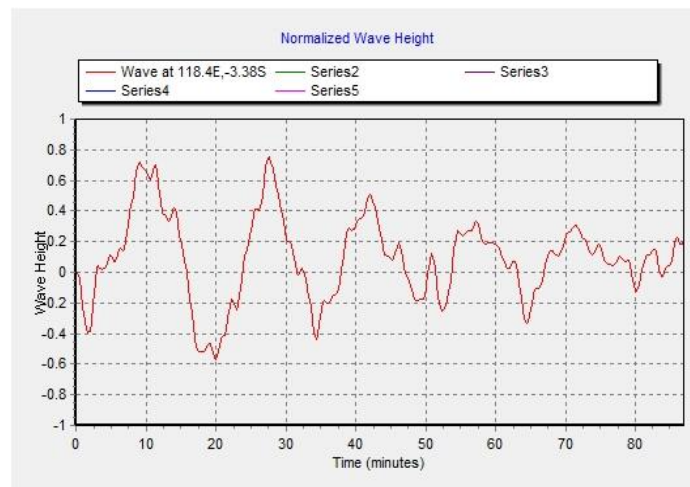
Figure 5. A 6.9 Magnitude Banggae tsunami (normalized) and its time series in minutes
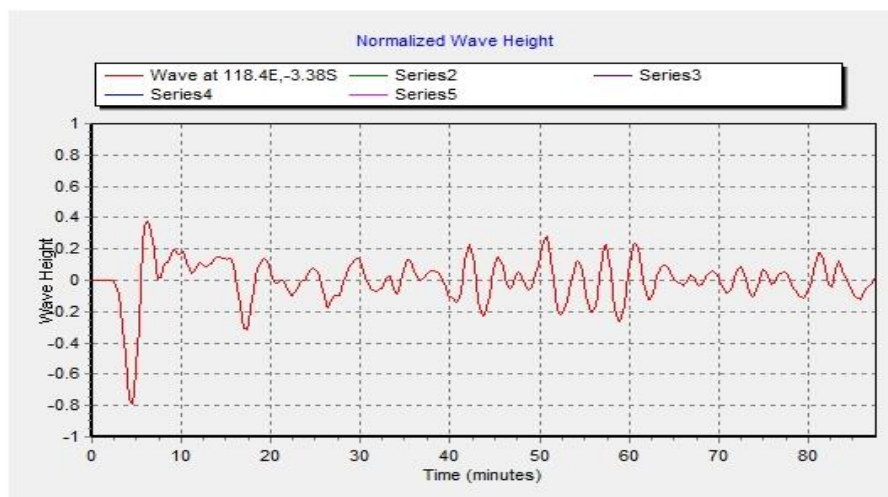
Figure 6. A 5.8 Magnitude Banggae tsunami (normalized) and its time series in minutes

Tsunami Simulation

The tsunami is generated by using underwater earthquake data in Makassar Strait which is taken from USGS and Global CMT. The epicenter of underwater earthquake is located in 118.72E and -2.77S depth 14.8 km with magnitude 6.9 and 118.12E and -3.44S depth 18.8 with magnitude 5.8.

Based on the simulation, tsunami reaches shore at 9 minutes with magnitude 6.9 after the main shock. The high-wave of tsunami can be seen in Fig.5.

Based on simulation result, it can be seen that the fluctuation happened at minute 3 (initial drawndown), and the arrival tsunami waves to shore at minute 9 (run-up). It is obviously seen that the fluctuation of tsunami waves happens repeatedly until minute 70. By using the Aydan's formula [3], it found out that the earthquake in epicenter of -2.77S and 118.72E has a moment magnitude (Mw) = 6.7, so;

$$Hm = A \times Mw \exp (b \times Mw)$$
$$Hm = 0.004 \times 6.7 \exp (0.9 \times 6.7)$$
$$Hm = 11.14 \text{ m}$$

Because the maximum wave height is 70% of the tsunami height, so;

$$Hm = 11.4 \times 0.7 = 7.80 \text{ m}$$

For the height of tsunami run-up:

$$\Delta Hr = B \times Hm$$

$$\Delta Hr = 2.5 \times 7.80$$

$$\Delta Hr = 19.50$$
$$Hr = Hm + \Delta Hr$$
$$Hr = 7.80 + 19.50$$
$$Hr = 27.30 \text{m}$$

The height of tsunami in buoy is 7.80 m with run-up 27.30. It is shows that the society in Banggae Beach only needs 9 minutes for evacuated.

In Fig. 6, we can see the arrival time for tsunami to shore at 6 minutes with magnitude 5.8 after the main shock. Based on simulation result, it can be seen that the fluctuation happened at minute 5 (initial drawndown), and arrival time for tsunami waves in shore at minute 6 (run-up). This indicates that the maximum wave crashing on the beach occurred at the first wave. By using the Aydan's formula (2008), it can be found out that the earthquake in epicenter of 118.12E and -3.44S has a moment magnitude (Mw) = 5.8 SR, so;

$$Hm = A \times Mw \exp (b \times Mw)$$
$$Hm = 0.004 \times 5.8 \exp (0.9 \times 5.8)$$
$$Hm = 4.29 \text{ m}$$

Because the maximum wave height is 40% of the tsunami height, so;

$$Hm = 4.29 \times 0.4 = 1.72 \text{ m}$$

For the height of tsunami run-up:

$$\Delta Hr = B \times Hm$$

$$\Delta Hr = 2.5 \times 1.72$$

$$\Delta Hr = 4.29$$
$$Hr = Hm + \Delta Hr$$
$$Hr = 1.72 + 4.29 = 6.01 \text{m}$$

The height of tsunami in buoy is 1.72 m with run-up 6.01. All the simulation shows that the short evacuating time is 6 minutes and the highest run up is 27.30m.

Tsunami Evacuation Time

According to simulation result by using SiTProS, this research found estimated time that can be used for evacuating. This evacuation time consist of early warning, preparation time, and evacuation time itself. This research takes the short time arrival tsunami waves to shore at 6 minute. The evacuation time analysis can be seen in Fig. 6.
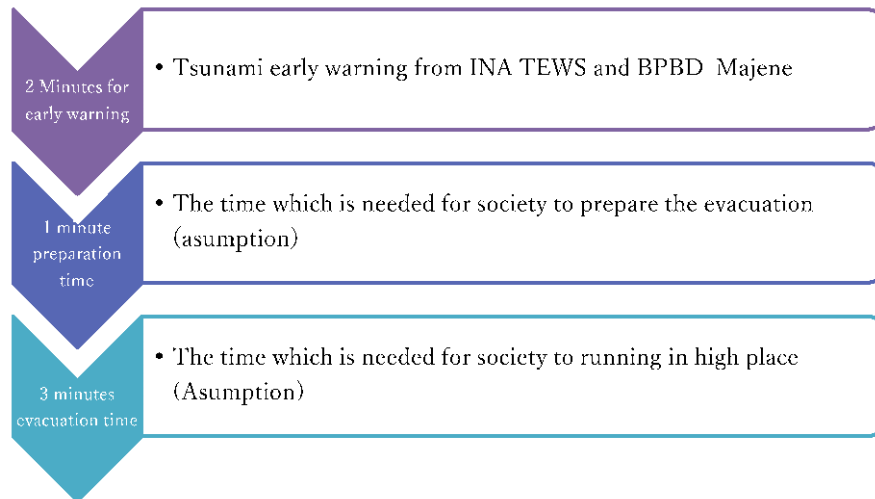
Figure 7. Tsunami Evacuation Time in Banggae Beach, Majene Regency, West Sulawesi Province
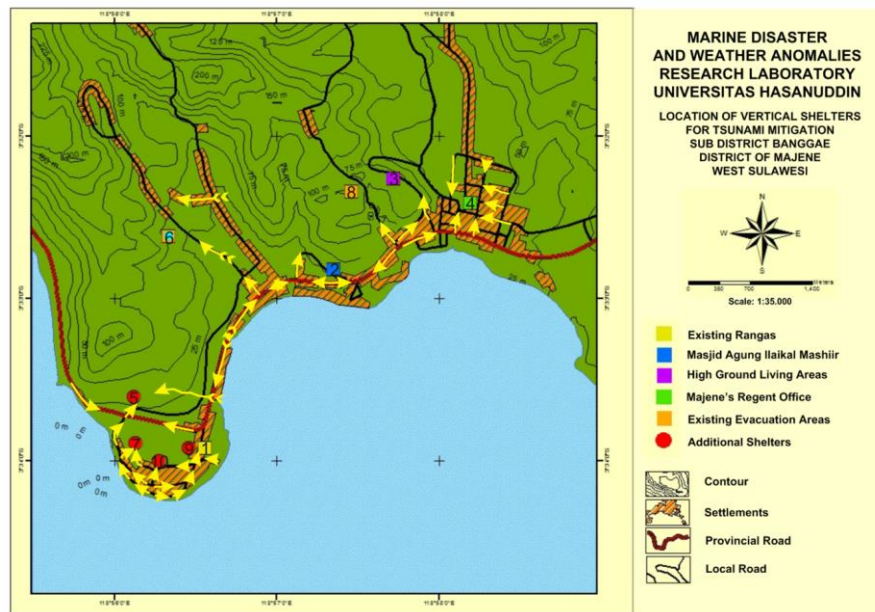
Figure 8. Shelters location for Banggae, Majene Regency, West Sulawesi Province

EvacuationWalking Speed and Evacuation Distances

The evacuation walking speed applied is based on The Japan Institute for Fire Safety and Disaster Preparedness. The pace for Banggae beach is 0.751 m/s or 45.06 m/minutes. Because evacuation time is 3 minutes and evacuation walking speed is 45.06, so the evacuation distance is about 135 meters. Therefore the shelter location in Banggae beach should be around 135 meters. However, as seen the topographic and measured by the society walking speed, the shelter can be put around 300-500 meter.

Shelter capacity analysis

The temporary space requirements is 0.5 m² per person, so that two people can be placed in 1 m². In condition that the refugees will sit without chair for several hours. This sit position will take 0.42 m² until 0.55 m² per person [4].

Especially in Rangas district, the number of population is 7300, so that the space requirements that is needed 0.55 m² x 7300 = 4015 m².

Shelters Location

There will be 10 shelters location in Banggae, those shelters consist of 6 existing shelters and 4 additional shelters. All the additional shelters will be built in Rangas district. For society around Rangas the shelters location are shown in 1,5,7,9 and 10. While For society around Jl. Tenne Heiko, Jl. Kartini, Jl. Gatot Subroto the shelters location are shown in 2, 3, and 4. For society around Sandeq Monument Boat the shelter location is shown in 8. And for society around Jl. Ahmad Yani the shelter location is shown in 6. All of these shelters are located in crowded population so that society can be evacuated themselves when tsunami happens.

4. Conclusions

The tsunami mitigation in Banggae is focused for shelters location that it can be reached by local society when tsunami occur. In order to maximize the shelters location and reduce the number of victim and broken infrastructure during tsunami, they have to be well-managed due to the time arrival for tsunami to shore only 6 minutes. The shelters location and awareness about tsunami also should be socialized to the society. The evacuation can be done by fast walk, run, and by using motorcycle.

References

[1] Baeda, A.Y., et al., Tsunami Mitigation Plan for Manakarra Beach of West Sulawesi Province, Indonesia, 8th International Conference on Asia and Pasific Coast (APAC 2015), Procedia Engineering Vol. 116: 134-140, 2015.

[2] Baeda, A.Y., et al., Mitigation plan for future tsunami of Seruni Beach Bantaeng, 2nd International Seminar on Ocean and Coastal Engineering, Environment and Natural Disaster Management, ISOCEEN 2014, Procedia Earth and Planetary Science, ELSEVIER, Vol. 14 (2015): 179-185, 2015.

[3] Aydan O., Seismic and Tsunami Hazard Potential in Indonesia with a special emphasis on Sumatra Island, Journal of The School of Marine Science and Technology, Tokai University, Vol. 6 No. 3. pp 19-38, 2008,

[4] Neufert, E., 1980, Architects' Data, Blackwell Science Ltd. London.

Massive Fire Incidents of Multiple Aboveground Storage Tanks due to Vapor Cloud Explosion

Shoichi Yoshida[a],*

[a] Institute of Advanced Sciences, Yokohama National University, Yokohama, Japan. Email:yoshida-shoichi-pg@ynu.ac.jp

Abstract

The vapor cloud explosion (VCE) begins with a release of a large quantity of flammable vaporing liquid from a storage tank, transportation vessel or pipeline. If VCE occurs in an oil storage facility, multiple tanks burn simultaneously. There is no effective firefighting method for multiple tanks fire. It will be extinguished when oil burned out spending several days. Many incidents of multiple tanks fire due to VCE have occurred all over the world in recent 50 years. This paper reviews the past 6 incidents of multiple tanks fire due to VCE.

Keywords: Aboveground storage tank; incident; multiple tanks fire; overfill; vapor cloud explosion

1. Introduction

The VCE begins with a release of a large quantity of flammable vaporing liquid from a storage tank, transportation vessel or pipeline. After vapor diffuses like clouds in the atmosphere, it ignites explosively. If VCE occurs in an oil storage facility, multiple tanks burn simultaneously. Today there is no effective firefighting method for multiple tanks fire. It will be extinguished when oil burns out after several days. In addition, the fire causes severe environmental problem.

During the last half century, many VCEs have occurred in oil storage facilities. This paper reviews the VCEs at oil storage facilities that occurred in United States in 1975 and 1983, Italy in 1985, United Kingdom in 2005, and Puerto Rico and India in 2009.

2. Gulf Oil refinery in Philadelphia [1]

On August 17, 1975, at 5:57 am, VCE occurred in a refinery of Gulf Oil Corporation at Girard Point in Philadelphia, Pennsylvania, USA. One crude oil storage tank and two naphtha storage tanks exploded, causing massive fire, and extinguishing 10 days later. In this incident, 8 firefighters died and 14 were injured. This refinery was built

in 1905 and had a crude oil refining capacity of 180,000 barrel per day. As shown in Fig.1, the refinery is near the Philadelphia International Airport with the Schuylkill River at the confluence of the Delaware River.

At 0:45 am on the incident day, No.231 internal floating roof tank with nominal capacity 11,900 m^3 received crude oil from the tanker "Afran Neptune" by a pipeline. The tank was jointed by rivets, built in 1929. Even when the maximum liquid level was exceeded, the tank continued to receive crude oil, the oil leaked onto the floating roof and the hydrocarbon vapor began to leak from the vents on the fixed roof.

The boiler room next to the west side of the tank became the ignition source, and a small explosion occurred outside the tank at 5:57 am. The explosion caused crude oil leakage from the tank's vent. In addition, a fire broke out in a small sized No.114 fuel storage tank located in the same dike area. The fire contained at 8:44 am, 8 hours later.

The drains inside the refinery did not function, and the fire extinguishing agent used for firefighting activities and water for fire extinguishing were mixed with leaked crude oil and naphtha and collected like a pool on the east side of the No. 231 tank. An explosion and fire occurred again at this location at 4:41 pm, and many firefighters were killed and injured. This fire also burned No. 239 and No. 240 naphtha storage tanks and extinguished on August 26.

*Corresponding author. Tel.: +81-45-339-4458
79-5, Tokiwadai, Hodogaya-ku
Yokohama, Japan, 241-8501

Figure 1. Philadelphia, Pennsylvania, USA (from Google Earth)

Figure 2. Former Gulf Oil refinery in Philadelphia taken on October 8, 2011 (from Google Earth)

Figure 2 is a Google earth photo taken on October 8, 2011. The burned tank had already been removed, but the tank foundation remained. The cause of this incident is that the No. 231 tank overflowed while receiving crude oil, and the leaked hydrocarbon vapor ignited at the boiler room. In 1985, Gulf Oil Corporation merged with Standard Oil of California Co. to become Chevron Corporation. A massive fire broke out again at this refinery on June 21, 2019. The refinery was owned by Philadelphia Energy Solutions Inc. at the recent incident.

3. Texaco tank terminal in Newark [2]

On January 7, 1983, at 0:25 am, there were three large-sized gasoline storage tank fires due to VCE at the Texaco tank terminal in Newark, New Jersey, USA. The impact of the explosion was felt even in metropolitan areas such as Manhattan, Queens, Brooklyn in New York City. As shown in Fig.3, the site is several kilometers east of Newark Liberty International Airport. Figure 4 is a Google earth photo of the site taken in July 2007. The tank had already been removed, but the foundation remained. TK65, TK66, and TK67 were gasoline storage tanks where a fire broke out at the terminal.

Table 1 shows the size of the three gasoline storage tanks. The distance between each tank was 15 feet (4.6 m) to 30 feet (9.1 m). A small-seized TK66 was also in the same area.

The terminal supplied fuel to gas stations in northern New Jersey.

From January 6, 1983, the day before the incident, the TK67 tank had received gasoline from the pipeline. According to the company's operation manual, liquid level measurement was to be performed sequentially during acceptance to understand the liquid volume inside the tank, but this was not done on this day. Therefore, the liquid level reached the tank height and the gasoline overflowed. The worker noticed it at 11:50 pm, and a lot of gasoline had already leaked and vapor cloud had been generated. The tank was not equipped with a high level alarm or overfill prevention system.

The point marked "Ignition Site" in Fig.4 is a steel drum repair plant of Central Steel Drum Company, which is about 300 m away from TK67. An incinerator was ignited at this plant, and VCE occurred at 0:25 am on January 7. At the time of the explosion, the wind speed was 5 m/s from the southeast. In Fig.4, the incinerator was on the leeward side of TK67, and it was easy for vapor cloud to flow.

The three tanks continued to burn for three days and were extinguished when the gasoline was burned out. The burned gasoline is 3 million gallon (11,400 m^3). The incident killed a 40-year-old Texaco truck driver and injured 24 people. In addition, 45 freight cars were damaged in the freight train yard of Oak Island Conrail, which is adjacent to the southwest side of the site at the lower left of Fig. 4.

Figure 3. Newark, New Jersey, USA (from Google Earth)

Table 1. Tank list of Texaco tank terminal in Newark

Tank No.	Diameter	Height	Nominal capacity (Estimated)
TK64	57.0 m	17.1 m	41,000 m^3
TK65	36.6 m	17.1 m	16,800 m^3
TK67	24.4 m	14.6 m	6,300 m^3

Figure 4. Former Texas tank terminal in Newark taken in July, 2007 (from Google Earth)

Texaco merged with Chevron in February 2001 to become Chevron Texaco, and changed its name to Chevron Corporation in May 2005. There are several dozen tanks on the north side of the Texaco terminal at the top of Fig.4. These tanks were also present at the time of the 1983 incident. The owner at that time is unknown.

4. AGIP tank terminal in Naples [3]

On December 21, 1985, at 5:13 am, 24 oil storage tanks out of 37 tanks fired due to VCE at the Italian oil company AGIP's tank terminal in the San Giovanni a Teduccio district of Naples, Italy, and burned for 6 days.

On the afternoon of the day before the incident, the tankers "Agip-Gala" started to transfer gasoline to No. 17 and No. 18 tanks in the terminal. It was not normal for this tank terminal to accept multiple tanks at the same time, but the reason is unknown. Both tanks were scheduled to reach full capacity on December 21, at 6:30 am. However, the valve of the No.18 tank inlet line was closed, and as a result, the No.17 tank received all gasoline. No. 17 tank became full sooner than planned, and overflowed at 3:20 am on the 21st. The leaked gasoline remained inside the dike area, and vapor cloud was generated.

By 5:13 am, two hours after overflow occurred in the No. 17 tank, about 700 ton of gasoline leaked and VCE occurred. The ignition source is the nearby pump room. 24 tanks burned, and the fixed roof of 6 tanks flew about 50 m. The fire extinguished on December 27, seven days later. The incident killed 5 people, injured 170, and evacuated more than 2,000 nearby residents.

At the tank terminal, fuel such as gasoline and diesel was stored in 37 tanks up to 100,000 m³. The temperature at the time of the explosion was 8°C and the wind speed was 2 m/s. AGIP was merged with Eni Corporation in 2003.

5. Buncefield tank terminal in Hemel Hempstead

At 6:01 am on December 11, 2005, VCE occurred in Buncefield Hertfordshire Oil Storage Depot (Buncefield tank terminal) in Hemel Hempstead, 35 km northwest of

London, UK. The fire that burned 23 oil storage tanks lasted for five days. Forty-three people were injured and about 2,000 residents were temporarily evacuated in this incident, but fortunately there were no victims. The incident investigation committee jointly established with the UK Health and Safety Executive and the Environmental Agency issued a final report [4] in December 2008. Figure 5 is a Google earth photo of the Buncefield tank terminal taken on December 31, 2000 before the incident.

The Buncefield tank terminal was built in 1968 and was an oil storage facility jointly operated by three companies. Three pipelines received petroleum products from domestic refineries and ports, supplied them by tanker trucks to London and southeast England, and also supplied aviation fuel to Heathrow International Airport by pipelines.

The TK912 internal floating roof tank began accepting unleaded gasoline from a pipeline at 7 pm on December 10, the day before the incident. The liquid level of the tank was controlled in the control room by the Automatic Tank Gauging System, but the indication of the liquid level gauge stopped working around 3 am the next day. Filling continued, the liquid level reached the tank height around 5:30 am, overflowed from the top of the tank, and a vapor cloud was generated. The explosion occurred at 6:01 am and the ignition source is unknown.

This VCE burned 23 oil tanks. The massive fire contained on the afternoon of 12th, 32 hours later, but the small fire continued on the 13th. On the 14th, a new fire broke out in one oil storage tank, and the fire extinguished on the 15th. Due to this fire, 750 m³ foam extinguishing agent and 55,000 m³ fire extinguishing water were used. The amount of gasoline leakage until the explosion is 300 ton.

Figure 6 is an aerial photo of this fire, and Figure 7 is a Google earth photo taken on December 31, 2006, one year after the incident. It is confirmed that the burned tanks remained and did not hold the prototype.

Figure 5. Buncefield tank terminal taken before the incident (from Google Earth)

Figure 6. Massive fire in Buncefield tank terminal [4]

Figure 8. CAPECO location in Perto Rico (from Google Earth)

Figure 7. Buncefield tank terminal after the incident
taken on December 31, 2006 (from Google Earth)
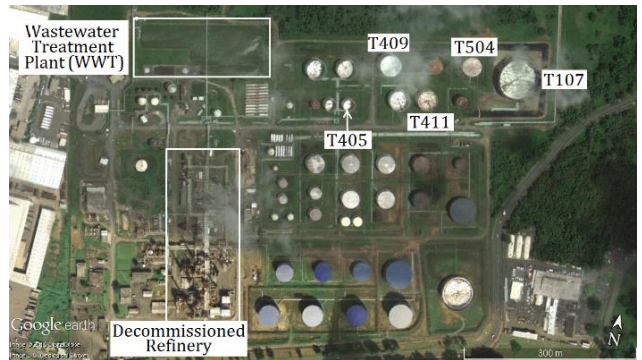
Figure 9. CAPECO tank terminal before the incident
taken on November 30, 2006 (from Google Earth)

6. CAPECO tank terminal in Puerto Rico

6.1. CAPECO tank terminal

On October 23, 2009, at 0:23 am, there was a massive fire of 17 oil storage tanks due to VCE at the Caribbean Petroleum Corporation (CAPECO) tank terminal in Bayamon near the capital of San Juan, Puerto Rico. It took 59 hours to extinguish. Three nearby residents were slightly injured and hundreds of houses were damaged by the impact of the explosion, but fortunately there were no victims. The cause of the incident was investigated by the U.S. Chemical Safety and Hazard Investigation Board (CSB), and a final report[5] was issued on October 25, 2015.

Figure 8 shows the location of CAPECO in Bayamon. The company had opened as a refinery in 1955, but went bankrupt in 2001. After that, the refinery was abandoned and the operation continued as a tank terminal with 170 gas stations in the island, which continued until the day of this incident. In San Juan Bay, 4 km northeast of the tank terminal, there was a dock where tankers are anchored, from which oil was transferred to tanks in the terminal by pipelines. The terminal had 48 oil storage tanks that store 90 million gallons (340,000 m^3) of gasoline, aviation fuel,

diesel, etc. Figure 9 shows this tank terminal layout before the incident.

CAPECO site consists of four areas: a tank terminal, an abandoned refinery, a wastewater treatment plant(WWT), and a management building as shown in Figure 9. WWT is a pond for storing rainwater and oil containing water, and has its treatment facility.

6.2. Incident of CAPECO

On October 21, 2009, a tanker loaded with 11.5 million gallon (43,600 m^3) of unleaded gasoline and anchored at the CAPECO dock in San Juan Bay. Gasoline was decided to transfer to four tanks, that is T405, T504, T409 and T411, from the tanker by pipeline.

The transfer to T405 and T504 was completed by noon on October 22. Next, transfer of T409 and T411 was prepared. The inlet lines for both tanks were the same. The operator set the T409 valve to "full open" and the T411 to "partially open". It was sent to T409 at 7,000 gallon/min. (26.5 m^3/min.) and to T411 at a lower flow rate. Around 6:30 pm, the tank operator read the liquid level of T409 from the on-site indicator of the float-type liquid level gauge, and reported it to the manager. The manager estimated the T409 full liquid time at 9 pm on October 21.
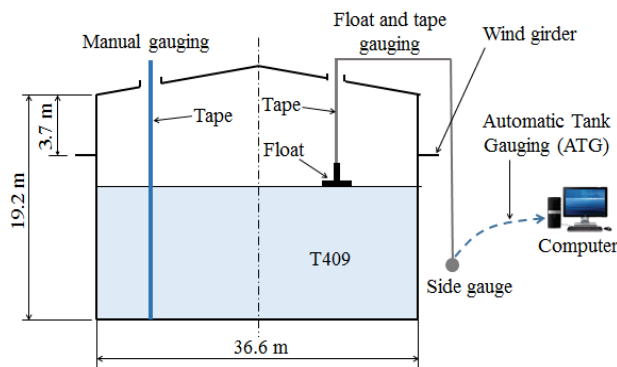
Figure 10. Tank gauging system in T409 tank

Figure 11. Massive fire in CAPECO tank terminal [5]

Figure 10 shows a liquid level gauging system of the T409 tank. As the transmitter of the float type liquid level gauge was in failure, the liquid level could not be controlled by computer using the automatic tank gauging. In addition, the high level alarm and the overfill prevention system, which were independent from the liquid level gauge, were not installed. As shown in Figure 10, T409 had a diameter of 36.6 m, a height of 19.2 m and a nominal capacity of 19,000 m^3. It was a fixed roof tank with an aluminum internal floating roof.

If the T409 tank continued to be receive gasoline, the estimated full liquid time would overlap with the work shift time. The operator set the T411 valve to "full open" and the T409 to "partially open". The scheduled full liquid time of T409 was delayed, and T411 would become full at 10:00 pm. After 10:00 pm, the valve of T409 was set to "full open", and the manager estimated full liquid time at 1 am on October 23. However, this estimation was not accurate, and gasoline overflowed from T409 between 11:00 am and midnight on the next day. It leaked from six vents on the fixed roof and flowed into the dike area while generating vapor clouds.

When the operator came near T409 to measure the liquid level at 0:00 am on October 23rd, he felt something like a white mist up to 3 feet (0.91 m) high from the ground and gasoline odor. Because the lighting on the site was dark, he could not see gasoline flowing down from T409 and hear the sound. The operator asked the other operator in the dog to cancel to transfer gasoline using wireless. The fog condensed on his hands. The temperature was 26 °C and it was light wind. T409 was located on a high ground in the tank terminal, and it was a terrain where vapor clouds could easily flow downward.

At 0:23 am on October 23, the surveillance camera at the facility adjacent to CAPECO caught the vapor cloud in the WWT area suddenly shining and ignited. Seven seconds later, a big explosion equivalent to Richter scale 2.9 occurred. As a result, 17 of the 48 oil tanks fired simultaneously. CSB final report [5] could not identify the ignition source. The leak start time was at 11:57 pm on October 22, 26 minutes before the ignition. The fire extinguished at 11:30 am on October 25, 59 hours later. Figure 11 is a photo of a fire in the CAPECO tank terminal [5].

CAPECO went bankrupt on August 12, 2010 due to this incident. On May 11, 2011, Puma Energy Caribe, LLC acquired the terminal and 147 gas stations in the island. In addition, the company took over the post-incident clean-up and various improvements that the regulatory authorities imposed on CAPECO.

7. IOCL tank terminal in Jaipur

7.1. IOCL tank terminal

On October 29, 2009, at 7:25 pm, massive fire of 11 oil storage tanks occurred due to VCE at the tank terminal of Indian Oil Corporation Limited (IOCL), a state owned oil company, in Jaipur, Rajasthan, India. It took 11 days to extinguish. Eleven people were killed and about 45 injured in this incident. The Ministry of Petroleum and Natural Gas constituted the investigation committee consisting of seven experts the day after the incident, and its final report[7] was submitted on January 29, 2010.

Figure 12 is a Google earth photo showing the layout of the tank terminal taken on November 14, 2011, two years after the incident. In the tank yard, which is upper middle in this figure and called "Main Tank Area", nine tanks which burned in the incident remained. These tanks stored fuel transferred from the IOCL refinery in Kojari, Gujarat. Piping Division Area was the pipeline relay station that sent crude oil to other IOCL refineries. There were two fire water storage tanks in the Fire Water & Pumping Area.

Figure 13 shows the enlarged Main Tank Area. Table 2 shows the tank list of this terminal. There were 11 oil storage tanks, and the total nominal capacity was 110,370 m^3. Nine of the eleven were located in the Main Tank Area and were grouped by three. "Motor spirit" in the table means gasoline.

Figure 12. Layout of IOCL tank Terminal (from Google Earth)

Figure 13. Main Tank Area of IOCL tank terminal (from Google Earth)

Table 2. Tank list of IOCL tank terminal

Tank No.	Material stored	Nominal capacity (m^3)	Diameter (m)	Height (m)	Tank type
401A	MS	6,110	24	15	FRT
401B	MS	6,110	24	15	FRT
401C	MS	6,110	24	15	FRT
402A	SKO	5,080	18	20	CRT
402B	SKO	5,080	18	20	CRT
402C	SKO	5,080	18	20	CRT
403A	HSD	20,000	36	20	CRT
403B	HSD	20,000	36	20	CRT
403C	HSD	20,000	36	20	CRT
409A	MS	8,400	28	15	FRT
409B	MS	8,400	28	15	FRT
T-401A	Fire Water	2,460	14	18	CRT
T-401B	Fire Water	2,460	14	18	CRT

MS : Motor spirit   FRT : Floating roof tank

SKO : Super kerosene oil   CRT : Cone roof tank

HSD : High speed diesel

7.2. IOCL incident

The terminal received an order for 1,567 m^3 of gasoline and 850 m^3 of kerosene from a customer on the morning of October 29, 2009, and was transferred by pipeline from the evening. In the Market Division, one manager and three operators were responsible for this transfer work. After starting kerosene transfer from 402A tank, they moved to 401A tank for gasoline transfer. At this time, one operator came home without permission.

At around 6:10 pm, the manager heard an operator "A" screaming on the opposite side of the 401A tank. When he rushed to there, he saw gasoline squirting from the Hammer Blind Valve vertically to the height of a human like a fountain. The operator A was soaked and had difficulty breathing. The manager took the operator A and tried to carry him to a safety place outside the dike, but the manager also became difficult to breathe due to gasoline vapor. He lowered the operator A, went out the dike, shouted for a gasoline leak, and then fell on the road between the 401A tank and the 403C tank.

Another operator "B" was drinking tea in the cafeteria at that time. He heard the sorrowful cry of the manager and rushed to the 401A tank. Furthermore, he entered the tank yard over the dike. Eventually, the operator B could not stop the leak, rescue the operator A, or return himself again. His key was found east of the 401A tank after the fire was extinguished, but nothing else was specified. The operator A's relics were also found between the 410A and 401B tanks.

Around 7:25 pm, a thick vapor cloud spread throughout the terminal, and then a major explosion occurred. The ignition source is unknown. This explosion killed 11 people and injured 45 people. Simultaneously, nine oil storage tanks in the Main Tank Area also exploded, and the fire lasted for 11 days until the fuel was burned out. The 409A and 409B gasoline storage tanks, which were away from the Main Tank Area, burned after several hours from the explosion. Figure 14 is a photo of this fire.

Figure 14. Massive fire in IOCL tank terminal [6]

7.3. Cause of IOCL incident

In the outlet line of the IOCL tank terminal, an automatic gate valve (Motor Operated Valve: MOV), a Hammer Blind Valve, and a manual gate valve (Hand Operated Valve: HOV) were installed from the tank in order. The MOV was opened and closed remotely from the control room, but it was inconvenient to change the operation because the tanks were far from the control room. Therefore, since 2003, a panel with three buttons "open", "closed", and "stop" has been placed in front of the MOV and changed to button operation.

Hammer Blind Valve has the advantages of simple shape and easy operation, and can completely block the flow in the piping at one location. In addition, the "open" or "closed" state can be easily visually confirmed from the outside. Figure 15 shows the same type as the Hammer Blind Valve used in the 401A gasoline tank outlet line.

When the Hammer Blind Valve is "close", the solid wedge is inserted into the body of the valve. When performing the operation from "closed" to "opened" or vice versa, both wedges are pulled out temporarily and the inside of the pipeline is exposed to the atmosphere. In 10 inch piping, the opening size is 305 mm x 152 mm. When changing the Hammer Blind Valve from "closed" to "open" or vice versa, the gate valves on both sides must be closed before operation. According to the photo taken after the incident of the 401A tank Hammer Blind Valve, both solid wedge and hollow wedge were outside the body, and the opening was made. In this outlet line, both the upstream MOV and the downstream HOV were "open". Therefore, gasoline was ejected from the opening of the Hammer Blind Valve.

The investigation committee [6] assumes the following valve operation errors. The operator A first opened the downstream HOV and then tried to open the Hammer Blind Valve. During this operation, there was a leak from downstream due to backflow in the opening, and the MOV "close" button should have been pressed. However, he was panicked and accidentally pressed the "open" button.

In this tank terminal, the automatic gate valve on the outlet line could be remotely operated from the control room until 2003, but at the time of the incident, only the button was operated near the valve. Leakage could be stopped if the button panel was outside the dike area or the valve could be operated remotely.

8. Conclusions

The simultaneous fires of multiple oil storage tanks due to VCE is extinguished when the oil is burned out after several days without effective firefighting method. VCE is also affected by weather conditions such as temperature and wind speed, and topography. In January, 2013, a gasoline tank leakage occurred in Idaho, USA. At this time, the temperature was below freezing and no vapor cloud was generated.
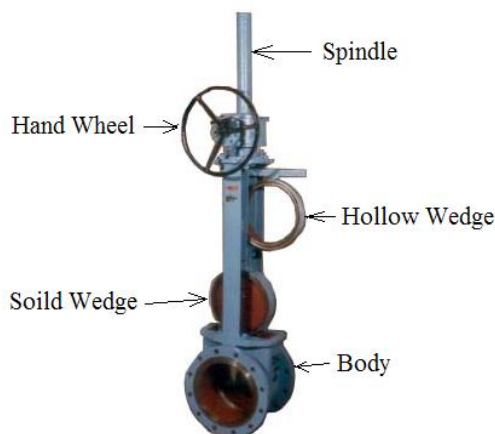
Figure 15. Hammer blind valve [6]

In the 2005 UK and 2009 Puerto Rico incidents, gasoline leaked from the fixed roof of the tank to the ground and collided with intermediate wind girders. In the 2009 India incident, gasoline erupted like a fountain. Such a diffusive situation seems to promote the generation of vapor clouds. In addition, as in the case of the 2009 India, humans have difficulty breathing in the vapor cloud.

To prevent VCE, the most important thing is not to cause a leakage, but if a leakage occurs, it must have equipment to stop it remotely. It is also important to conduct risk assessment for simultaneous fires of multiple oil storage tanks and to have training and equipment for this purpose.

References

[1]   Wikipedia, 1975 Philadelphia Gulf refinery fire, https://en.wikipedia.org/wiki/1975_Philadelphia_Gulf_refinery_fire, 2019.
[2]   Wikipedia, 1983 Newark explosion, https://en.wikipedia.org /wiki/1983_Newark_explosion, 2019.
[3]   Maremonti, M., Russo, G., Salzano, E. and Tufano, V., Post-incident analysis of vapor cloud explosions in fuel storage areas, Trans. IChemE, Vo.77, Part B; 1999, p.360-365.
[4]   Buncefield Major Incident Investigation Board, The Buncefield incident, 11 December 2005, The final report of the major incident investigation board; 2008.
[5]   U.S. Chemical Safety and Hazard Investigation Board, Final investigation report, Caribbean Petroleum tank terminal explosion and multiple tanks fire; 2015.
[6]   Independent Inquiry Committee, "IOC fire accident investigation report", Ministry of Petroleum & Natural Gas, Government of India; 2010.

Basic Study on Deformation Evaluation of Steel Wire Mesh for Rational Gabion Structure Design

Hiroshi Nakazawa[a,*], Tsuyoshi Nishi[b], Hiroyuki Kurihara[c], Daisuke Suetsugu[d], Tadashi Hara[e]

[a] Earthquake Disaster Mitigation Research Division, National Research Institute for Earth Science and Disaster Resilience. Email: nakazawa@bosai.go.jp
[b] Construction Project Consultants, INC. Email: t_nishi@cpcinc.co.jp
[c] Kurihara Kenzai Sangyou Co., Ltd. Email: h-kurihara@kurihara-kenzai.co.jp
[d] Department of Civil and Environmental Engineering Faculty of Engineering, University of Miyazaki. Email: suetsugu@cc.miyazaki-u.ac.jp
[e] Center for Disaster Prevention Promotion, Kochi University. Email: haratd@kochi-u.ac.jp

Abstract

Gabion structures are used in a variety of ways in Japan and around the world because they allow for the creation of simple structures at highly reasonable construction costs and completion periods. Previous earthquake damage surveys have shown that, in many cases, gabion structures did not collapse even though deformation was allowed, and have demonstrated that the wire mesh used in their construction has a high confinement effect on the stones filling the gabion. Despite this, gabions have not been actively utilized, nor have they been used to construct permanent structures in Japan because the design and construction of such structures are based on experience, and a standardized design method has not been developed. Hence, in order to facilitate development a design method for gabion-based structures, we must first go back to the basics and establish a detailed explanation of the wire mesh deformation mechanism of such structures. In this study, we performed tensile tests on wire meshes of different shapes in order to determine their strength and deformation characteristics and then conducted numerical analyses using the results obtained. The tensile tests revealed that deformation characteristics differed depending on the mesh shape and tensile direction. We also showed that the direction in which the tension acts and the mesh nodes are important, and that the test results could be reproduced via numerical analysis with the finite element method by using beam elements.

Keywords: Deformation characteristics; gabion; steel wire mes;, tensile tests

1. Background

The origins of gabions have been traced back as far as circa 361-251 BC to the river embankments of the ancient Dujiangyan irrigation system in Sichuan Province, China. They began as cylindrical cages with a turtle-shell-shaped mesh made of bamboo that were filled with quarry stones, cobblestones, and such, as shown in Fig. 1. Today, their use has spread all over the world, and the most commonly used material for the cage has changed to steel, which is more advantageous in many ways, including productivity [1].

The "Guidelines for Galvanized Steel Wire and Structure of Gabions" was established in Japan in April 1953 and the Japanese Industrial Standards for Galvanized Steel Wire Gabions (JIS A 5513) was established in August 1954 to improve and ensure the quality of gabion-based structures [2]. Despite this, there are currently no detailed design

guidelines such as those in concrete and other structures, and there have been very few studies or practical design cases that measure and evaluate the seismic resistance of gabion-based structures while taking into account their beneficial properties such as high flexibility, trackability, and permeability.

Therefore, the designs for gabion retaining walls and similar structures are still supported by road earthwork concrete retaining wall design standards [3]. Hence, in the fields of agricultural and civil engineering works in Japan, gabion-based structures remain a traditional construction method, with almost no track record as semi-permanent structures that make good use of their merits.

Several case examples have confirmed the benefits of gabions such as the abovementioned high flexibility, trackability, and permeability in previous earthquake disasters. For example, after the Gorkha Earthquake that struck Nepal on April 25, 2015, a survey was conducted on road embankment damage in flat areas and slope collapses

---

*Corresponding author. Tel.: +81-29-863-7308
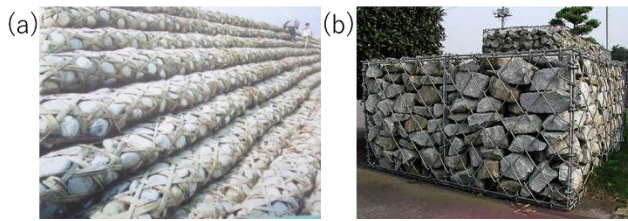*Tennodai 3-1,*
Tsukuba, Ibaraki, Japan, 305-0006

Figure 1. (a) Gabion-based embankment (Photo of a project description board in Dujiangyan, Sichuan Province, China); (b) Recent Gabion-based structure

Figure 2. Breakdown of gabion structures along the Araniko Highway (revised from [5])

in mountainous areas, together with damage to road retaining walls. The findings showed that while there were

Some cases of cracking in concrete retaining walls, the gabion retaining walls were only slightly deformed and did not collapse [4]. According to the report, the gabion-based structures were prevented from collapsing by the confinement effect of steel wires, thereby demonstrating that such structures are highly flexible and persistent.

Consequently, in order to take advantage of this durability and promote the broader use of gabions as a disaster prevention technique, the deformation mechanism of gabions must be determined, and standardized technology for producing gabion-specific designs must be developed. To accomplish these goals, a technological system underpinned by a theoretical background must first be established. In this study, tensile tests and replication analyses performed on wire meshes were conducted to obtain basic data, after which a foundational study was performed as a precursor to establishing a design method.

2. Significance of This Study Based on Previous Studies

Following the 2015 Nepal Gorkha Earthquake, a field survey and analysis of the causes of damage to gabion-based retaining walls were conducted, after which shaking table tests using full-scale models were performed. A description of these tests is shown below, followed by a discussion of the significance of this study.

2.1. Damage survey in Araniko Highway

Figure 2 shows the survey locations along the Araniko Highway that were investigated after the Nepal Earthquake. For the 115 gabion-based structures along the Araniko Highway, the use, structure, surrounding conditions, gabion dimensions and damage conditions, as well as the grid and wire dimensions, and the filling material quality and dimensions, were all surveyed. The results show that gabion-based structures were used as retaining walls at 56 locations (49%), as crash barriers at 22 locations (19%), for riverbank and channel protection, etc. at 17 locations (15%), for erosion control dams at six locations (6%), and as retainment barriers to prevent earth collapse, etc. at 13 locations (11%). Many of the retaining wall gabion units appeared to have sizes that were adjusted to match field conditions, although their widths, heights, and depths generally measure around 100 cm, and many upright walls had heights of about 3 m.
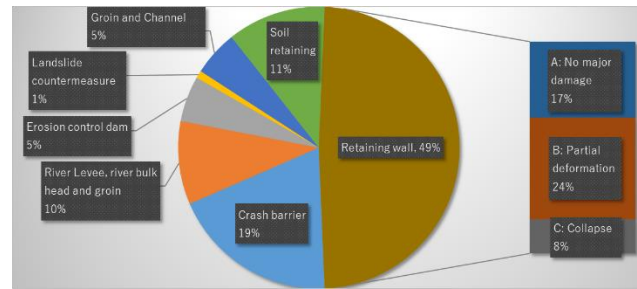
Figure 3. Example of damage; (a) No major damage; (b) Partial deformation; (c) Collapse

Figure 3 shows examples of the damage types observed. Damage patterns were classified into three levels: no damage, partial damage, and collapse, with around 80% of those surveyed classified as partial or no damage. These findings showed that the minimum road function had been maintained in many cases, which demonstrates the durability of gabion-based retaining walls. Details of the field survey have also been reported by Hara et al. [5].

2.2. Full-scale shake table test of gabion retaining wall

A full-scale model experiment was conducted to verify the seismic performance and dynamic behavior of gabion-based retaining walls during an earthquake. This has been reported in detail by Nakazawa et al. [6]. Based on the field survey findings, an experiment was carried out on a retaining wall model with a wall height of 3 m, using gabions with unit sizes of about 100 cm in width, height, and depth.

For the gabion wire mesh, a rhombus-shaped galvanized product procurable in Japan, with a wire diameter of 3.2 mm and a mesh 13 cm long based on the Japanese Industrial Standards (JIS A 5513), was used because it was difficult to obtain the same products used in Nepal. Note that in Nepal, wire diameters range from 3 to 5 mm, and meshes were turtle-shell-shaped, square, or rhombus-shaped, with a minimum mesh size of 9 cm and a maximum of 18 cm.

In this set of experiments, tests were conducted using three gabion retaining wall types shown as Cases 1 to 3, one of which consisted of the vertically upright triple-stacked gabion retaining wall common in Nepal and two which involved newly proposed gabion structures [6]. As an example here, the model specifications and test results for Case 1, which show the vertically upright triple stacks common to Nepal, are shown in Figs. 4 to 6.

Shaking was performed by regulating the acceleration amplitude of a 3 Hz sinusoidal wave in four stages: 65, 132, 203, and 257 gals. The dynamic behavior results showed that there was a buildup of retaining wall horizontal

displacement with increased shaking, and that cracks appeared on the ground behind the retaining wall. After the shaking had completely ended, significant forward tilting of the retaining wall and severe ground collapse behind the wall were observed, as shown in Fig. 6.

In particular, there was pronounced deformation on the second layer of gabion and about 80 cm of horizontal displacement at the top. However, the retaining wall did not collapse even though it tilted about 18 degrees forward. This type of retaining wall deformation was also commonly observed in Nepal. This durability, which is also termed persistence, is believed to be the reason why the wall did not eventually collapse.
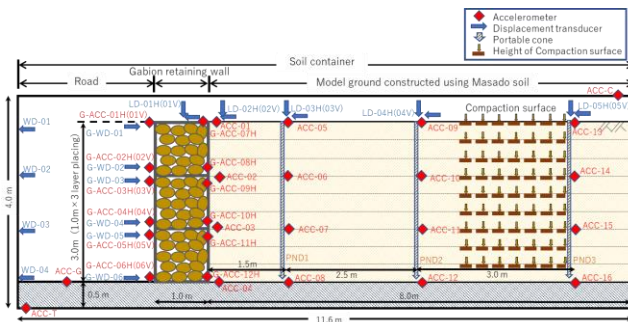
Figure 4. Cross-section of the full-scale gabion retaining wall experiment (revised from [6])
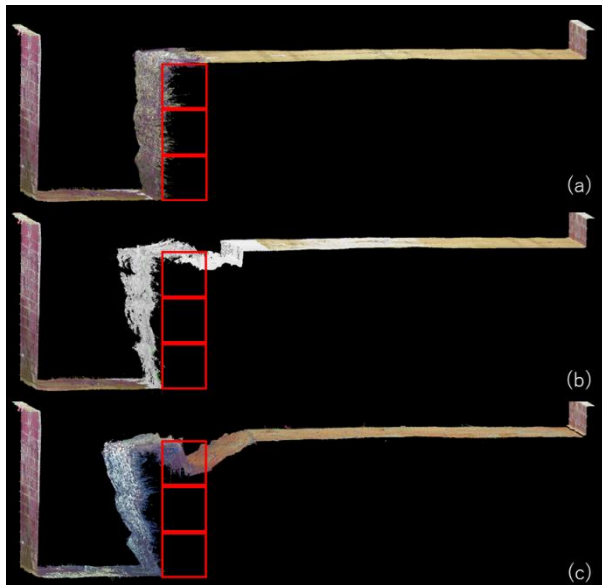
Figure 5. Results of 3D measurements. (a) Before shake test. (b) After shaking at 203 Gals. (c) Residual deformation after final shake test by 257 Gals. [6] The red lines show the original position of the gabion wall
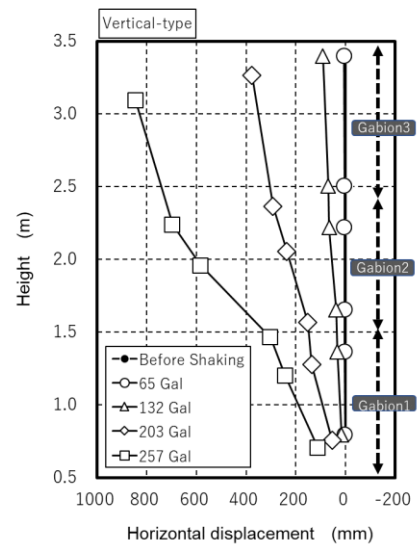
Figure 6. Horizontal displacement of gabion retaining wall front face [6]

2.3. Purpose of this study

In the set of surveys and experiments discussed above, emphasis was placed on the filling material and method used for stacking the gabions. The deformation of the gabion retaining wall is thought to be dependent on the deformation characteristics of the filling material and the confinement effect of the wire mesh that restrains it. For example, in Fig. 7, it can be inferred that the confinement effect of the wire mesh on the front side of the retaining wall is different from that on the rear side. That is, deformation on the front face is considered to be restrained by tensile resistance of the wire mesh on the rear side when bending deformation occurs in the flexible gabion retaining wall structure.

However, mesh shapes and their corresponding deformation and strength characteristics have yet to be studied. In a field trial construction case in Nepal [7], as shown in Fig. 8, the direction of the wire mesh in relation to the assumed direction of retaining wall deformation had not been taken into account, and whether or not this may be a dominant factor remains unclear.
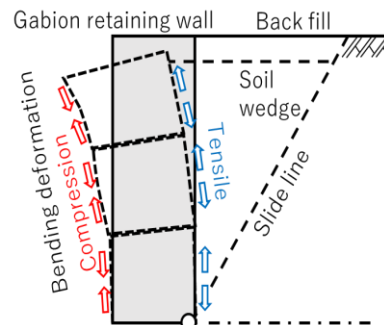
Figure 7. Schematic diagram of gabion-based retaining wall deformation

Figure 8. Trial construction of a gabion-based retaining wall [7]. The direction of the turtle-shell-shaped wire mesh had not been considered. (a) Mesh line is vertical. (b) Mesh line is horizontal
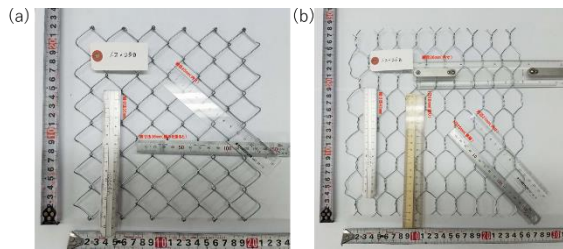
Figure 9. Wire meshes used in the tensile test. The panels consist of 200 mm × 200 mm galvanized wire with a wire diameter of 1.2 mm. (a) Rhombus-shaped wire mesh. (b) Turtle-shell-shaped wire mesh

The rhombus-shaped wire mesh is common in Japan, although in other countries such as Nepal, the turtle-shell-shaped wire mesh is more widely used. Accordingly, to take into consideration the loop shape and friction properties of the wire mesh nodes, tensile tests were carried out using 200 mm × 200 mm wire mesh with two mesh shape types: rhombus and turtle shell, as shown in Fig. 9, in order to determine their basic mechanical properties.

Moreover, to find out whether the test results can be simulated, a replication analysis using the finite element method (FEM) was performed and the results were examined to determine whether it can be applied to the design of gabion-based retaining walls.

3. Tensile Test of Steel Wire Mesh

The tests were conducted in order to determine the mechanical properties of the gabion wire mesh itself. Based on the test results, a replication analysis using the FEM was performed, as will be described in the following section.

Gabions have a simple structure consisting of a steel wire mesh box filled with stones. However, the deformation performance of single gabion units may differ depending on the arrangement of the filling stones. A gabion-based retaining wall is an assembly of gabion units, but the deformation resistance performance of the structure as a whole can be increased by increasing the deformation performance of individual gabion units.

When the gabion unit deforms, it is necessary to examine what kind of wire mesh shape effectively provides the confinement effect and the connection between the filling stones and direction of the wire mesh. After completing this level of study, there will eventually be issues such as the productivity of the most effective mesh types.

Next, in order to take the first step in improving the deformation resistance performance of gabion structures as a whole, tensile tests were conducted to determine the basic

mechanical properties of gabion wire meshes according to the mesh shape differences. Table 1 shows the test cases. Basically, the objective of this test was to compare mesh shapes and tensile direction, although differences in loading rates were also investigated. The effect of the loading rate was also checked because rearrangement, strength development, etc. may possibly occur depending on the rate, even if the structure breaks partially during tensioning.

3.1. Specification and properties of steel wire mesh

The wire specimen used in the tensile test was a 1.2 mm diameter galvanized steel product, from which panels were fabricated with a mesh size of 200 mm × 200 mm, as shown in the lower part of Table 1. The tensile strength of the wire was 350 to 380 N/mm^2.

Using the test apparatus shown in Fig. 10, tensile tests were carried out after running bolts through the edges of the wire mesh and fixing them in place. Note that due to the difference in shapes between the rhombus and turtle shell meshes, the number of bolts secured at the edges depends on the mesh shape and could not be standardized. In this paper, the test results were evaluated by comparing the tensile behavior with respect to the relationship between the applied tensile force T (kN) and the stroke of the testing apparatus. In principle, the rate of tensioning used was 40 mm/min using displacement control. For Case 1, the test was also conducted at 10 mm/min in order to investigate the dependence on the loading rate.

Table 1. Tensile test cases. The ● indicates bolt fixing positions

Case1 (a)	Case1 (b)	Case2 (a)	Case3 (b)
Lateral direction	Longitudinal direction	Lateral direction	Longitudinal direction

Figure 10. Test apparatus
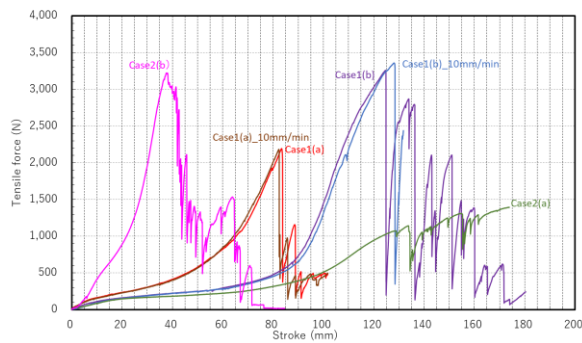
Figure 11. Results of tensile tests
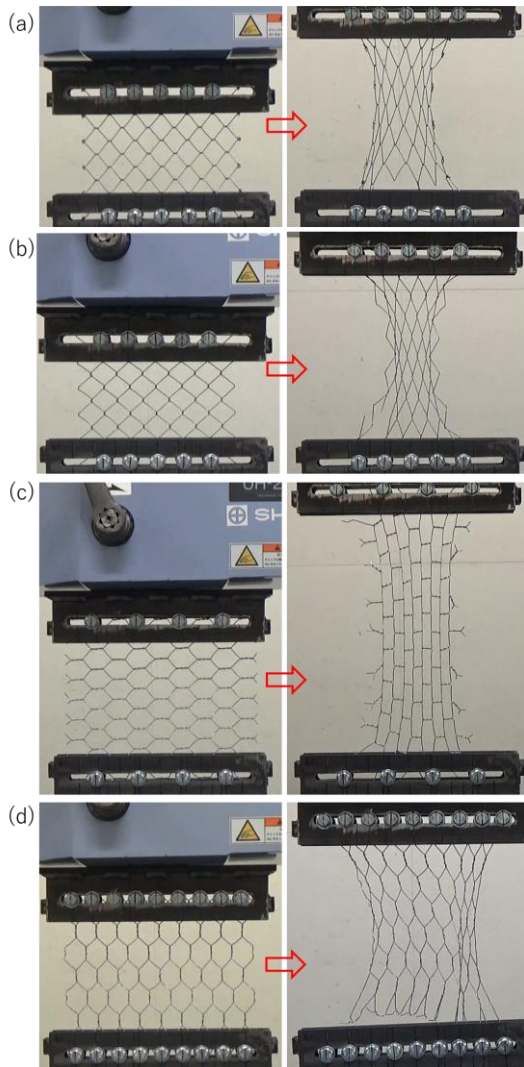
Figure 12. Shapes before and after Tensile tests. (a) Rhombus shape (Case 1(a)). (b) Rhombus shape (Case 1(b)). (c) Turtle shell shape (Case 2(a)). (d) Turtle shell shape (Case 2(b)) in Table 1

3.2. Results of tensile tests

Figure 11 shows the test results for all cases, while Fig. 12 shows photos of post-testing wire mesh deformation. For the effect of tensioning rates, which was tested in Cases 1(a) and (b), there were no differences in results observed between 10 mm/min and 40 mm/min. Therefore, only the

test results from a tensioning rate of 40 mm/min are discussed in this paper.

Looking at Case 1 with a rhombus shape, we see that the load-displacement relationship did not change regardless of the direction of the wire mesh. However, Case 1(a) carries a more significant portion of the tensile force at the mesh nodes than (b), so the tensile load developed early and the edges ruptured significantly, thus causing the peak value to be small. Although both of these cases showed a dramatic decrease in tensile force after peaking, it can be seen afterward that the nodes that did not rupture cycled between tensile loading and rupture until reaching their ultimate state. As a whole, their post-test deformation characteristics did not appear to be significantly different from each other, as shown in Fig. 12.

In contrast, for Case 2 with the turtle-shell-shaped wire mesh, it can be seen that the pattern of the load-displacement relationship is completely different depending on the tensile direction. For (b), in which the twists are parallel to the tensile direction, it can be seen that the tensile loading developed at the smallest level of displacement. In this case, the mechanism does not involve taking up the tensile force at the nodes as in Case 1, and the deformation does not seem to have loosened the twists, thereby suggesting that friction at the twists is the dominant factor.

For (a), the twists are perpendicular to the tensile direction. After the test, Figure 12 shows that the mesh shape deformed into rectangles with the twists on the short side. From the load-displacement relationship shown in Fig. 11, it can be seen that although the effect of ruptures can be observed, the tensile force did not peak as it gradually increased with the increased displacement, even at displacement levels where the test ended for other cases.

4. FEM Analysis for Tensile Tests of Steel Wire Mesh

When evaluating the stability of gabion-based retaining walls, it is crucial to verify the confinement effect of the wire mesh on the filling material. In the FEM analysis, a replication analysis of the tensile test results was performed in order to determine the mechanical properties of the gabion wire mesh. By comparing the deformed shape between the replication analysis and the test results, the validity of the FEM model could be checked and model improvements were identified.

4.1. Analysis cases and modeling

Similar to the test cases shown in Table 1, the rhombus-shaped and turtle-shell-shaped wire mesh diagrams are shown in Fig. 13. The member was considered as a linear elastic body, and the load was applied to nodes at the upper end while the lower end was fixed. Table 2 shows the physical properties of the steel wire mesh material.

The nodes are a vital requirement in the modeling. The rhombus shape was given uniform dimensions overall. In contrast, because the turtle shell shape twisted parts have two twined wires, the cross-sectional area and moment of inertia were doubled.

Table 2. Physical properties of the steel wire mesh model.

Diameter (mm)	1.2
Cross section (m^2)	1.131E-06
Moment of inertia (m^4)	1.018E-13
Torsional moment (m^4)	2.036E-13
Young's modulus (kN/m^2)	2.000E+08
Poisson's ratio	0.30
Unit weight (kN/m^3)	77.0
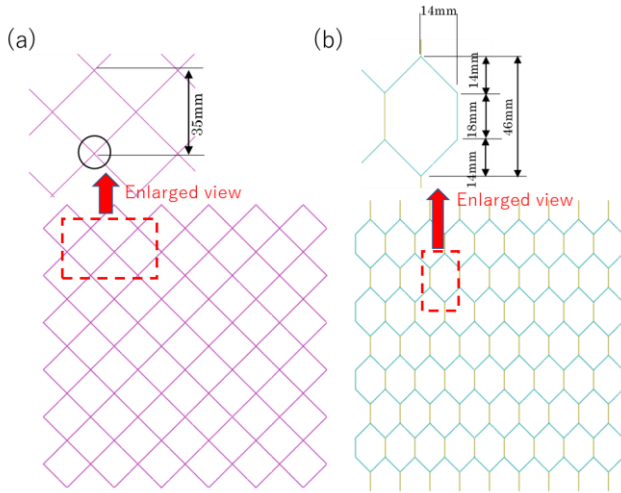
Figure 13. FEM models. (a) Rhombus shape. (b) Turtle shell shape
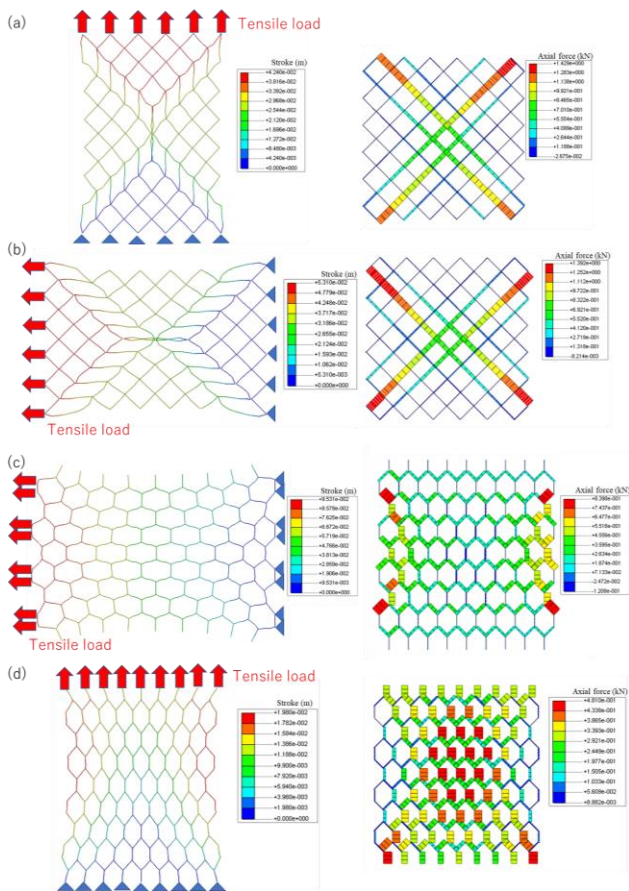
Figure 14. FEM model

In the replication analysis of the rhombus-shaped wire mesh, joint springs were set at the intersecting points shown by the circle in Fig. 13. The spring properties were 1.0×10^7 kN/m in the y-direction and 1.0×10^3 kN/m in the x-direction. In other words, the joint was fixed when loaded in the y direction, while slipping occurred when loaded in the x-direction.

For the turtle-shell-shaped mesh, when loading in the direction of the mesh line, the lower end was fixed while the upper end was loaded at nine points with the load increasing by 1 kN increments in each of the 100 steps. When loading in the direction perpendicular to the mesh line, the loading points were set as eight points at the hexagonal vertices with 1 kN applied in 100 steps at each point same as the case loading in the direction of the mesh line.

4.2. Results of FEM analysis

Figure 14 shows the deformation and axial force diagrams based on the analysis for each case. Looking at the results on the 50th step with 3.0 kN for Case 1(a) and (b) with the rhombus-shaped mesh, it can be seen that loading in the x-direction has a slightly larger deformation, but the axial force acting in the x-direction is larger. On the other hand, looking at the results of 37 steps with 2.96 kN acting in Case 2 with the turtle-shell-shaped mesh, we can see that the value of the loads in (a) and (b) are almost the same, but the amount of deformation in (b) is much larger than in (a), and the axial force is nearly double.

The above results show that for the turtle-shell-shaped wire mesh, in particular, the highly anisotropic property, in which the deformation characteristics differ depending on the direction of the acting tensile force, can also be expressed by numerical analysis.

4.3. Comparison of results between analysis and tensile tests

Similar to Figure 11, which summarizes the tensile test results, Figure 15 shows a summary of the numerical analysis results. Looking at the relationship shown in 15(a) between the displacement until 2 mm stroke and the tensile force, we can see that the tendency for tensile resistance to develop and the deformation performance for all the cases are similar in both the test results and the analysis results. In both, the deformation of (a) is larger than (b) in Case 1 as well as in Case 2.

On the other hand, for the build-up after loading, it can be seen that, overall, the analysis results are larger than the test results. This may conceivably be due to the fact that the analysis used elastic analysis and that in the test, looseness occurred at the wire mesh crossings, which means that large acting forces were not generated at the initial stage of loading until those loose sections were closed and tensile resistance was exerted.

(a)

(b)
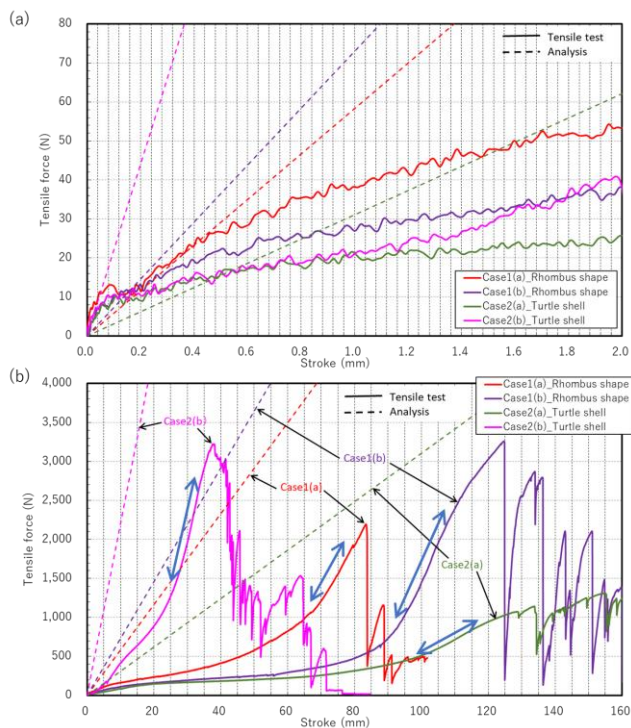
Figure 15. Comparison FEM analysis and Tensile test results.

Next, looking at Fig. 15(b), it can be considered that deformation performance in the tensile test results, from the development of tensile resistance until the start of partial rupture or damage (indicated by ↔), is not significantly different from those in the analysis results. In actual gabions, the filling material is granular and is not self-supporting, so there are always tensile forces acting on the wire mesh at the sides of the structure. Therefore, the fact that deformation performances are consistent between the analysis results and the tensile test results for the section indicated (↔), in which the stiffness has recovered in the tensile tests, may be considered to be a very significant finding of this study.

5. Conclusion

Gabions have advantages, such as high flexibility, trackability, and permeability, which means that highly disaster-resistant gabion-based structures that will not collapse even when deformed can be built. However, a design system has not yet been established because their mechanisms remain unclarified. In this study, tensile tests and replication analyses were conducted on wire meshes to obtain basic data, after which a foundational study was performed as a precursor to establishing a design method.

From a series of test results, it was found that, regardless of shape, wire meshes had strength anisotropy depending on the tensile direction, and that both types of wire mesh examined in this study displayed tensile properties that showed stronger behavior in the direction of the mesh line. For the turtle-shell-shaped wire mesh, friction at the twists formed by winding the wire three times was found to be the dominant factor resisting tension, and the results showed that

its anisotropy is stronger than the rhombus-shaped wire mesh, which is only hooked at the looping point.

On the other hand, in the replication numerical analyses performed for the above tensile test results, because a certain amount of displacement is needed until tensile resistance is exhibited for all of the test results, it is difficult to interpret a direct comparison with linear analysis, which has stiffness from the initial stage. However, the relationship between the amount of displacement and tensile force showed that, in the elastic deformation range in which looseness in the wire mesh has disappeared and stiffness has recovered in the tensile test, there was consistency between the test and analysis results in each case. This suggests that the wire mesh can be modeled and simulated until it becomes damaged or ruptured.

The above findings provided an understanding of a part of the fundamental behavior of wire meshes. Moving forward, a design method will have to be created through the development of a tensile strength evaluation method that considers factors such as the wire mesh thickness, the number of nodes, and the amount of wire used. Additionally, it will be necessary to develop a method for determining the mesh direction for the wire mesh that considers the direction of external force and the deformation characteristics of the filling material.

References

[1] Japan Jakago Association. Guide and commentary on gabion engineering method, 2008. [in Japanese]
[2] Association of Nationwide Disaster Prevention and Japan River Association, Knowledge of gabion, 1963. [in Japanese]
[3] Japan Road Association. Road Construction Works on Soil Retaining Wall Guidelines, pp.97-109, 2012. [in Japanese]
[4] Nakazawa, H., Manandhar, S., Hara, T., Suetsugu, D., Kuribayashi, K., Nishi, T., Sakuraba, T., Kariya, T., Ko-chi, Y. and Hazarika, H. Report on damages caused by the 2015 Nepal Gorkha Earthquake, JAEE International Symposium on Earthquake Engineering, P2-36, 2015.
[5] Hara, T., Nakazawa, H., Suetsugu, D., Kuribayashi, K., Nishi, T., Tadokoro, Y., Miyoshi, K. and Zhang, H. Field survey on damages of gabion structures caused by the 2015 Nepal Gorkha Earthquake and examination of specific measures for earthquake resistaance improvement, Journal of Japan Society of Civil Engineers, Ser. A1 (Structural Engineering & Earthquake Engineering), Vol.74, No.4, pp. I_586-597, 2018. [in Japanese]
[6] Nakazawa, H., Hara, T., Suetsugu, D., Nishi, T., Kuribayashi, K., Miyoshi, K. and Shimomura, S. Experimental evaluation on earthquake-resistance of road retaining wall using gabion, Journal of Disaster Research, Vol.13, No.5, pp.897-916, 2018. (doi: 10.20965/jdr.2018.p0897)
[7] Kimura, S., Hara, T., Suetsugu, D., Nakazawa, H., Nishi, T., Shimomura, S., Shibahara, R. and Kuribayashi, K. An issue of seismic structure and construction regarding gabion wall in rural area of Nepal, Proc. of 7th Asia Conference on Earthquake Engineering, No.0151, pp.1-10, 2018.

Evaluation of Numerical Analysis forEarthquake Resistance of Retaining Wall Using Gabions

Tsuyoshi Nishi[a]*, Tadashi Hara[b], Hiroshi Nakazawa[c] , Daisuke Suetsugu[d]

[a]Construction Project Consultants, INC. Email: t_nishi@cpcinc.co.jp
[b]Centor for Disaster Prevention Promotion, University of Kochi. Email: haratd@kochi-u.ac.jp
[c]Earthquake Disaster Mitigation Research Division, National Research Institute for Earth Science and Disaster Resilience. Email:nakazawa@bosai.go.jp
[d]Department of Civil and Environmental Engineering Faculty of Engineering, University of Miyazaki. Email:suetsugu@cc.miyazaki-u.ac.jp

Abstract

In developing countries, gabions are widely used in several construction works, like road, river, countermeasures against slope failure and so on, because of their easy operation and low cost. In 2015 Nepal Gorkha Earthquake, a lot of retaining walls using gabions were not damaged against the strong earthquake because of their high flexibility. However, some deformation or declination were reported dpending on retaining wall types and ground conditions behind retaining walls. Therefore, in order to evaluate the earthquake resistance and residual deformations of retaining walls using gabions widely observed in Nepal, full-scale shake table tests and laboratory tests were conducted in previous studies. In this study, elemental simulations for determination of the analysis parameters based on the results of triaxial compression tests were carried out to check the validity of parameters. Then, a series of numerical analysis using proposed model was performed to reproduce the dynamic behaviors of full-scale shake table tests and evaluate the earthquake resistance of retaining wall using gabions. According to the results of these numerical analysis, it was confirmed that proposal model adequately could simulate the dynamic response of retaining walls in the full-scale shake table tests. and it was also cleared that the stepwise type retaining wall was superior to that of vertical type from the standpoint of earthquake stability against sliding and overturning.

Keywords: Earthquake resistance; gabion; numerical analysis; retaining wall; shaking table test

1. Background

The structures using gabions are widely used also in Japan as the structures on rivers, roads and coasts [1].

When the authors executed research of damage of civil/architectural structures caused by Nepal Gorkha Earthquake in 2015, it was confirmed that the retaining walls using gabions are widely used in Nepal [2]. Araniko Highway, objective of the research, is located about 10km west of the place where the biggest aftershock occurred (Dolakha county), and at Barhabise along the Highway 42% of houses were completely destroyed [3]. Almost all of the retaining walls using gabions were gravity type that gabions were straightly piled up, and some of them suffered from stick out or fall forward that are considered to be affected by external factor such as earthquake (Nepal Gorkha Earthquake) and rainfall. But in the area of the authors' research, the retaining wall itself using gabions did not reach

the stage of collapse, but due to characteristics of soft structure of retaining walls using gabions, it was confirmed that minimum required performance to support life is held [2, 4-6]. That is to say, minimum earthquake resistance that structure is deformed but not collapsed is proved in these retaining walls.

To evaluate the characteristics, and to grope more stable structures, the authors executed full-scale shake tests[7-11]. As the result of test, it was proved that upright retaining wall with height of 3m widely used in Nepal does not collapse though big fall forward occurs by a large-scale earthquake [12]. This means that minimum performance proved in the above-mentioned examples of damages in Nepal was confirmed by the tests, but due to soft structure, measurement of deformation is considered to be in the range of not-negligible for the use conditions such as traffic of roads. Therefore, shape of leaning structure and stacking structure with improved stability was proposed, and judging from the deformed situation of structures, it was confirmed by tests that deformation related with stability such as fall down or sliding can be deterred.

*Corresponding author. Tel.: +81-3-5337-4065
YSK Building 3-23-1 Takadanobaba Shinjuku-ku
Tokyo, Japan, 169-0075

In this report, aiming to obtain basic data for the evaluation of the seismic stability of the retaining wall using gabions, reproductive analysis of the tests was conducted, comparison of superiority of structural shape on the seismic stability by the structural shape of the retaining wall using gabions and evaluation of structural problems were made.

2. General Outline of Tests on the Earthquake Resistance of The Retaining Wall using Gabions

Based on the utilization record of the retaining wall using gabions in Nepal, full-scale shake table tests were conducted to evaluate the earthquake resistance of them. This report is analytic evaluation of tests, and first of all, outline of full-scale tests and objective structural shape are stated.

Tests were conducted in 2016 and 2017 at National Research Institute for Earth Science and Disaster Resilience of Japan. Table 1 shows the outline of them. Basis of input

earthquake motion of tests was sine wave of 3Hz (peak shaking 12 waves) as the easily resonating frequency, and assumed maximum input acceleration was divided into 3 steps and was increased step by step. Further, test by white-noise wave of 20gal of assumed maximum input acceleration was executed.

Figure 1 shows residual displacement of retaining wall using gabions as the result of tests. Legend in the Fig. shows maximum acceleration of input earthquake motion in the final stage. For the reference, maximum acceleration at the surface point of background was 400gal~600gal for the input acceleration. Input is sine wave, and as it has big energy compared with normal earthquake motion, actual earthquake motion works bigger than that shown in the figure with maximum acceleration.

In Fig. 1, residual displacement of the retaining wall is biggest in Case 1, and horizontal displacement in the levee

Table 1. Test Case (Objectives of analysis are Case 1 & Case 2)

Test Case	Characteristics	Model Shape	
		Structure	Shape
Case1	Greatest number of shape of retaining wall in Arniko Highway, Nepal. Many damaged places.	3-tiered series wall	
Case2	Though cost is low, quake resistance depends upon stability of back ground.	3 stepped piling up	
Case3	Though cost is high, stability is great in spite of back ground.	Gravity form (3 steps in 2 rows)	

crown of 80cm occurred, but such displacement I Case 2 and Case 3 is less than 20cm which comparatively small. Angle to lean forward in Case 1 is more than 15 degrees, but from the fact that the wall does not fall down in spite of pressure of background, effect of soft structure was confirmed. After shaking test, dynamic corn penetration test was conducted. In case 1 and Case 3 straightly piled up, test was executed in the nearest place to the back side of retaining wall using gabions shown in Fig. 1, and the result shows that there is a tendency that penetration resistance decreases after test, but there was not a big change in Case 2.The reason for the difference is that Case 1 and Case 3 shows gravity resistance based on the self-standing structure of retaining wall using gabions, while in Case 2 of leaning structure, displacement of back ground is small.

Table 2 shows displacement of back ground in Case 1 and Case 2. The place where crack occurred is shown in Fig. 1, too. As a whole, there is a tendency that displacement of back ground in Case 1 is bigger, but especially in Case 2, first crack is occurred at very near the retaining wall using gabions, and cracks after it are occurred at the places nearer to the retaining walls than in Case 1. In this report, based on the abovementioned features, analytical evaluation is made about Case 1 with gravity resistance and Case 2 with lean forward structure surrounded by double red line in the table.
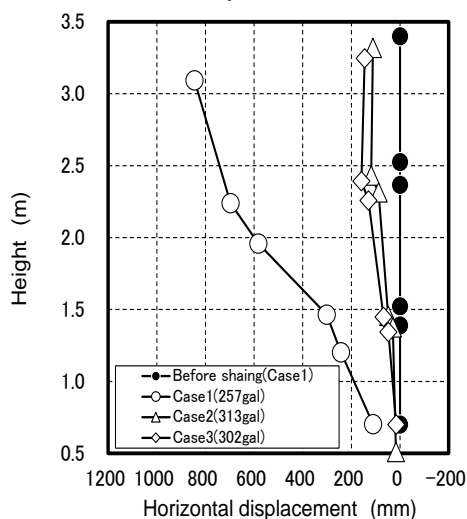
Figure 1. Residual displacement of Gabion [8]

Table 2. Situation of damages of back ground by test in Case 1 , case 2

Case	Structure of gabions	Input Acceleration	Situation of the back ground
Case1	3-tiered series wall	65gal	No deformation
		132gal	Crack is generated at o.7m from back face of wall and sliding collapse was caused
		203gal	cracks at 1.1m，1.6m，2.1m，2.8m from wall
		257gal	By development of cracks in the range of 1.1m, sliding collapse was caused
Case2	3-stepped piling up	85gal	No deformation
		162gal	Cracks at 0.11m from wall
		244gal	At 0.55m from wall cracks were generated and sliding collapse was caused
		313gal	By development of cracks in the range of 1.1m, sliding collapse was caused

3. Analysis Model

3.1. Analysis Model1

Static analysis considering normal situation and dynamic analysis to evaluate seismic dynamic behavior were conducted. In static analysis, to get reference data for the future design of retaining walls, inertia force was worked statistically taking into consideration of measuring earthquake intensity. For analysis general-purpose FEM analysis program (Soil Plus) with two-dimensional finite element procedure (FEM) was used. Filling materials of gabions and back ground were modeled as plane twist factor, and gabions were modeled as the spring to prevent from deformation of filling materials. Joint factor was set, considering evaluation of sliding behavior between the gabions on the vertical line. And joint factor was set between gabions and back ground to consider sliding and detachment.

In static analysis, step analysis was made taking into consideration of construction stage. As Step 1, support base and earth tank were set, and in the order of 1st step of gabions, 1st layer of back ground, 2nd step of gabions, 7 steps were set up to 3rd layer of back ground. The stress inside the ground under the above conditions was set as the initial stress, and in the next step, horizontal inertia force was worked from back ground side to the side of retaining wall using gabions.

3.2. Damage survey in Aranico Highway

Filling materials, background and support ground were modeled as ground material with plane twist factor. Set value of physical property of each material is shown in Table 3. Unit volume weight of filling material was set with weight of rocks filled in the gabions. Back ground and support ground are set as solid ground compacted enough. Set rigidity modulus, strength parameters and so on are shown below. Characteristics of joint factor was set as very big value ($K=10^7 kN/m^2$) so that joint rigidity in orthogonal direction against joint face would not encroach. Shear direction was set as $Ks=10^4 kN/m^2$ which is a little bit bigger than spring value of band of gabions, and friction coefficient was set as $\mu=0.6$ which is a little bit smaller than $\mu=0.67$ comparable with inner friction angle of filling materials.

3.2.1. Value of physical property used in static analysis

In static analysis, strength-deformation characteristics of filling materials was set based on hyperbolic model by Duncan-Chang [13]. Fitting of hyperbolic model was based on the result of triaxial compression test of materials with particle size similar to filling materials used for test[14]. Figure 3 shows the result of triaxial compression test in laboratory and outcome of fitting. Here, actual height of retaining wall using gabions used for shaking table test was 3m, and as action stress was supposed to be maximum 50kN/m^2, in fitting, conformity of σ_c=32kN/m^2 with small

Test Case	Shape of Model
Case1	
Case2	
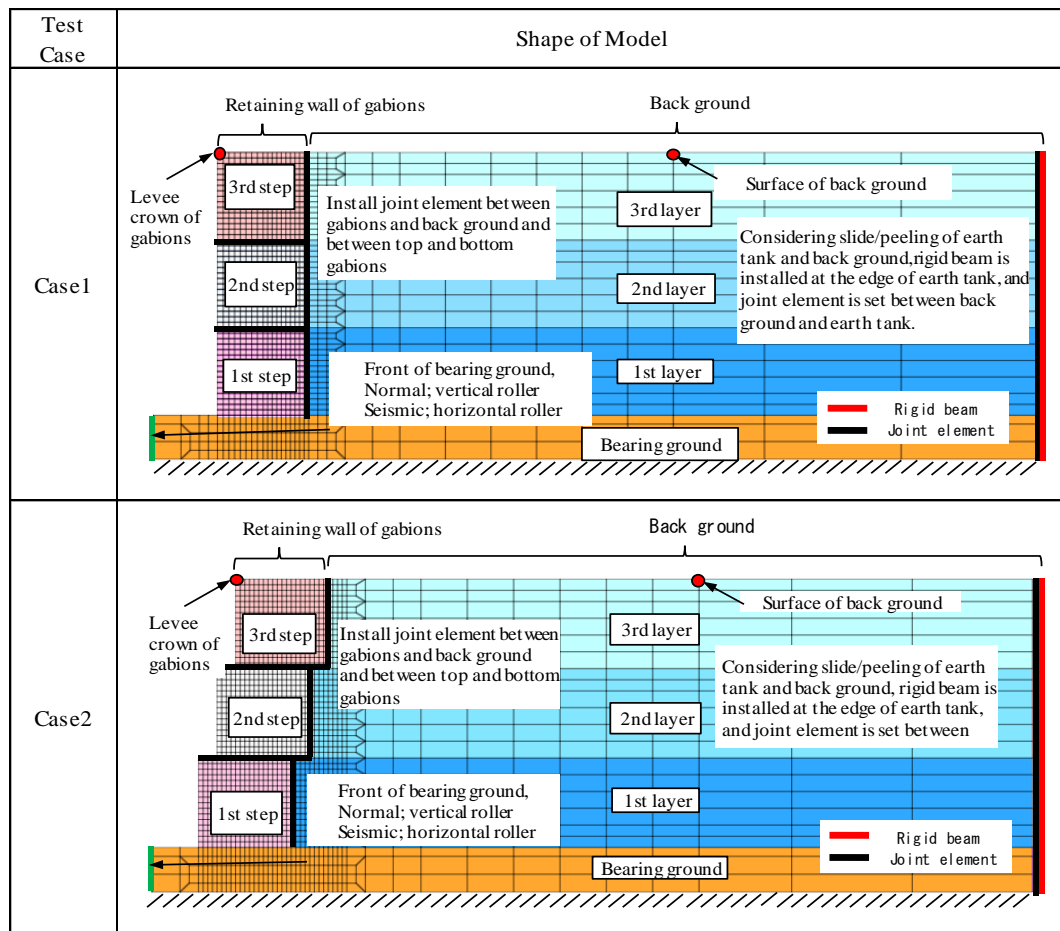
● Point of obseravation of the result of analysis

Figure 2. Model of analysis

confined pressure and 64kN/m² was fully considered. Figure 4 shows result of triaxial compressive test (CD test) of background and materials of support ground. From Fig. 4, it was judged to be more appropriate to apply elasto-plasticity conditions of by-linear type than applying hyperbolic model to the relations of stress-twist of these materials, and non-linear characteristics was evaluated with by-linear model by Mohr-Coulomb. Figure 4 shows result of test and setting value on analysis. Deformation coefficients are set, like the filling materials, to conform to the area with confined pressure. In test, phase difference was confirmed between retaining wall using gabions and back ground. Therefore, judging that tensile stress works on the back ground with the horizontal power under the conditions that back ground is not restrained after gabions move by themselves, model with non-tension type was adopted.

In this study, as having been mentioned in the above, influence of fictious force was considered in static analysis. In tests, as deformation of back ground by shaking occurs especially in the back of retaining wall using gabions, twist is considered to reach the size of several % exceeding rupture zone. Therefore, as peak strength in Table 3 can not be exerted, in analysis to exert inertia force, strength of back ground was applied with residual strength shown in ( ) of Table 3.

3.2.2. Value of physical property used in dynamic analysis (R-O model parameter)

Dynamic characteristics of filling materials and back ground are shown in Table 4. Here, non-linear nature was considered by Ramberg-Osgood (R-O) model. For back ground dynamic deformation characteristic test by indoor triaxial compressive test is conducted, and standard twist γ_r and maximum decay rate h_{max} were set to make fitting with the test. Figure 5 shows the result of fitting. Here, standard twist is set so that it would fit to the twist with size of $\gamma=1.0 \times 10^{-3}$. In small twist area less than $\gamma= 10^{-4}$ and large twist area more than $\gamma=10^{-2}$ there is a small gap, the reasons for having considered middle twist area of around $\gamma=10^{-3}$ are as follows; judging from size of shaking, test was supposed to be in the twist area bigger than 10^{-4}, twist is not supposed to be in the range evaluated by R-O model, because in the large twist area, ground rupture will be accompanied as a real phenomenon.

On the other hand, regarding filling materials, as there is not any result of dynamic deformation test, value was estimated from the existing documents. Tanaka.et.al.[15] conducted dynamic deformation characteristic test and the result shows that reduction of rigidity occurs in comparatively small twist area (standard twist $\gamma_r \leqq 4 \times 10^{-4}$).

Table 3. Static value of physical property of ground material

Name	Poisson ratio v	Young's modulus E(kN/m^2)	Unit Volume weight γ(kN/m^3)	Strength parameter※)		Remarks
				Cohesive Force c(kN/m^2)	Angle of internal friction φ(deg)	
Filling material	0.330	29,037	16.0	15.0	34.0	**DC model**
Back ground	0.330	15,000	20.0	20.5(4.0)	38.0(38.5)	**Mohr-Coulomb**
Foundation	0.330	20,000	20.0	-	-	**Elasticity**

※( )inside is residual strength

Table 4. Dynamic value of physical property of ground material

Name	Poisson`s ratio v	Velocity of elastic wave Vs(m/s)	Initial rate of shear rigidity G$_0$(kN/m^2)	Unit weight γ(kN/m^3)	Non linear characteridtic		Standard confined pressure※)
					Standard strain γ$_r$	Maximum damping factor h$_{max}$	
filling material	0.450	200.0	65,262	16.0	5.00E-05	0.20	σ$_c$=24kN/m^2
Back ground	0.450	200.0	81,577	20.0	1.60E-04	0.20	σ$_c$=50kN/m^2
Foundation	0.450	200.0	81,577	20.0	1.60E-04	0.20	σ$_c$=50kN/m^2

※)Rate of shear regidity and standard twist are supposed to be proportionate to 0.5th power of standard confined pressure
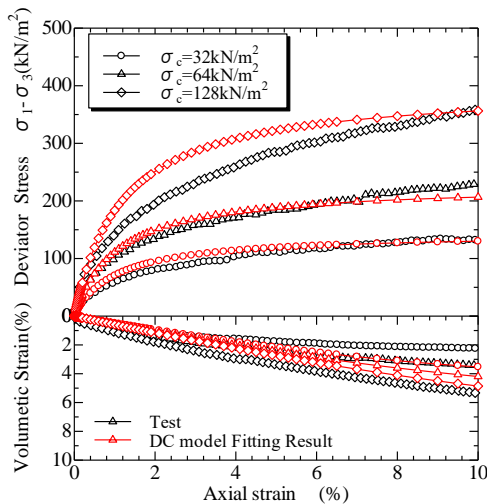
Figure 3. Deviator Stress-Axial Strain-Volumetic Strain - Relation of Filling materials
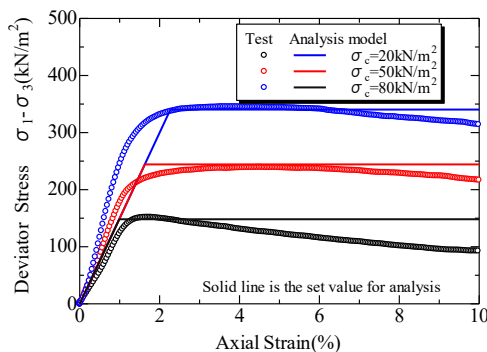
Figure 4. Deviator Stress-Axial Strain Relation of Back ground and Foundation

As filling materials are composed of rocks without fine grain, and confined pressure on the three-tiered gabions is small, ratio of reduction of rigidity against twist is supposed to be bigger than the result of test by Tanaka et.al. So, standard twist under confined pressure at the height of center of gabions (1.5m) was set as γ$_r$ =5.0 x 10^{-5}. As for maximum decay rate h$_{max}$, h$_{max}$=0.20 as general value was set.

Among the dynamic values of physical property, initial shear modulus of rigidity G$_0$ and standard twist in Table 4 are given as the value under standard confined pressure in the Table, and these are set to change in proportion to power of 0.5 of confined pressure.

3.2.3. Value of physical property used in dynamic analysis (initial ratio of shear modulus of rigidity)

Initial shear modulus of rigidity G$_0$ was obtained from this full scale test and full scale test of simple body of retaining wall using gabions. Based on the response characteristics at the moment of input of white noise wave, trial analysis with parameter of speed of shear bouncing wave Vs was executed.

Figure 6 shows Fourier spectrum ratio (transfer function) between response acceleration at levee crown and input acceleration by white noise wave against simple body model of retaining wall using gabions shown in Fig. 9. The results of analysis with the conditions of Vs =180m/s, 190m/s, 200m/s under standard confined pressure of gabions are shown with result of tests. In the cases of Vs=180m/s, 190m/s, primary peak of frequency is a little bit lower compared with result of test, and the case of Vs=200 expresses most nearly result of tests. In Fig. 6, except primary peak, result of analysis exceeds that of tests. Therefore, in analysis it is possible to give rather big response acceleration. There is possibility that frictional force between rocks of filling materials influence to response, and decay effect bigger than supposition was born, but tendency as a whole does not change so big. The purpose of Fig. 6 is setting of initial stiffness of filling materials of retaining wall using gabions, from this viewpoint, as primary
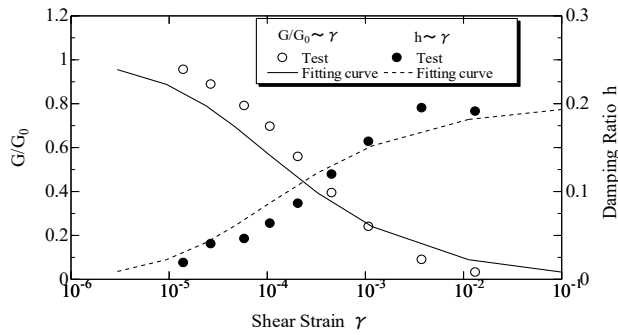
Figure 5. Dynamic deformation characteristics of Back ground and Foundation
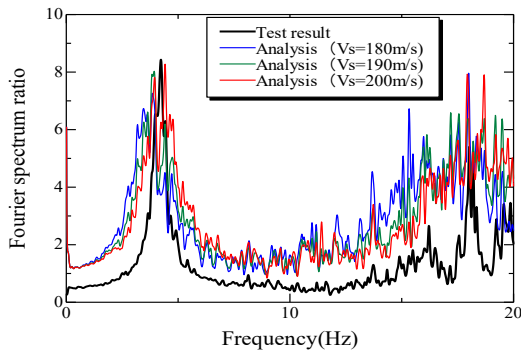
Figure 6. Transfer function of the gabions
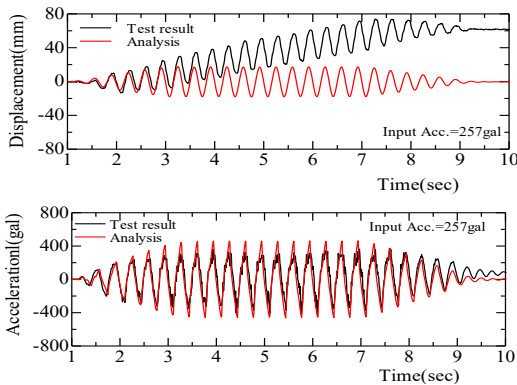
Figure 7. Comparison of the top response of gabions
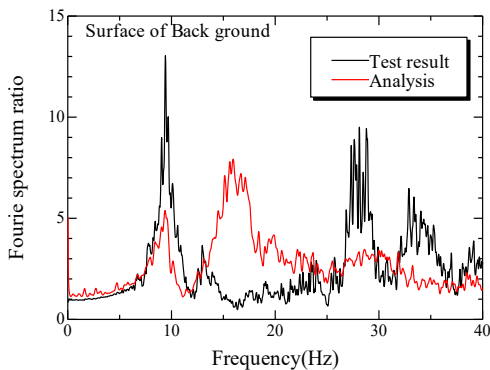
Figure 8. Transfer function of Test case1
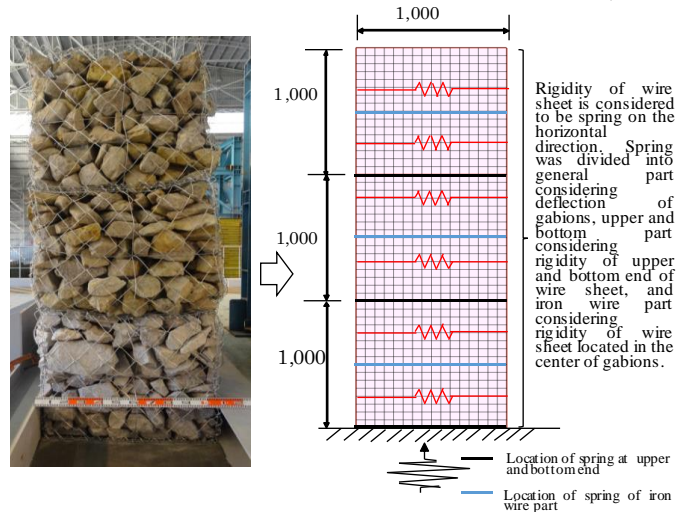
Figure 9. Modelization of band of gabions
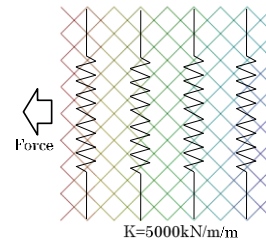
Figure 10. Calculation model for bando of gabions

Table 5. Spring coefficient band of gabions

location	Value	Unit
general part	269.8	kN/m/m
upper and bottom end	4071.7	kN/m
iron wire	426.4	kN/m

peak of result of test coincide with that of result of analysis, it is concluded that there is applicability as a result.

Figure 7 shows response acceleration and response displacement at the levee crown of retaining wall using gabions at the time of inputting sine wave of 257gal in the same model. In Fig. 6, though analysis showed possibility to give a little bit big acceleration, rather big acceleration is given. Regarding response displacement, displacement amplitude itself does not change so much between the result of analysis and that of test, result of test is accumulated in one direction. This is effect of asymmetric nature of retaining wall using gabions, it is supposed that direction of accumulation will differ by conditions of placement of filling materials with random form. The purpose of this analysis is evaluation of stability by structure shape. From this viewpoint, comparatively good result including Fig. 6 was obtained.

Figure 8 shows, using model of Case 1 in Fig. 2, spectral ratio of input acceleration at the levee crown of retaining wall using gabions and at surface of back ground (ref. Fig. 2) when Vs=200 is set under confined pressure of

background. In each point, primary proper period reproduces result of test. Displacement of secondary and onwards peak is seen, but effect of boundary conditions by earth tank which are not expressed in two-dimensional analysis is supposed. As shaking wave is basically 3Hz, effect of wave of more than 10Hz to the result is supposed to be small. Like in Fig. 6, from the viewpoint that this figure aims setting of initial stiffness of back ground, applicability of result is proved.

As above, Vs=200m/s is appropriate as Vs under standard confined pressure of back ground. For the reference, initial stiffness ratio Go by dynamic deformation test of back ground is about 67000kN/m2, if it is converted to Vs, it become about 180m/s. It is a little bit smaller than supposition, but as difference is about 10%, it shows comparatively good coincidence. If you compare Fig. 6 and Fig. 8, proper period of the levee crown of retaining wall using gabions are around 4Hz and 9Hz, differs by Figures. It is supposed that in a model with back ground, response of back ground with bigger mass will govern.

3.3. Modeling of band of gabions (wire sheet)

Retaining wall using gabions is a structure composed of filling materials and wire sheet holding them (here it is called band of gabions). In modeling of band of gabions, it is necessary to consider stereoscopic behavior, but in this study two-dimensional model is used, and if beam model is applied to band of gabions, constraint effect of filling materials cannot be expressed. So, as Figure 10 shows, modeling was made by supposing band of gabions as horizontal spring.

Value of spring was obtained as follows. Tensile resistance of rhombus wire sheet used for band of gabions is affected by compressive stiffness of filling materials. That is to say, if deformation of filling materials does not occur, deformation of band of gabions by pull force depends only on tensile stiffness of wire sheet, but actually, by compressive deformation of filling materials, band of gabions become deformable. Considering this fact, as Fig. 10 shows, under the conditions that compressive stiffness of filling materials is considered as confined spring of band of gabions in the vertical direction, from the displacement obtained by giving horizontal power to band of gabions, value of spring was calculated from relationship with active horizontal power. Compressive stiffness of filling materials is set based on Young's modulus (E=5,000kN/m^2) under the condition of low confined pressure (σc=32kN/m^2) based on Fig. 3. Spring values of band of gabions obtained in the said way are shown in Table 5. Spring is divided into general part that deflection of gabions is considered as above, part of top and bottom end considering stiffness of wire sheet set in the top and bottom end of gabions, and part of iron wire considering stiffness of wire sheet put on the center of gabions. In the table, as general part is supposed from displacement of whole gabions, and the others are supposed from stiffness of wire sheet as iron wire, unit of both differs.
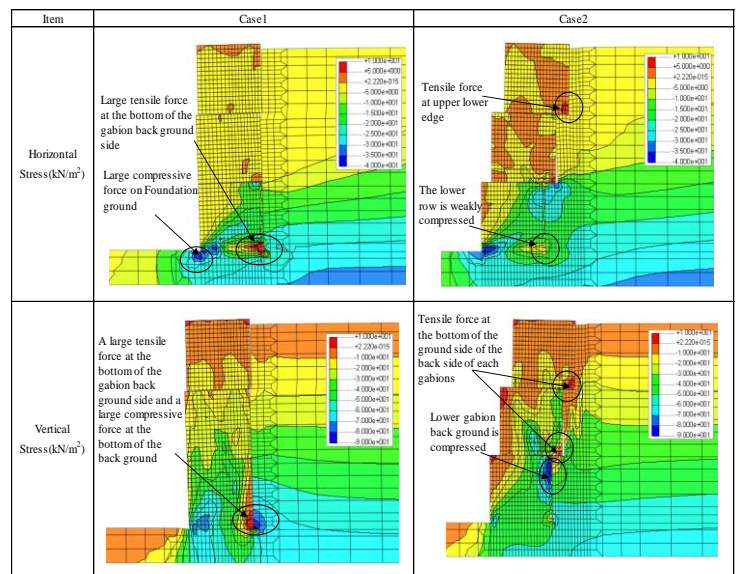
Figure 11. Horizontal and vertical stresses by static analysis
(Deformation magnification 10x)

4. Result of Analysis and Consideration

4.1. Static analysis

As the result of static analysis considering situation before shaking, distribution of horizontal stress and vertical stress in the ground is shown in Fig. 11. Minus of stress in the figure shows compressed state. Here, deformation mode is shown with condition that magnification ratio of deformation was decupled of actual one.

In case where horizontal stress is compared, in Case 1, pull force of more than 10kN/m2 works on retaining wall using gabions in the bottom end on the side of back ground. On the front side, tensile stress of more than 40kN/m2 works on the support ground. This is considered to be caused by sliding power of retaining wall using gabions. On the other hand, in Case 2, pull force occurs on the gabions put on upper stage, but in the lower stage, there is not pull force area, but whole lower stage become compression area.

In case where distribution of vertical stress is compared, in Case 1, tensile stress of more than 10kN/m^2 occurs in the lower part of retaining wall using gabions on the side of back ground, and compression stress of more than 90kN/m2 occurs on the adjacent back ground. This phenomenon is considered to occur by fall down mode of retaining wall. On the other hand, in Case 2, pull force area occurs on the upper stage and bottom end of middle stage of gabions, but lowest stage is in compression state, structure that is difficult to fall down is brought. If you consider relationship between stress of back ground and twist shown in Fig. 4, stability is not diminished by stress inside ground, but stability against sliding by external power of earthquake and rain fall etc. and fall down is relatively low in Case 1.

Figure 12 shows minimum main stress at time of working horizontal inertia force. Like Fig. 11, deformation mode is shown with condition that magnification ratio of

deformation was decupled of actual one. In the figure, location where crack occurs and area of sliding disruption after final shaking which were obtained from damage state of back ground at time of stage shake shown in Table 2. While in Case 1 first crack occurs at the location of 70cm from retaining wall, in Case 2 location of crack was the very near point of 11cm from the retaining wall using gabions. In Case 2, big tensile stress is generated at the point very near the retaining wall using gabions, it is supposed that crack is generated very near the back side of retaining wall using gabions. In case 1, such local tensile stress as being observed in Case 2 is not found, but work of tensile stress is observed in rather wide area near the surface layer. Range of tensile stress near the surface layer, both in Case 1 and Case 2, is inclined to spread, and coincide with the process to generate crack at the distant place from the retaining wall using gabions with increase of shaking acceleration observed in test. Figure 13 presents maximum shear stress at time of action of horizontal inertia force. Like Fig. 12, location of generating crack and range of sliding disruption are shown. Like minimum principal stress, shear stress increases near location of generating crack, the range with big shear stress spreads on the back side with the increase of earthquake intensity. Both minimum principal stress and maximum shear stress are bigger in Case 2 at the location of back side of gabions shown in the figure. This is supposed to be caused by following factors. That is to say, as unit volume weight of back ground is bigger than that of filling materials of gabions, acting load on back ground is bigger than that just beneath the gabions. For this reason, vertical stress just beneath the gabions differs from that of back ground near the gabions, and gap is generated on the ground under the gabions. Then, gabions fall down on the back ground. As the result, shear force by friction is generated between back ground and the retaining wall using gabions, and local sliding disruption occurs. Further, if inertia force is worked, retaining wall using gabions leans forward and at the same time, because of step shape, gabions on the step give upward shear force to back ground, and with this big shear force and tensile force work to back ground near the gabions. For this reason, crack is generated very near the gabions. If inertia force increases, lean forward of retaining wall using gabions increases, gap will be born between back ground. For this reason, active disruption is generated on the back ground, and with the increased lean of the retaining wall using gabions, as gap progresses towards deep part, range of active disruption is widened. On the other hand, in Case 1, size of fall increases due to problem of stability of retaining wall itself using gabions, back ground will be destabilized. In Fig. 12 and Fig. 13, leaning line of retaining wall using gabions under conditions of intensity 0.2 was shown. Lean in Case 1 is a little bit bigger, and stability against falling is higher in Case 2.
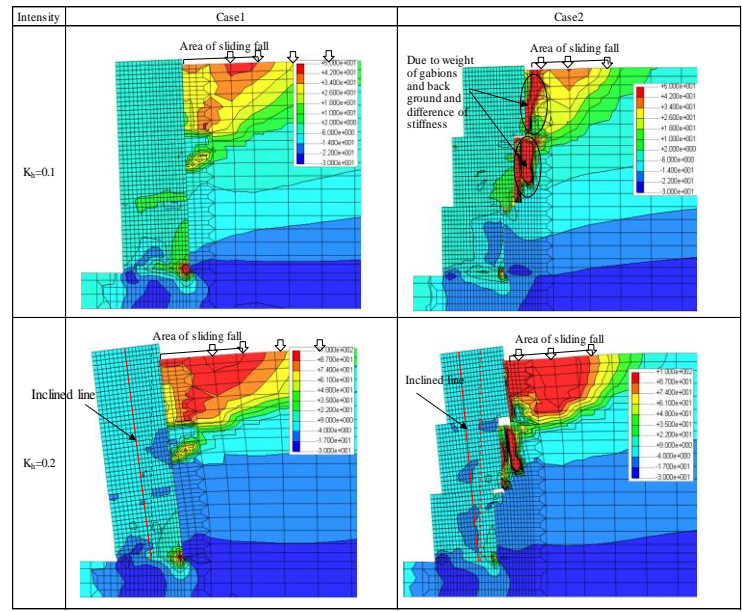
Figure 12. Minimum principal stress under horizontal inertial force
(Deformation magnification 10x)
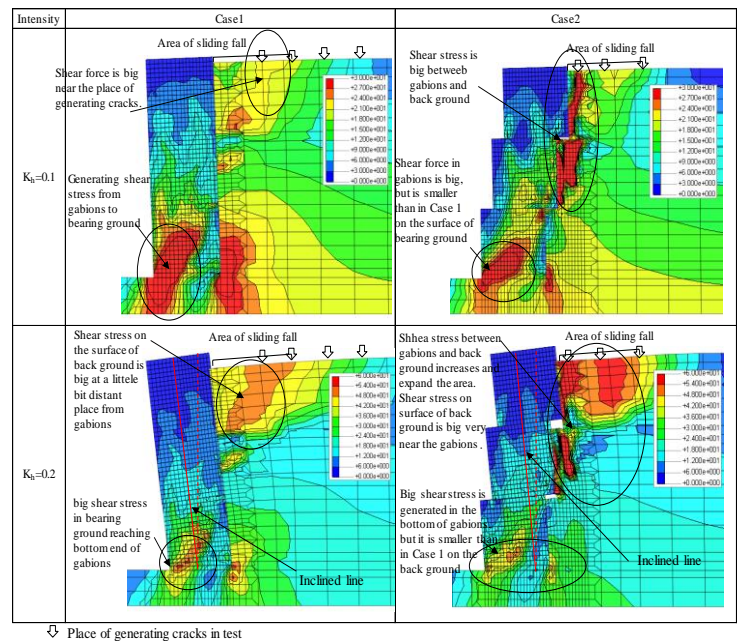
Figure 13. Maximum shear stress under horizontal inertial force
(Deformation magnification 10x)

4.2. Dynamic analysis

Figures 14~17 show time history of acceleration and displacement by dynamic analysis at the levee crown of the retaining wall using gabions and on the surface of back ground (ref. Fig. 2). In every case, objective is 1st, 2nd step of shaking step of sine wave. In the result of Case 1 shown in Fig. 14, under conditions of input acceleration 65gal, acceleration at the at the levee crown of the retaining wall using gabions and on the surface of back ground in the result of test and that in the result of analysis almost coincide. Regarding displacement, result of analysis shows a little bit

123

bigger value on the surface of back ground, but result of test and analysis almost coincide at the levee crown of the retaining wall using gabions. On the other hand, under the conditions of shaking 132gal shown in Fig. 15, acceleration at the levee crown of the retaining wall using gabions in the result of analysis is a little bigger at minus side than that in the result of test, and displacement in the result of test shows tendency to be accumulated by shaking, but accumulation of displacement by shaking is small in the result of analysis. In Case 2 shown in Fig. 16, result of test and result of analysis of acceleration at the stage of 85gal almost coincide, but displacement at the levee crown, like the case of shaking 132gal in Case 1, does not express accumulated displacement in the result of test. Further, in the case of 162gal shaking shown in Fig. 17, acceleration at the levee crown of the retaining wall using gabions in the result of analysis is smaller than that in the result of test, and the displacement at the same place in the result of analysis is smaller too than that in the result of test. From the above, it can be concluded that at the stage of low shaking level, result of test and result of analysis in Case 1 coincide well, but that at the higher shaking level, result of analysis cannot express result of test. In Case 2, in the degree of shaking 85gal, result of analysis cannot express displacement of the retaining wall using gabions in the result of test.

It is indicated that in the test, at the stage of low shaking level, the retaining wall using gabions behaved as a unit, but at the higher shaking level phase difference of response occurs. It is possible that by the said behavior, relative displacement occurs between the retaining wall using gabions and back ground. From this, Figure 18 shows time history of relative value, by analysis, of displacement between the levee crown of the retaining wall using gabions (back ground side) at the time of shaking 132gal in Case 1 and the back ground at the same location. Relative displacement (difference of displacement) has tendency to be increased, but there is a moment of displacement 0 when both crashes.

Figure 18 shows the time when space between the both become big (t=4.18 second and 4.16 second, input acceleration 132gal), and Fig. 19 shows deformation mode (magnification ratio of deformation 20 times) at the time of crash (t=4.36 second and 4.30 second, input acceleration 162gal). Upper line of the light green zone in Fig. 19 indicates horizontal stress. In Case 1, at the moment of opening, tensile stress (plus side) in the horizontal direction occurs, and at the moment of crash, stress at the side of compression (minus side) occurs on the whole.

If you consider real behavior in the test, back ground is disrupted by the above mentioned repetition of compression-tensile, sliding disruption occurs by generation of cracks and progress of them. Earth and sand on the sliding surface sinks between the retaining wall using gabions and back ground at the moment when space opens and fulfill the space. For this reason, retaining wall using gabions cannot return to the original location at the time of next closing behavior, and as
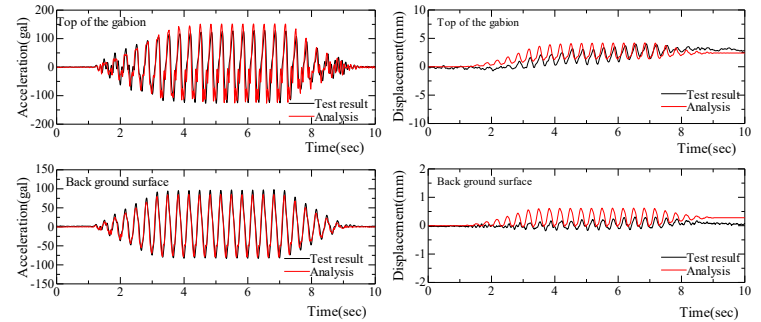
Figure 14. Response value in test case 1 (Input Acc.=65gal)
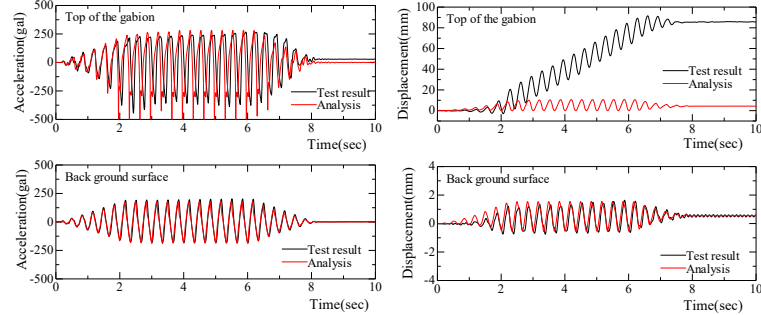
Figure 15. Response value in test case 1 (Input Acc.=132gal)
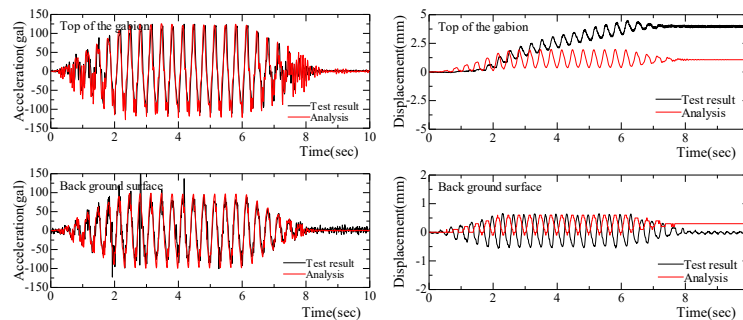
Figure 16. Response value in test case 2 (Input Acc.=85gal)
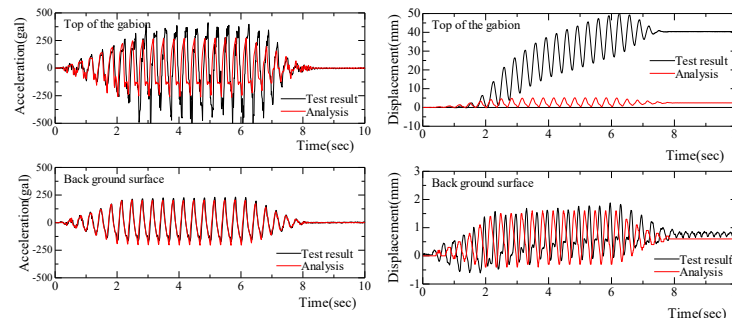
Figure 17. Response value in test case 2 (Input Acc.=162gal)

a result, displacement cumulatively increases. At the stage of low shaking level, this influence is small and big difference does not occur between the result of test and that of analysis, but with increase of shaking level, difference of displacement behavior increases, and result of test cannot be adequately expressed by analysis. Further, as adequate evaluation of crash behavior between the retaining wall

124
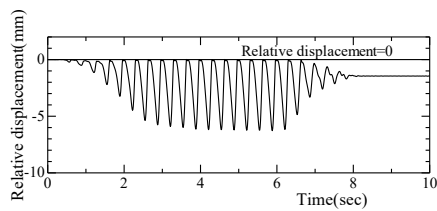
Figure 18. Relative displacement of gabion retaining wall and back ground in test case1(Input Acc.=132gal)

Figure 19. Deformation mode and horizontal stress distribution by dynamic Analysis (Deformation magnification 10x)

using gabions and back ground is difficult, with the increase of shaking level, difference of acceleration increases.

Regarding discordance of result of analysis in Case 2, as Fig. 12 and Fig. 13 shows, local tensile stress and shear stress work between the retaining wall using gabions and back ground, and though it cannot be confirmed visually, it is possible that local breaking surface is generated very near the retaining wall using gabions even at comparatively low shaking level. Therefore, like the case of high shaking level in Case 1, it is supposed that displacement at the levee crown of gabions takes behavior to increase cumulatively. However, though in Case 2 local breaking behavior is watched, as having been indicated, from the viewpoint of stable behavior as a whole, stability is better than Case 1. In Fig. 19, like Fig. 12 and Fig. 13, inclination line is shown about the result of time when space expands, and angle of inclination in Case 1 become comparatively bigger than in Case 2. For this reason, as Fig. 1 shows the result of test, residual displacement after shaking in Case 2 is considerably smaller than that in Case 1.

As above, in this analysis, there is a part that behavior in test is not adequately evaluated. However, it is very difficult to express in analysis behavior of cumulative displacement generated by falling of local breaking surface, and it is considered to be limit of analysis. Purpose of this analysis is comparison of superiority of structural shape with a view to establish a future design method and evaluation of structural

problems and so on. From this viewpoint, like evaluation of local point of stress concentration by static analysis, evaluation of behavior of each structure was made in the analysis conducted this time.

5. Conclusion

With the retaining wall using gabions widely used in Nepal, full-scale shake table test was conducted. From the outcome of this test, about test Case 1 with gravity resistance and test Case 2 of lean type, evaluation by static analysis with finite element method (FEM) and dynamic analysis were conducted. Findings obtained in the study are as follows:

(1) As the result of static analysis, from the viewpoint of stability, it is possible that in Case 1 problems of sliding and falling occur easily and stability of lean type in Case 2 is higher.

(2) In case 2, partially big tensile stress and shear stress works on the back ground near the retaining wall using gabions. This is because of difference of weight of retaining wall using gabions and back ground and difference of behavior of retaining wall using gabions and back ground at the moment when inertia force works, and with these influence, in Case 2 cracks are easily generated very near the retaining wall using gabions.

(3) Both in Case 1 and Case 2, if static analytical power increases, the range where tensile stress and shear stress of background increase is widened.

(4) From the result of dynamic analysis, in Case 1, at the stage of small shaking level, it comparatively well coincide with result of test. On the other hand, if shaking level is increased, analysis cannot express adequately displacement of retaining wall using gabions by test. As well, in Case 2, at the stage of low shaking level, cumulative displacement generated on the retaining wall using gabions cannot be expressed. This comes from the fact that influence of local ruin of back ground generated by collision of retaining wall using gabions back ground and increase of local stress cannot be well expressed.

(5) From the tests and the results of dynamic analysis and static analysis, there is a possibility that in Case 2 of lean type, local cracks are easily generated on the back ground near the retaining wall using gabions and it is supposed that a little bit of swelling is generated in gabions, but problem of stability such as leaning forward is difficult to be generated compared with Case 1, and therefore Case 2 shows the shape with better earthquake resistance.

References

[1] Association of Nationwide Disaster Prevention and Japan River Association, Knowledge of gabion (in Japanese), p.166, 1963.

[2] Nakazawa, H., Manandhara, S., Hara, T., Suetsugu, D., Kuribayashi, K., Nishi, T., Sakuraba, T.,Kariya, T.,Ko-chi, Y. and Hazarika, H., Report on damages caused by the 2015 Nepal Gorkha Earthquake, JAEE International Symposium on Earthquake Engineering, pp.2-36, 2015.

[3] Yamada, M., Hayashida, T., Mori., J, Mooney., W, Building damage survey and microtremor measurements for the source region of the 2015 Gokha, Nepal Earthquake, Annuals of Disas. Prev. Res. Inst, Kyoto Univ., No.59 A,2016, pp.65-73, 2016.

[4] Hara, T., Nakazawa, H., Suetsugu, D., Kuribayashi, K., Nishi,T., Tadokoro, Y., Miyoshi, K., Zhang, H., Field survey on damages of gabion structures caused by the 2015 Nepal Gorkha earthquake and examination of specific measures for earthquake resilience improvement, Journal of the Japan Society of Civil Engineers A1, Vol.74, No.4, pp.I_586- pp.I_597, 2018.

[5] Suetsugu, D., Hara, T., Nakazawa, H., Kuribayashi, K., Shinagawa, D., Nishi, T. and Zhang, H., Damage survey on 1gabion structures in the 2015 Nepal Gorkha Earthquake – Physical properties of stone materials packed in the gabion –, 51st Japan National Conference on Geotechnical Engineering(in Japanese), pp.1661-1662, 2016.

[6] Kuribayashi, K., Nishi, T., Zhang, H., Bhattarai, P. K., Hara, T., Suetsugu, D. and Nakazawa, H., Damage survey on gabion structures in the 2015 Nepal Gorkha Earthquake – Construction method to filling materials in gabions –, 51st Japan National Conference on Geotechnical Engineering(in Japanes), pp.1663-1664, 2016.

[7] Nakazawa, H., Hara, T., Suetsugu, D., Kuribayashi, K., Nishi, T. and Hazarika, H., Residual deformation in full-scale shake table test of a gabion retaining wall for road, The 15th International Symposium on Geo-disaster Reduction (15th IS-GdR), p.109, 2017.

[8] Nakazawa, H., Hara, T., Suetsugu, D., Nishi, T., Kuribayashi, K., Miyoshi, K. and Shimomura, S. , Experimental evaluation on earthquake-resistance of road retaining wall using gabion, Journal of Disaster Research , Vol.13, No.5, 2018.

[9] Nakazawa, Hara, T., H., Suetsugu, D., Nishi, T., Miyoshi, K., Shimomura, S., Usukura, K., Kuribayashi, K., Kimura, S., Shibahara, R.：Full scale experiments and stability evaluation on earthquake resistance of gabion retaining wall -part1 overview of residual deformation- , Japan Society of Civil Engineers 73th Annual Scientific Conference(in Japanese), pp.689-690, 2018.

[10] Usukura, K., Nakazawa, H., Nishi, T., Hara, T., Suetsugu, D., Miyoshi, K., Shimomura, S., Kuribayashi, K., Kimura, S., Shibahara, R., Full scale experiments and stability evaluation on earthquake resistance of gabion retaining wall -part2 Stability evaluation-, Japan Society of Civil Engineers 73th Annual Scientific Conference(in Japanese), pp.691-692, 2018.

[11] Nishi, T., Nakazawa, H., Usukura, K., Hara, T., Suetsugu, D., Miyoshi, K., Shimomura, S., Kuribayashi, K., Kimura, S., Shibahara, R, Full scale experiments and stability evaluation on earthquake resistance of gabion retaining wall -part3 Evaluation by FEM analysis-, Japan Society of Civil Engineers 73th Annual Scientific Conference(in Japanese), pp.693-694, 2018.

[12] Hara, T., Suetsugu, D., Manandhar, S., Nakazawa, H., Kuribayashi, K., Nishi, T., Sakuraba, T., Kariya, T., Kochi, Y. and Hazarika, H.: Damage survey on gabion structures in the 2015 Nepal Gorkha Earthquake – Outline of survey –, 51st Japan National Conference on Geotechnical Engineering(in Japanese), pp.1657-1658, 2016.

[13] Duncan, J. M. and Chang, C. , Nonlinear analysis of stress and strain in soils, Journal of the Soil Mechanics and Foundations Division, ASCE,Vol.96, No.SM5, pp.1629-1653, 1975.

[14] Hara, T., Tadokoro, Y., Shibahara, R., Suetsugu, D., Nakazawa, H., Nishi, T., Kuribayashi, K., Evaluation on earthquake resistance of retaining wall using gabions by laboratory tests -Part.1 Shear strengths characteristic of infilling materials-53st Japan National Conference on Geotechnical Engineering(in Japanese), pp.1795-1796, 2018.

[15] Tanaka, Y., Kudo, K., Nishi, K., Okamoto, T., Kataoka, T. and Ueshima,T., Small strain characteristics of soil in Hualien, Taiwan, Soils and foundations, Vol.40, No.3, pp.111-125, June 2000.

Crab Larvae Counter Using Image Processing

Furqan Zakiyabarsi[a,*], Muhammad Niswar[b], Zahir Zainuddin[c]

[a]Electrical Engineering Department, Engineering Faculty, Hasanuddin University. Email: thb.zone@gmail.com
[b]Electrical Engineering Department, Engineering Faculty, Hasanuddin University. Email: mniswar@gmail.com
[c]Electrical Engineering Department, Engineering Faculty, Hasanuddin University. Email: zainuddinzahir@gmail.com

Abstract

Very small larval size, high mortality rate of crab larvae, the absence of an accurate crab larva counter at affordable price, the density of larvae that are not known accurately, the ratio of feed that not in accordance with the number of larvae to damage water quality and cannibalism, water quality cannot be adjusted to the density of distribution, and economically unprofitable both in terms of feed efficiency and buying and selling transactions. By knowing the number of crab larvae accurately the survival rate of crab larvae increases and is economically beneficial. In this study, larvae counters were designed and developed. This tool uses digital imagery to detect and count crab larvae zoea-1 phase. The accuracy of the crab larva counter is 89,8%.

Keywords: Counter application; crab; high mortality; image processing; larval; pattern recognition

1. Introduction

The increasing number of population drives the need for better food and nutrition continues to increase. The phenomenon of shifting orientation towards meeting people's food needs that prioritizes safe and healthy food consumption, has directly triggered a high demand for alternative protein needs. In other words, the consumption pattern has shifted from red meat-based food products to white meat-based food products, in this case is seafood, one of the highest demand is crab.

This has driven the market demand for the need for protein-rich consumption of crabs to increase and Indonesia is one of the crab producing countries for domestic and foreign market needs. However, the survival rate from crab larvae to adult crabs is very low, the highest survival rate of zoea to megalopa is $14.12 \pm 031\%$ [1] and in general crab larvae only have the highest survival rate between 20 - 50% [2] has become a serious problem in terms of crab production in order to immediately find a solution in terms of technology implementation. The absence of a tool that is able to accurately calculate crab larvae at an affordable price in an easy way to do is forcing farmers to count traditionally with sampling methods and estimates that are very at risk of increasing mortality in the cultivation process because the level of larval density is not known accurately causing feed ratio and number of larvae are not comparable. The ratio of feed that exceeds the needs of larvae will be polluted, high levels of cannibalism due to lack of feed, and economically the number of larvae that is

inaccurate can harm both cultivators with high mortality rates and consumers with the number of larvae purchased are not known accurately and can reduce market trust. Larva counting methods currently carried out by aquaculture practitioners only use the population sampling method and look for the average of several sampling. Even traditional aquaculture practitioners use more estimates in terms of determining the number of crab larvae.

Digital image processing is one of the technologies that can fill this gap. Image processing utilizes digital images with certain techniques to get more information from these images. The increasingly advanced and affordable image processing technology infrastructure makes image processing technology very good and easy to implement and absorb by the public.

Based on this, the author raised the title of the Crab Processing Larvae Using Image Processing to provide information about the number of crab larvae that can be used for aquaculture needs and economic needs in an easy and affordable price.

2. Methodology

2.1. Image Acquisition

Taking pictures using a smartphone with camera specifications above 8 Mega Pixels that have been used by most Indonesian people, so that the implementation of this research can be well absorbed by the public. This research uses the following instrumentation:

- Software
  a. Mac OS Sierra
  b. Anaconda (Python)
  c. OpenCV
- Hardware
  a. Laptop MacBook Air with Prosesor Core i5 (1.40 GHz)
  b. Solid State Drive 128 GB Intel
  c. Memory DDR3 4 GB
  d. Monitor 11"
  e. Handphone Android Oppo F7, Vivo V9, dan Vivo V15

2.2. Model Description

The system design in this study was designed so that this technology is easily absorbed and used by the public. The larvae to be counted are put into special containers that have special lighting, after that using a mobile camera the larvae picture is taken. The results of the images obtained are then processed using image processing methods to get an accurate number of crab larvae.

Image processing method, using an image processing technique as shown in Fig. 2.
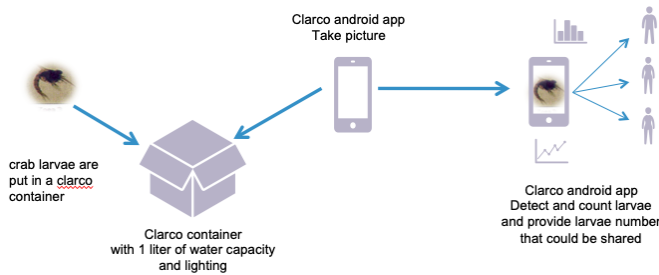
Figure 1. System design
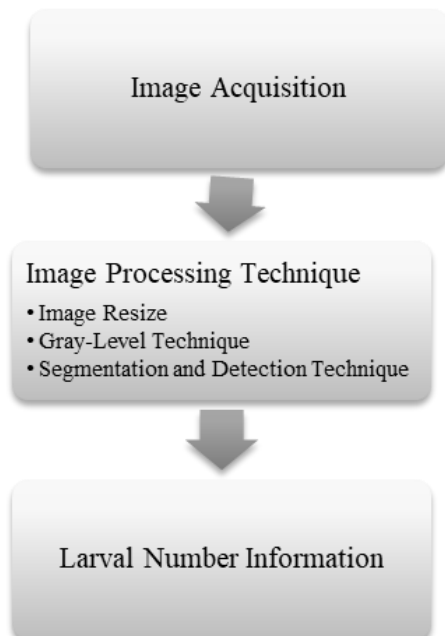
Figure 2. Model research methods

2.3. Image Processing Technique

Pixels represent picture elements and it is the smallest unit of picture information that is stored as bits to form a digital image. In general, more bits stored per pixel will result in a clearer image due to higher greyscale or color resolution in the image, and the more pixels used to represent an image, the closer the image resembles the original. In imaging science, the analysis, manipulation, storage, and display of pixel information from sources as photographs, drawings, and video refers to image processing. Output of the image processing is an image or a set of characteristics or parameters related to the image [3].

2.3.1. Image Resize

The initial step to do is to resize the image size so that the number of pixels is as desired and does not overload memory performance.

2.3.2. Grey-Level Technique

Thresholding or gray-level segmentation is an essential concept related to image processing and machine vision. Thresholding is a conversion between a gray-level image and a bi-level image. Bilevel image is a monochrome image only composed of black and white pixels. It should contain the most essential information of the image (i.e., number, position, and shape of objects), but is not comparable with the information offered by the grey-level image. Most of the time pixels with similar grey levels belong to the same object. Therefore, classifying the image by grey-level pixels may reduce and simplify some image processing operations such as pattern recognition, and classification [4].

Thresholding operations select pixels whose component values lie within a specified range. The operation may change the values of either the selected or the unselected pixels. A pixel pattern can be highlighted, for example, by setting all the pixels in the pattern to 0. Pixel maps and lookup tables provide a simple mechanism for thresholding using individual component values. However, pixel maps and lookup tables only allow replacement of one component individually, so lookup table thresholding is trivial only for single component images [5].

All methods so far assumed that the background and object pixels have non-overlapping grey levels. Most of the time in real-life that ideal assumption is not true. Therefore, the selection of a single threshold for an image is not possible in most of the case. However, all that is needed is for the two classes of pixels not to overlap over each of a set of regions that collectively form the image. The first step is to determine how many independent regions form the image and their sizes. For each of them, it is possible to apply some thresholding methods. Therefore, there is not a single threshold value, but one per region. Only one thing to take care of when using regional thresholding method, it is necessary to make sure that either each region contains a sample of both object and background pixels, or that no thresholding is attempted when only a pixel class exists [4].

128
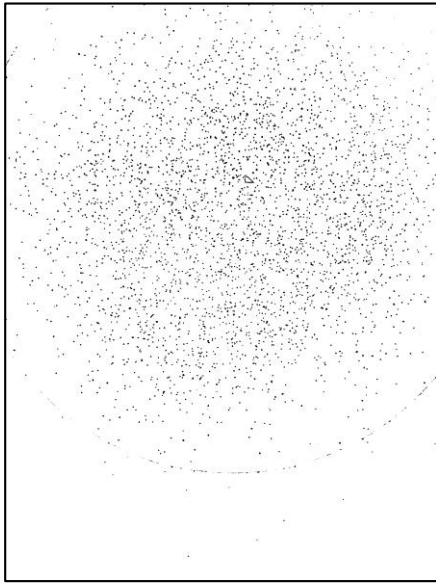
Figure 3. Picture of the results of the Gray-Level technique

2.3.3. Segmentation and Detection Technique

1. Segmentation Technique

The treatment of image segmentation can be realized by using four different principles, threshold method, zone method, boundary method, and edge method [6]. In the very small sample size of larvae, the segmentation is done by using a combination of the four methods to get good results.

2. Detection Technique

The BLOB analysis algorithm is used to find and count objects, and to make measurements based on their characteristics [7]. The purpose of the analysis is to determine whether the results are obtained from operations that are accurate, logical and correct. Image processing software consists of complex algorithms that have pixel values as input. Image analysis software packages today include old and new technology. Most significant is the relationship between the old BLOB analysis method and the new detection technique. For image processing, BLOB is defined as the area of connected pixels. BLOB analysis is the identification and study of this region in images [8, 9]. This algorithm distinguishes pixels by their value and places them in one of two categories. That is. foreground (usually a pixel that has a non-zero value) or background (a pixel with a zero value).

Because the blob is the touching pixel area, the analysis tool usually considers touching the foreground pixels as part of the same blob. As a result what is easily recognized by the human eye as several different but touching blobs can be interpreted by the software as one blob. Furthermore, any part of the blob that is in the background pixel state due to lighting or reflection is considered as background during the analysis [10].

The performance of the BLOB analysis operation depends on successful image segmentation, separating the good blobs from the background and from each other and eliminating everything else in the image that is not attractive. Segmentation involves binarization operations [11]. If simple segmentation is not possible due to poor lighting or a blob with the same gray level as the background, we must develop a segmentation algorithm that is suitable for a particular image. Images obtained may contain fake noise or blobs or holes that may be caused by noise or lighting. Such foreign BLOB can interfere with the results of the BLOB analysis [12]. If the image contains several unfamiliar blobs, we must pre-process the image before using it. Preprocessing refers to whatever steps are taken to clean the image before analysis and can include thresholds or filtering [13].

3. Result And Discussion

Image data of zoea-1 larvae samples were taken and processed using image processing techniques using mobile camera instrumentation of three different types. Where the zoea phase is a phase that is very vulnerable in the life cycle of crab larvae. Overall the use of image processing techniques provides satisfactory results. We can see in one example of larval detection in Figure 5, that crab larvae can be detected and counted well.

Figure 4. The results of taking pictures on the container
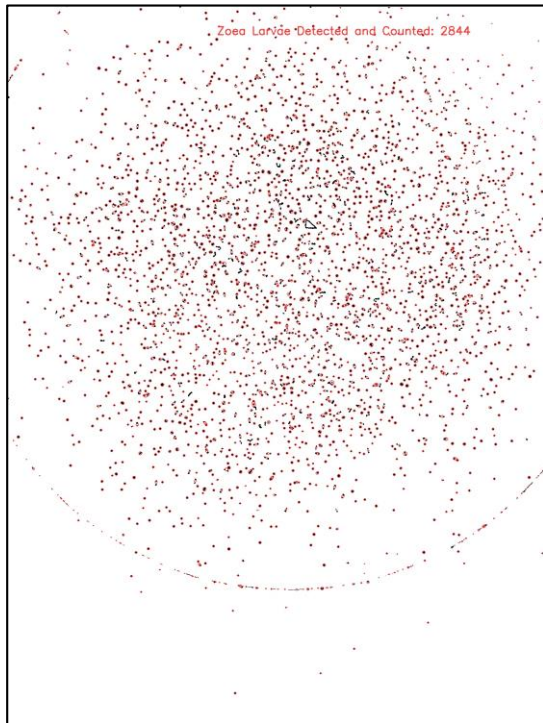
Figure 5. Detection and calculation results with counter application

In testing the system, the amount of image data on the Zoea-1 phase larvae is validated using the Confusion Matrix with the following accuracy testing results shown in the table.

$$Accuracy = \frac{TP + TN}{TP + TN + FP + FN}$$

where,

- TP is the number of larvae observations that are actually detected as larvae
- TN is the number of observations not larvae
- FP is the number of non-larvae detected as larvae
- FN is the number of larvae that cannot be detected
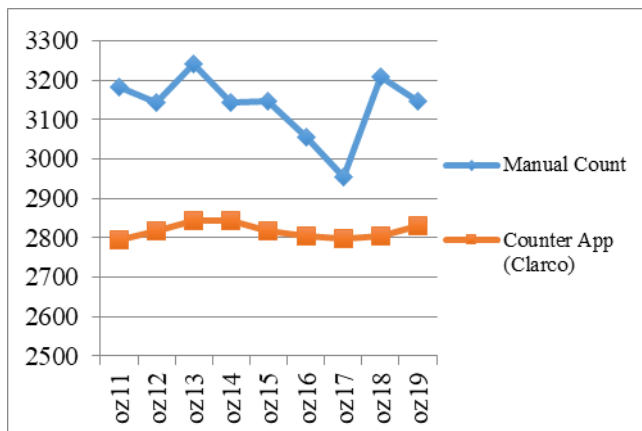
Figure 6. Comparison chart of counter application and manual calculations

Table 1. Zoea-1 system accuracy comparison

Name	Manual Count	Counter App	Accuracy (TP+TN/TP+TN+FP+FN) %
oz11	3183	2794	87.78
oz12	3145	2817	89.57
oz13	3242	2844	87.72
oz14	3144	2844	90.46
oz15	3146	2817	89.54
oz16	3055	2804	91.78
oz17	2955	2799	94.72
oz18	3210	2804	87.35
oz19	3147	2832	89.99
Average			**89.88**

Table 2. Confusion matrix

n = 28227	Prediction = True	Prediction = False
Actual = True	TP = 25355	FN = 2872
Actual = False	FP = 0	TN = 0

$$Accuracy = \frac{25355 + TN}{28227}$$
$$= 0.898$$

It can be seen from the table that the presentation accuracy of larvae detection results in the zoea-1 phase is 89.8%. Containers containing defects, camera focus, reflected light, water level, and larval distance from the water surface are some of the things that affect the accuracy of larval detection.

4. Conclusion and Future Work

Calculation of the number of crab larvae in the zoea-1 phase using image processing techniques has a pretty good accuracy with an accuracy of 89.8%. In this study, the image sample used was in the zoea-1 phase and the image was taken in a special container with a limited volume of water so the larvae had to be removed from the hatchery tank. Taking pictures in various phases of zoea and direct calculation in the hatchery container and by using high-level image recognition and intelligent algorithms is our next research in the future.

Acknowledgment

References

[1] A. Journal, V. Faj-, and P. In, "Survival Rate and Development Period of the Larvae of Survival Rate and Development Period of the Larvae of Portunus," vol. 2012, 2012.

[2] R. Nicholas and Z. Chaoshu, "Blue swimmer crabs: emerging species in Asia," *Glob. Aquac. Advocate*, vol. 11, no. 3, pp. 34–36, 2008.

[3] F. H. Ahmad, "From Pixels to Medical Imaging," *ICSIPA 2013*, p. 2013, 2013.

[4] A. Martin, S. Tosunoglu, and W. F. Street, "Image processing techniques for machine vision," pp. 1–9, 2000.

[5] M. Reynolds, "Image Processing Techniques," pp. 211–245, 2005.

[6] C. Yuchao and L. Hui, "Study on the Meso-Structure Image of Shale Based on the Digital Image Processing Technique," 2009.

[7] C. Damerval, S. Meignen, and A. O. Case, "Blob Detection With Wavelet Maxima Lines," vol. 14, no. 1, pp. 39–42, 2007.

[8] P. Forss, "Robust Multi-scale Extraction of Blob Features," no. 2, pp. 11–18, 2003.

[9] G. Gerig, G. Szekely, G. Israel, and M. Berger, "Detection and Characterization of Detection and Characterization," June, pp. 165–176, 1995.

[10] S. Hinz, "Fast and Subpixel Precise Blob Detection and Attribution Stefan Hinz Remote Sensing Technology."

[11] A. Ming, "A blob detector in color images," pp. 364–370, 2007.

[12] N. Khanina, E. Semeikina, and D. Yurin, "Color Blob and Ridge Detection," no. January 2010, 2014.

[13] A. Patil, M. E. Student, and M. Dhanvijay, "Blob Detection Technique using Image Processing for Identification of Machine," vol. 2, pp. 1–8, 2015.

Docking Unit Joining Omni Wheel Robot and Mobile Robot

Naoki Igo[a,*], Daichi Fujita[b], Ryoma Hanabusa[c], Yasuto Nagase[d], Satoshi Mitsui[e], Toshifumi Satake[f]

[a]Department of Systems, Control and Information Engineering, National Institute of Technology, Asahikawa College. Email:igo@asahikawa-nct.ac.jp
[b]Graduate School of Information, Production and Systems, Waseda University. Email:daichi0312mwam@gmail.com
[c]Advanced Course of Production System Engineering, National Institute of Technology, Asahikawa College. Email:p188014@edu.asahikawa-nct.ac.jp
[d]Advanced Course of Production System Engineering, National Institute of Technology, Asahikawa College. Email:p188012@asahikawa.kosen-ac.jp
[e]Department of Systems, Control and Information Engineering, National Institute of Technology, Asahikawa College. Email:mitui@asahikawa-nct.ac.jp
[f]Department of Systems, Control and Information Engineering, National Institute of Technology, Asahikawa College. Email:satake@asahikawa-nct.ac.jp

Abstract

This research realizes a docking unit joining omni wheel robot and mobile robot. The omni wheel robot cannot move on rough ground. In order to move on rough ground, a mobile robot that can move with the omni wheel robot is required. The docking unit aims at a unit that can be used without remodeling omni wheel robot. The docking unit realized by this research can store the fixed part of the omni wheel robot. When omni wheel robot is mounted, the mounting surface is flat because the fixed parts are stored, and the omni wheel robot can be mounted by sliding. As a result, we designed a mechanism to connect the fixed parts to store the parts that fix the omni wheel robot. And the fixed parts with the mechanism were made.

Keywords: Docking unit, omni wheel robot, mobile robot

1. Introduction

In human life, robots are getting familiar. For example, there are robots to talk [1, 2], pet robots [3, 4], healing robots [5], physical ability extension robots [6-8], moving assistance robot [9, 10], and the like. In the human life, the ultimate form of the robot being targeted is a humanoid robot. If the robot is a humanoid, it will be possible to work with the tool just like a human being. Previous humanoid robots occupied the majority for research and commercial use, and it was a price that ordinary people can not purchase. Pepper was released from SoftBank Robotics Corp. as a humanoid robot at a price that ordinary people can purchase. Pepper moves by the omni wheel. Omni wheels are effective mobile devices when moving in various directions. However, it is difficult to freely move the floor with structurally large steps and irregularities. Therefore, Pepper can be used only within the limited space of the room. When this problem is solved, the range of use of Pepper expands. Therefore, this research realizes an extended movement unit for expanding the movement range of Pepper. The extended movement unit aims at a unit that can be used without remodeling Pepper.

2. Omni Wheel Robot

2.1. Overview of Pepper

In this research, we used Pepper as an omni wheel robot. Pepper is an inexpensive humanoid robot released by SoftBank Robotics Corp. in 2015. Figure 1 is a picture of Pepper. Pepper is a humanoid robot developed coexisting with people and focusing on communicating with people. As

Table 1. Specification of Pepper [11].

Size	1210 x 480 x 425 [mm]
Weight	29 [kg]
Battery	Li-ion battery
Head sensor	Microphone x4, RGB camera x2, 3D sensor x1, Touch sensor x3
Chest sensor	Gyro sensor x1
Hand sensor	Touch sensor x2
Leg sensor	Sonar sensor x2, Laser sensor x6, Bumper sensor x3, Gyro sensor x1
Actuator	Motor x20
Display	10.1 inch touch display
Communication method	Wi-Fi : IEEE 802.11 a/b/g/n (2.4GHz/5GHz), Ethernet port x1 (10/100/1000 base T)
OS	NAOqi OS

*Corresponding author. Tel.: +81-166-55-8028
2-2-1-6, Shunkodai, Asahikawa, Hokkaido, Japan, 071-8142

a feature, it has feelings and has a tablet on the chest. Currently, Pepper is used for reception at the store, work of customer service, and communication robot at home. Table 1 is a list of basic specifications of Pepper [11].

(a) Overall view

(b) Pepper's omni wheel

Figure 1. Picture of Pepper.
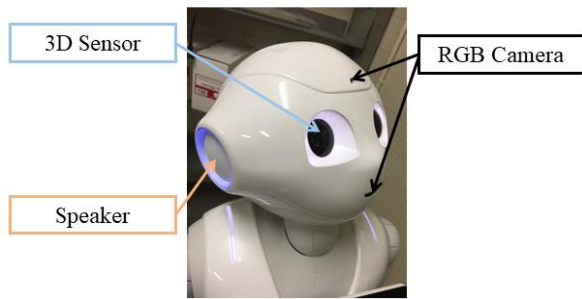
(a) Sensors on head
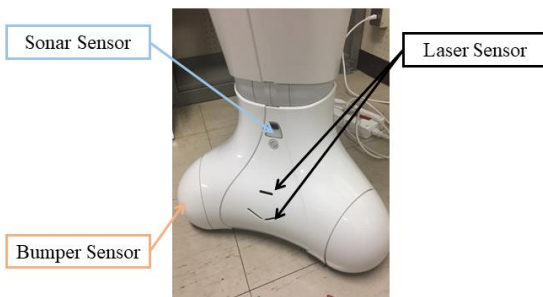
(b) Sensors on leg

Figure 2. Sensor locations of Pepper

2.2. Sensors of Pepper

Pepper has many sensors. In particular, sensors are concentrated on the head and the leg, and Figure 2 shows the arrangement of the various sensors. The head is equipped with cameras and the like necessary for communicating with humans. The legs are equipped with necessary sensors to avoid obstacles during movement and to keep the distance between humans and distance proper. Also, there are touch sensors on the head and hand, Pepper can get tactile sense. Gyro sensors are used to keep Pepper moving upright.
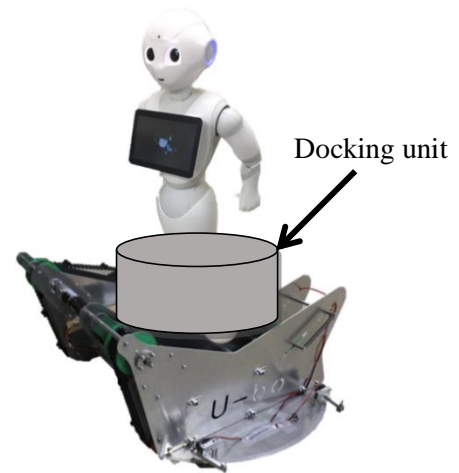
Figure 3. Combined image of Pepper and extended movement unit
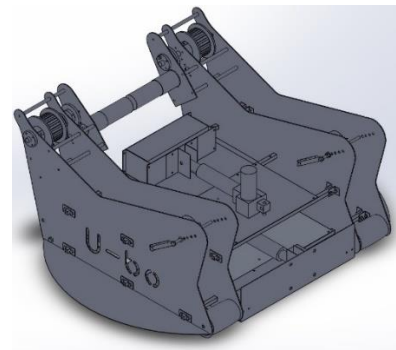
(a)   Image of 3DCAD

(b) Picture of mobile robot

Figure 4. Mobile robot

2.3. Application development environment of Pepper

There are Choregraph, Python SDK (Software Development Kit), ROS (Robot Operating System) as environments for developing applications for Pepper. Choregraphe can develop applications for Pepper on the GUI as shown in Fig. 1. By linking prepared blocks and blocks with lines, it is possible to create Pepper's motion and develop applications easily. Application development for remote control using Choregraphe is not suitable for the characteristics of Choregraphe. Therefore, it can be solved by using Python SDK. However, it is not a development environment using a GUI like Choregraphe, but it is the same as a normal programming environment. ROS is an open source application development environment for robots. However, since it basically moves on Ubuntu, caution is necessary.

3. Docking Unit

3.1. Overview of extended movement unit

The extended mobile unit is made up of a mobile robot and a docking unit. The docking unit is a unit for combining with the mobile robot without modifying the body of the Pepper. Figure 3 is an image diagram combining Pepper and extended movement unit. Figure 4 shows the mobile robot for the extended movement unit.

3.2. Overview of docking unit

Figure 5 is a view of the docking unit as viewed from above. It consists of three pillars arranged around Pepper and a disk for storing them. The pillar is composed of a plurality of units (extension units), and the disc is fixed with the robot body that has been made. Figure 6 is an enlarged view of the interior of the broken line in Fig. 5. Figure 6 shows a state in which the extension units are stacked up and the pillars are completed. At the time of placing the Pepper on the docking unit, the extension unit is stored in the circular plate, and the column does not exist. In this way, the pillars can be made by sticking and leaving child machines coming in and going out of the circular plate.
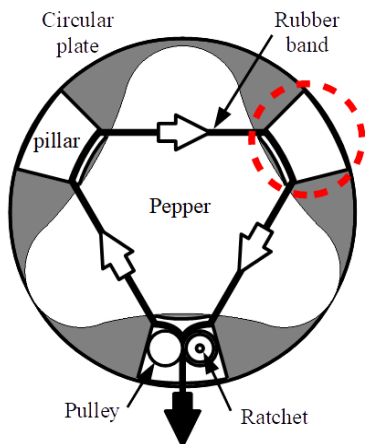
Figure 5. Schematic diagram of docking unit

3.3. Mobile robot

The 3D CAD data and the actual image data of the mobile robot are shown in Fig. 4. This mobile robot [10] is a pair of crawler type with tension applied to both side pulleys and tensioned respectively. This makes it possible to move forward, backward and turn. In addition, this robot participated in the 1st Creative Robot Contest for Decommissioning [13], loaded a load of 5 kg weight, and was able to climb the stairs with a slope of 41 degrees. As a feature of lifting up the stairs, a cylinder was attached to the lower part of the robot for stabilization, but in this study, since it is assumed to run on flat ground at first, there is no cylinder (it was installed for unloading The same applies to the upper cylinder).
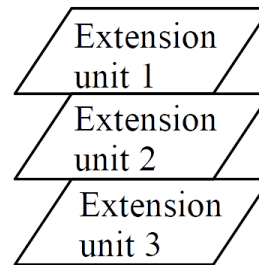
Figure 6. Stacked image of extension unit

(a)   Overall view

(b)   Enlarged view of the connection
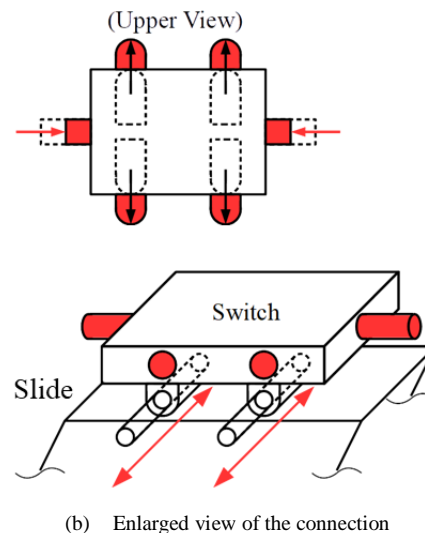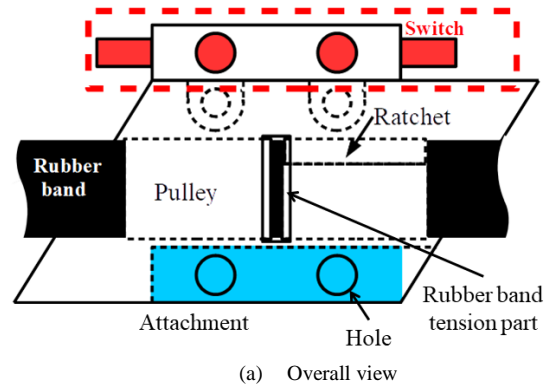
Figure 7. Structure diagram of extension unit
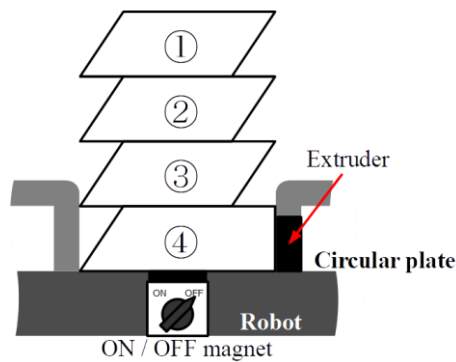
(a)   Mechanism of extruder and pillar fixing method
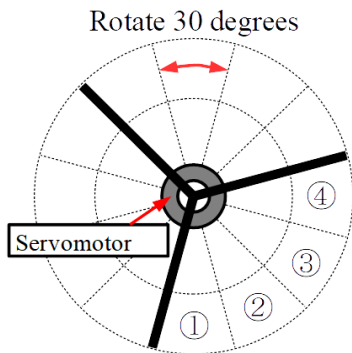
(b)   Image diagram of extension unit storage

Figure. 8. Extension unit pushing mechanism and pillar fixing method

(a)   Image of omni wheel robot mounted on the docking unit
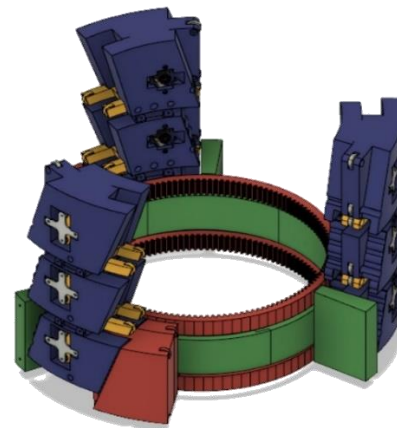
(b)   Image excluding omni wheel robot and exterior
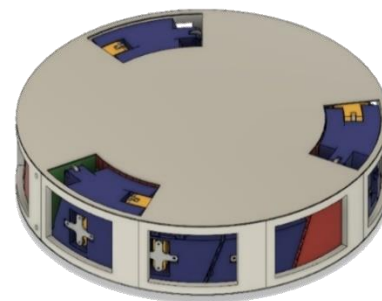
(c)   Overall view

Figure 9. 3DCAD images of docking unit

Since this robot was not originally designed to carry Pepper, we carried out a test run with a weight of 30 kg exceeding the weight of Pepper. As a result of the test run, the robot was able to run normally.

The created mobile robot is a robot that moves by autonomous traveling. In the extended mobile unit realized by this research, remote control using a controller is performed. To make the controller and the robot wirelessly communicate, use the PS3 controller for the controller. Wireless communication is realized by attaching a Bluetooth receiver to a single board PC that gives instructions to the actuator of the robot. Since there is no cable between the controller and the extended movement unit, the operator can operate with high degree of freedom.

3.4. Mechanism of extension unit

The structure of the extension unit is shown in Fig. 8. When looking at the extension unit from the side, it is a parallelogram, but this is because if you place two extension units, apply one of the extension units to the wall and apply force to the other extension unit from the side, It slides at the hypotenuse of the parallelogram, and the extension unit which applied the force enters under the other, so that the stacking operation becomes possible. The force to be applied is the force obtained by rotating the propeller-type extension unit extruder composed of three servo motors and three plates as shown in Fig. 8 (b) in the circular plate.

The method of only stacking parallelograms collapses. Therefore, we devised how to connect extension units. Every time the switch in Fig. 7 is pressed, four bars expand and contract from two directions. By this method, handsets connected to each other. Only extension unit located at the bottom of Fig. 5 is constituted by a pulley, a ratchet, and a rubber band pulling portion. Other extension units have a hole through which the rubber band passes on both sides of the main body. The switch section is independent from the extension unit main body and can be slid back and forth. In addition, since the pillar is composed of a plurality of extension units, it is possible to arrange pillars along the curved body line of Pepper.

135

3.5. Fixing method of Pepper using docking unit

This section shows the procedure of fixing the Pepper using the docking unit. The fixing method is realized by the following six steps.

(1) The extruder rotates clockwise (counterclockwise when stored), and the first extension unit is pushed out from the disk exit.

(2) When rotation of the extruder stops, press the switch to connect the two extension units. In this step, the first stage of the pillar is completed.

(3) Repeat step (1) and step (2) until the four extension units are connected.

(4) Turn on the magnet switch, fix the number 4 of extension unit and Pepper. When the pillar is completed, it becomes as shown in Fig. 8 (a).

(5) Wrap the rubber band around the Pepper in the direction of the white arrow in Fig. 5 and insert it on the ratchet side of the pulley.

(6) Turn the pulley on the ratchet side counterclockwise, and when the rubber band comes out from the rubber band pulling part, pull out in the direction of the black arrow in Fig. 5. When this step is completed, Pepper and the docking unit are fixed.

4. Creating a Real Model

4.1. 3D CAD images

We created a 3D model of the docking unit using 3DCAD. Figure 9 shows the 3D CAD images of the docking unit. Figure 9 (a) is a 3D CAD image with an omni wheel robot mounted on the docking unit. Figure 9 (b) is a 3D CAD image with the omni wheel robot and exterior removed from Fig. 9 (a). Figure 10 shows 3DCAD images of extension unit connection, and Figure 11 does 3DCAD images of extension unit protrusion.

4.2. Finished product

We created a real model using the 3D CAD data created in section 4.1. Many parts were created using a 3D printer. Figure 12 (a) shows a picture with the extension unit connection off. Figure 12 (b) shows a picture with the extension unit connection part turned on. Figure 13 shows the state where the protruding part for stably fixing the omni wheel robot protrudes from the extension unit. Figure 14 shows the extension unit connected to the extension unit. The extrusion part and the exterior of the docking unit have not been completed yet.

Figure 10. 3DCAD images of extension unit connection
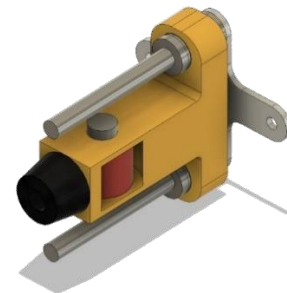
Figure 11. 3DCAD images of extension unit protrusion
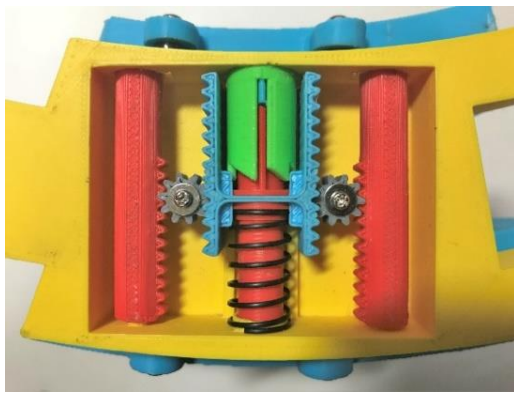
(a)   Extension unit connection off
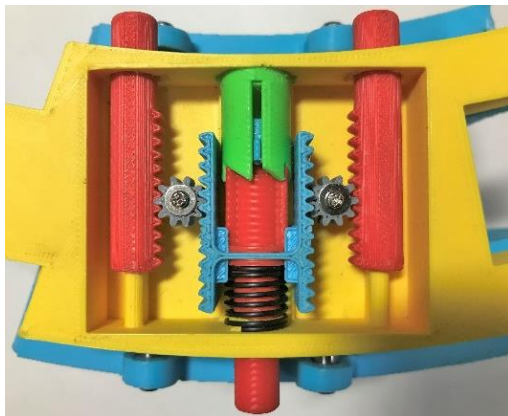
(b) Extension unit connection on

Figure 12. Real model images of extension unit connection
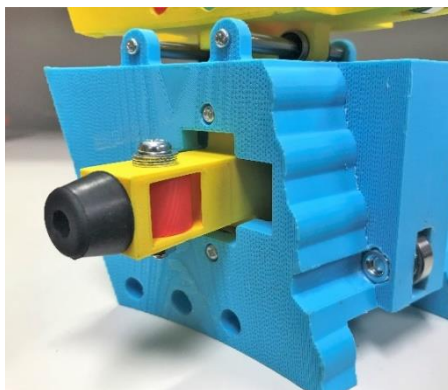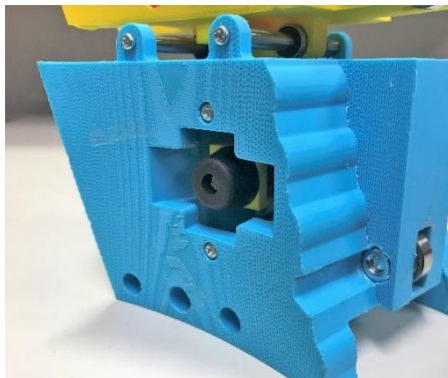
Figure 13. Real model images of extension unit protrusion
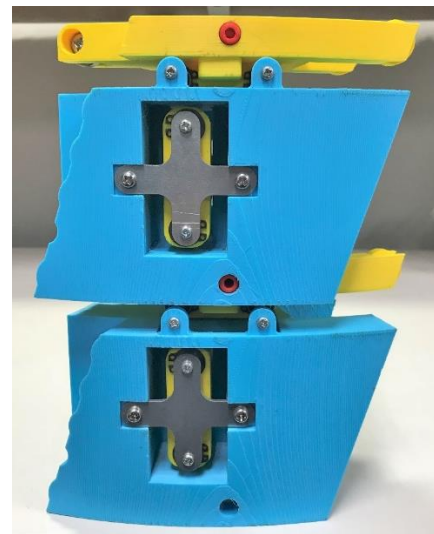
(a) Front view
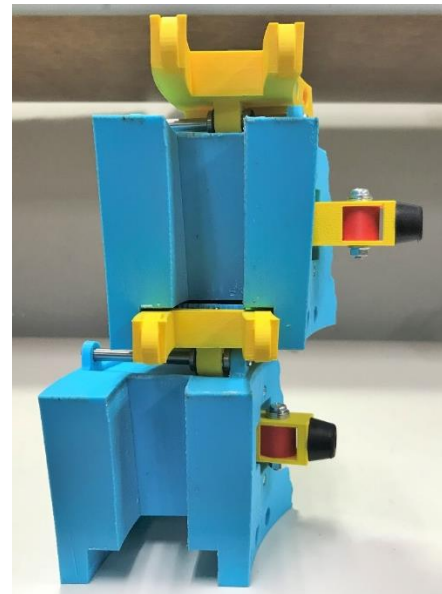
(b) Side view

Figure. 14. Real model images of concatenated extension unit

5.   Conclusions

Problems existed in the omni wheel robot when the movement area was limited due to the movement device. Therefore, in this research, we aimed to realize an extended movement unit to expand the omni wheel robot of action. The extended movement unit was a unit that can be used without remodeling the omni wheel robot. The extended movement unit consists of a mobile robot that extends mobility and a docking unit that joins the omni wheel robot and mobile robot. The mobile robot was based on the robot we developed. The docking unit is a mechanism that can be joined to the mobile robot without modifying the omni wheel robot.

By docking the extended movement unit and the omni wheel robot in this research, it became possible to move steps and uneven floors that the omni wheel robot had been

137

difficult to move until now. The expansion of the omni wheel robot's range of action made it possible for outdoor activities that had been difficult until now.

Acknowledgements

References

[1] Y. Takase, T. Yoshino, Y. Nakano, "Conversational Robot with Conversation Coordination and Intervention Functionality in Multi-party Conversations," Transactions of Information Processing Society of Japan, 58(5), pp.967-980, 2017.

[2] T. V. Nhu, H. Sawada, "Singing performance of the talking robot with newly redesigned artificial vocal cords," 2017 IEEE International Conference on Mechatronics and Automation (ICMA), pp.665-670, 2017.

[3] B. Salem, "PetRo: Development of a modular pet robot," The 23rd IEEE International Symposium on Robot and Human Interactive Communication, pp.483-488, 2014.

[4] SONY aibo: http://aibo.sony.jp/en/, accessed 01/Nov./2017.

[5] Y. Muramatsu, K. Tokoro, H. Kobayashi, "Development and assessment of muscle suit (Evaluation of the auxiliary operation using the surface EMG)," Transactions of the JSME, Vol. 83(847), p.16-00078, 2017.

[6] T. Shibata, "Neurological Therapeutic Seal Robot PARO for Elderly [6] Care," The Journal of the Institute of Electrical Installation Engineers of Japan, 37(9), pp.660-663, 2017.

[7] M. Controzzi, F. Clemente, D. Barone, A. Ghionzoli, C. Cipriani, "The SSSA-MyHand: A Dexterous Lightweight Myoelectric Hand Prosthesis," IEEE Transactions on Neural Systems and Rehabilitation Engineering, 25(5), pp.459-468, 2017.

[8] J. Huang, W. Huo, W. Xu, S. Mohammed, Y. Amirat, "Control of Upper-Limb Power-Assist Exoskeleton Using a Human-Robot Interface Based on Motion Intention Recognition," IEEE Transactions on Automation Science and Engineering, 12(4), pp.1257-1270, 2015.

[9] B. Tang, C. Jiang, H. He, Y. Guo, "Human Mobility Modeling for Robot-Assisted Evacuation in Complex Indoor Environments," IEEE Transactions on Human-Machine Systems, 46(5), pp.694-707, 2016.

[10] P. Di, Y. Hasegawa, S. Nakagawa, K. Sekiyama, T. Fukuda, J. Huang, Q. Huang, "Fall Detection and Prevention Control Using Walking-Aid Cane Robot," IEEE/ASME Transactions on Mechatronics, 21(2), pp.625-637, 2016.

[11] Product specifications of Pepper: https://www.softbank.jp/robot/consumer/products/spec/, accessed 11/Oct./2017.

[12] D. Fujita, R. Yamamoto, S. Mitsui, T. Satake, N. Igo, "U-bo -Robot for 1st Creative Robot Contest for Decommissioning-" Proceedings of The second Conference for R&D Initiative on Nuclear Decommissioning Technology by the Next Generation, oral session(b)-1,pp.21, 2017.

[13] Creative Robot Contest for Decommissioning: http://www.fukushima-nct.ac.jp/~fdecomi/conte5.html, accessed 05/Oct./2017.

Processing of Drone's Digital Image for Determining border of Rice Fields with Edge Detection Method

Suhardiman[a,*], Zahir Zainuddin[b], Salama Manjang[c]

[a]Department of Electrical Engineering, Engineering Faculty, Hasanuddin University. Email:diman@unhas.ac.id
[b]Department of Informatics, Engineering Faculty, Hasanuddin University. Email:zahir@unhas.ac.id
[c]Department of Electrical Engineering, Engineering Faculty, Hasanuddin University. Email:salamamanjang@unhas.ac.id

Abstract

Edge detection was the basic thing used in most image processing applications to get information from the image frame as a beginning for extracting the features of the segmentation object that will be detected. Nowadays, many edge detection methods create doubts in choosing the right edge detection method and according to image conditions. Based on the problems, a study was conducted to compare the performance of edge detection using methods of Canny, Sobel and Laplacian by using object of rice field. The program was created by using the Python programming language on OpenCV. The result of the study on one image test that the Canny method produces thin and smooth edges and did not omit the important information on the image while it has required a lot of computing time. Classification is generally started from the data acquisition process; pre-processing and post-processing. Canny edge detection can detect actual edges with minimum error rates and produce optimal image edges. The threshold value obtained from the Canny method was the best and optimal threshold value for each method. The result of a test by comparing the three methods showed that the Canny edge detection method gives better results in determining the rice field boundary, which was 90% compared to Sobel 87% and Laplacian 89%.

Keywords: Canny; edge detection; drone; rice field

1. Introduction

The agricultural sector has a very important role in national development because it utilizes enormous natural and human resources. Rice field is agricultural land that is patched and bounded by a dike, a channel to hold or distribute water, which is usually planted with rice [1]. Agricultural land in the form of rice fields is usually characterized by the presence of embankments surrounding it to restrict between the rice field and the other one. Besides, the embankment of the rice field is also made to prevent an excessive influx of water so that the water conditions can be adjusted as needed. Rice fields have many functions, both for human life and the environment [2]. As technology develops, so many developments and innovations were carried out for research, especially in the agricultural sector in the rice fields like the detection of changes in paddy planting patterns [3], and detection of flood zoning in paddy fields using satellite imagery [4, 5].

---

*Corresponding author. Tel.: +62-852-9961-1858
Jalan Poros Malino km. 6 Bontomarannu
Gowa, Sulawesi Selatan, Indonesia, 92171

Availability of advanced computer vision technology with the increase in the computing capabilities of the computer that facilitate the development of automated farming systems be able to solve problems, effectively increase flexibility and efficiently made a lot of research done [6].

The study conducted by Kania, et al. [7] who monitor rice phenology and planting schedules in very large paddy fields by using satellite images and the method used with the results of the system that can detect changes in the phenology stage of paddy with a composite time series of 8 days, planting and harvest date while the system still has to be developed to produce a good correlation in the detection system. The research conducted by Yi-Hsing, et al. a remote sensing technology for automatic detection of rice fields using the Profile Matching (PM) method, peak Detection (PD), and difference classification (DC) on multi-temporal images with results of accuracy 20% good results Enhancement when using large images [8].

Edge detection was a basic thing that used in most image processing applications to get information from image frames as a beginning for features extraction of segmentation objects that will be detected. The edge detection segmentation process can be used to detect object

lines and boundaries between objects by detecting discontinuities in one image [9]. Research conducted by Lakshmi, et al. [10] use Canny edge detection to find the closest edge of the object to maximize the location of the pixel size in the image. While research by Ambarwati et al. [11] using Canny edge detection to detect the image side of a former mine, in this study, results show that Canny is an edge detection algorithm that provides good edge detection results that can localize the right edge points.

The development of an area will be accompanied by changes in geographic information. It requires a long process to be able to recreate geographic information. By observation, inventorying quality and environmental conditions, if carried out by field surveys, sometimes can not follow the significant growth of geographic information changes. The drone's image data can use to follow the growth of geographic information changes.

Problem-related to the agricultural sector is the lack of information about these rice fields. This information can include the boundaries of rice fields, ownership of rice fields, plants, as well as the areas affected by floods and pests. The determination of plots of rice fields usually relies on direct observation to see one by one from each plot of rice fields. This manual process takes a long time and is not efficient. To increase the productivity in the agricultural sector, drones are used to extract data and automation technology in the process of detecting rice fields to find the boundaries of each plot out with the resulting picture. This study used the pre-processing image method and image segmentation technique in image processing that using transformation BGR to GRAY color. The result of color transformation would be used in the segmentation phase for determining the boundary of the rice field.

2. Literature Review

2.1. Canny Operator

Canny is one of the modern edge detection algorithms. In 1986, John Canny proposed three criteria for optimizing edge detection in images. These criteria are [12]:

- Good detection, the purpose of this criterion is to maximize the signal to noise ratio (SNR) so that all edges can be detected properly or nothing is undetected.
- Good localization. The edge detected by the operator must be as close as possible to the center of the actual edge.
- One response to a single edge. The detector does not provide an edge that is not the actual edge.

The optimal edge detection algorithm can be obtained by combining the Canny criteria above. Primarily, the Canny algorithm consists of six parts [12]:

- Processing original images into gray images. Using images in the GBR format, for example, the gray conversion formula can be seen as follows:

$$g(x, y) = 0.299R + 0.587G + 0.114B \qquad (1)$$

- With a Gaussian smoothing template, the original data is convoluted. The produced image is slightly blurred from the original one.
- G_x and G_y can be calculated using a template. The gradient magnitude is calculated using Eq. (2) and the direction angle gradient is calculated using Eq. (3).

$$mag(\nabla f) = \left[G_x^2 + G_y^2 \right]^{\frac{1}{2}} \qquad (2)$$

$$\phi(x, y) = \arctan\left(\frac{G_y}{G_x} \right) \qquad (3)$$

- The pixel corresponding to the local gradient of non-maximum is determined. This pixel is suspended by a higher threshold, and it is considered as the wrong edge.
- With the lower threshold, the boundary initial pixels are searched, and new edge pixels are collected according to the pixels sought. Finally, the entire edge of the image is closed.
- The edges of the image are tracked based on the edges of the pixels found.

2.2. Sobel Operator

The operator of Sobel is based on the first-order differential. This operator combines images with small integer filters that can be separated in horizontal and vertical directions. Computationally, it is not expensive. This is a type of orthogonal gradient operator which is a partial derivative in the x and y direction calculated using the environment 3×3 from $f(x, y)$, as follows [13]:

$$Sx = \left\{ f(x+1, y-1) + 2f(x+1, y) + f(x+1, y+1) \right\} \\ - \left\{ f(x-1, y-1) + 2f(x-1, y) + f(x-1, y+1) \right\} \qquad (4)$$

$$Sx = \left\{ f(x-1, y+1) + 2f(x, y+1) + f(x+1, y+1) \right\} \\ - \left\{ f(x-1, y-1) + 2f(x, y-1) + f(x+1, y-1) \right\} \qquad (5)$$

The gradient in the oblique direction:

$$g(x, y) = \sqrt{S_x^2 + S_y^2} \qquad (6)$$

For digital images, the formula above can be reduced to the following:

$$g(x, y) = |Sx| + |Sy| \qquad (7)$$

Convolution operator:

$$\begin{bmatrix} -1 & 0 & -1 \\ -2 & 0 & 2 \\ -1 & 0 & 1 \end{bmatrix} \qquad (8)$$

$$\begin{bmatrix} -1 & -2 & -1 \\ 0 & 0 & 0 \\ 1 & 2 & 1 \end{bmatrix} \qquad (9)$$

There are two main advantages of Sobel edge detection: (a) It has a soothing effect on unwanted noise in an image, (b) Because 2 lines or 2 columns differential has been used, it increases the edge element until the edges become thick and bright.

2.3. Laplacian Operator

Laplacian is a scalar differential operator for scalar functions ϕ defined by [14]

$$\Delta f = \nabla^2 f = \nabla \cdot \nabla f \qquad (10)$$

Laplacian is used in digital image processing for edge detection purposes because it shows an area of rapid intensity change. There are two types of Laplacian operators:

- Positive Laplacian Operator: This operator consists of a standard mask where the angle element must be zero and the middle element must be negative from the mask.

$$\begin{pmatrix} 0 & 1 & 0 \\ 1 & 4 & 1 \\ 0 & 1 & 0 \end{pmatrix} \qquad (11)$$

- Negative Laplacian Operators. This operator consists of a basic mask where the angle element must be zero and the middle element must be positive from the mask and the remaining element must be -1. The edges in the image are taken in a positive Laplacian operator.

$$\begin{pmatrix} 0 & -1 & 0 \\ -1 & 4 & -1 \\ 0 & -1 & 0 \end{pmatrix} \qquad (12)$$

2.4. Transformation of RGB Colour to Grayscale

The use of grayscale images is because it requires a little information given to each pixel compared to the color image. The gray color in the grayscale image is R (Red), G (Green), B (Blue) color which has the same intensity. In grayscale image only requires a single intensity value compared to the color image requires three intensities for each pixel. The intensity of grayscale images is stored in 8-bit integers which gives 256 possibilities which start from level 0 to 255 (0 for black and 255 for white and the value between them is the degree of gray). RGB color transformation to Grayscale can be done by taking the average values of r, g, and b so that with the following equation [15].

$$S = \frac{r + g + b}{3} \qquad (13)$$

2.5. Threshold

Thresholding is the process of converting grayscale images into a binary image, which means images in black and white color. The equation used for the threshold process.

$$g(x,y) = \begin{cases} 0, f(x,y) < 1, \\ 1, f(x,y) \geq 1, \end{cases} \qquad (14)$$

Where g is the result of the Thresholding binary image and (x,y) is the position of each pixel. If the image pixel f (x,y) is above the threshold value, the pixel will be changed to white and the value will be 1. If the image pixel f (x,y) has the same value or is a level below the threshold value, so the pixel is changed to black and the value becomes 0 [16].

3. Proposed Method

3.1. Data Input

The input data used in this study is in images form. The picture was taken using a camera of DJI Phantom 3 Pro drone with resolution 12 Megapixel with a height of 50 meters from the ground with a 90^0 camera tilt angle facing down. Image data of rice fields are taken directly in Bone Regency, South Sulawesi, Indonesia. Fifty pictures were taken and then mosaicking to combine them to produce 1 image with resolution 14235 x 12725 pixels. The scenario for taking image data can be seen in Fig. 1.

3.2. General System Design

The proposed system is a system for detecting rice fields, images were taken by a drone device, then the Image processing process will be carried out; pre-processing and image segmentation techniques. Figure 2 shows the rice field plot system.
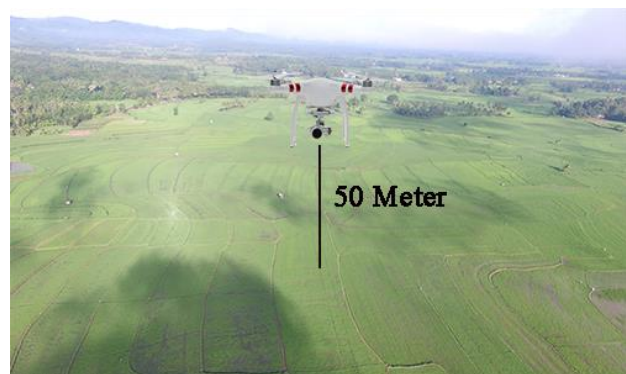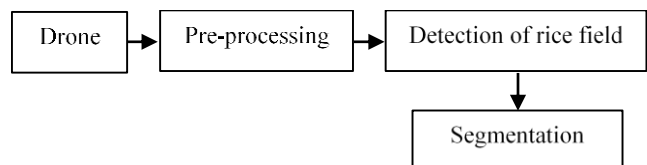

Figure 1. Shooting scenario
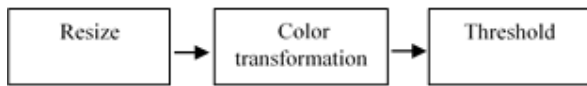

Figure 2. General system design.

Figure 3. Preprocessing Design

3.3. Preprocessing Design

To be more effective, the process carried out is using image processing technique as a solution to minimize errors in visual detection of human eyes. However, the research focus to be carried out in this study is at the preprocessing stage for the detection of rice fields; the BGR color transformation process which is transformed into a Grayscale image for further processing with binary image threshold. The preprocessing design can be seen in Fig. 3.

The process of image acquisition is the stage of taking objects at the initial step of image processing. In this study, the image of rice fields will be taken using a drone's camera.

- Resize: Image from the camera of a drone device have a large size, so the system takes a long time to process it. Image size will be reduced without affecting its quality.
- Color Transformation: The resized image is transformed from RGB color to Grayscale.
- Threshold: After color transformation to grayscale, then the threshold process is carried out. In the threshold process, the pixel value that meets the threshold is mapped to a satisfying value. The threshold value used in this study is 125. So, all pixels in a range of less than 125 will be worth 0, while for all pixels in the range 125-255 are worth 1.

3.4. Segmentation Design

- Canny
  The first process is the thinning of the image to eliminate the noise with the gaussian filter. The results of the thinning process are used for the process of obtaining edge strength with the gaussian operator like in Eq. (2). For edge strength results, previously used for the process of removing dotted lines in the image. Therefore, to help edge tracking, the Gx and Gy gradients are each calculated by the matrix operator CannyMask 3x3.

- Sobel
  The process of Sobel detection, which given one zero buffer. The advantage of this Sobel method is the ability to reduce noise before making detachment calculations. The kernel filters used in the Sobel method are shown in Table 2.

Table 1. Matrix 3x3 Canny Operator

G_x	1	0	-1	G_y	-1	-1	-1
	1	0	-1		0	0	0
	1	0	-1		1	1	1

Table 2. Matriks 3x3 Sobel Operator

$S_x=$	-1	0	1	and	$S_y =$	1	2	1
	-2	0	2			0	0	0
	-1	0	1			-1	-2	-1

- Laplacian
  The Laplace operator detects edge location more accurately, especially on steep edges. The beginning process is blur image using a gaussian, then find zero-crossing of Laplacian and compare it with the threshold.

4. Results and Discussion

The process of determining rice field boundaries with edge detection starting in preprocessing. The images taken by a drone device camera have a large size, the system needs a long time to process it. Therefore, the resize process is carried out to change the size of the image without affecting its quality. The results of the image resize process are shown in Fig. 4(a).

Next, the resized picture is converted to a grayscale image by transformation color. The result of the color transformation process to the grayscale image can be seen in Fig. 4(b). The results of the color transformation process, then become the input to the image threshold process with a threshold value of 125 as a threshold value to obtain a binary image. The result can be seen in Fig. 4(c).

After the preprocessing process, the edge detection process is then carried out using Canny, Sobel, and Laplacian operators. The results are shown in Figs. 5(a) to (c).

- Canny
  Based on the Canny edge detection process, this study uses gradient G (x,y) which is a vector consisting of two elements, namely Gx and Gy. Edge detection in this process is done by reading each pixel on the image by reading the pixel from the top-left pixel and moving to the bottom right pixel. The results of the edge detection process using Canny edge detection can detect 90% rice field boundary as shown in Fig. 5(a).

- Sobel
  In this process to detect edge is to read each pixel on the image by reading from the leftmost pixel and moving to the bottom right pixel. Therefore, to guide edge tracking, the Gx and Gy gradients are each calculated by the matrix of Sobel Mask3x3 method. The result of Edge detection using the Sobel operator can detect rice field plot boundaries by 87% as shown in Fig. 5(b).

- Laplacian
  The Laplacian operator in this study is looking for zero values in the second derivative of the image because when the first derivative is at the maximum value, the second derivative will produce a zero value. The second derivative of the x and y direction are combined into one operator value. This value is represented in the form of a sum of two convolution matrices from the x and y directions. If the threshold meets, then it is expressed as an edge. The results of the Laplacian operator process can detect the rice plot boundary by 89% can be seen in Fig. 5(c).

142
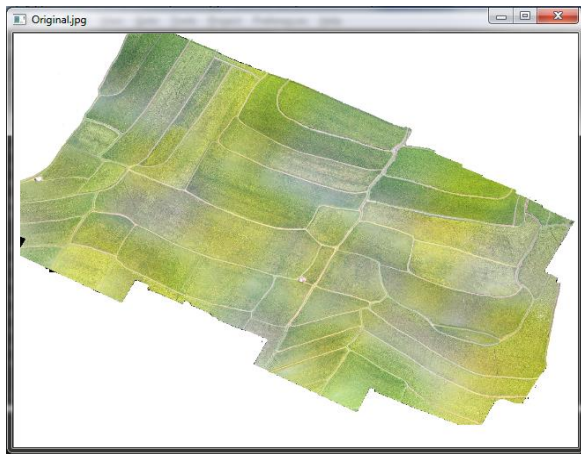
(a) Resized Picturer
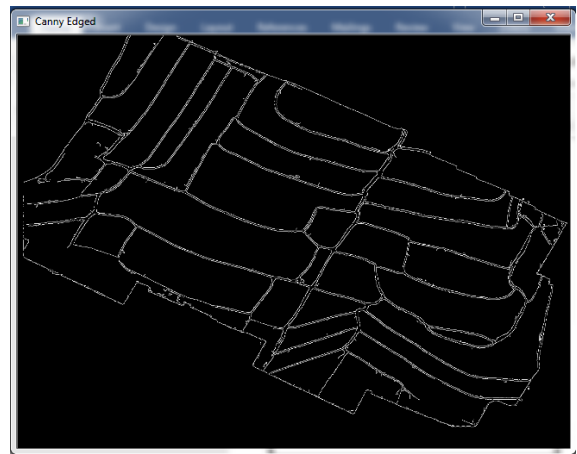
(a)   The result of Canny edge detection
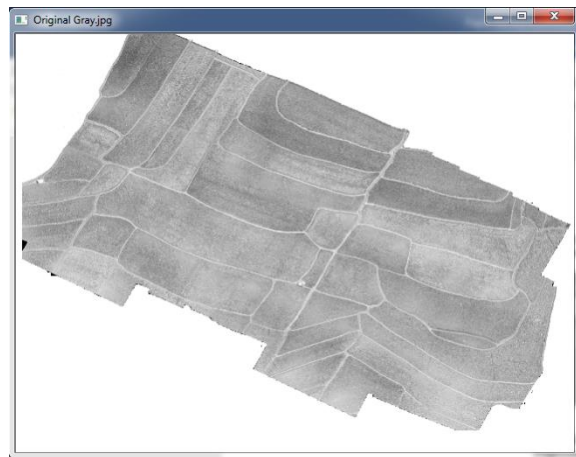
(b) The image has been made a color transformation
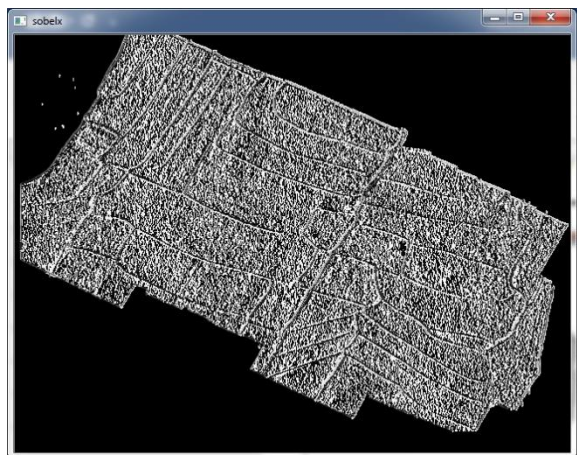
(b)   Result of Sobel edge detection
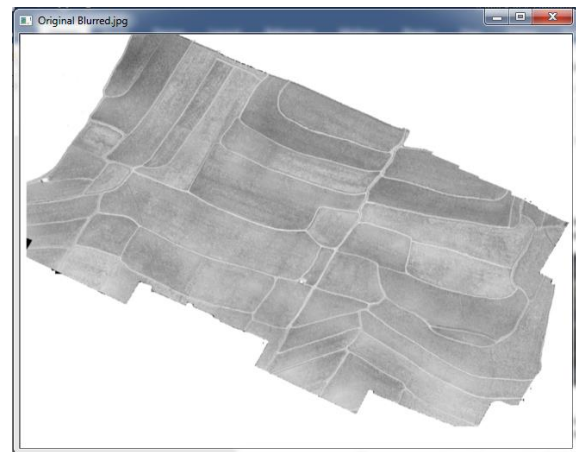
(c) Picture by threshold

Figure 4. Preprocessing process for determining rice field plot boundaries
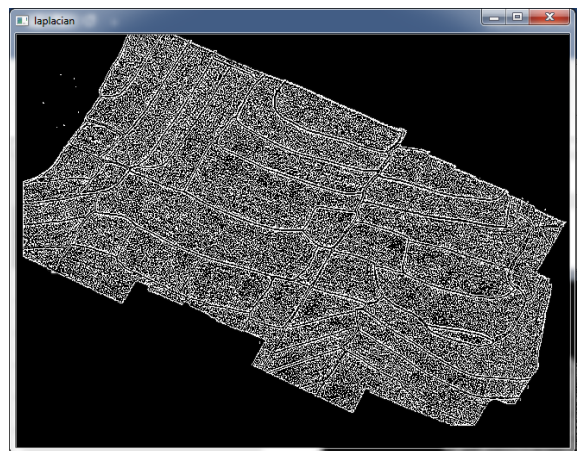
(c) The result of Laplacian edge detection

Figure 5. The result Laplacian edge detection

5. Conclusion

This research used data of the image taken in Kahu District, Bone Regency, South Sulawesi. Image captured by a DJI Phantom 3 Pro camera drone with 12 Megapixel resolution with a height of 50 meters from the ground with 90^0 camera tilt angle facing down. The edge detection method used to determine the boundary of rice fields, namely Canny, Sobel, and Laplacian. The test results by comparing the three methods showed that the Canny edge detection method gives better results in determining the rice field boundary, which 90% compared to Sobel 87% and Laplacian 89%.

References

[1] Badan Pusat Statistik. [Online]. Available: https://www.bps.go.id/istilah/index.html?Istilah_sort=deskripsi_ind&Istilah_page=23. [Accessed: 04-Jul-2019].

[2] Sudrajat, Knowing Rice Fields and Understanding Its Functions for Humans and the Environment. Gadjah Mada University Press, 2015. [in Bahasa]

[3] D. R. Pratama, Detection of Changes in Paddy Planting Patterns in East Java Based on MODIS Imagery Using the Cross Correlation Method, 2017. [in Bahasa]

[4] L. Rahmadany, A. L. Nugraha, B. Sasmito, and N. Febrianti, Jurnal Geodesi Undip Oktober, 2014, vol. 3, p. 7, 2014.

[5] Flood risk zonation Pre-monsoon land use and land cover Land, *Research Gate*. [Online]. Available: https://www.researchgate.net/figure/Flood-risk-zonation-Pre-monsoon-land-use-and-land-cover-Land-use-and-land-cover-map-of_fig4_294089869. [Accessed: 09-Jul-2019].

[6] X. Li and W. Zhu, "Apple Grading Method Based on Features Fusion of Size, Shape, and Color," *Procedia Eng.*, vol. 15, pp. 2885–2891, 2011.

[7] D. K. Sari, I. H. Ismullah, W. N. Sulasdi, and A. B. Harto, "Detecting Rice Phenology in Paddy Fields with Complex Cropping Pattern Using Time-Series MODIS Data," *J. Math. Fundam. Sci.*, vol. 42, no. 2, pp. 91-106–106, 2010.

[8] G. World, "Automatic detecting rice fields by using multitemporal satellite images, land-parcel data and domain knowledge," *Geospatial World*, 11-Sep-2009.

[9] G. M. H. Amer and A. M. Abushaala, "Edge detection methods," in *2015 2nd World Symposium on Web Applications and Networking (WSWAN)*, Sousse, Tunisia, 2015, pp. 1–7.

[10] S. Lakshmi and Dr. V. Sankaranarayanan, "A study of Edge Detection Techniques for Segmentation Computing Approaches," *Int. J. Comput. Appl.*, no. 1, pp. 35–41, Aug. 2010.

[11] A. Ambarwati and R. Passarela, "Segmentasi Citra Lahan Bekas Tambang Terbuka Menggunakan Metode Deteksi Tepi Canny," p. 9, 2017.

[12] X. Yan and Y. Li, "A Method of Lane Edge Detection Based on Canny Algorithm," p. 5.

[13] A. Kalra and R. L. Chhokar, "A Hybrid Approach Using Sobel and Canny Operator for Digital Image Edge Detection," in *2016 International Conference on Micro-Electronics and Telecommunication Engineering (ICMETE)*, Ghaziabad, India, 2016, pp. 305–310.

[14] R. Bansal, G. Raj, and T. Choudhury, "Blur image detection using Laplacian operator and Open-CV," in *2016 International Conference System Modeling & Advancement in Research Trends (SMART)*, Moradabad, India, 2016, pp. 63–67.

[15] Y. Wan and Q. Xie, "A Novel Framework for Optimal RGB to Grayscale Image Conversion," in *2016 8th International Conference on Intelligent Human-Machine Systems and Cybernetics (IHMSC)*, Hangzhou, China, 2016, pp. 345–348.

[16] M. F. N. Wahidah, N. Mustafa, M. Y. Mashor, and S. S. M. Noor, "Comparison of color thresholding and global thresholding for Ziehl-Neelsen TB bacilli slide images in sputum samples," in *2015 2nd International Conference on Biomedical Engineering (ICoBE)*, Penang, Malaysia, 2015, pp. 1–6.

Design and Fabrication of an Automatic Trash Remover for Open Channel Waterway for Micro Hydropower Plant Application

A. M. Shiddiq Yunus[a,*], Musrady Mulyadi[b], Apollo[c]

[a]Energy Conversion Engineering, State Polytechnic of Ujung Pandang, Indonesia. Email: shiddiq@poliupg.ac.id
[b]Energy Conversion Engineering, State Polytechnic of Ujung Pandang, Indonesia.
[c]Energy Conversion Engineering, State Polytechnic of Ujung Pandang, Indonesia.

Abstract

Mitigation of catastrophic impacts of exhausted pollutants from conventional based power plants can be performed by extensively using renewable energy-based power plants. One of the promising renewable energy-based power plants in already matured technology is hydropower. However, large scale hydropower should be located on an appropriate site and is not economically effective for isolated and remote small communities. Micro-hydropower plants (MHPPs) can applied to fulfill the power requirements of such communities due to its inexpensive capital and low maintenance cost. Normally, MHPPs projects are finalized by civil construction to powerhouse. A simple trash filter is usually located before the intake of the penstock. This simple trash filter usually causes a problem related to trash collection that blocks the water debit into the penstock intake. This low capacity might cause the reduction of turbine's rotation, which in turn downgrade the voltage and frequency. Low voltage and frequency might harm consumers. In this paper, a new control mechanism based on Arduino Mega is introduced for automatic trash removal.

Keywords: Automatic; MHPP; remover; filter; trash

1. Introduction

It is inevitable to construct more renewable energy-based power plants to mitigate the negative impacts of conventional based power plants on the global environment [1]. Therefore, many developed countries recently increase the installation of wind and PV panels to support their main grids [2-5]. However, these two types of power plants have some limitation including high initial cost [6], high maintenance cost [7] and problems related intermittency of its main energy sources [8]. One of the old and matured renewable energy technologies that have been widely installed all around the world is hydropower plants (HPPs). This type of power plant could be scaled up to several MWs, free of air pollutants and has low maintenance cost [9]. Construction of a new hydropower plant (HPP) should be in consideration of some perspectives, including the economic point of view [10].

For isolated and remote small communities, long power transmission and distribution are not cost-effective and impractical by large scale power plants such as HPP. However, the equality principle of giving electricity service is a must. For example, Indonesia targets to achieve 100 %

electrification ratio in 2020 [11]. Currently, the electrification ratio has reached about 91.16%, meaning that some other 8.84% of people do not enjoy electricity yet [12]. To achieve the aforementioned target of electrification ratio, Indonesian government has promoted the large projects of micro hydropower plants (MHPPs) which is the most suitable for isolated and remote communities. Moreover, it has several advantages including cost-effectiveness based on its type mostly Run-off-Rivers, where no large dam and water storage system are required [13]. It also could reach about 50 years of live operation period [14]. The implemented projects of MHPPs in Indonesia itself have been reached about 134.21 MW in range projects of 2011-2015 [15].

An MHPP normally is constructed with a small budget due to its kWs scale [16, 17]. Operation and maintenance are also managed in a very simple way. In Indonesian case for an instant, an MHPP operation and maintenance cost are collected from the community each month, therefore some technical designs as part of MHPP facilities are installed in the minimum standard. One of the common problems related to MHPP operation is blocked water to penstock intake by trash collection on the trash filter. The low debit of water could reduce the turbine rotation which in turn reduces the frequency and generated a voltage of the

*Corresponding author. Tel.: + +62-823-4752-1449
Jalan Perintis Kemerdekaan km. 10, Tamalanrea
Makassar, 90245

connected generator. This condition causing houses lights to be dimmed and become a clear indicator for the operator to visit the site and clean the trash. The problem might become even worst for the operator when the MHPP site, as usual, is located on the highland and quite far from the residence center. Moreover, the trash that commonly comes from leaves, branches and dry grasses that are flowing within the open channel waterway more potentially occur during the rainy session. The most horrible situation for the operator is if this condition occurs in the night time. In this paper, a design of automatic trash remover is proposed. The control mechanism is introduced to allow trashes to be removed automatically to prevent blocked water in the penstock intake.

2. Research Methodology

A trash filter in MHPP is normally placed on the penstock intake and used to filtrate trashes to avoid the trashes come along with the water into the penstock [18]. Traditionally, a trash filter is made simply like iron nets that capable of filtering the trashes and allowing the water to flow, the sample of a common trash filter is depicted in Fig. 1. To avoid trashes blocking the water into the penstock, the operator should regularly check the filter and cleaned it if necessary. As aforementioned above, sometimes a task to clean the filter becomes very challenging for the operator when it should be done in the night even in the worse rainy session. To anticipate it, an automatic scenario of trash rack is designed and proposed in this paper.

Work process of the automatic trash remover can be figured out in the flowchart diagram shown in Fig. 2.

The control system of the proposed system is set up in Microcontroller called Arduino Mega [19]. Some of the advantages of this type of controller are cheap, optimal power consumption and easy to implement [20].

There are only two controllers are employed in this mechanism: Flow and Limit Censor. A flow sensor has a duty to measure the flow capacity of water that pass the open channel before go through the intake of the penstock, when water flow lesser than 3.0 m/s it is indicating that the trash has been blocked by some amount of trashes, therefore, in this point, trash rack should lift the trashes (in rotation mechanism) and in 90º position, when other wing

trash rack press the limit switch, the rotation mechanism stop and trashes will be dropped on the conveyor which also run to transport the trashes into the bin. The design of the automatic trash remover can be seen in Fig. 3.
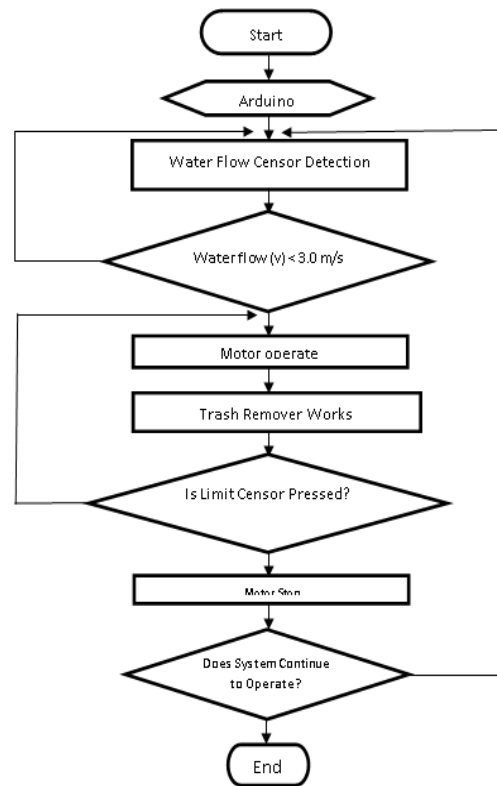
Figure 2. Flowchart of automatic trash remover for MHPP

Figure 1. A typical type of MHPP trash filter
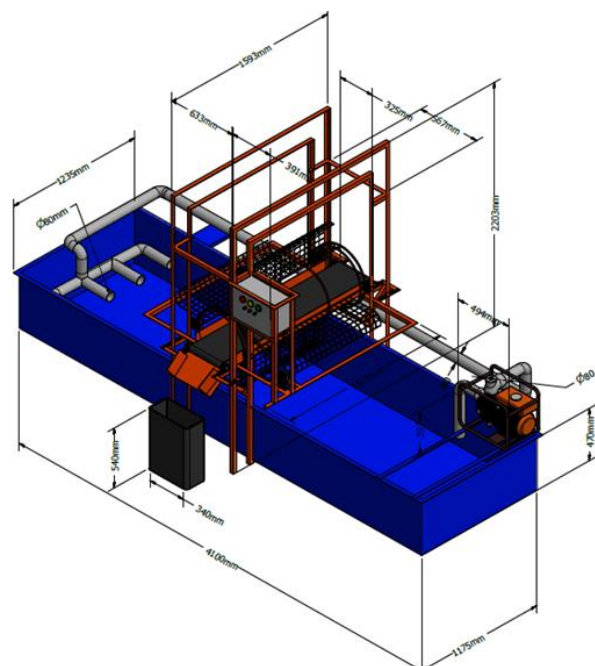
Figure 3. Lab scale of automatic trash remover for MHPP application
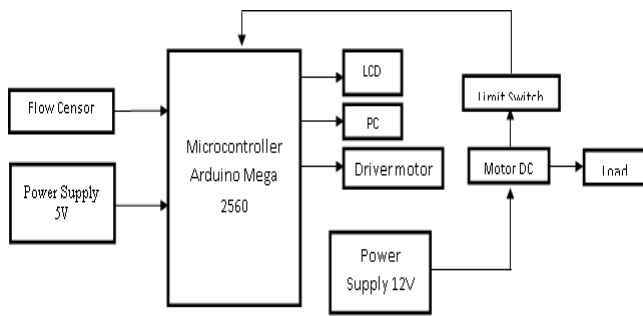
Figure 4. Block diagram of I/O of automatic trash remover microcontroller for MHPP application

The block diagram of the working steps of the device is shown in Fig. 4. Flow sensor and limit switch become the inputs of the Microcontroller to dictate whether the drive motor working to lift the trash or not. LCD is used to show the real-time data of the device such as Current, Voltage and Selector Position. All data can also be downloaded to the PC.

3. Results and Discussion

To test the performance of the device, two scenarios are applied; no-load test and with load test. The loads applied in the test are simulated with dried leaves which commonly fall into the open channel of MHPP and transport into the intake of the penstock. The mass variation of trash (shown in Fig. 5) is applied to see the performance of the device. Table 1 shows the performance of trash remover for some mass variation of the trash.

As noted in Table 1, when the laboratory test of the prototype was made, the automatic trash remover proved working properly to lift the trash using rotating trash filter shown in Fig.1 for water flow less than 3 m/s. As observed in Table 1, the heavier the mass of trash becomes, the lesser the water velocity would be. Overall, the mechanical and control system of the device is working properly.

Figure 5. Common trash type (dried leaves) in open channel of MHPP

Table 1. Working performance of the automatic trash remover

Mass of Trash (gram)	Average Water Velocity (m/s)		Status of Trash Remover	
	Before Trash Filter	After Trash filter	Trash Filter	Conveyor
0	10	9.8	Not Work	Not Work
55	9.44	3.56	Not Work	Not Work
100	5.87	1.21	Work	Work
155	5.18	1.11	Work	Work
210	4.82	1.00	Work	Work
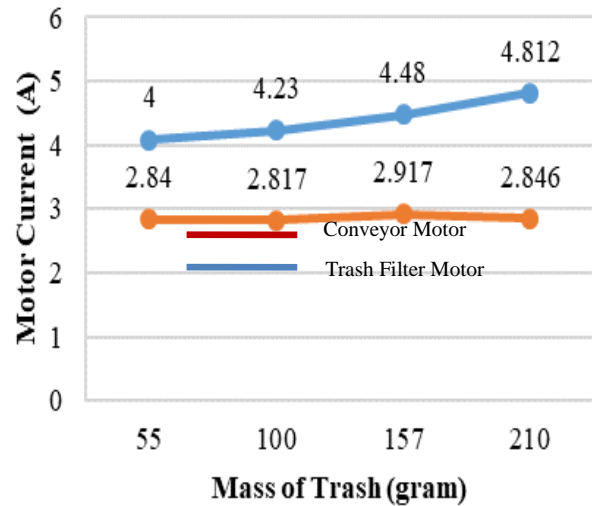
Figure 6. Current measurement for both trash filter motor and conveyor motor

To investigate the power consumption, current for both DC motors for Trash Filter and Conveyor is measured. As shown in Fig. 6, motor works harder when the load (trash mass) is larger, but still in the range of motor capability. Meanwhile, conveyor motor exhibits rather a stagnancy in consuming power.

4. Conclusion

In this paper, design, construction and experiment test of an automatic trash remover for MHPP application is introduced. It can be concluded that the system could work properly to remove the commonly dried leaves trash type automatically. The device eventually could avoid trashes in blocking the filter before intake of the penstock, thus, prevent the turbine from reduced speed. The benefits of this solution can be addressed as follows:

• Maintain the normal MHPP service
• Improve the MHPP operation lives.
• Reduce the working hours of MHPP operator

147

Acknowledgments

References

[1] Yah, N. F., Oumer, A. N. and Idris, M. S. 2017. Small scale hydro-power as a source of renewable energy in Malaysia: A review. *Renewable and Sustainable Energy Reviews*, Vol. 72 (2017), pp. 228-239.
DOI: https://doi.org/10.1016/j.rser.2017.01.068

[2] Yunus, A.M.S., Abu-Siada, A., and Masoum, M.A.S. 2011. Effects of SMES on dynamic behaviors of type D-Wind Turbine Generator-Grid connected during short circuit. *IEEE Power and Energy Society General Meeting*. pp.1-6. DOI: 10.1109/PES.2011.6039276

[3] Shiddiq Yunus, A. M., Abu-Siada, A., and Masoum, M. A. S. 2011. Effect of SMES unit on the performance of type-4 wind turbine generator during voltage sag. *IET Conference Publications.* 2011(579 CP), pp. 94
DOI: 10.1049/cp.2011.0137

[4] Macias, E., and Ponce, A. 2006. Photovoltaic Solar Energy in Developing Countries. *IEEE 4th World Conference on Photovoltaic Energy Conference*, pp. 2323-2326
DOI: 10.1109/WCPEC.2006.279638

[5] Shiddiq Yunus, A. M., Abu-Siada, A., and Masoum, M. A. S. 2011. Improvement of LVRT capability of variable speed wind turbine generators using SMES unit. *2011 IEEE PES Innovative Smart Grid Technologies, ISGT Asia 2011 Conference*, pp. 1-7
DOI: 10.1109/ISGT-Asia.2011.6167122

[6] https://www.windpowermonthly.com/article/1487102/first-indonesian-wind-farm-online (accessed, 06 February 2019)

[7] Ziegler, L., Gonzales, E., Rubert, t., Smolka, U., and Melero, J.J. 2018. Lifetime extension of onshore wind turbines: a review covering Germany, Spain, Denmark, and the UK. *Renewable and Sustainable Energy Reviews*, Vol. 82, Part 1. pp. 1261-1271
DOI: https://doi.org/10.1016/j.rser.2017.09.100

[8] https://www.conserve-energy-future.com/disadvantages_windenergy.php (accessed, 01 October 2018)

[9] Manzano-Agugliaro, F., et. al. 2017. An overview of research and energy evolution for small hydropower in Europe. *Renewable and Sustainable Energy Reviews*, Vol. 75, pp. 476-489.
DOI: https://doi.org/10.1016/j.rser.2016.11.013

[10] Wongphat, M., and Premrudeepreechacharn, S. 2015. Evaluation of engineering and economic feasibility of micro-hydropower plant project. *5th International Youth Conference on Energy (IYCE),* pp. 1-6
DOI: 10.1109/IYCE.2015.7180813

[11] Achieving Universal Electricity Access in Indonesia. 2016. *Asian Development Bank*.

[12] Handbook of Energy and Economic Statistic of Indonesia. 2017. Ministry of Energy and Mineral Resources Republic of Indonesia.

[13] Palish, O. 2012. Small hydro power: technology and current status. *Renewable and Sustainable Energy Reviews*. Vol. 6 (2012), pp. 537-556.
DOI: https://doi.org/10.1016/S1364-0321(02)00006-0

[14] Palish O. Micro-hydropower: status and prospects. 2002. *Proc Inst Mech Eng, Part A: J Power Energy* Vol. 216 (1):31–40.
DOI: https://doi.org/10.1243/095765002760024827

[15] Anenomous, Statistic of New and Renewable Energy in Indonesia. 2016. Ministry of Energy and Mineral Resources of Indonesia

[16] www.esdm.go.id (accessed in August 2018)

[17] Erinofiardi, P., Gokhale, A., Date, A., Akbarzadeh, P., Bismantolo, A.F., Suryono, A.K., Mainil, A. and Nuramal. 2017. A review on micro hydropower in Indonesia, *Energy Procedia* 110 (2017), pp. 316-321
DOI: https://doi.org/10.1016/j.egypro.2017.03.146

[18] https://www.nrcan.gc.ca/sites/www.nrcan.gc.ca/files/canmetenergy/files/pubs/Intro_MicroHydro_ENG.pdf (accessed, 06 February 2019)

[19] https://www.arduino.cc/en/Guide/HomePage (accessed, 06 February 2019)

[20] Lomo, L., and Abraham. 2016. SMART Greenhouse using Microcontrollers Arduino Mega 2650 REV 3. *Final Year Project*. Yogyakarta. Electrical Engineering Department, Universitas Sanata Dharma.

The Visitors' Perception toward the Comfort of Social Interaction in Public Space (A Case study in Karebosi Field Makassar)

Andi Muhammad Ichsan Djainuddin[a,*], Afifah Harisah[b], Abdul Mufti Radja[c]

[a]Department of Architecture, Engineering Faculty, Hasanuddin University. Email: andimuhammadichsan85@gmail.com
[b]Department of Architecture, Engineering Faculty, Hasanuddin University. Email: ifahhussein@yahoo.co.id
[c]Department of Architecture, Engineering Faculty, Hasanuddin University. Email: muftiradja@unhas.ac.id

Abstract

Public space has an important role to increase physical health and social interaction of city communities. Karebosi field is a public space that is in the development priority by Makassar city government. Karebosi field is the most ideal facility to represent the concept of an open public space in Makassar. After going through revitalization process, the government still continues to reform and refine the Karebosi field functions. This research aims to find out the visitors' perception towards the comfort of social interaction in the Karebosi field, and what factors which are influence them as well. This research was conducted in 2018 at Karebosi field, Makassar. The method used in this research is mixed method (qualitative-quantitative). The technique of data collection is done by evidentiary method through data triangulation (observation, questionnaire, and interview). The result of this research can be concluded that the facility in Karebosi field is quite successful in attracting the visitors to do sport activities in public space, yet the level of success is still not optimal because it is still in the range of 60.89%, which is due to the facility development that has not been varied, the facilities are considered as not being able to stimulate the diversity of social interaction and increasing the number in public space. Designing, Karebosi field is not able to give an impression and meaning for the people who do the activities in it. It is expected to be a reference for Makassar government in formulating the steps to increase the service quality and the functions of the Karebosi field in the future.

Keywords: Perception, public space, social interaction

1. Introduction

Public space is the representative image of a city and it has an important role in increasing physical health and social interaction of city communities. The issue discussed in this research is the revitalization of Karebosi field which is done by the government in Makassar. As public space, Karebosi field is a facility that portrays historical journey of Makassar which has position and function that quite important in Makassar nowadays. Based on this issue, the effect of the revitalization of Karebosi field needs to be examined toward the increasing of the quality and function of Karebosi field. To find out that case, so it needs to do identification processes based on the visitors' perception of the convenience of social interaction in Karebosi field. Perception is the most complete source of information on every individual in evaluating, perception has an important role in deciding someone's attitude and behavior. Therefore, the result of identification which is gotten from

the visitors' perception is expected to be a complete source of information in measuring the convenience level of visitors' social interaction in the Karebosi field. Generally, the area of Karebosi field is divided into three zones of public spaces, namely Zone A with area development of 45.77%, zone B 30.93% and zone C 12.84% from the total area of 11.29 hectares, it can be seen in Fig. 1.

(a)   (b)

Figure 1. (a) the map of area allocation in Karebosi field area (b).The area of research location

*Corresponding author. Tel.: +082-394-414-188
*Jl. Poros Malino km. 6 Gowa – Sulawesi Selatan
91711*

From these three zones, based on assessment of nature publicity, the aspect of freedom accessibility, the amount of activity and intensity of visitors, so it can be concluded that zone A is the most suitable area to be used as the limitation of observation scope in Karebosi field area, zone A is considered suitable with the criteria of public space [1] everyone has the same right to come and use public space.

2. Method

This research uses descriptive/qualitative and quantitative method or mixed method. The scope of this research includes the facility of public space, social interaction, and perception to find out the visitors' perception, the observation scope is done in visitors' behavior aspects toward the facility by using controlling and observation method and place center mapping technique. The visitors' attitude aspects of the facility in Karebosi field are measured qualitatively based on Likert scale through questionnaire data validation. The purpose of the research is to find out the visitor's perception toward the convenience of social interaction in Karebosi field.

Theory in [2] is used to measure the visitor' perception toward the quality of social interaction in public space, by using three points, namely structural dimension which is related to accessibility and the use of space, interactive dimension which is related to social relations, kind of activities, the possibility of participation in activity and the participation of decision making in local level, subjective dimension which relates to personal satisfaction of environmental management [2].

There are three problem formulations used to measure the visitor's perception. (1) How is the condition of activities and facilities in Karebosi field, the technique of data collection used is controlling and observation with place center mapping system, (2) How is the quality of Karebosi field if being reviewed by using the quality theory of public open space, based on the theory, the technique of data collection used is the method by giving question to respondents through questionnaire and interview, (3) Visitors' perception toward the convenience of social interaction in public space, the technique of data collection is doing data reduction and concluding the correlation between the visitors' attitude and behavior to the condition of Karebosi's field facility.

3. Result and Discussion

The research results concerning the condition of Karebosi field, based on the observation generally, the condition of facilities in Karebosi field is observed through the aspects of facility condition shown in Fig. 2, so in general the wide of development facility area in Karebosi field area consists of main facilities and supporting facilities.

(a). Main Facilities (b). Supporting Facilities
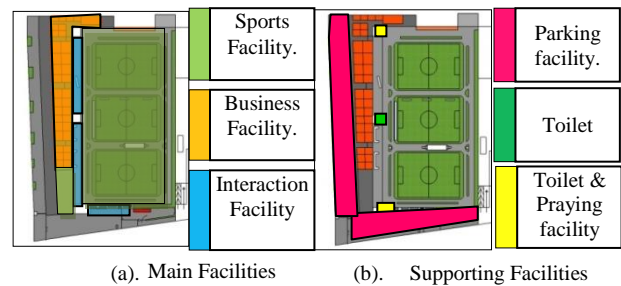
Figure 2. (a) Map of facility zone allocation in the research location (b) The allocation area of the main facility allocation area of the supporting facility

The main area of developing facility is divided into three zones based on the function of the facility. Zone A is the area for sports, Zone B is the facility area for social interaction and Zone C is the facility area for business.

3.1. Correlation aspects among behavior and the condition of facilities and activities

Based on the literature review in [2], there are some conclusions gotten from observation and place center mapping method.

a. The scope of subjective dimension

Based on the observation on accessibility aspects in Fig. 3, it can be concluded that Karebosi field has a strategic location so it can be reached easily, it is located in the central of Makassar city, which is passed by city transportations and it is completed with access alternative which makes easier either for the transportation accessibility or the visitor, in Jl.Jend. Sudirman and Jl. R.A Kartini. This is consistent with the theory in [3] and [4] outlining that one important aspect in a democratic public space is the availability of good accessibility. With good accessibility, it will encourage the use of public space by diverse users.

(a) (b)
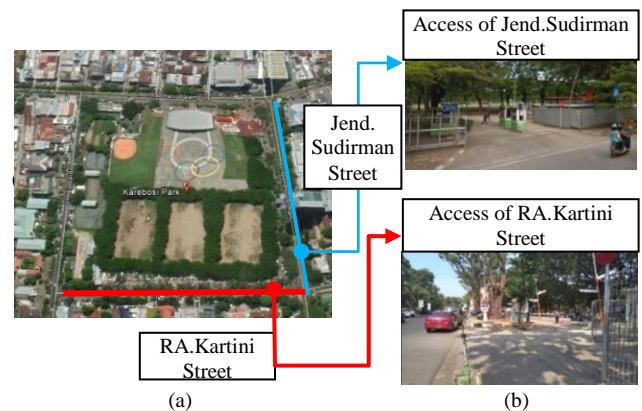
Figure 3. (a) Circulation map in Karebosi field; (b) the situation of access facility on Jnd. Sudirman street (the situation of access facility on R.A. Kartini street)

(a)

(b)
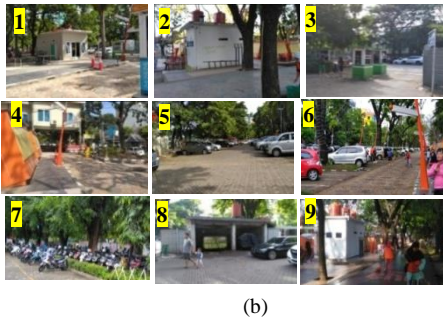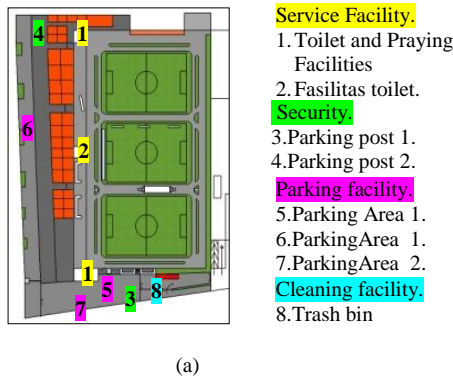
Figure 4. (a) The map of facilities and infrastructure location, (b) The situation of facilities and infrastructure service in Karebosi

Based on the observation on the aspects of use, the availability of supporting facilities in the location is quite complete. It can be seen in Fig. 4 the supporting facilities in Karebosi field consist of service facility, security, sanitary, and parking facility which is quite enough for supporting the visitors in doing their activities. This is following the ideal criteria for public spaces. Public spaces are planned and designed according to the needs of users so that they can provide comfort and convenience in carrying out their activities [5].

Based on the observation on the aspects of the use, if it is observed through physical observation, from Fig. 5, it describes that the condition of sports facility is in the amount of developing area of 79.75%, the second facility namely business facility is about 10.33%, the third facility of the location is social interaction facility which is about 9.92%. Based on the data, it can be concluded that physical condition of Karebosi field area as public space has not been run in balance yet. The sports facility is so dominant in area usage of the facility.

Based on the observation of the usage aspects, Karebosi field area is successful in creating the diversity of the visitors who do activities in it.
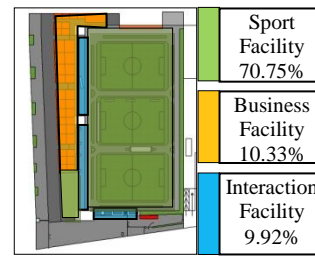
Figure 5. (a) Map of the area allocation for facility development

In Fig. 6, it can be seen the presence of various types of visitors who are intensely doing some activities in Karebosi field area. The regularity visits to Karebosi happens every day with the intensity of the visits constantly increasing at the weekend. The diversity of the visitors in Karebosi in the morning is dominated by the visitors of elder people, men and women (Sunday – Friday). Besides at noon, the number of visitors is dominated by youth, both men and women. Whereas, visits activity on the weekend (Saturday – Sunday) neither in the morning nor at noon is dominated by the youth with a higher visit intensity.

(a)

(b)
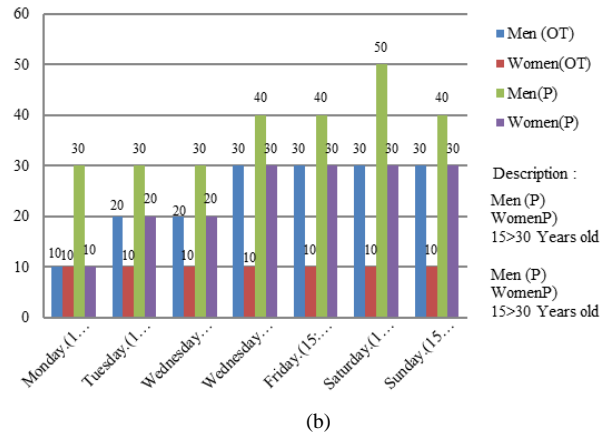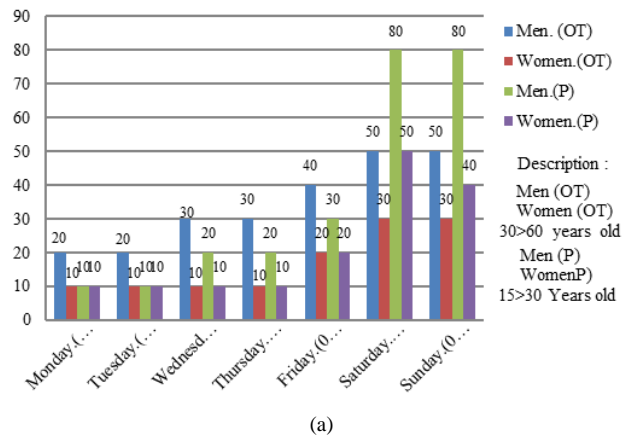
Figure 6. (a) Diagram of visits intensity in the morning. (b) Diagram of visits intensity at noon
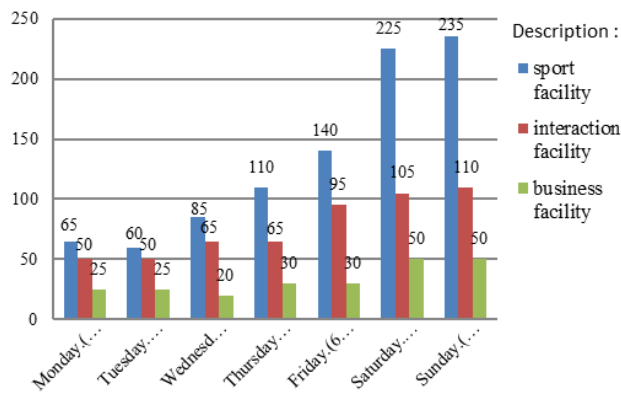
(a)
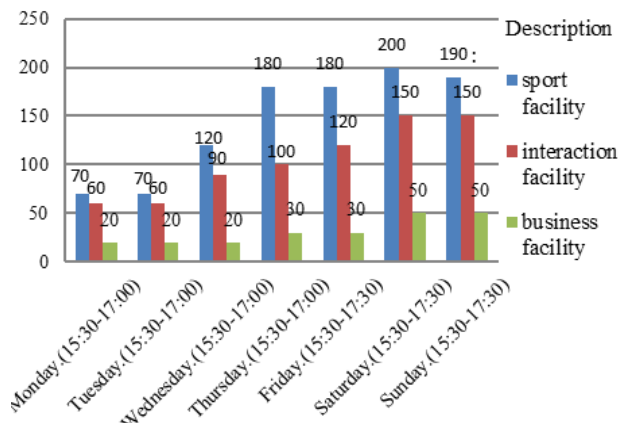
(b)

Figure 7. (a) Diagram of facility usage in the morning. (b) Diagram of facility usage at noon

b. *The scope of interactive dimension*

Based on observation of sociality aspects on the user's behavior in Fig. 7, it can be seen that the main facility in Karebosi field area consists of 3 facilities, namely; sports facility, social interaction facility, and business facility. Based on the measurement of the activities which happen every morning and noon, the highest intensity in the location of the research is sports activity and the second activity is interaction. The third activity is trading/business activity. Based on the diagram, it can be concluded that the behavior of the facilities usage has not run in balance yet. The physical condition of Karebosi field area as public open space has not been optimal in creating an interaction atmosphere among the visitors. It can be seen from the amount of sports activities which are so dominant in the location. This contradicts the theory that public space is a place or space formed because of the need for a place to meet and communicate [6].

Based on the observation of interactive dimension on sociality aspects in Fig. 8, it can be concluded that Karebosi field has not been successful yet in creating a conducive public space to provide the needs of interaction for their visitors. It can be seen in the minimum amount of different types of behavior happens in Karebosi field. Generally, the characteristics of the visitors' interaction behavior found are the same. they are interacting while resting after doing some exercises. They prefer to sit, have conversations, and gather in a crowd, while the other visitors also buy some snacks around the location before they left of their visits in Karebosi.

Based on the data, it can be concluded that Karebosi's field did not provide different types of interaction choices for visitors. The visitors' interaction activities run monotonously. The public space has not been able to create recreation and entertainment choice which could give pleasing experience and meaning for the people who do some activities in public space. This is contrary to aspects that stimulate social interaction in public space [7]. Sociality is the level of a person's ability to make social relations in a setting. The observation on interaction behavior aspects based on the visitors' behavior interaction in Fig.98 shows that generally, people interact in area 1 and 2, they prefer to gather and interact in the area which has higher flurry intensity, generally, and they tend to choose seat facilities and gathering area that close to entrance and parking area where the area is quite crowded of the visitors who come and leave in the facility of this area in which is easy to access their vehicles.

(a)   (b)
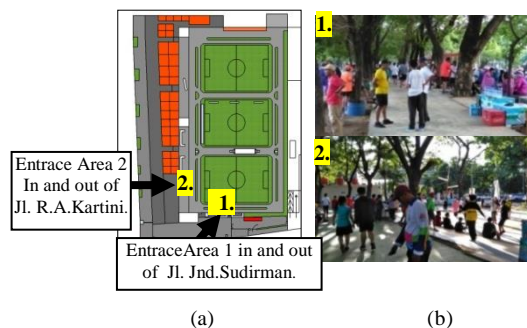
Figure 8. Map area of communal room in Karebosi. (a) The situation of communal area entrance 1, (b) The situation of communal area entrance 2

(a)

(b)

Figure 9. (a) the situation of sports activity diversity. (b) The situation of interaction activity diversity

152

Based on the observation of interaction dimension on the activities diversity aspects in the previous figure, it describes that sports facility in Karebosi's field has the highest different types of activity choices, such as jogging, football, fitness, gymnastics, and strolling. The diversity of the second type of activities in the location is interaction activity which happens in activity form of sitting together, talking, gathering, and some of them enjoy snacks sold in some area in Karebosi. While the third one is trading/business facility, which is buying and selling activities on sale stalls that happens along R.A. Kartini street, and another area that are generally crowded by the visitors.

Based on this case, it can be concluded that development facilities in Karebosi is still unbalanced. The diversity activities of the sports facility in the location is so dominant compared to the other diversity of interaction activitiy choice provided. This is contrary to the theory of Weisman [7] that says sociality is the level of a person's ability to make social relations in a setting.

(a)

(b)

Figure 10. (a) Diagram of intensity and the diverse activities of the visitor in the morning, (b) Diagram of intensity and the diverse activities of the visitor at noon

c. The scope of structural dimension

Based on the observation of the usage aspects, Karebosi field is considered as a successful public space to create the diversity of the types of the visitors. It can be seen by the presence of the different types of the visitors who do some activities in Karebosi, and the routine visits happen every day with the intensity that is increasing at the weekend.

Based on the observation of activity diversity aspects, it can be concluded that Karebosi as a public space is quite successful in creating the diversity of activities in public space. It is based on the diversity of activity behavior that happens regularly in the facility. Generally, there are three types of activities happen in the Karebosi field, namely; sports, social interaction, and business which happens regularly with its intensity that increasing on the weekend.

Based on the observation of diversity sociality aspects, it can be concluded that Karebosi field area is considered as an unsuccessful public space in creating a comfortable environment for the people to interact. It can be seen from the minimum diversity types of interaction behavior found in Karebosi, which makes the visitors' interaction in Karebosi runs monotonously.

3.2. The correlation aspects of response to the condition of facilities and activities

Based on the literature review in [8], there are some conclusions gotten from several visitors through questionnaires and interviews.

a. The scope of subjective dimension

Based on the observation on accessibility aspects, the conclusion shows that generally, the visitors are quite satisfied with the service facilities provided. The utility of facilities and infrastructures is considered to be quite supporting the people during they are doing some activities in Karebosi. Based on the visitors' perception of the utility of the facilities, the convenience of accessibility is quite enough even though it still needs to do some refinement. Yet generally, the visitors are quite satisfied with the location that is supported with strategic location to the accessibility of the facilities that is easily accessible. It is in line with Weisman theory [7] that says accessibility concerns to the ease of moving through and using the environment so that the circulation becomes smooth and it does not make difficulties for the users.

Based on the observation on the facility usage aspects, the visitors said that Karebosi field as public space does not have identity, landmark, and characteristics that visually can be remembered easily and known in the area. It is contrary to theory in [7] that says the easiness for someone to recognize and understand the main elements and the relation in an environment which causes the person to find a way or direction.

As public open space, the visitors said that visual access of Karebosi environment is not enough. It still seems closed to the environment around, and it is contrary to the principle that every public space has a meaning as location designed and has huge access to the environment around [9, 10].

As public open space that needs open access, the visitors argued that the development of stalls PK.5 which covered along R.A. Kartini street limits the visitors' view to see the condition of the environment from outside and inside Karebosi field area. It contrasts with Weisman's theory [7] that says the ability to see the object aimed without being blocked visually.

b. The scope of interactive dimension

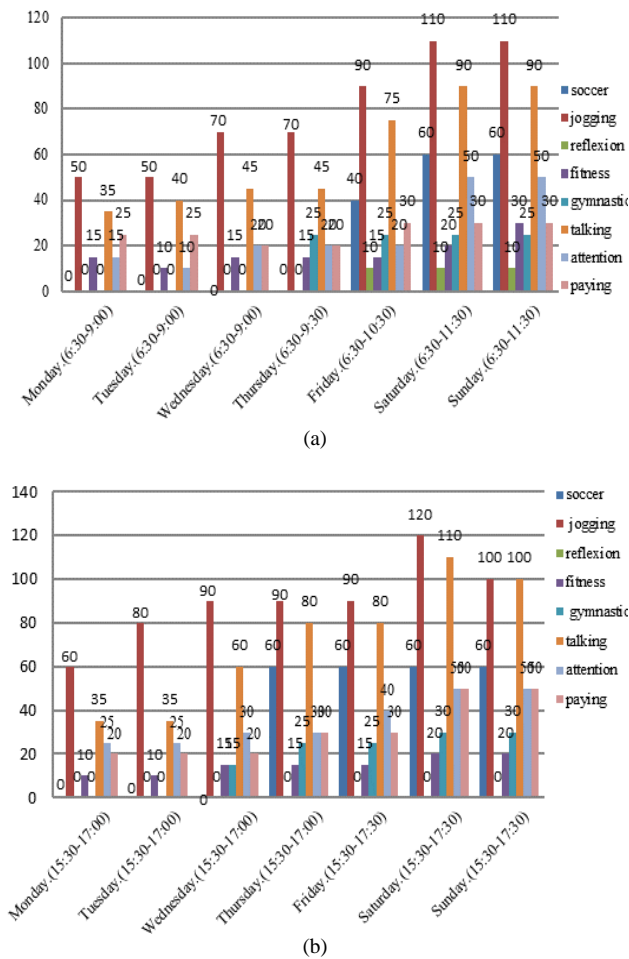Based on the observation of interactive dimension, after a review based on the parameter quality theory of social interaction in public space, some conclusions are obtained.

Based on observation of social aspects, the facilities and infrastructures are considered to be not optimal in facilitating the diversity activity of social interaction in Karebosi. It contrasts with the White theory [11] that says the success of a public space can be seen by social interactions, facilities, and infrastructures.

As public open space, Karebosi does not have public spaces' elements that designed interestingly so that it attracts the visitors' reaction to observe and comment. It can stimulate the fellow visitors to interact in public space. The condition is contrary that concerning the environment's characteristics that stimulate social interaction of sensory stimulation that is the quality and intensity of the sensory as the experience felt by human sense [7].

A flurry that happens continually can increase social interaction in public space. As public space, Karebosi field has flurry in which the intensity is increasing at the weekend. It is in line with successful aspects of public space that activity is the feeling of the intensity existence on behavior that happens continually in an environment [7].

Based on the observation on diversity activity aspects as public space, Karebosi field is considered to be not optimal in giving service of social interaction activity needs for people. It can be seen in the diversity of interaction choices for the visitors in which the amount is still minimum. It contrasts with Mehta [12] in relation to social activities implementation in public space. It depends so much on the variation of usage, which is measured based on the diversity or the number of typology activities implemented outside.

Sports facilities are quite successful in facilitating the interest of different types of community to exercise. The activity that happens in Karebosi commonly is sport activity with the number and condition of facilities that quite enough, so it attracts people's interest to visit Karebosi. It is in line stated that the success of a public space can be seen from the diversity of the users who are having activities in the area [11].

c. The scope of structural dimension

Based on the observation on structural dimension of personal assessment aspects by questionnaire from data validation processes through actual score comparison to ideal score, the percentage of respondents responses are as follow:

$$\frac{Actual\ score}{Actual\ score} \times 100\% = \frac{7632}{12500} \times 100\%$$
$$= 61.056\%$$

The quality of public space can be considered successful if the total percentage of the statement of 60.89 %, in which it is in the success range of 60 – 79.9 %. Generally, based on questionnaire and interview methods, seen by the visitors' behavior, the sports facility is quite successful to give meaning and interest of Karebosi field as public space and attracts people' interest to exercise in Karebosi. However, the visual facility condition which is covered from surroundings is not attracting the visitors to stop by and do activities in Karebosi. As public space, the facilities in Karebosi do not have facility design that could give meaning and impression for the visitors which can stimulate the diversity interaction increasing of fellow visitors.

3.3. The correlation of visitors' attitude and behavior response to the condition of surroundings

Based on the personal assessment aspects of environmental management, some conclusions are obtained:

a. The scope of subjective dimension

Based on the observation of accessibility, the similarities of response on visitors' attitude and behavior to the facility condition are obtained, even though based on theory and questionnaire measurement visually the quality of access design of Karebosi field is not fully ideal, yet generally, the visitors are quite satisfied with the facility services provided in Karebosi. It can be seen by the routine of the visits to the location. Likewise, the utility of the facility as well as the condition of supporting facilities has been supportive generally.

b. The scope of interactive dimension

Based on the scope of interactive dimension, there is a similarity in the visitors' attitude and behavior response to the facility condition. Based on the literature review of main facility condition seen by the intensity of sports and interactions happen regularly, the sports facilities in Karebosi field is considered to be successful to facilitate and stimulate the increase of physical health and interaction activity for the visitors. Yet the condition of the surrounding is still not conducive. As a public facility, Karebosi field is considered to be not optimal in facilitating the types and diversity of facility choices which can stimulate the improvement of social interaction quality for the visitors.

Figure 11. The situation of environmental planning of the facilities

Figure 12. The situation of site plan planning and the attributes in the location

Figure 13. The situation of environmental carrying capacity of facilities

Figure 14. The wide area carrying capacity on facilities

Figure 15.The routine of lively activities on location

c. The scope of structural dimension

An assessment of visitors to the overall condition and management of the facility to improve the quality of public open space services.

Based on the scope of structural dimension, there is a correlation between the facility condition, the response of behavior and the response of attitude. Through an interview with some of the visitors, it can be concluded that

(1) They agree that the condition of environmental design is not interesting. This is not following the theory of passive attachment by Stephen [13] that says passive attachment to the environment can be presented through elements of observation, scenery, public art, performances and attachment to nature that can be fulfilled for visitors who do passive activities.

(2) Supporting facility of interaction such as landscape planning, park design, the characteristics of public area, and the condition of seat facilities which are not interesting.

(3) They agree that the orientation of development trade facilities in the location is too huge compares to the visitors' needs. This is contrary to the stimulus theory that says influences social interaction on congestion is the feeling of density in an environment [7].

(4) They intensely visit Karebosi field area because of the wide of facility area which can make the visitor feel spacious while they are doing some activities in it so they can exercise optimally.

(5) Elderly visitors stated that they feel comfortable for a shady environment and the quality of the oxygen which is quite good because there are a lot of shady trees surrounding Karebosi field area. This is in accordance with Carr's theory [12] that says the comfort of public spaces is influenced by environmental comfort in the form of protection from natural influences such as sunlight, wind; (physical comfort) in the form of availability of adequate supporting facilities such as seating; (social and psychological comfort).

(6) Teenage female visitors feel happy for shady environment, but they feel happier because they can do gymnastics after jogging. This is following relaxation theory. In urban public space settings, elements of nature such as trees, plants, and water can make the body and mind more relaxed [13].

(7) According to most visitors, they think that the jogging facility in Karebosi is the best in Makassar. The jogging track has an ideal track and a long range.

(8) Male teenagers intensely visit Karebosi due to the lively atmosphere of sports activities. There are three soccer fields provided and a jogging track area which makes them feel comfortable and more energetic to exercise.

(9) In the Karebosi field area, we can gather and play soccer with friends (Student, 19 years old).

(10) "I like to visit Karebosi because it is one of cool places for " (Student, 25 years old).

(11) "My intention to visit Karebosi in the morning is because the fresh air since there are a lot of trees in here" (Entrepreneur, 45 years old).

(12) The situation that can stimulate visitors to interact in Karebosi is the convenience of talking to visitors who have the same hobbies and activities. This is following a theory on the aspect of comfort in public spaces (livability) is the comfort of staying or the sense of comfort to live or move in the region [3].

(13) The convenience of paying attention to the crowd of the visitors who have activities in Karebosi. The intensity of activities happen in the field can increase the visitors' energy to exercise. This is following the theory of Weisman [7] that says activity is a feeling of the intensity of behavior that is continuous in an environment.

155

4. Conclusions

The condition of facilities and activities provided in Karebosi is considered to be quite successful in facilitating people's needs in doing their activities on public space, it can be seen by intensity levels and routine visits of the facility which happen consistently and continually. Yet as public open space, the orientation of facility development and the different types of activities in Karebosi have not been running in balance. Service quality in sports activity is not balanced by the increase of service on interaction activities. Based on this case, it can be concluded that Karebosi field has not been able to provide a conducive interaction service facility for people to interact in Karebosi. Karebosi field area as the representative of public space in Makassar is considered to be unsuccessful to create the diversity activity of social interaction in public area.

Facility and activity services provided in Karebosi field are quite successful to attract people interest to do some activities and interact in Karebosi. However, as public space, the carrying capacity of the facility is not fully ideal. The success rate achieved was still at 61.056 %. People quite satisfied with the condition of Karebosi nowadays. Yet they still complaining about the lack of carrying capacity of the facility. They stated that the condition of facility in Karebosi is not conducive to do interaction activities. The facility of the public area has not been able to provide various choices for interaction activities. Generally, as a public area, the facility design and activity scenario of the public area has not been able to present various entertainment and impression for the visitors.

As a public area, Karebosi is quite successful to increase people's participations on public area, yet the success was still at 61,056%. Generally, the convenience is gotten by the visitor through the environment carrying capacity which is quite ideal because it is supported by oxygen quality and the coolness of the temperature obtained from a shady place in Karebosi. The convenience of social interaction in Karebosi field is based on the crowd of the visitors who have activities and tend to have the same hobbies. The crowd in Karebosi is caused by the convenience of sport facility service in Karebosi supported by comfortable environmental conditions and the quite ideal of scale facility. The number 39.044 were obtained from not optimal carrying capacity of physical design. The orientation of facility development has not been optimal to stimulate the increase of social interaction in public area. Karebosi field area is considered to be unsuccessful to be a public area that provides various needs and activities of the people who have different purposes and needs.

Recommendation

This research can be an input for the government to decide the orientation of facility development in Karebosi in the future. As a public area which is the representative of the public area in the city, the government should be able to design a conducive and interesting public area for the communities. Karebosi field area needs to get a better visual design for the area. By the aspects of environmental design quality, it is better for the government to designing in landscape which is completed by interesting design of public space attributes that functioned as identity and characteristics that could increase the visual beauty so that the public space could fulfill the need of entertainment and also have meaning as refreshing facilities for the visitors.

This research can be an input for the manager to be more creative in creating the scenario of the area which could give entertainment and refreshing facilities for the visitor. The intensity of social interaction of fellow visitors can be increased by providing a conducive area to seat and for having a conversation which is connected with friends that are designed interestingly, providing a playground for children and providing water fountain which can increase the visitors' interest to sit and interact each other.

This research can be the first step to do the next research related to the determination of design definition that can be a reference for designing facilities of the public area in an urban area in the future.

References

[1] Karen Malone in children, Youth, and sustainable Cities, Local Environment vol. 6 No. 1(2001).

[2] Sauter, .D. Huettenmoser, M.2008. liveable Street and Social in´clusion-urban Design. International Volume 13.

[3] Carr, et. all dalam Carmona (2003) . Public Place-Urban Spaces, The Dimension of Design. Burlington : Arcitektural Press.

[4] Parkinson, John. 2012. Democracy and public space. Oxford University Press.

[5] Sirvani, Hamid (1985). The Urban Design process. Van Nostrand Reinhold: New York.

[6] Rustam Hakim, Hardi Utomo, Component of landscape architecture design [in Bahasa] (Jakarta,2003), hal 50.

[7] Weisman, J, 1981. Modeling Environment Behavior Sistem. Journal Of Man Envirronment Relatition Persilvania. USA.

[8] Sauter, .D. Huettenmoser, M.2008. liveable Street and Social in´clusion-urban Design. International Volume 13.

[9] SC Ruton, Roger, 1984. Public Space and The classical Vernacular.Singapore: The Public.

[10] White, F, William, 1987. The American Sociologist Vol .14. No.1(Feb, 1978), PP. S6-66. New York State School Of Industrial and Relations.

[11] Mehta. 2007. A toolkit for performance measures of public space. 43rd ISOCARP Congress 2007.

[12] Carr, Stephen et al. 1992. Public space,new York: Cambridge university.

[13] Sirvani, Hamid (1985). The Urban Design process. Van Nostrand Reinhold: New York.

Air Quality Characteristics in Junior High School Classroom with Natural Ventilation in Pangkep Regency

Nur Mutmainnah[a,*], Rosady Mulyadi[b], Baharuddin Hamzah[c]

[a]Department of Architecture Research, Engineering Faculty, Hasanuddin University. Email: mutmainnahn15p@student.unhas.ac.id
[b]Department of Architecture Research, Engineering Faculty, Hasanuddin University. Email: rosady@unhas.ac.id
[c]Department of Architecture Research, Engineering Faculty, Hasanuddin University. Email: baharsyah@unhas.ac.id

Abstract

The indoor air quality room has turned out to be a major concern due to its adverse effects on human health. This is related to the level of activity of human spent almost 90 percent of their time indoors. This study aims to identify the characteristics of air quality in classrooms with natural ventilation systems in three different schools, which vary in topography and the surrounding environment, namely coastal areas, lowlands, and mountains. Air quality measurement focuses on carbon monoxide (CO), carbon dioxide (CO_2) concentration, total dust content, temperature (T), humidity (RH), and airflow velocity. The statistical results showed significantly different ($p < 0.05$) in air quality parameters among those three schools. The CO and CO_2 concentrations in the three schools are below the recommendations required by DOSH and ASHRAE. This clarifies that a well-used natural ventilation system is able to maintain the air quality in the classroom. The measurement of total dust levels was above the threshold required by the Ministry of Health of the Republic of Indonesia No.1405/MENKES/SK/XI/2002. In addition, there was a significant relationship ($p < 0.05$) between air pollutants and meteorological factors such as temperature and air humidity in the classroom. This study found that there was an influence of human activity level and the surrounding environment on the amount of pollutants concentration in the classroom.

Keywords: Carbon monoxide (CO), carbon dioxide (CO_2); indoor air quality; natural ventilation; total dust content

1. Introduction

The issue of indoor air quality began to get public attention when a study conducted by EPA in 1989 stated that the impact of air pollution in space is heavier than outdoors. In addition, according to the Green Building Council, Indonesia indoor air pollution is more dangerous 4 times than outdoor pollution, especially if the room does not have a good ventilation system and uses unattended mechanical ventilation.

Humans spend an average of 70% - 90% in the room both for work, study, and rest. Whereas in the world of education, students and teaching staff tend to spend at least 6-8 hours/day at school. Therefore, the school must pay attention to and create an atmosphere of a conducive, healthy, and comfortable teaching and learning room, so that the school's mission to educate students is achieved.

In the previous study, it was found that air quality in the classroom can affect students' learning processes both from

concentration and presence [1]. Poor air quality in the classroom has an impact on the health of children in schools such as respiratory problems, irritation/allergies, and others that can reduce students' learning performance [2]. Rooms that have good air circulation can produce good air quality inside. Air circulation is influenced by various factors, one of which is the ventilation system.

In general, educational buildings in Indonesia have relied on air conditioning systems and natural lighting for thermal comfort and air quality. However, the average state school in Indonesia are built on the same standard/prototype, without being based on consideration of local climate conditions and taking into account the comfort of its users, as a result, the existing classrooms are far from comfortable [3]. In addition, air quality is influenced by various factors, including location, various activities, pollutants, and meteorology and topography that affect the spread of pollutants in the air [4-6].

This research was conducted at junior high schools in Pangkep. As we know, there are many factories in Pangkep, such as cement, marble and so on. This has the potential to contribute to air pollution in the environment.

*Corresponding author. Tel.: +6281354630436
Jalan Poros Malino km. 6 Bontomarannu
Gowa, Sulawesi Selatan, Indonesia, 92171

This study aims to evaluate the air quality in the classroom and compare the air quality of the school according to the surrounding environment including schools in coastal areas, lowland areas, and mountainous regions. This study focuses on the concentration of pollutants of carbon monoxide (CO), carbon dioxide (CO_2), total dust levels and meteorological parameters (humidity (RH), temperature (T), and airflow velocity.

2. Method

This research employs survey and experimental design. The samples involved were public junior high schools (SMPN) in three regions, namely 1 school in the coastal area (SMPN 1 Mandalle), 1 school in the lowland area (SMPN 2 Bungoro), and 1 school in the mountainous area (SMPN 2 Balocci). The school located in coastal areas directly adjacent to provincial highways, the school in the lowlands are in ring 1 of the PT. Semen Tonasa II with distance about ± 500 meters from Tonasa II Region, while the school in the mountain is bordered by mountains and rice fields.
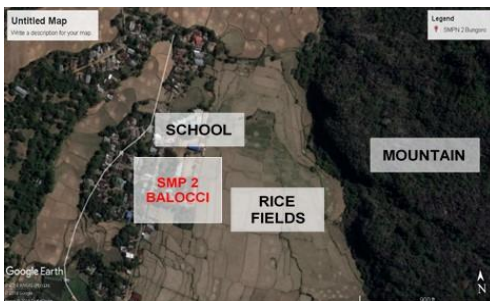
Figure 1. Samples of Schools in Pangkep: (1) School in Coastal, (2) School in Lowlands, (3) School in Mountain.

1. Anemometer Hobo
2. Termometer Dig. Hobo
3. LSI Lastem (CO & CO_2) and Dust trak (total dust content)
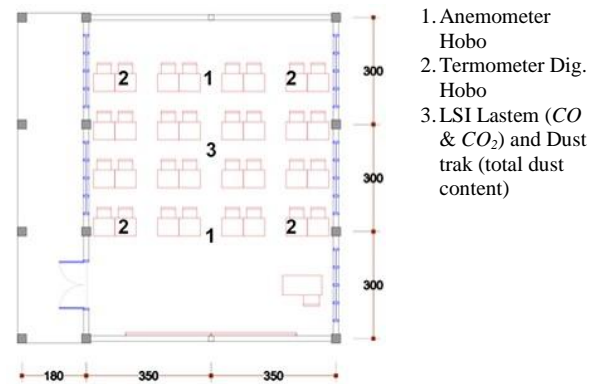
Figure 2. Placement of the measurement spot

Measurements were conducted for three days in each sample location. Measurements of temperature, humidity, CO and CO_2 levels were carried out for six hours a day from 7:30 a.m. to 1:00 p.m. for each sample. Measurement of total dust levels was carried out by the method of instantaneous / grab sampler for 1 day per sample at certain hours, namely at 08.00-9.00; 10:00 - 11:00 and 12:00 to 13:00. The study was conducted on August 8, 2018 - August 30, 2018. Placement of the measuring instrument refers to Mahyuddin and Awbi [7] which is in the middle of the room above the height of the students' breathing zone in a sitting position.

Quantitative data analyzed with statistical analysis using SPSS. ANOVA analysis with *Kruskal Wallis H* to determine the significance of differences in air quality values in classrooms at different locations, while the *Spearman* bivariate correlation test to determine the relationship between pollutants and meteorological parameters in three measurement regions.

3. Discussion

3.1. Classroom occupancy rate

Classroom size in accordance with the Minister of Education Regulation No. 24 of 2007 is 7 meters x 9 meters x 3.20 meters. The number of students in the classroom is around 25-27 people. The density of classrooms with these sizes is 2.33-2.52 m²/student, higher than the standard/ provision in the Minister of Health Decree No.1429/ MENKES/SK/2006, which is at least 1.75 m² /student with 3m height ceiling.

3.2. Comparison of classroom air quality in 3 locations (coastal, lowlands, and mountains).

To compare the classrooms air quality in three measured locations, the F- test using a nonparametric test with Kruskal Wallis H was employed. The hypothesis of this study is as follows.
- Ho: all three groups/locations have the same average value
- H1: all three groups/locations have different mean values.

158

Table 1. F Test- Kruskall Wallis air quality in 3 measured sample locations

Test Statistics[a,b]						
	Co	CO2	T	RH	Airflow	Total dust content
Chi-Square	424.509	110.136	130.017	328.012	82.248	161.548
df	2	2	2	2	2	2
Asym p. Sig.	.000	.000	.000	.000	.000	.000
a. Kruskal Wallis Test						
b. Grouping Variable: School						

Table 2. result of temperature and humidity measurement

		school in the lowland area	school in the coastal area	school in the mountainous area
Min		27.58 °C	25.75 °C	28.52 °C
		41.07%	51.00%	36.84%
Max		35.00 °C	33.24 °C	33.80 °C
		70.41%	84.32%	71.57%
Mean		32.11 °C	29.88 °C	31.19 °C
		56.27%	66.06%	50.21%

While the conditions used in determining the acceptance criteria for the hypothesis are:

- Ho rejected if X^2 count > X^2 table ($p=0.05$) means that the three groups have different mean values.
- Ho accepted if X^2 counts < X^2 table ($p=0.05$) means that the three groups have the same average value.

Based on the results of the *Kruskal Wallis* test, the calculated X^2 values of each variable are different, namely $CO = 424.50$, $CO_2 = 110.13$, *T*emperature (T) = 130.01, Air Humidity (RH) = 328.01, Airflow rate = 82.24 and Total dust levels = 161.548. The value of X^2 table ($p= 0.05$) with a free degree of 2 (df2) of 5.99. The calculated X^2 value greater than the X^2 table value indicates that all air quality variables (CO, CO_2, T, RH, air flow, and total dust content) in three locations have significantly different mean values. To find out the comparison of the concentration values of air quality variables in the three measurement locations is explained as follows.

a. *Comparison of temperature and humidity values*

From Table 2, we can see the measurement of temperature and humidity in 3 schools. It is recommended for thermal comfort in space is 24°C - 27°C with air humidity 55% - 65% of SNI 6390: 2011. For air temperature at the measurement of 3 schools above the recommended standard. Of the three schools, schools in the lowlands have high-temperature values from 2 schools. The location of the school located in ring 1 of the Semen Tonasa II plant is one factor in the high temperature in the classroom, besides other factors such as classroom openings, student numbers and activities also affect temperature and humidity in the room.

Table 3. Air flow velocity result

	school in the lowland area	school in the coastal area	school in the mountainous area
Min.	0.05 m/s	0.05 m/s	0.09 m/s
Max.	0.71 m/s	0.77 m/s	1.00 m/s
Mean	0.17 m/s	0.21 m/s	0.26 m/s

Table 4. Measurement result of CO dan CO_2

		school in the lowland area	school in the coastal area	school in the mountainous area
Min	CO	1.0 ppm	1.4 ppm	1.1 ppm
	CO_2	354.4 ppm	377.8 ppm	362.7 ppm
Max	CO	1.6 ppm	2.1 ppm	1.6 ppm
	CO_2	586.6 ppm	679.9 ppm	499.6 ppm
Mean	CO	1.2 ppm	1.8 ppm	1.39 ppm
	CO_2	438.54 ppm	475.92 ppm	409.07 ppm

b. *Comparison of air flow velocity values*

Table 3 presents comparison of air flow velocity of three measured locations. It is observed that mean velocity increases in the sequence of lowland, costal and mountainous areas.

c. *Comparison of CO dan CO_2*

The recommended value of CO_2 levels in space should not exceed 1000 ppm per 8 hours and CO levels should not exceed 9 ppm in 8 hours and 35 ppm in 1 hour to be able to feel the air of good quality according to DOSH standards [8] and ASHRAE [9]. From Table 4, the CO_2 concentration in 3 schools is below the threshold of the DOSH standard [8] and ASHRAE [9]. In addition, the measurement results of CO and CO_2 in this study belonged to the category "excellent" as the concentration values below 800 ppm and 1.7 ppm as suggested by the Hong Kong EMSD [10].

The value of CO and CO_2 concentrations below the threshold concludes that natural ventilation systems are used well and are able to maintain the air quality in the classroom. As seen in Table 4, schools located in coastal areas precisely in traffic areas have the highest CO and CO_2 concentration values. Besides being due to location factors, the number and activity of students around the measurement points and openings design also causes high values of CO and CO_2 concentrations.

There are not many differences in the value of CO_2 among 3 schools because the number of students in each class is almost the same 25-27 people as recommended by the Indonesian Ministry of National Education. In general, the value of CO_2 concentrations in classrooms in each school is significantly higher when the teaching and learning process is compared if the room is in a state of the recess (most students leave the classroom). The results of the measurement of CO_2 concentrations in 3 schools in this study were lower than the results of a study conducted by Talarosha [11] in elementary schools that were naturally ventilated in Medan.

Table 5. Total dust measurement result

	school in the lowland area	school in the coastal area	school in the mountainous area
Min.	0.09 mg/m^3	0.05 mg/m^3	0.05 mg/m^3
Max.	0.49 mg/m^3	0.47 mg/m^3	0.37 mg/m^3
Mean	0.28 mg/m^3	0.15 mg/m^3	0.22 mg/m^3

d. Comparison of total dust level

The threshold value of total dust in the air according to the Decree of the Minister of Health of the Republic of Indonesia No.1405/MENKES/SK/XI/2002 concerning the health requirements of office and industrial work environments is 0.15 mg/m^3 with air exchange 0.283 m^3/minute/person with airflow rate 0.15-0.25 m/s.

The measurement results of dust levels in 3 schools in Table 5 showed that 2 schools had total dust content values above the regulatory threshold used, namely schools in lowland areas and schools in the mountains. School locations in the lowlands adjacent to the Tonasa cement factory and schools in the mountains bordered by rice fields are the source of dust in the space. In addition, another factor is the lack of awareness of students to clean the room regularly.

3.3. Relationship between meteorological parameter variables and the concentration of air quality in the classroom.

To determine the relationship between meteorological parameters and the concentration of air quality in the classroom, statistical tests are carried out in Table 6 with a "*Spearman*" bivariate correlation test analysis. The analysis was carried out by correlating between pollutants (CO, CO_2, total dust content) and temperature (T) parameters, humidity (RH) and airflow velocity in the classrooms at each measured location.

From the tables, the overall relationship between indoor variables studied in all three schools was significant at $p < 0.05$. The temperature (T) value had a very strong negative relationship with air humidity ($0.719 > r > -0.872$) in all three schools. In addition, the temperature value in junior high school coastal areas had a strong r value and a significant relationship with several other variables compared to the other 2 schools, where the r value between T and CO is -0.554, T and CO_2 were -0.658 and T and airflow is 0.217. This is influenced by the location of the school which is on the side of the road, the activity of students in the classroom, the environment, and surrounding activities.

Temperature values also have a negative relationship with CO and CO_2 concentrations in all three schools, while air humidity had a low positive/weak relationship ($0.289 \geq r \geq 0.545$) with CO and CO_2 concentrations in 2 schools namely low land area and coast. The negative relationship between temperature and CO and CO_2 concentrations shows a tendency for a relationship between reduced CO and CO_2 concentrations with rising air temperatures in space. This is in line with research conducted by Talarosha [12] and Nagendra & Harika [13].

Table 6. Correlation of air quality in classrooms

a. Air quality correlation at SMP in the mountains

Variable	T	RH	Air flow (m/s)	CO	CO_2	total dust content
T	1					
RH	-0.872**	1				
Air flow (m/s)	0.051	-0.145**	1			
CO	-0.245**	0.030	0.124	1		
CO_2	-0.261**	0.136	0.025	0.161**	1	
total dust content	0.864**	-0.842**	-0.076	-0.069	-0.171	1

b. Air quality correlation at SMP in the lowland areas

Variable	T	RH	Air flow (m/s)	CO	CO_2	total dust content
T	1					
RH	-0.854**	1				
Air flow (m/s)	0.036	-0.001	1			
CO	-0.502**	0.545**	0.043	1		
CO_2	-0.244**	0.289**	-0.078	0.172**	1	
total dust content	0.832**	-0.579**	0.017	-0.074	-0.090	1

c. Air quality correlation at SMP in the coastals

Variable	T	RH	Air flow (m/s)	CO	CO_2	total dust content
T	1					
RH	-0.719**	1				
Air flow (m/s)	-0.217**	-0.062	1			
CO	-0.554**	0.353**	-0.015	1		
CO_2	-0.658**	0.322**	0.354	0.280**	1	
total dust content	0.103	0.335**	-0.184	0.056	-0.155	1

**. Correlation is significant at the 0.05 level (1-tailed)

In addition, there was a low/weak positive relationship between CO concentration values and CO_2 concentration values ($0.161 \geq r \geq 0.280$) in measurements in three schools. The velocity of airflow has no relationship with CO and CO_2 pollutants. This is because the velocity of airflow in three schools is very weak below 0.25 m/s.

The concentration of the total dust level has a significant relationship with temperature and humidity. A very strong positive relationship found between total dust level and temperature ($0.822 \geq r \geq 0.864$) in the lowland junior high school and lowland area. This shows that the higher the air temperature in the room, the greater the concentration of total dust. This is consistent with previous relevant research such as in India [14] which has seasonal variations and meteorological conditions similar to Indonesia. The positive correlation of air temperature with total dust concentration can occur because of the increasing air temperature, the emitted dust becomes lighter, so it settles to the ground longer. The result can be crashed and inhaled easily by receptors.

160

In contrast to temperature, air humidity has a very strong negative relationship with total dust content ($-0.57 \geq r \geq -0.84$) in the lowland area and junior high school areas. This is in accordance with previous relevant research which states a negative correlation between air humidity and total dust concentration [14, 15]. In general, high air humidity results in increasingly heavy dust and accelerates the deposition of dust to the surface of the soil thereby reducing dust emissions that are exposed to a human.

4. Conclusions

The results of this study show significant differences in air quality parameters in the classroom at 3 different schools. The measurement results of CO and CO_2 concentrations indicate that the location of schools in the coastal near the traffic area has the highest CO and CO_2 concentration values from the other 2 schools. Whereas the location of the school in ring 1 of the industrial area of Semen Tonasa factory shows a high total dust content of 0.283 mg/m^3 above the regulatory threshold stipulated by the Decree of the Minister of Health of the Republic of Indonesia No.1405/ MENKES/SK/XI/2002 which is 0,15 mg/m^3.

Measurements of CO and CO_2 concentrations in classrooms are below the threshold of concentration values set by DOSH and ASHRAE. This indicates that the natural ventilation system is used well and is able to maintain the air quality in the classroom. In addition, the result of this study indicates a tendency for a relationship between the reduction of CO and CO_2 concentrations and the increasing air temperatures in the classroom. While humidity has a positive relationship with the concentration of CO and CO_2, which means that the higher the humidity in the room indicates the higher the concentration of CO and CO_2 in space. Meanwhile, the concentration of the total dust level has a significant relationship with temperature and humidity. This shows that the higher the air temperature in the room, the greater the concentration of total dust. In contrast to temperature, air humidity has a very strong negative relationship with total dust levels.

Reference

[1] Mendell, M.J., & Heath, G.A. 2004. *Do Indoor Environments in School Influence Student Performance? A Critical Review of The Literature.* Indoor Air, 15(1), pp.27–52.

[2] Mendell, M.J. 2007. *Indoor Residential Chemical Emissions as Risk Factors for Respiratory and Allergic Effects in Children: A Review.* Indoor Air Journal, 17, pp.259–277.

[3] Baharuddin, Mulyadi, R., Amin, S. 2016. *Thermal Comfort Analysis of Elementary School Classrooms in Makassar City - Case Study of Toddopuli Elementary Primary School.* Prosiding Temu Ilmiah IPLBI. [in Bahasa]

[4] EPA. 2013. *Technology Transfer Network: National Ambient Air Quality Standards* (Online), (http://www.epa.gov/ttn/naaqs/, accessed 22 Maret 2018).

[5] SM for European Local Ports. 2010. Pollution Part 1 of 2 Overview.

[6] British Columbia Air Quality, 2016. Factors Affecting Air Quality. (Online), (http://www.bcairquality.ca/101/air-quality-factors.html, accessed 3 April 2018).

[7] Mahyuddin, Norhayati dan Awbi, H.B. 2012. *A Review of CO_2 Measurement Procedures in Ventilation Research.* International Journal of Ventilation: ISSN 1473-3315.

[8] DOSH. 2010. *Industry Code of Practice On Indoor Air Quality Malaysia*: Department of Occupational Safety and Health (DOSH), Ministry of Human Resources.

[9] ASHRAE. 2004. *ASHRAE Standard 62.1-2004: Ventilation and Acceptable Indoor Air Quality.* Atlanta, Georgia: American Society of Heating, Refrigerating and Air-Conditioning Engineers, Inc.

[10] EMSD. 2003. *Guidance Notes for the Management of Indoor Air Quality in Offices and Public Places.* Hong Kong: Electrical and Mechanical Services Department (EMSD), The Government of the Hong Kong Special Administrative Region, Indoor Air Quality Management Group.

[11] Talarosha, B. 2016. *CO2 Concentration in Classrooms with Natural Ventilation System, A Preliminary Study.* Prosiding Temu Ilmiah IPLB, 099-0104. [in Bahasa]

[12] Talarosha, B. 2015. *Building Adaptation to Thermal Comfort and Its Impact on Air Quality in the Classroom, A Preliminary Study.* Proceeding of TAU Conference: Mitigating and Adapting Built Environments for Climate Change in The Tropics. School of Architecture, Tanri Abeng University, Jakarta, Indonesia, 30-31 March 2015. [in Bahasa]

[13] Nagendra, S.M & Harika, S.P. 2010. *Indoor air quality assessment in a school building in Chennai City, India.* WIT Transactions on Ecology and the Environment, Vol 136.

[14] Sivaramasundaram, K., & Muthusubramanian, P. (2010). *A preliminary assessment of PM10 and TSP concentrations in Tuticorin, India.* Air Qual Atmos Health 3, 95–102.

[15] Monn, C., Braendli, O., Schaeppi, G., Schindler, C., Ackerman-Liebrich, U., Leuenberger, P., et al. (1995). *Particulate Matter <10 (PM10) and Total Suspended Particulates (TSP) in urban, rural and alpine air in Switzerland.* Atmospheric Environment Vol. 29, No 19,2565-2573.

Stability Analysis of Aifa Bridge Abutment in Fafurwar District, Bintuni Bay Regency, West Papua Province

Muhammad Yunus[a,*], Zharin Fahra Syahdinar[b]

[a]Department of Civil Engineering, Polytechnic State of Fakfak. Email: muhammadyunus@polinef.id
[b]Department of Civil Engineering, Polytechnic State of Fakfak. Email: zharinfsyahdinar@gmail.com

Abstract

In the construction of public infrastructures, especially road infrastructure, bridge construction work plays a very important role besides the construction of the road itself. One of the matters that deserves the attention of the planners in designing a bridge structure is the design of the substructure, this is because the substructure determines the quality and service life of a bridge. Besides, at present many cases of bridge structure failures are caused by failures of the substructure in holding the load acting on the bridge. This study aimed to determine the stability of the abutment to sliding failure and the stability of the abutment to overturning failure on the construction of the Aifa bridge in the Bintuni Bay Regency. From the results of the calculation of the stability of the abutments to sliding failure, when the abutments were in normal conditions, the obtained safety factor (SF) was 1.907. In the condition of the upper structure load was not working, the obtained safety factor (SF) was 1.045 and during earthquake conditions, the obtained safety factor (SF) was 1.419. While the results of the calculation of the stability of the abutments to overturning failure, when the abutments were in normal conditions, the obtained safety factor (SF) was 4.640. In the condition of the upper structure load was not working, the obtained safety factor (SF) was 1.658 and during earthquake conditions, the obtained safety factor (SF) was 3.159. Because the obtained safety factor (SF) values were greater than 1, the stability of the abutment to sliding failure and overturning failure are considered to be safe.

Keywords: Bridge abutment; overturning failure; sliding failure; substructure

1. Introduction

Indonesia is one of the developing countries which is currently aggressively carrying out development in all fields. One of these is the development in the field of public works infrastructure. One of the public infrastructures that gets more attention from the government is the development of transportation infrastructures, such as roads and bridges. Road and bridge infrastructure as one of the transportation infrastructure has a very vital role which is directly as a liaison to facilitate transportation between two or more regions [1]. In addition, indirectly, the construction of road and bridge infrastructure can increase the economic growth of a region.

Along with its development, bridge structures have progressed very rapidly, starting with bridges with short spans to long-span bridges that connect between islands and countries [2]. To answer the challenge, a civil engineer must

be involved in adjusting to all the available progress, so that knowledge of the structure of the bridge is sufficiently good and sufficient to anticipate the possibilities that will arise [3].

Every bridge that is built must have a high level of security and comfort for the users so that it can avoid unwanted events. A common problem that is often encountered in bridge construction is the occurrence of structural failures, especially at the bottom of the bridge structure such as the existence of cracks or damage to the abutment of the bridge caused by overloading experienced by the foundation, the occurrence of a large decrease in the bridge foundation which over time can result in structural failure [4].

The bridge structure is composed of elements that are the upper structure, substructure, and complementary bridge structures [5]. The substructure is a component located under the upper structure, which functions to channel all the forces and loads that work on the upper building to the ground. The substructure of a bridge consists of abutments and foundations [6].

*Corresponding author. Tel.: +62-811-4212-748
Jalan TPA Imam Bonjol Atas Air Merah, Kelurahan Wagom
Fakfak, Papua Barat, Indonesia, 98611

The substructure of the bridge, which is the abutment structure is used as a retaining wall and to forward the force to the foundation and must be able to provide stability to the influence of external and internal forces [7]. Therefore, in planning abutments, the stability of the construction must be reviewed against the influence of external forces, which can cause overturning failure, sliding failure, and bearing capacity failure, as well as internal forces that can cause construction failure. The stability of the bridge abutment construction must meet the value of the safety factor (SF) so that it can meet the service criteria of a bridge.

2. Literature Review

2.1. Abutment structure

Abutment is the component of buildings on the upper part of the bridge and also used as a retaining wall. The abutments are adjusted based on the results of land investigations, and as far as possible, they should be placed on hard land so that the tension of the bearing capacity allowable.

By calculating the risk of erosion, the abutment base at least must be 2 m below the original land surface, especially for abutments with a direct foundation. The function of this abutment is as a bridge beam placement, as a stepping plate placement, as a successor to forces acting on the upper structure to the foundation, as a barrier to active soil pressure. Abutment consists of several types, namely [8] :

- Abutment gravity type

These abutments gain strength and resistance to forces that work by using their weight. Gravity type abutments are often used in structures that are not too high and have good foundation soil. In general, the material used is a pair of river stones or mashed concrete. Usually, gravity type abutments are used on bridges that have a not too long span.

- Abutment reverse T type

This abutment is a retaining wall with cantilever beams composed of an elongated wall and as a strength plate from the wall. The durability of the force acting is obtained from its own weight and the weight of the ground above the support plate/heel. The difference in reverse T type abutments is slimmer than gravity type abutments.

In general, reverse T type abutments are used when the abutment height ranges from 6-12 m. This inverted T type abutment can be carried by a pile foundation, or a caisson or even directly dependent foundation, on soil conditions under the abutment.

- Abutment support type

This type of abutment is almost similar to the inverted T type abutment, but this type of abutment is supported on the backside (counterfort), which aims to reduce the force acting on the longitudinal wall and the support. Generally, a support type abutment is used in high structural conditions and using reinforced concrete.

2.2. Abutment forces

The forces acting on the abutment are taken from [2].
- Forces due to dead load
In determining the amount of the dead load, the weight of the building materials below must be used [8].
  - Cast steel   = 7.85 t/m^3
  - Cast iron   = 7.25 t/m^3
  - Aluminum alloy   = 2.80 t/m^3
  - Reinforced concrete   = 2.50 t/m^3
  - Ordinary concrete, cyclops = 2.20 t/m^3
  - Stone pair / brick   = 2.00 t/m^3
  - Wood   = 1.00 t/m^3
  - Soil, sand, gravel   = 2.00 t/m^3
  - Asphalt pavement   = 2.50 t/m^3
  - Water   = 1.00 t/m^3

- Live load
  - "T" load
    "T" load is a load which is a truck vehicle that has a double wheel load of 10 tons with sizes and positions as shown in Fig. 1 [2].
  - "D" load
  a) D" load or line load is the load arrangement in each traffic lane consisting of an equally divided load of "q" tons per meter length per lane, and the load line "P" ton per lane [2]. "D" load as shown in Fig. 2. The size of "q" is determined as follows:

q = 2.2 t/m   = for L < 30 m
q = 2.2 t/m–1,1/60x(L-30) t/m   = 30 m<L<60 m
q = 1.1 (1+30/L) t/m   = for L > 60 m
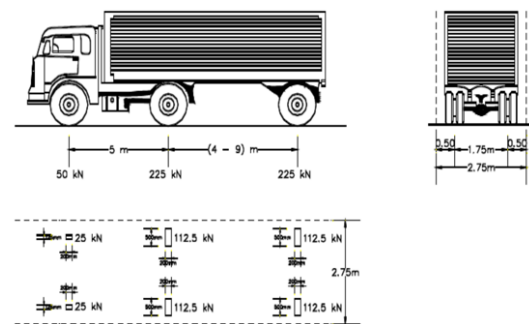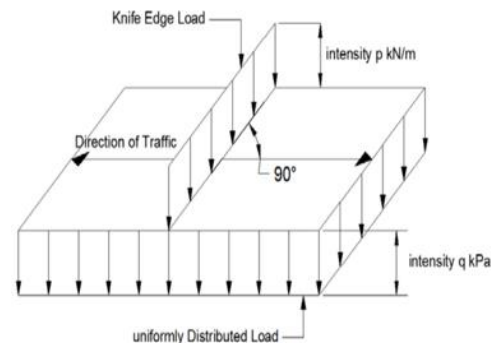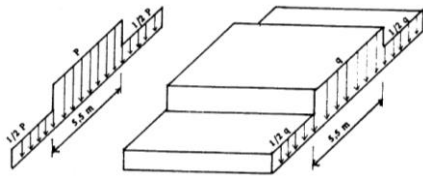

Figure 1. "T" load

Figure 2. "D" load

Figure 3. Terms use of "D" load

b) Provisions for using the "D" load in the transverse direction of the bridge are as follows [2]:
(1) For bridges with a vehicle floor width equal to or smaller than 5.50 meters, the full "D" load (100%) must be charged to the entire bridge.
(2) For bridges with a vehicle floor width greater than 5.50 meters, the full "D" load (100%) is charged to the 5.50 meters track width while the remaining width is loaded with only half the "D" load (50%), see Fig. 3.
(3) In determining live loads (evenly divided loads and line loads) it is necessary to note that provision
   ▪ Spread length (L) for evenly divided loads is in accordance with the provisions in the formulation of the shock coefficient.
   ▪ The live load per meter of bridge width is

$$RqL = \frac{q(ton/m)}{2.75} \times l \qquad (1)$$

$$RPL = \frac{P(ton)}{2.75} \times k \times l \qquad (2)$$

c) Loads on sidewalks, kreb, and backs
(1) Construction of sidewalks must be calculated against live loads of 500 kg/m². In calculating the strength of the girder due to the effect of the live load on the sidewalk, a load of 60% of the sidewalk live load is taken into account.
(2) Kreb which is found on the floor edges of a vehicle must be calculated to be able to withstand a horizontal load across the bridge of 500 kg/m which works on the crest peak in question or at a height of 25 cm above the floor level of the vehicle.
(3) The back pile on each edge of the sidewalk must be calculated to be able to withstand a horizontal load of 100 kg/m, which works at 90 cm above the sidewalk floor.

• Wind load
The wind load is distributed evenly on the side plane of each structural element that forms a curved portal in the transverse direction of the bridge. The largest vertical contact area for each side frame element of the bridge structure is taken.
- The wind that blew the side of the bridge
The force due to the wind that blows the side bridge of the bridge is calculated by

$$Tew1 = 0.0006 \times Cw \times (Vw)^2 \times Ab \qquad (3)$$

- The wind that blew the vehicle
Horizontal wind force on the floor surface of the bridge due to wind loads is calculated using the following formula:

$$Tew2 = 0.0012 \times Cw \times (Vw)^2 \times \frac{L}{2} \qquad (4)$$

• Shock load
To take into account the effects of vibrations and other dynamic influences, the stresses due to the load line "P" must be multiplied by the shock coefficient which will give the maximum yield, while the evenly distributed "q" and load "T" are not multiplied by the shock coefficient. The shock coefficient is determined by :

$$K = \frac{1+20}{(50+L)} \qquad (5)$$

where,
K = shock coefficient
L = span length (m)

• Forces due to soil pressure
The load of the vehicle behind the retaining wall of the ground is calculated to be as high as 60 cm.

• Brake force and traction
The effect of forces in the longitudinal direction is calculated with the effect of the brake force of 5% of the load "D" without a shock coefficient that meets all existing traffic lanes and in one direction. The brake force is considered to work horizontally in the direction of the bridge axis with a catch point of 1.80 meters above the floor level of the vehicle.

$$Traction\ Rrt = \frac{5\% \times (RPL + RqL)}{2} \qquad (6)$$

where,
Rrt = forces due to brakes and traction
RPL = line load
RqL = uniformly distributed load

• Earthquake load due to the upper structure

$$G1 = K \cdot Rvd \qquad (7)$$

where,
K = 0.07
Rvd = vertical force due to dead load

• The force due to friction on the pedestal moves
The friction that arises is only reviewed due to the dead load, while the amount is determined based on the coefficient of friction on the support concerned with the following values:
- Between steel with a mixture of hard copper & steel……0.5
- Between steel and steel or cast iron…….0.25
- Between rubber and steel/concrete……0.15 – 0.18

- Mashed force

To calculate the force due to collisions between vehicles and pillars can be used one of the two most decisive horizontal mash forces:
   - In the direction of traffic = 100 ton
   - In the direction of perpendicular traffic = 50 ton

2.3. Abutment planning criteria

In planning the bridge abutment many forces and loads will be taken into account in the abutment [7]. These forces can be seen in Fig. 4.

2.4. Calculation of abutment stability

The stability analysis of the bridge abutments is calculated as follows [5] :

- Stability for overturning

Safety factor (FS) is used to ensure the safety of an abutments structure against overturning.

$$S = \frac{\sum Mx}{\sum My} \geq 1 \qquad (8)$$

where,
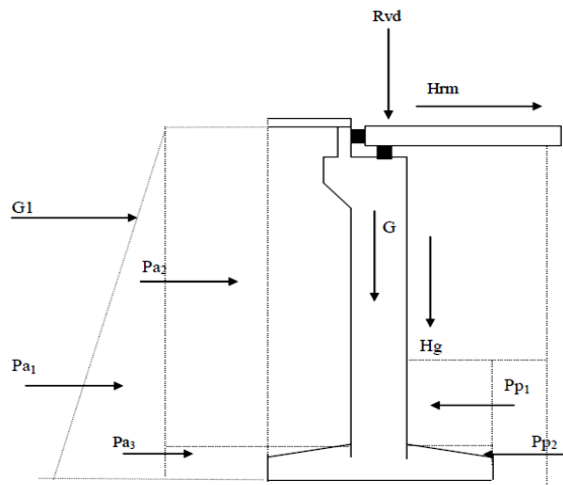$\sum M_x$ = total retaining moment
$\sum M_y$ = total overturning moment

Figure 4. The forces acting on the abutment

Remarks,
P_{a1}, P_{a2}, P_{a3} = the active earth pressure behind at he abutment
P_{p1}, P_{p2} = the passive earth pressure at the front of the abutment
G = self-weight abutment
G_1 = earthquake due to the upper building
H_g = friction due to moving support
H_{rm} = forces due to brakes
R_{vd} = press force due to load from above

- Stability for sliding

Safety factor (SF) used to ensure the safety of the structure against the sliding

$$SF = \frac{\sum V \cdot \tan \frac{2}{3} \phi^o + c \cdot B}{\sum H} \geq 1 \qquad (9)$$

where,
$\sum V$ = total force that holds backsliding
$\sum H$ = total force that causes the sliding

3. Research Methodology

3.1. Time and place of research

This research was carried out on the Aifa bridge construction project located in Tanibar Village, Fafurwar District, Bintuni Bay Regency, West Papua Province.

3.2. Detail engineering design and technical data

Detail engineering design and technical data Aifa bridge obtained from the Ministry of Public Works of the Directorate General of Highways BPJN XVII Manokwari Satker West Papua Province. Detail engineering design which obtained drawing layout, the long section and cross-section of the bridge can be seen in the Figs. 5 and 6. While technical data of Aifa bridge are among others:
- Bridge type   = concrete reinforcement
- Bridge width   = 10 meter
- Length of the bridge   = 30 meter
- Number of main girder   = 6 pieces
- Distance between girder   = 1.6 meter
- Bridge height   = 5.146 meter

3.3. Research flow chart

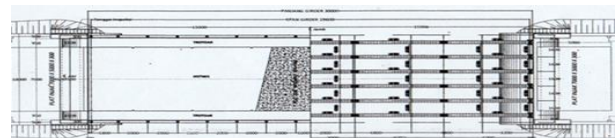The research is conducted by following a research flow chart shown in Fig. 7
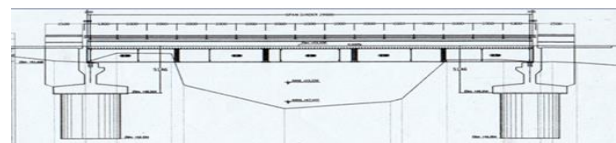

Figure 5. Layout Aifa bridge

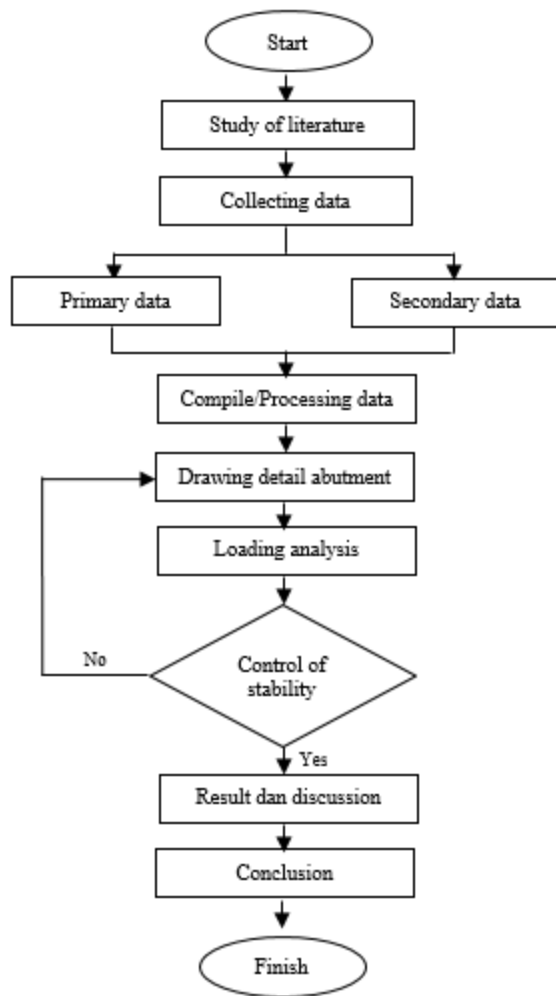Figure 6. Long section Aifa bridge

165

Figure 7. Flow chart of the reserach methodology

4. Results and Discussion

4.1. Overview of abutment dimensions

- Abutmen drawing detail point 1
  From detail engineering design and technical data of Aifa bridge, the abutment detail can be drawn as shown in Fig. 8.
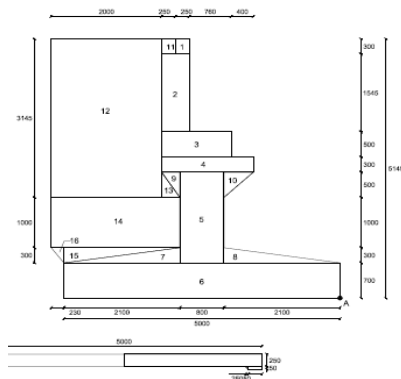

Figure 8. Detail abutment

Table 1. Calculation of dead load

Dead load	Height (m)	Width (m)	Length (m)	Weight Vol (t/m³)	Σ(t)
Vehicle floor	0.2	10	30	2.5	150
Rainwater (3 cm)	0.03	10	30	1	9
Asphalt (7 cm)	0.07	10	30	2.2	46.2
Sidewalk	0.2	10	30	2.5	30
Backrest pipe	4	0.00091	30	7.25	0.7804
Backrest pile	0.1	0,15	1	2.5	0.3
Main girder IWF 900.300.28.16	1.845	0.4	30	7.85	1390.39
Unexpected Load					5.0
				P$_{total}$ =	1631.68

- Loading analysis
  - Dead load
    For the calculation of dead loads that work on abutments can be seen in Table 1.

    $$RvD = \frac{Ptotal}{2} = \frac{1631,68}{2} = 815,841 \ ton \quad (10)$$

  - Live load
    Live load LL = 12 ton, qL = 2.2 t/m (from PPJJR article 1).
    Traffic width = 7 m

    $$RqL = \frac{q}{2.75} \times l = \frac{2.2}{2.75} \times 7$$
    $$= 5.6 \ ton \quad (11)$$

    $$RPL = \frac{P}{2.75} \times k \times l = \frac{12}{2.75} \times 1250 \times 7$$
    $$= 38.182 \ ton \quad (12)$$

  - Shock coefficient (k)
    $$K = 1 + \frac{20}{50 + L} = 1 + \frac{20}{50 + 30}$$
    $$= 1.250 \ ton \quad (13)$$

    $$RvL = \left(k \times RPL \right) + \left(\frac{1}{2} \times RqL \right)$$
    $$= \left(1.250 \times 38.182 \right) + \left(\frac{1}{2} \times 5.6 \right)$$
    $$= 50.527 \ ton \quad (14)$$

  - Forces due to brakes and traction
    Calculated 5% of load D without a shock coefficient with a catch point 1.8 m above the vehicle floor Surface.

166

$$Rrt = \frac{5\% \times (RPL + RqL)}{2}$$

$$= \frac{5\% \times (36.099 + 5.6)}{2} = 1.095 \text{ ton} \qquad (15)$$

- Friction force on the moving pedestal
  Price of motion coefficient taken 0.25 from PPPGJR article 2.6.2.

$$Gg = coefficien\ to\ friction \times RvD$$

$$= 0.25 \times 815.841 = 203.960 \text{ ton} \quad (16)$$

- Earthquake forces

$$El = K \times RvD$$

$$= 0.07 \times 815.541 = 57.109 \text{ ton} \qquad (17)$$

- Analysis of abutment appearance and earth pressure
  a) Cross-section abutment
     Based on the area of the abutment reviewed, the weight for the abutment body was obtained as shown in Table 2.

$$Xc = \frac{\sum Mx}{\sum Ac}$$

$$= \frac{19.779}{7.761} = 2.549 \text{ m} \qquad (18)$$

$$Yc = \frac{\sum My}{\sum Ac}$$

$$= \frac{11.299}{7.761} = 1.456 \text{ m} \qquad (19)$$

b) Earth in front of and behind the abutment
   Based on the area of earth beside the abutment, we obtain data on the center of gravity for the earth behind the abutment as shown in Table 3. From Table 3 obtained the distance from the center of weight to point Z is

$$Xc = \frac{\sum Mx}{\sum Ac}$$

$$= \frac{54.069}{10.407} = 4.331 \text{ m} \qquad (20)$$

$$Yc = \frac{\sum My}{\sum Ac}$$

$$= \frac{33.255}{10.407} = 3.196 \text{ m} \qquad (21)$$

c) Earth pressure
   From the results of soil testing at the Soil Testing Laboratory Polytechnic State of Fakfak obtained soil characteristic as follows :
   Angle friction internal (ϕ) = 19.60°
   Cohesion (c) = 7.133
   Weight volume soil (γ) = 1.1 t/m^3
   Soil depth (h_1) = 5.146 m
   Soil depth (h_2) = 1.200 m

(a) Calculation of coefficient of active earth pressure

$$Ka = tg^2\left(45° - \frac{\phi}{2}\right)$$

$$= tg^2\left(45° - \frac{19.60°}{2}\right)$$

$$= 0.751 \qquad (22)$$

Table 2. Calculation of abutment own weight

No.	Calculation of Abutment Load		Cross Section (m²)	Spesific Gravity (ton/m³)	Arm from Z		Mx = Ac.X	My = Ac.Y
	P (m)	L (m)			X (m)	Y (m)		
1	0.3	0.25	0.075	2.5	2.855	4.996	0.214	0.375
2	1.546	0.5	0.773	2.5	2.980	4.073	2.304	3.148
3	0.5	1.26	0.630	2.5	2.600	3.050	1.638	1.922
4	0.3	1.66	0.498	2.5	2.400	2.650	1.195	1.320
5	1.8	0.8	1.440	2.5	2.500	1.600	3.600	2.304
6	0.7	5.0	3.500	2.5	2.500	0.350	8.750	1.225
	T (m)	A (m)						
7	0.3	2.1	0.315	2.5	3.600	0.800	1.134	0.252
8	0.3	2.1	0.315	2.5	1.400	0.800	0.441	0.252
9	0.33	0.5	0.083	2.5	3.010	2.333	0.248	0.192
10	0.5	0.53	0.133	2.5	1.923	2.333	0.255	0.309
	Total =		7.761				9.779	1.299

Table 3. Calculation of soil weight behind abutment

No.	Calculation of Abutment Load		Cross Section (m²)	Spesific Gravity (ton/m³)	Arm from Z		Mx = Ac.X	My = Ac.Y
	P (m)	L (m)			X (m)	Y (m)		
11	0.30	0.25	0.075	2.5	3.105	4.996	0.233	0.375
12	3.146	2.000	6.292	2.5	4.230	3.573	26.615	22.481
13	1.00	2.33	2.330	2.5	4.065	1.500	9.471	3.495
	T	A						
14	0.330	0.500	0.083	2.5	3.120	2.167	0.257	0.179
15	0.300	2.100	0.315	2.5	4.300	0.900	1.355	0.284
16	0.230	0.300	0.035	2.5	5.077	0.900	0.175	0.031
		Total =	9.1290				38.107	26.844
	P (m)	L (m)						
17	0.25	5.00	1.250	2.5	5.450	5.021	6.813	6.276
18	0.05	0.25	0.013	2.5	7.825	4.871	0.098	0.061
19	0.05	0.25	0.013	2.5	3.075	4.871	0.038	0.061
	T (m)	A (m)						
19	0.05	0.05	0.001	2.5	3.216	4.879	0.004	0.006
20	0.05	0.05	0.001	2.5	7.683	4.879	0.010	0.006
		Total =	1.2775				6.9624	6.4102

Table 4. Calculation of soil weight front abutment

No	Calculation of Abutment Load		Cross Section (m²)	Spesific Gravity (ton/m³)	Arm from Z		Mx = Ac . x	My = Ac . y
	P (m)	L (m)			X (m)	Y (m)		
21	0.300	1.800	0.270	2.5	0.600	0.900	0.162	0.243
	Total =		0.270				0.162	0.243

Table 5. External forces when normal conditions

Forces	V (ton)	H (ton)	Moment Arm		Mx = V . x Retaining Moment (tm)	My = H . y Overtuning Moment (tm)
			X (m)	Y (m)		
R_v	859.623		2.500		2149.058	
W_c	194.025		2.549		494.476	
W_{td}	2.959		0.600		1.776	
W_{tb}	114.055		4.331		493.955	
R_{rt}		1.000		5.450		5.450
G_g		10.568		7.000		73.973
P_{a1}		84.979		3.196		271.554
P_{a2}		108.927		1.598		174.042
		ΣH = 205.473				
P_p		19.187		0.600		11.512
T_b		50.000		2.800		140.000
	ΣV = 1170.662				3139.264	676.530

Table 6. External forces when the upper structure load is not working

| Forces | V (ton) | H (ton) | Moment Arm | | Mx = V . x | My = H . y |
			X (m)	Y (m)	Retaining Moment (tm)	Overtuning Moment (tm)
W_c	194.025		2.549		494.476	
W_{td}	2.959		0.600		1.776	
W_{tb}	114.055		4.331		493.955	
P_{a1}		84.979		3.196		271.554
P_{a2}		108.927		1.598		174.042
		ΣH = 193.906				
P_p		19.187		0.600		11.512
T_b		50.000		2.800		140.000
Σ	ΣV = 311.039				990.206	597.107

Table 7. External forces during earthquake conditions

| Forces | V (ton) | H (ton) | Moment Arm | | Mx = V . x | My = H . y |
			X (m)	Y (m)	Retaining Moment (tm)	Overtuning Moment (tm)
R_v	859.623		2.500		2149.058	
W_c	194.025		2.549		494.476	
W_{td}	2.959		0.600		1.776	
W_{tb}	114.055		4.331		493.955	
R_{rt}		1.000		5.450		5.450
G_g		10.568		7.000		73.973
P_{a1}		84.979		3.196		271.554
P_{a2}		108.927		1.598		174.042
E_1		57.109		5.146		293.882
E_2		13.582		1.715		23.297
		ΣH = 276.164				
P_p		19.187		0.600		11.512
T_b		50.000		2.800		140.000
	ΣV = 1170.662				3139.264	993.709

(b) Calculation of coefficient of passive earth pressure

$$Kp = tg^2\left(45° - \frac{\phi}{2}\right)$$
$$= tg^2\left(45° - \frac{19.60°}{2}\right)$$
$$= 1.332 \tag{23}$$

(c) Calculation of active earth pressure

$$Pa_1 = k_a \times q \times h_1 \times b$$
$$= 0.751 \times 2.2 \times 5.146 \times 10$$
$$= 84.98 \; ton \tag{24}$$

$$Pa_2 = \frac{1}{2} \times k_a \times \gamma \times \left(h_1\right)^2 \times b$$
$$= \frac{1}{2} \times 0.751 \times 1.1 \times 26.4814 \times 10$$
$$= 108.93 \; ton \tag{25}$$

(d) Calculation of passive earth pressure

$$Pp = \frac{1}{2} \times k_p \times \gamma \times \left(h_2\right)^2 \times b$$
$$= \frac{1}{2} \times 1.332 \times 1.1 \times 1.44 \times 10$$
$$= 19.19 \; ton \tag{26}$$

(e) Calculation of abutment stability
- When normal conditions
  Based on the calculation results of the reaction on the building under the bridge obtained external forces when normal conditions in Table 5.
  a) Stability to the foundation sliding

$$\sum V = vertical\ forces$$
$$= 1170.662\ ton \qquad (27)$$

$$\sum H = horizontal\ forces$$
$$= 205.473\ ton \qquad (28)$$

$$SF = \frac{\sum V \times \tan\frac{2}{3} \times \phi° + c \times B}{\sum H}$$
$$= \frac{1170.662 \times 0.012 \times 19.60° + 13.430 \times 10.000}{205.473}$$
$$= 1.907 \geq 1 \rightarrow OK \qquad (29)$$

b) Stability of the foundation overturning

$$\sum Mx = retaining\ moment$$
$$= 3139.264\ ton \qquad (30)$$

$$\sum My = overturning\ moment$$
$$= 675.530\ ton \qquad (31)$$

$$SF = \frac{\sum Mx}{\sum My} = \frac{3139.264}{676.530}$$
$$= 4.640 \geq 1 \rightarrow OK \qquad (32)$$

- When the upper structure load is not working
  Based on the calculation results of the reaction on the building under the bridge, the obtained external forces when the upper structure load is not working in Table 6.
  a) Stability to the foundation sliding

$$\sum V = vertical\ forces$$
$$= 311.039\ ton \qquad (33)$$

$$\sum H = horizontal\ forces$$
$$= 193.906\ ton \qquad (34)$$

$$SF = \frac{\sum V \times \tan\frac{2}{3} \times \phi° + c \times B}{\sum H}$$
$$= \frac{311.039 \times 0.012 \times 19.60° + 13.430 \times 10.000}{193.906}$$
$$= 1.045 \geq 1 \rightarrow OK \qquad (35)$$

b) Stability of the foundation overturning

$$\sum Mx = retaining\ moment$$
$$= 990.206\ ton \qquad (36)$$

$$\sum My = overturning\ moment$$
$$= 597.107\ ton \qquad (37)$$

$$SF = \frac{\sum Mx}{\sum My} = \frac{990.206}{597.107}$$
$$= 1.658 \geq 1 \rightarrow OK \qquad (38)$$

- During earthquake conditions
  Based on the calculation results of the reaction on the building under the bridge obtained external forces during earthquake conditions in Table 7.
  a) Stability to the foundation sliding

$$\sum V = vertical\ forces$$
$$= 1170.662\ ton \qquad (39)$$

$$\sum H = horizontal\ forces$$
$$= 276.164\ ton \qquad (40)$$

$$SF = \frac{\sum V \times \tan\frac{2}{3} \times \phi° + c \times B}{\sum H}$$
$$= \frac{1170.662 \times 0.012 \times 19.60° + 13.430 \times 10.000}{276.164}$$
$$= 1.419 \geq 1 \rightarrow OK \qquad (41)$$

From the results of the analysis carried out above, dimensions of the planned abutment can withstand the loads that work, both loads that work from within such as the weight of the bridge structure, earth pressure from the side and loads that work from outside such as vehicle loads, wind loads and earthquake loads.

5. Conclusion

Based on data analysis that has been implemented, the following conclusions can be drawn:
1. From the results of the calculation of the stability of the abutments to sliding failure, when the abutments are in normal conditions was obtained safety factor (SF) values 1.91, in condition of the the upper structure load is not working was obtained safety factor (SF) values 1.05 and during earthquake conditions was obtained safety factor (SF) values 1.42. Because obtained safety factor (SF) values greater than 1, so that the stability of the abutment is safe against sliding failure.
2. From the results of the calculation of the stability of the abutments to overturning failure, when the abutments are in normal conditions was obtained safety factor (SF)

values 4.64, in condition of the the upper structure load is not working was obtained safety factor (SF) values 1.66 and during earthquake conditions was obtained safety factor (SF) values 3.16. Because obtained safety factor (SF) values greater than 1, so that the stability of the abutment is safe against overturning failure.

Acknowledgment

References

[1] Anonim, (1996), *"Bridge Management System"*, Publishers : Public Works Foundation, Jakarta.

[2] Anonim, (1987), *"Planning Guidelines for Loading Street Bridges"*, Publishers : Public Works Foundation, Jakarta. [in Bahasa]

[3] Anonim, (2015), *"General Guidelines for Bridge Planning"*, Publishers : Public Works Ministry, Jakarta. [in Bahasa]

[4] Bowles, J.E., (1996), *Foundation Anaysis and Design*, McGraw-Hill, New York

[5] Hartanto, Tri. Kurniawan, Achendri M., (2018), *"Calculation of Structure and Volume of Concrete Bridge Abutment Buildings (Case Study of Reinforced Concrete Bridges in Jolosutro Blitar Village)"*, Jurnal *Qua Teknika*, 8 (1) : 1-10. Fakultas Teknik Universitas Islam Blitar, Blitar. [in Bahasa]

[6] Hidayat, Gawit, (2011), *"Study Abutment Damage Bridge Analysis Study in Bahalang River, Central Kalimantan"*, Jurnal Teknologi Berkelanjutan, Vol. 1 Ed. 1, pp : 9-17. [in Bahasa]

[7] Lapis, J. O. Balamba, S. Sompie, O. B. A. Sarajar, Alva N., (2013), *"Bridge Foundation Stability Analysis (Case Study: Essang-Lalue Bridge)"*, Jurnal Sipil Statik Vol. 1 No. 11, Fakultas Teknik, Jurusan Teknik Sipil, Universitas Sam Ratulangi Manado. [in Bahasa]

[8] Manu, Agus Iqbal, (1995), *"Fundamentals of Planning a Reinforced Concrete Bridge"*, Publishers : Public Works Foundation, Jakarta. [in Bahasa]

The Corrosion Erosion of Ship Propeller Al 7075 Produced by Gravity Sand Casting

Milka Rante[a,b,*], Muhammad Syahid[c], Onny Sutresman[d]

[a]Department of Mechanical Engineering, Engineering Faculty, Universitas Kristen Indonesia Toraja. Email: milka_rante@yahoo.com
[b]Foundry Laboratory, Mechanical Engineering, Engineering Faculty, Universitas Hasanuddin.
[c]Foundry Laboratory, Mechanical Engineering, Engineering Faculty, Universitas Hasanuddin.
[d]Foundry Laboratory, Mechanical Engineering, Engineering Faculty, Universitas Hasanuddin.

Abstract

Propeller is one of the important components of ships and boats that function as motor or boat propulsion. The mechanical properties required in propeller material are high toughness, easy to cast, and good engine capability, as well as good resistance to corrosion and erosion. One of the aluminum alloys that have been widely used in major vessels in propeller systems is the Nickel-aluminum-bronze (NAB) alloy because it has an excellent combination of mechanical properties and corrosion-erosion resistance. Another type of aluminum alloy that is widely used as a machining component is the Al 7075 T651 because it has the highest strength among other aluminum alloys. The mechanical properties of the Al 7075 T651 are directly proportional to the erosion resistance of the propeller which agrees with the pot tester porridge. The higher the value of the erosion propeller failure that occurs also increases with increasing testing rotational speed. For corrosion, a propeller with air testing media at a speed of 1000 rpm which results in significant corrosion products.

Keywords: Al 7075 T651; corrosion erosion; slurry pot tester

1. Introduction

Propeller is one of the important components of ships and boats that function as a motorboat or boat propulsion. For vehicles operating at sea, the main criteria for material selection depend on strength, stiffness, heavy thermal expansion and corrosion resistance to seawater. The material used to make a propeller depends on the strength, ease of manufacture, production methods, environment, weight, and others. Also, the material used for the propellers must be lightweight, strong and resilient, easily installed and resistant to erosion and corrosion.

Materials that are widely used as propeller materials are brass (brass) or aluminum alloy (aluminum alloy), both of these materials are widely used because they are easily cast and relatively resistant to corrosion [1]. One of the aluminum alloys that are widely used in ships, especially in propeller systems, is the Nickel-aluminum-bronze (NAB) alloy because it has an excellent combination of mechanical properties and corrosion-erosion resistance [2]. Another aluminum alloy that is starting to be used is Al 7075. Al 7075 is an aluminum alloy with Al-Zn-Mg-Cu as its main element [3] because it has good mechanical properties such as high

strength comparable to steel [4]. Comprehensively, Al 7075 has interesting properties such as high strength, toughness, ductility and good fatigue resistance [5].

As a driving component of the ship, the ship's propeller rotates at high speed and experiences corrosion erosion due to the accumulation of rotational speed and particles present in the water which ultimately results in cavitation Corrosion is a phenomenon of material quality degradation or material degradation [6] that will not stop. Corrosion is caused by the influence of the surrounding environment. In addition to chemical reactions, the corrosion process by electrochemical processes involves the transfer of electrons from the reduction of metal ions and the deposition of metals from the surrounding environment (air, acid, dew, seawater, lake water, and river water) [7].

In his research [8] said that in addition to the influence of turbulence of flow, salinity in seawater has a very big influence on the rate of corrosion of the propeller. The greater the salinity the greater the rate of corrosion that occurs. In addition to salinity, the rotation speed is also very influential on the corrosion rate. The greater the rotational speed the greater the corrosion rate. This is influenced by solids dissolved in seawater that experience friction with the sample surface so that it can erode the surface of the sample.

*Corresponding author. Tel: +62 813-4226-6124
Jl. Nusantara No.12 Makale , Kabupaten Tana Toraja 91811

Another thing that also affects the rate of corrosion is the temperature of seawater.

It can be concluded that Al 7075 alloy has good mechanical strength to be applied as a propeller material. Although not yet known how its resistance to erosion-corrosion. Davis [9] in his book states that giving a slightly higher temper treatment can provide a better combination of strength, corrosion resistance, and fracture resistance. In this study, the aluminum alloy used was Al 7075 T651 in Table 1.

2. Research Materials and Methods

The material used in this study is aluminum Al 7075 T651 in the form of plates. The test specimen was made in the form of a propeller with 3 leaves with detailed dimensions as shown in Fig. 1(a). Propeller is made by casting using sand molds according to the design shown in Fig. 1(b). Leaking using the upper channel or direct channel, as shown in Fig. 1(c). The propeller that has been cast finished using sandpaper with the same grade to remove uneven parts on the surface of the propeller.
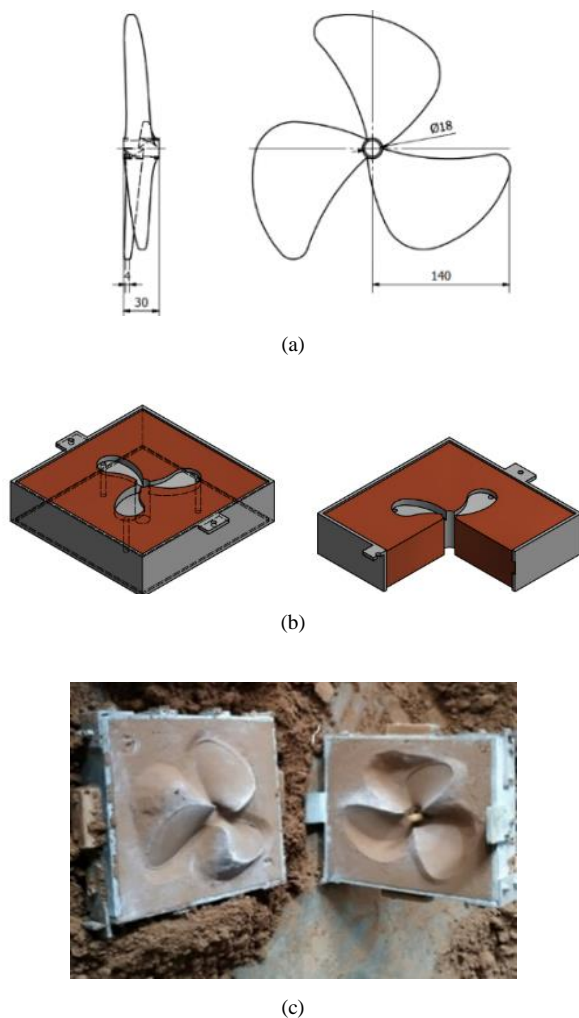
Table 1. Composition of Al 7075 plate

Al %	Zn %	Mg%	Cu%	Cr%	Fe%	Si%
89.72	5.57	2.39	1.67	0.28	0.25	0.13

Grades: AA-7075 (0.00), AA-7050 (0.22)

After the propeller is finished, initial characterization is done by weighing and mechanical testing using Portable Hardness Test. Hardness testing is carried out on the Tip and Propeller Hub sections. After initial mechanical testing and weighing, erosion-corrosion testing is then carried out. Erosion corrosion testing is done by using the pot tester method. Fig. 2(a) is a design pot tester. Pot tester container is made of 2 80 litre plastic containers. The mechanical system uses 2 types of electric motors so that 2 variations of rotational speed, 1000 and 700 rpm are obtained in each container. The transmission system uses a pulley that is connected to 2 shafts with a tilt of 150 where the propeller will be installed. Propeller position as shown in Fig. 2(b). To the test water, 3% of silica sand is added from the total volume of the test water. The size of the silica sand used is 354 μm. Tests using seawater and river water with a 16-hour long test for each propeller.
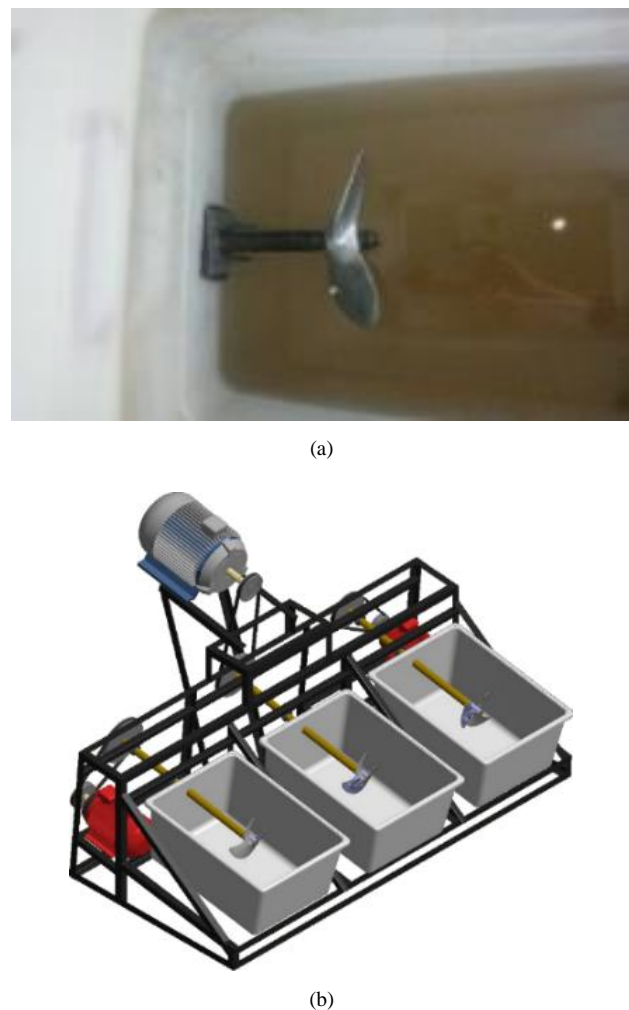

(a)

(b)

(c)

Figure 1. (a) Design propeller, (b) Sand mold design, (c) Ready-made sand mold

(a)

(b)

Figure 2. (a) Design pot tester, (b) Propeller position in pot tester

173

3. Data Analysis and Discussion

3.1. Foundry propeller

The casting propeller as shown in Fig. 3 is then observed for its microstructure. From the microstructure observation shown in Figs. 4(a) and (b), there is no visible porosity in the casting product. The α-Al phase appears as the main phase with a little MgZn2 on the grain line. The size of the grains on the hub and left propeller tend to have the same size and density.
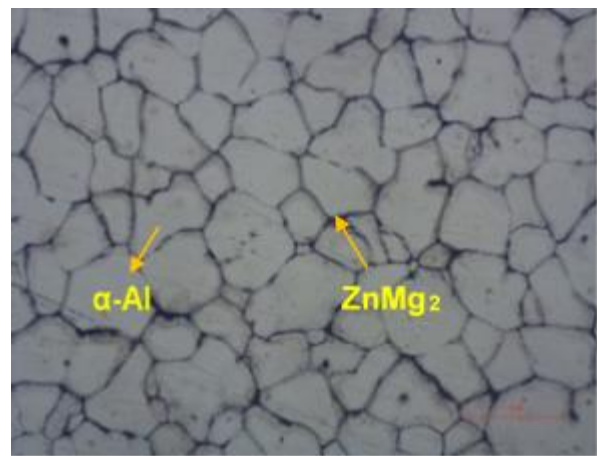
3.2. Hardness test

The hardness test results in Fig. 5 show the hardness value at the hub is higher with a hardness value of 270.8 HL, while the tip part of the hardness value is 255.8 HL. This hardness value is related to the results of the microstructure where the results of the microstructure observation show that the grain size of the tip part of Fig. 4(a) and hub in Fig. 4(b) of propeller has a size that is not much different. It also appears that the tip of the grain spacing is denser than the grain spacing of the tip.
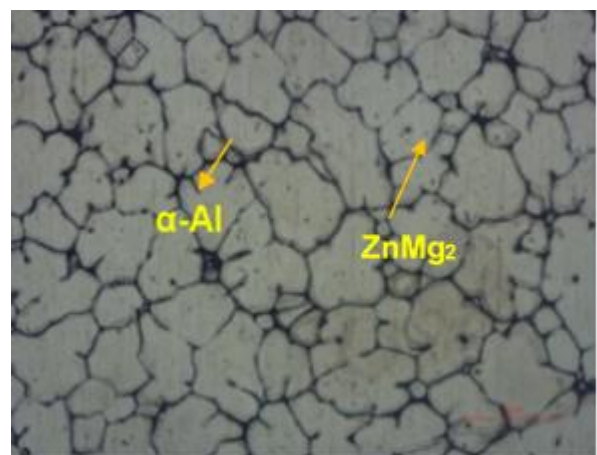
3.3. Weight Loss

Measurement of weight loss is done before and after testing with a pot tester. Figure 6 shows a graph of the percentage of propeller weight loss that has been tested with a pot tester in seawater testing media. In general, the greater the weight loss with increasing the rotational speed of the pot tester. The greatest weight loss occurs at a speed of 1000 rpm with seawater testing media with 0.28 grams of weight loss. Likewise, propellers tested with river water media lost the greatest weight at a rotational speed of 1000 rpm with 0.13 grams of weight loss.

(a)

(b)

Figure 4. Casting tip propeller micro structure (a) Hub, (b) Tip
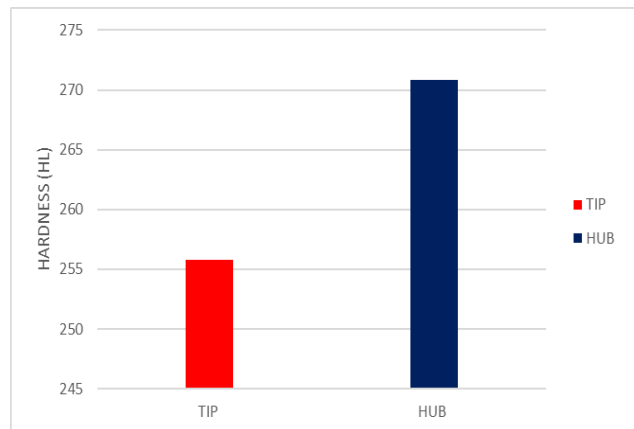

Figure 3. Foundry propeller
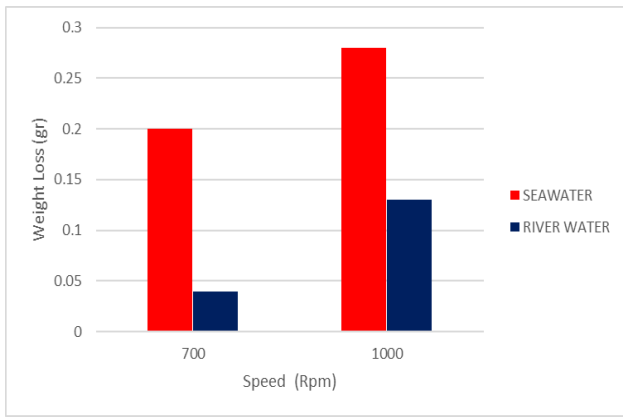

Figure 5. Hardness tip and hub propeller values

Figure 6. Graph of the effect of speed on propeller weight loss

The greatest weight loss at a speed of 1000 rpm is an indication of erosion-corrosion which is the accumulation of velocity of fluids and solid particles that damage the metal surface and the protective film layer. The erosion-corrosion mechanism starts with the attack of air bubbles that attach to the surface of the metal protective layer because the turbulent flow that passes through the metal surface then the air bubbles erode and damage the protective layer which will further accelerate the corrosion rate.
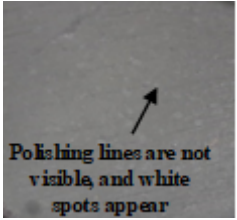
Table 2. Macro photo tip propeller

Speed (Rpm)	Tip Sea Water	Tip River Water
0	Polishing lines are still visible	Polishing lines are still visible
700	Polishing lines are not visible, and white spots appear	Polishing lines are not visible, and white spots appear
1000	Polishing lines are not visible, and white spots appear	Polishing lines are not visible, and white spots appear
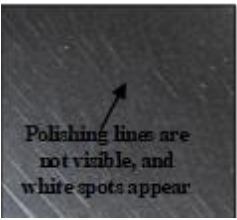
Table 3. Macro photo hub propeller

Speed (Rpm)	Tip Sea Water	Tip River Water
0	There are no white spots yet	There are no white spots yet
700	White spots as the initiation of corrosion	White spots as the initiation of corrosion
1000	White spots as the initiation of corrosion	A color change has occurred

Table 4. Microscope optic tip propeller

Speed (Rpm)	Tip Sea Water	Tip River Water
0	Polishing line	Polishing line
700	Damage due to fluid and sand friction	The polishing lines are no longer visible
1000	Damage due to fluid and sand friction	The polishing lines are no longer visible

175
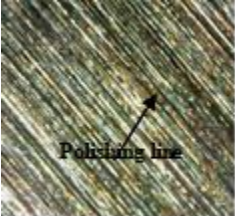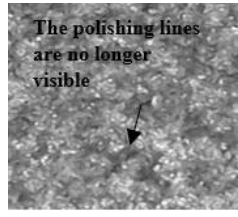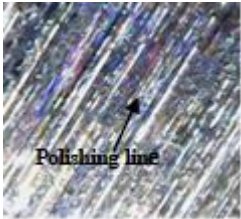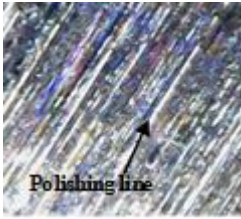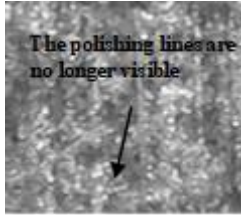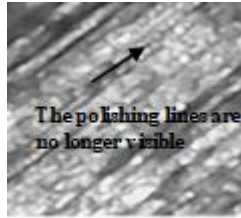
Table 5. Microscope optic hub propeller

Speed (Rpm)	Tip Sea Water	Tip River Water
0	Polishing line	Polishing line
700	Damage due to fluid and sand friction	The polishing lines are no longer visible
1000	Damage due to fluid and sand friction	The polishing lines are no longer visible

3.4. Segmentation design

From the results of the surface roughness test, it can be seen the difference in the surface of the propeller before and after the test which is also compared with the weight reduction of the propeller. The surface roughness value has decreased significantly after testing, especially at the tip of the propeller. In this study, the roughness value has decreased rather than increased due to the friction of the fluid and the particles in the water working like sandpaper on the surface of the propeller so that the surface of the propeller becomes smoother.

	SEA WATER	RIVER WATER
HUB BEFORE TESTING	10.874	10.874
TIP BEFORE TESTING	8.518	8.518
HUB AFTER TESTING	2.484	2.388
TIP AFTER TESTING	2.385	1.754
WEIGHT LOSS	0.28	0.13

Figure 7. The relationship between surface roughness and propeller weight loss

The comparison is shown in Fig. 7. The greater the decrease in surface roughness value, the greater the decrease in the weight of the propeller. Changes in the surface roughness of the blades can be seen in macro photography and optical microscopy which were carried out before and after testing with a pot tester.

3.5. Macro Photo and Microscope Optic

With macro photos, it can be seen visual differences on the surface of the propeller. The surface of the propeller tested in seawater corrosion products is seen more clearly, both on the tip and the hub. At 1000 rpm, white spots that are indicated as corrosion initiation are followed by significant color changes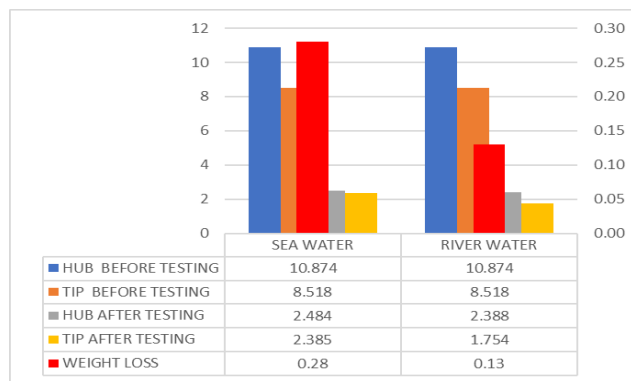 from bright colors to dull colors. White spots and color changes appear more on the propeller hub of Table 3 when compared to the tip of in Table 4, colors change and fewer white spots. Turbulence flow has a significant impact because where in turbulent flow, air bubbles will be more pressurized so that attacks in the form of collisions and friction become stronger attacking metal surfaces due to mechanical wear that causes corrosion.

Another thing that affects is surface roughness. Huda and Aristianto [10] said that rough surfaces are the most susceptible to corrosion because on these surfaces bubbles form faster. These bubbles themselves are the effect of reducing the hydrodynamic pressure in certain parts as a fluid effect that attacks the surface of the propeller. From surface roughness testing, the hub of the propeller is rougher than the end of the propeller. At the end of Table 5 the difference in the surface of the propeller before and after being tested. The blades that have not been tested are still clearly visible traces of polishing lines from sandpaper that can be seen clearly on an optical microscope in Table 5 and Fig. 7. The higher the round polishing line the more invisible. This also shows that erosion has occurred on the surface of the blades due to fluid and sand friction.

In addition to macro photos, optical microscopy was also carried out to see more clearly the erosion-corrosion that occurs in the propeller. The optical microscope results in Table 5 and Fig. 7 show the erosion and corrosion that occurs on the surface of the propeller. This is indicated by the holes that occur on the surface of the propeller. The propeller with seawater testing media suffered the most damage compared to the propeller tested with river water media. In the Hub and tip propeller tested with seawater media, the hole is seen caused by friction from the fluid and sand. The formed hole is then filled with silica sand. As for the hub section, it was tested with river water testing media, no holes were seen as a result of fluid and sand friction. The most severe damage occurred in the propellers tested at 1000 rpm on the hub and tip. Damage to the propeller with Al 7075 T651 material is identified as hole corrosion, crevice corrosion, and peeling.

This is by Sasono et al. [11] which states that Al 7075 T6 tends to be susceptible to local corrosion, such as pitting, intergranular corrosion, or peeling skin. In the results of the study in [12], the corrosion that occurred on Al 7075 T651 has a relationship with the Cu-rich intergranular phase, which increases local corrosion susceptibility. In testing

176

using river water testing media, no significant changes were seen on the surface of the propeller. Although pitting occurs quite clearly on propellers with Al 7075 T651 material, it is not followed by peeling as happened in seawater testing.

4. Conclusion

From the results of this study, several conclusions are drawn as follows:
1. The higher the rotational speed of the propeller, the greater the weight reduction of the propeller.
2. The smaller the surface roughness value, the greater the weight loss due to fluid friction and silica sand on the surface of the propeller.
3. The propeller with seawater testing media with 1000 rpm rotation experiences the most severe erosion-corrosion.

References

[1] S. Siproni, M. Rasid, D. Seprianto, dan Y. Yahya, "Effect of Casting Process on Mechanical Properties of Motor Boat Propellers," *Austenit*, vol. 10, no. 1, 2018. [in Bahasa].

[2] Z. Wu, Y. F. Cheng, L. Liu, W. Lv, dan W. Hu, "Effect of heat treatment on microstructure evolution and erosion-corrosion behavior of a nickel–aluminum bronze alloy in chloride solution," *Corrosion Science*, vol. 98, pp. 260–270, 2015.

[3] A. Naimi, H. Yousfi, dan M. Trari, "Microstructure and corrosion resistance of molybdenum and aluminum coatings thermally sprayed on 7075-T6 aluminum alloy," *Protection of Metals and Physical Chemistry of Surfaces*, vol. 48, no. 5, pp. 557–562, 2012.

[4] Y. Liu, J. Mol, dan G. Janssen, "Combined corrosion and wear of aluminum alloy 7075-T6," *Journal of Bio-and Tribo-Corrosion*, vol. 2, no. 2, pp. 9, 2016.

[5] A. D. Isadare, B. Aremo, M. O. Adeoye, O. J. Olawale, dan M. D. Shittu, "Effect of heat treatment on some mechanical properties of 7075 aluminum alloy," *Materials Research*, vol. 16, no. 1, pp. 190–194, 2013.

[6] M. G. Fontana, *Corrosion engineering*. Tata McGraw-Hill Education, 2005.

[7] K. R. Trethewey dan J. Chamberlain, "corrosion for students and Engineering," *Jakarta: Gramedia*, 1991. [in Bahasa].

[8] D. H. Sutjahjo dan others, "Time and Salinity of Sea Water Against Corrosion Rate of Bronze Metal (Bronze) As Ship Propeller," *Jurnal Teknik Mesin*, vol. 5, no. 02, 2017. [in Bahasa]

[9] J. R. Davis, "Aluminum and aluminum alloys," 2013.

[10] S. Huda dan A. Aristianto, "Effect of Artificial Aging on Corrosion Rate of Aluminum Motor Boat Propellers," *Teknologi*, vol. 4, 2011. [in Bahasa]

[11] E. J. Sasono, E. Canepa, R. Stifanese, L. Merotto, dan P. Traverso, "Corrosion behavior of aluminum alloys in deep-sea environment: A review and the KM3NeT test results," *Marine Structures*, vol. 59, no. 2, pp. 271–284, 20092018.

[12] E. Canepa, R. Stifanese, L. Merotto, dan P. Traverso, "Corrosion behavior of aluminum alloys in deep-sea environment: A review and the KM3NeT test results," *Marine Structures*, vol. 59, pp. 271–284, 2018.

Study on Transverse Strength of the Deck-Container Ships Due to Laying All Containers on Deck

Rosmani[a], Andi Ardianti[b]*, Ganding Sitepu[c], Hamzah[d], Andi Mursyid Nugraha[e], Muhammad Ichsan Hayatuddin[f]

[a]Department of Naval Architecture, Engineering Faculty, Hasanuddin University. Email: rosmanimunandar@ymail.com
[b]Department of Naval Architecture, Engineering Faculty, Hasanuddin University. Email: aardianti@gmail.com
[c]Department of Naval Architecture, Engineering Faculty, Hasanuddin University. Email: sitepu.unhas@gmail.com
[d]Department of Naval Architecture, Engineering Faculty, Hasanuddin University. Email: anca_naval99@yahoo.com
[e]Department of Naval Architecture, Engineering Faculty, Hasanuddin University. Email: andi.mursid08@gmail.com
[f]Department of Naval Architecture, Engineering Faculty, Hasanuddin University. Email: ichsan.hayat13@gmail.com

Abstract

The strength of transversal structure of the ship has a great effect on the safety of the ship. Ships will experience conditions that affect the strength of the ship's structure. Deck-Container ships are the ships that all containers are loaded on deck such as MV. Khendaga Nusantara series ships. The transversal strength of the ships is loaded mainly by the weight of cargo laying on the deck. This research aims to determine the transverse strength of a deck-container ship due to all container loads on deck. The research was done by using finite element method through modeling transverse ship structure, the simulation is conducted by varying the amount and layout of containers on deck. The loads applied to the model are side loads, bottom loads, and deck loads according to BKI rules. The results show that the stress that occurred in the web frame was 140.63 N/mm^2 due to the placement of the entire container on the deck (full loading). For ship structure response, a deformation of 2.86 mm occurred in the web frame area at maximum loading. Stress ratio that occurs in all ship's structures does not exceed 1 in other words the working stress does not exceed the allowed stress according to BKI rules.

Keywords: Container deck; FEM; stress; transversal strength

1. Introduction

Nowadays, transportation by using ships has become an important aspect in the field of transportation. There is an increasing need for transportation of logistics goods to natural resources in various places, especially in the island's areas. Sea transportation is considered the most efficient because it can carry large amounts of cargo and is also the most economical because of the lower costs than other modes of transportation.

In carrying out its operational activities, the ship will experience various conditions that can affect the strength of the ship's structure, whether it is caused by weather, sea waves, or internal factors such as the weight of the ship itself, load weight, or load shifting. As for the loads that work on the ship include load on deck, load on ship side, and load on ship bottom. The strength of construction is one of the technical aspects that plays a very important role in fulfilling the safety of ships when sailing. A ship is eligible for the technical factors if the maximum stress that occurs in

the ship's structure during critical conditions is still smaller than the maximum stress of the material used as a component of the construction of the ship.

Ships with large loads, such as containers, will receive heavy loading on the deck structure due to the weight of the cargo, so it is very important to analyze the transverse strength of the deck structure. KM. KHENDAGA NUSANTARA 11 is a type of container ship that only loads containers on the deck and the space under the deck of the ship is left empty. Laying this load will automatically affect the strength of the ship construction, primarily on the transverse strength of the ship. So as to find out whether the ship construction still meets the requirements and to anticipate the failure of the ship structure due to the load laying system on the ship, this study was conducted to analyze the transverse strength of the ship due to laying containers only on the deck of the ship.

*Corresponding author. Tel.: +62 812 8785620
Jalan Poros Malino km. 6 Bontomarannu
Gowa, Sulawesi Selatan, Indonesia, 92171

2. Literature Review

2.1. Container ships

Container ships are cargo ships that are designed to transport cargo in containers [1]. The engine room and accommodation room are usually located at the rear so that the maximum length of the hull can be used for container storage. To avoid the container that is on the deck moving or falling into the sea during shipping, the container is bound to the ship.

Containers are reusable boxes made of steel or aluminum. Containers made in various types and sizes. Normal dimensions include lengths of 20, 40 and 45 feet, a width of 8 feet, and height of 8.5 or 9.5 feet. The internal volume and weight of goods that are usually carried vary according to the material [2].

In practical applications, container loads are usually assumed to consist of three loads namely the static weight of the container in perpendicular conditions, the addition of static loads due to rolling and pitching of the ship, and the inertia due to ship acceleration.

2.2. The ships transverse construction

The transverse construction components of the ship include deck beams, frames, Wrang (floor) and others. The transverse construction of the ship consists of frames as a place to attach the skin of the ship and it is reinforced with side strings. Installation of this transverse construction, the frame is formed rotating and covered with plates and supported by side stringer that installed horizontally.

2.3. The ships transverse strength

The transverse strength of the ship is the ability of the transverse structure of the ship to maintain the cross-sectional shape against interference with loads acting on the ship such as loads on the deck, loads on the sides, and loads on the bottom. So it is clear that the main components of the ship's structure are the bottom structure, the side structure, and the deck structure [1].

Loads that may influence of local structure and must be taken into account in the design of the transverse construction of the ship consists of two parts, namely: buoyancy, and gravity. The upward pressure is resultant from the distribution of hydrostatic pressure in the outer plane of the dipped ship hull. Gravity is the largest downward force on ships and its contents [3]. As a result of these loads, all parts of ship construction experience some type of stress. There are several factors that cause the actual or different stress distribution to occur from the ideal stress distribution. Because of the transverse shear stress, distortion occurs based on the length of the cross-section of the hull girder [4]. In this research, the vertical strength of the ships was calculated according to BKI Rules Vol. II [5].

2.4. Stress and Strain

Stress is defined as the amount of force acting per unit area. Mathematically formulated as Eq. 1 as follows:

$$\sigma = \frac{F}{A} \qquad (1)$$

Where, σ is stress (N/mm²), F is force or load (N) and A is face area (mm²). There are two types of stress: normal stress and shear stress. Normal stress (σ) is normal force or axial force per unit area [6].

Strain is expressed as the increase of length per unit length. Strain can be written as Eq. 2 as follows :

$$\varepsilon = \frac{\Delta L}{L} \qquad (2)$$

Where, ε is strain (N/mm²), ΔL is the total of length increase (mm) and L is initial length (mm). Hooke's law states that within certain limits, the stress on the material is directly proportional to the strain.

Stress is static amounts; it is a measure for pressure on structural materials. On the other hand, strains are kinematic amounts; it measures structural deformation. However, deformation depends on the load acting on the structure. Therefore, stress and strain are not independent. The physical relationship that links this number is called constitutive law. This describes the behavior of structures material under load. It depends on the material and can only be obtained with the help of experiments [7].

One of the most important experiments to find the relationship between stress and strain is the tension or compression test. Here, small specimens of material are placed into the test machine and are elongated or shortened. The force F applied by the machine to the specimen can be read at the engine speed; That causes normal stress $\sigma = F / A$. The change of Δl from the length of the specimen can be obtained and strain can be measured by using $\varepsilon = \Delta l / l$.
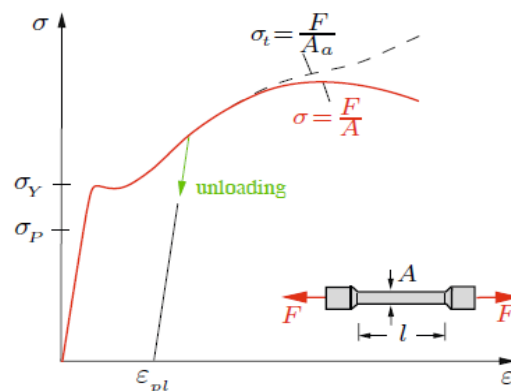

Figure 1. Stress-Strain curve [7]

The graph of the relationship between stress and strain is shown schematically (not scaled) for the steel specimen in Fig. 1. This graph is called a stress-strain diagram. The graph shows that for small values of strain, the relationship is linear (straight line) and the stress is proportional to the strain. This behavior applies until the stress reaches the proportional limit σ_P. If the stress exceeds the proportional limit, the strain begins to increase faster and the slope of the curve decreases. This continues until the stress reaches the yield stress σ_Y. From this point, the stress-strain diagram shows that strain increases at constant stress. Note that many materials do not show clear results points. At the end of the slope, the curve increases again which indicates that the material can maintain an additional load. This phenomenon is called strain hardening.

2.5. Permissible stress

Permissible stress is the stress that causes a construction to experience a large deflection. The deflection is the limit of construction that still safe to overcoming the load that occurring or working on it.

The stress acting on the structure can be evaluated by using the value of the permissible stress issued by the classification bureau which is 150/k [N/mm^2]. If the working stress that occurs in the conditions of loading, the vertical bending moment exceeds the permissible stress, the structure or object of the research is in an unsafe condition and if the working stress value is less than the value of the permissible stress, the structure is in a safe condition or meets the rule's standards.

Based on BKI rules, the normal strength of the steel hull structure is that the hull steel structure has a yield point of REH = 235 N/m^2 and tensile strength Rm = 400 - 520 N/m^2.

2.6. Finite Element Method

Finite Element Method is a numerical method used to solve technical and mathematical problems of a physical phenomenon. The types of physical and mathematical problems that can be solved by finite element methods are structural and non-structural analysis. The type of structural analysis problem includes stress analysis, buckling and vibration analysis. The type of non-structures analysis includes heat and mass transfer, fluid mechanics, and the potential distribution of electricity and magneticity [8].

By using the Finite Element method, all the complexity of the problem, such as various forms, boundary conditions and loads are maintained but the solutions obtained are estimates. This is because of its diversity and flexibility as an analytical tool. Quick improvements in computer hardware technology and reduced computer costs have driven this method because computers are a basic need for the application of this method. A number of popular brand element analysis packages are now commercially available to simplify a complex structure analysis [9]. Some popular packages for FEM are STAAD-PRO, GT-STRUDEL, NASTRAN, NISA, and ANSYS.
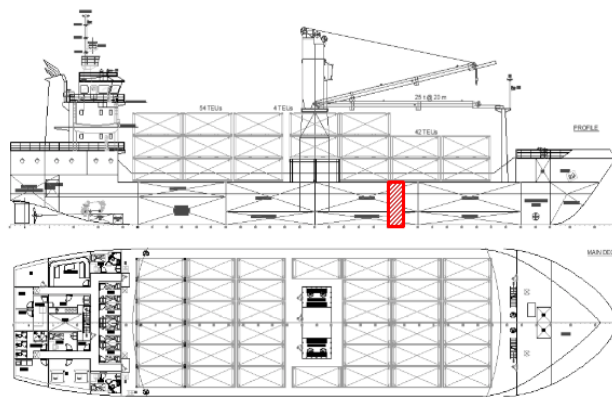

Figure 2. General arrangement

3. Research Methodology

3.1. Models data

The object in this study is the transverse construction of container ships of KM Khendaga Nusantara 11 with data as follows:

Type of Ship	: Container
LOA	: 74.05 m
LBP	: 69.22 m
B	: 17.2 m
H	: 4.9 m
T	: 3.7 m
DWT	: 3327 Ton

The ship loads containers only on decks with a capacity of 100 units and weighs 24 tonnes per unit. For more details, they can be seen in Fig. 2.

Figure 2 show general arrangement of ships. It can be seen that this ship has a unique construction that is loading all container only on the deck and below the deck consists of void tanks. The shaded part in the Fig. 2 is the ships part that will be modeled in this study. From the general arrangement, it can be seen that in frames 40 - 41, the distance of the frame is one of the most critical parts because this section holds the weight of three stack containers or 15 container units.

The planning of container loading at KM. Khendaga Nusantara 11 is based on the container stowage plan or Bayplan principle as shown in Figure 3.
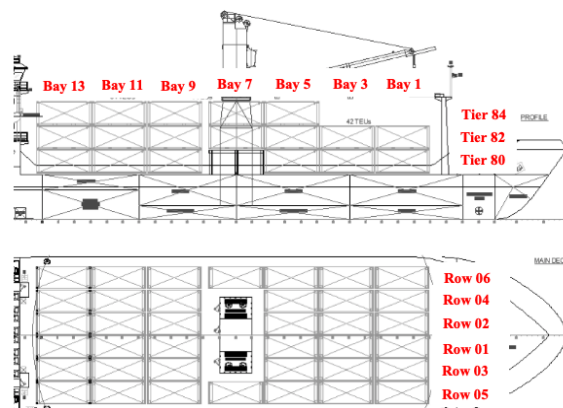

Figure 3. Container loading plan (bayplan)

3.2. Structure modeling

The aim of this study is to analyze the transverse strength of the ship, so in modeling the transverse structure of the ship is strived to be the same as the actual conditions such as the midship construction as shown in Fig. 4. The shape and arrangement of the transverse construction framework are analyzed based on the form of the installed construction, namely:

a. The structure being modeled starts from frames 40 to 41, where the distance between frames is 1800 mm and the width of frames is 17200 mm.

b. The type of construction used is longitudinal construction so that the number of modeled frames are 4 web frame, 4 longitudinal deck girder, 24 longitudinal deck beam, 10 side longitudinals, 22 longitudinal bottom, and 8 pillars, where the distance between frames is 600 mm.

c. The ship structure component that is modeled is a component that has an important role in the elongated strength of the ship.

d. This model uses the x, y, and z axes. The positive x-axis shows the width of the model from the left side of the hull to the right side of the hull, the positive y-axis shows the height of the ship from the baseline to the deck of the ship, and the z-axis shows the length of the ship from frame number 40 to number 41.

e. The type of element used is the shell element type 281. The type was chosen because it is more suitable for modeling plates and has six degrees of freedom for each node. In addition, this type allows analysis of three-dimensional stresses that occur on the x, y, and z axes.

f. Mounting the pedestal on the model is done at the neutral axis of the transverse construction of the ship. Restraints given at that point are restraints on translational x, translation y, translation z, rotation x, rotation y, and rotation z.

The ship construction framework is then modeled in 3D, the results of the modeling can be seen in Figure 5. In the model, the geometry is measured by matching all the coordinates that have been made in accordance with the actual geometry.
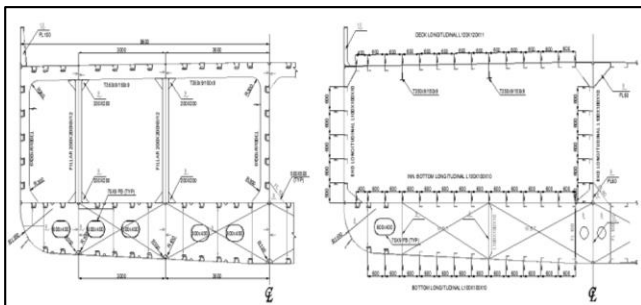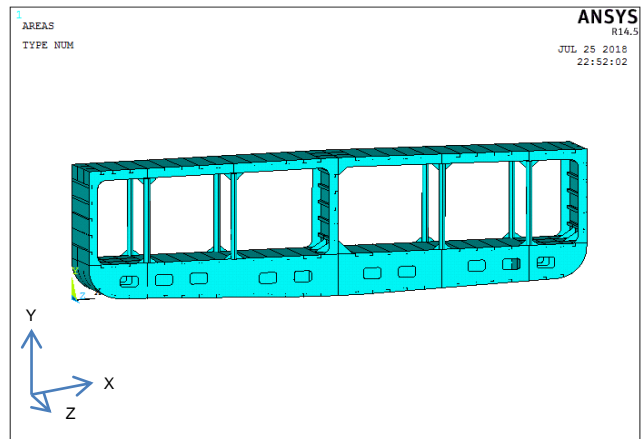

Figure 4. Midship construction

Figure 5. Numerical model

3.3. Load distribution

Calculation of the load distribution is conducted to divide the magnitude of the force with respect to the points (nodes) of the load on the deck, the bottom, and the sides of the ship. In this research, the input load is the side load where the center is located below or above the surface of the water where the wave direction is transverse to the ship's speed, the ship's bottom load, the weather deck load and the load of loads. Load input is done by changing the unit load from kN/m^2 to the unit N/mm^2 then inputted on the deck plate, side plate and bottom plate. These loads are pressure area loads and each direction is opposite. Load inputting for more details can be seen in Fig. 6.

The load used to the model is in accordance with the information obtained from the ships general arrangement in the part being modeled, Tier 80 on Bay(3)5 100% container contents, Tier 82 on Bay(3)5 100% container contents, and Tier 84 in Bay(5) contents of the container 100%. In other words, the transverse construction of frames 40 - 41 bear the burden of 2.5 stacks of containers.
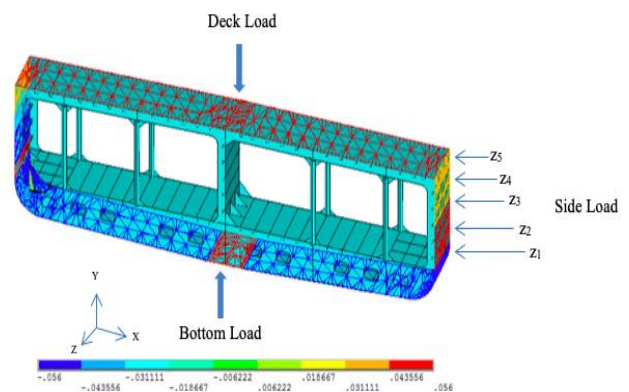

Figure 6. Input conditions of pressure loads on the sides, bottom, and deck of the ship

Table 1. Variation of loading in several conditions

Condition	Container Capacity		Evenly Distributed Load (kN/m²)	Total Deck Load (kN/m²)
1	Bay(3)5 Tier 80 =	100%	47.82	69.69
	Bay(3)5 Tier 82 =	100%		
	Bay(3)5 Tier 84 =	100%		
2	Bay(3)5 Tier 80 =	100%	43.835	65.71
	Bay(3)5 Tier 82 =	100%		
	Bay(3)5 Tier 84 =	75%		
3	Bay(3)5 Tier 80 =	100%	39.85	61.72
	Bay(3)5 Tier 82 =	100%		
	Bay(3)5 Tier 84 =	50%		
4	Bay(3)5 Tier 80 =	100%	35.865	57.74
	Bay(3)5 Tier 82 =	100%		
	Bay(3)5 Tier 84 =	25%		
5	Bay(3)5 Tier 80 =	100%	31.88	53.75
	Bay(3)5 Tier 82 =	100%		
	Bay(3)5 Tier 84 =	0%		
6	Bay(3)5 Tier 80 =	100%	27.895	49.76
	Bay(3)5 Tier 82 =	75%		
	Bay(3)5 Tier 84 =	0%		
7	Bay(3)5 Tier 80 =	100%	23.91	45.78
	Bay(3)5 Tier 82 =	50%		
	Bay(3)5 Tier 84 =	0%		
8	Bay(3)5 Tier 80 =	100%	19.925	41.79
	Bay(3)5 Tier 82 =	25%		
	Bay(3)5 Tier 84 =	0%		
9	Bay(3)5 Tier 80 =	100%	15.94	37.81
	Bay(3)5 Tier 82 =	0%		
	Bay(3)5 Tier 84 =	0%		
10	Bay(3)5 Tier 80 =	75%	11.955	33.83
	Bay(3)5 Tier 82 =	0%		
	Bay(3)5 Tier 84 =	0%		
11	Bay(3)5 Tier 80 =	50%	7.97	29.84
	Bay(3)5 Tier 82 =	0%		
	Bay(3)5 Tier 84 =	0%		

Table 2. Changes in ship draft (T) and bottom load due to variations in deck load

Load Condition	Draft (T) (m)	Bottom Load (kN/m²)
1	4.62	69.69
2	4.22	65.705
3	3.82	61.72
4	3.43	57.735
5	3.03	53.75
6	2.63	49.765
7	2.23	45.78
8	1.83	41.795
9	1.43	37.81
10	1.03	33.825
11	0.64	29.84

Next is the calculation of container weight (tons) which is then defined as uniform load (kN/m²). This load will then be included in the model. In the model, the load variations are given by varying the contents of the containers ranging from 100% to 0% with a stack of containers reaching 3 stacks, this is conducted to determine the deflection characteristics and stresses in ship construction. For more details, see Table 1.

By varying the load as shown in Table 1, the load on the bottom of the ship will be affected by reducing the contents of the container. Then the ship's draft (T) must be decreased so that the deck load value is the same at the bottom load value. The changes in the draft due to load variations were shown in Table 2.

4. Numerical Results

After calculating the load, the transversal strength of the ship is analyzed by using the structural response, such as the change in the shape of the ship's structure or displacement and stress due to external loads acting on the ship.

4.1. Stress on ships structure

Based on the simulation results, the value of the working stress that occurs at maximum load conditions is 2.5 stack (stack) of containers to the top, the stress that occurs is -140.631 N/mm² on deck and 89.729 N/mm² on bottom of the ship as shown in Fig. 7.

The greatest stress occurs due to external loads acting on the ship according to Fig. 7 is on the deck, precisely on the deck beam. The stress does not exceed the stress allowed by BKI rules, so the results of the analysis by using FEM meet the specified standards. The results of the recapitulation of stress in the x-direction can be seen in Table 3.

After analyzing the stress on the ship structure during maximum load conditions, an analysis is also carried out by varying the load according to Table 1. The results of the structural response analysis caused by the variation of loading were shown in Fig. 8.
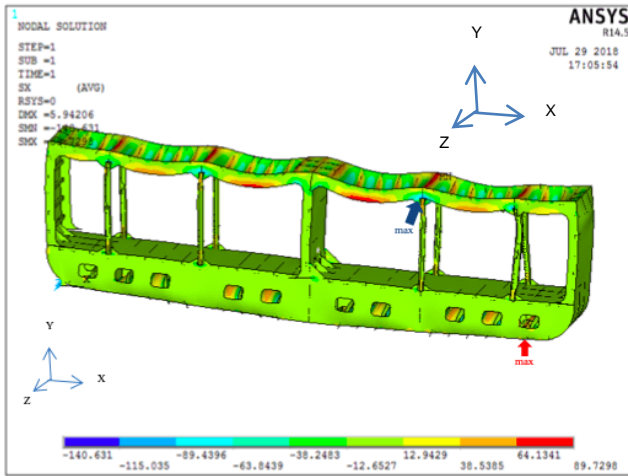
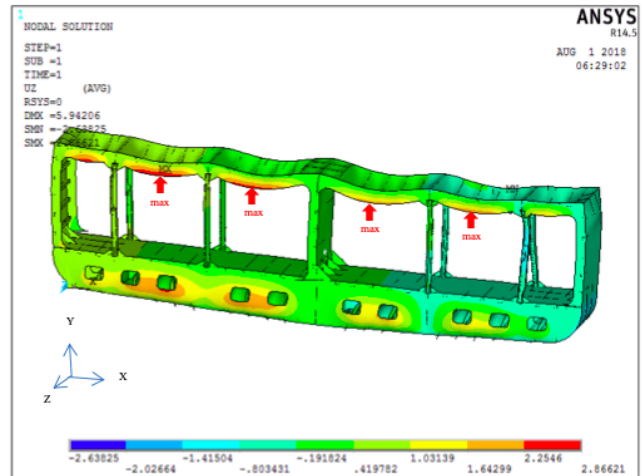Figure. 7 Behavior and stress distribution due to loading

Table 3. Recapitulation of stress in x-direction

Normal Stress (N/mm²)	
Deck (*deck beam*)	*Bottom* (*bottom plate*)
-140.63 < 150 Eligible	89.729 < 150 Eligible
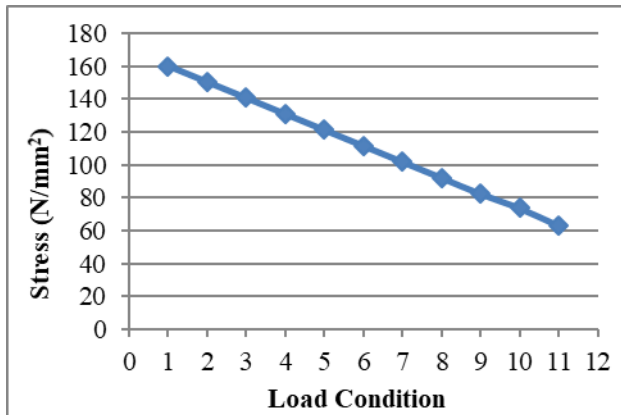
Figure 8. The Relation between load variation and stress

4.2. Deformation in ships structure

Based on the analysis result, the deformation that occurs in the transverse construction of the ship given a maximum loading of 2.5 stack containers to the top was shown in Fig. 9. The color gradation in Fig. 9 shows the amount of deformation experienced by ship construction. The red color depicts that in the construction part occur a large deformation while the green color represents smaller or relatively fixed deformations. Maximum deformation occurs in the deck beam with a value of 2.866 mm.

In addition to analyzing the structural deformation at maximum loading conditions, an analysis was also conducted on several loading variations in order to determine the response of the ship structure due to loading. The variations given in the model were shown in Table 1. The response of the structure caused by the variation of loading was shown in Fig. 10.

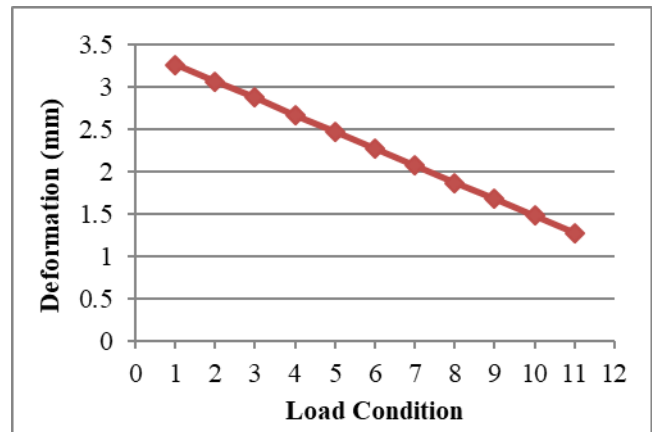

Figure 9. Deformation gradation in ship construction

Figure 10. The Relation between load variation and deformation

Table 4. Stress ratio at maximum load conditions

Load	$\sigma_{working}$ (N/mm²)	$\sigma_{permissible}$ (N/mm²)	*Stress Ratio*
Maximum	140.63	150	0.937

Based on the curve was shown in Fig. 10, it is known that due to constant load reduction, the deformation that occurs also experiences a linear reduction, as seen on the graph of the average deformation reduction of 0.18 mm.

4.3. Stress ratio

Normal stress acting on the transverse construction of ships due to external loads must not exceed 150/k [N/mm²], where k is a material factor whose value is equal to 1. This value is obtained based on BKI Vol II 2016 rules that the value of k is taken 1 for normal strength steel hull construction.

Stress Ratio is obtained by comparing the stresses that occur in construction due to external loads acting on the ship. Based on Table 4, the stress acting on the ship still eligible according to BKI rules because the stress ratio value is still smaller than 1 (<1). So, it can be concluded that the transverse construction design of the Container Ship, KM

Khendaga Nusantara 11 with a maximum load of 2.5 stack containers can be said to be feasible because they are still under the BKI permit stress.

5. Conclusions

This research was conducted using Finite Element Method (FEM). Based on the result, this research can be concluded as below:

- The response of the ship structure due to external loads acting on the ship will experience deformation with the largest value occurring on the deck beam that is 2.86 mm and ship construction experiences the greatest stress on the deck precisely on the deck beam about -140.63 N/mm^2 and at the bottom precisely on the base plate area about 89.73 N/mm^2.

- The strength of transverse construction of the ship with all the loads located above the deck and below the deck consisting of void tanks can be said to be eligible, with a maximum load of 15 container units or 2.5 stacks above (1 Row consist 6 units) because under these conditions, the stress which occurs in construction is still below the permissible stress.

- Stress ratio occurs to ship construction due to external loads working on ships is still smaller than 1 (<1). The largest stress ratio occurs at the maximum load condition of 15 container units or 2.5 stacks (stack) which is 0.93753.

References

[1] Shama, Mohamed. 2013. Buckling of Ship Structures. Alexandria University, Egypt.
[2] Molland, Anthony F. 2008. Maritime Engineering Reference Book. Elsevier Butterworth-Heinemann : Oxford.
[3] Rasyid, Daniel Muhammad. 2000. Strength of Ship Structure. Pradnya Paramita. Jakarta. [in Bahasa].
[4] Hughes, Owen F., dan Paik J.K. 2010. Ship Construction Analysis and Design. The Society of Naval Architecture and Marine Engineers: New Jersey.
[5] Biro Klasifikasi Indonesia. 2016. Rules For The Classification And Construction Seagoing Steel Ship, Volume II. BKI. Jakarta.
[6] Patnaik, Surya N., and Dale A Hopkins. 2004. Strength of Materials. Elsevier. Amsterdam.
[7] Gross, Dietmar. 2011. Engineering Mechanics 2 "Mechanics of Materials". Springer. London
[8] Susatio, Yerri. 2004. Basics of Finite Element Method. Andi. Yogyakarta. [in Bahasa]
[9] Bhavikatti, S.S. 2005. Finite Element Analysis. New age International Publisher. New Delhi.

Prediction of Propeller Performance using Computational Fluid Dynamics Approach

Ahmad Fitriadhy[a,*], Nur Amira Adam[b], W. S. Kong[c], Faisal Mahmuddin[d], C. J. Quah[e]

[a]Programme of Maritime Technology, School of Ocean Engineering, Universiti Malaysia Terengganu. Email: naoe.afit@gmail.com
[b]Programme of Maritime Technology, School of Ocean Engineering, Universiti Malaysia Terengganu. Email: amiraadam.nur@gmail.com
[c]Programme of Maritime Technology, School of Ocean Engineering, Universiti Malaysia Terengganu. Email: wsheng_95@hotmail.com
[d]Marine Engineering Department, Engineering Faculty, Hasanuddin University. Email: f.mahmuddin@gmail.com
[e]CEO Numit Enterprise, Seri Kembangan, Selangor, Malaysia. Email: seiko.q@numit.com.my

Abstract

A reliable prediction approach to obtain a sufficient thrust and torque to propel the ship at desired forward speed is obviously required. To achieve this objective, the authors propose to predict the thrust coefficient (K_T), torque coefficient (K_Q) and efficiency (η) of the propeller in open-water model test condition using Computational Fluid Dynamics (CFD) simulation approach. The computational simulation presented in the various number of rotational speed (RPM) within the range of advance ratio J=0.1 up to 1.05. The higher value of J leads to a decrease in $10K_Q$ and K_T. While the η increased steadily at the lower value of J and decreased at the higher value of J. The results also showed that the propeller with 1048 rpm obtains a better efficiency at J=0.95 with η= 88.25%, $10K_Q$=0.1654 and K_T= 0.0942. The computation result is very useful as preliminary data for propeller performance characteristics.

Keywords: CFD; efficiency; propeller; RPM; thrust

1. Introduction

The main purpose of a marine propeller to deliver the power and torque provided by the engine into the rotational motion to generate thrust. A proper specification of propeller design is required to make sure the propeller can produce a driving force to move the ship forward in the most effective ways [1, 2]. Other than that, improper propeller design and specification have a direct influence on the reduction of propeller performance and fuel efficiency of the ship propulsion system [3, 4]. The configuration of the propeller becomes a typical discussion among the naval architectures because the selection of the proper propeller design depends on the specification of the vessel and it also affects the manufacturing cost. Therefore, a hydrodynamics characteristic of the propeller is a very prominent aspect to be analysed in the early design stage using several methods in the form of open-water propeller model test.

Several researchers have been investigating the hydrodynamics characteristics of propeller using numerical and experimental approaches. According to [5-8], mathematical methods can be used to predict the hydrodynamics characteristics of the propeller based on circulation or lifting line theory. Meanwhile, hydrodynamics characteristics of the propeller are also predicted by using an experimental model test with towing tank [9-11]. This experimental method is very expensive, time-consuming, and have a complex procedure for various hydrodynamics analysis test configuration. Following the works of [12-16], the numerical methods are adopted to solve and analyze the fluid problem. The computational fluid dynamics (CFD) simulation are the best alternative with several advantages such as allow to simulate using actual and model geometry scale in extreme condition of the fluid flow and the CFD simulation also have a good agreement with experimental data [17-20].

This paper presents a CFD simulation approach for the extension work from [21, 22] to access the performance of propeller by K_T, K_Q, and η of the propeller. Here, a commercial CFD software, namely NUMECA Fine[TM]/Turbo v12.2 is utilized by grid generation, flow solver and post-processing capabilities. Fine[TM]/Turbo is specialized to simulate internal, rotating and turbomachinery flows for all types of fluids. The package has a fully hexahedral and highly automated grid generation module

_____

[*]Corresponding author. Tel.: +6-09-668-3350
Programme of Maritime Technology, School of Ocean Engineering, Universiti Malaysia Terengganu
Kuala Terengganu, Terengganu, 21030

AutoGrid^{TM}. The package uses a 3D Reynolds Averaged Euler and Navier Stokes flow solver EURANUS. CFView^{TM} is a post-processing module which is also part of the package. Basically, this is solved by means of a grid-independent study to estimate the optimal domain discretization. In this computation simulation, several numbers of rotational speed (rpm) are considered. The result is then comprehensively discussed to analyze their effect on K_T, K_Q, and η with the purpose of quantifying propeller performance quality.

2. Methods and Material

2.1. Governing equation

The cornerstone of computational fluid dynamics application, there is consists of fundamental governing mathematical statements of fluid dynamics such as continuity, momentum, and energy conservation equation. The 3-D propeller simulation defines that the flow around the propeller is complex, due to the combination between rotation and progression into the water [3]. Therefore, the CFD flow solver (ISIS-CFD) on NUMECA Fine^{TM}/Turbo V12.2 was based on the incompressible unsteady Reynolds-Averaged Navier-Stokes equation (URANSE) in which the solver applied the Finite Volume Method for representing the inflow and outflow areas, where the fluid flow is well behaved. Here, the governing equation has been discriminated using a Finite Volume Method with the velocity-pressure coupling and operated using a SIMPLE algorithm [23]. The Finite Volume Method also able to directly apply the integral spatial discretization in the physical space coordinate transformation to a computational space and this method also flexible to complex geometry structured and unstructured meshes.

2.2. Governing equation

To carry out the application of general conservation form of the Navier-Stokes equation using Finite Volume Method, the model of a finite volume has been considered fixed in space and the fluid element is moving. The continuity equation in conservation form presented in Eq. (1), where the ρ = density, U_i is the averaged Cartesian components of the velocity-vector in ith direction (i=1,2,3). Since the propeller simulated in steady and constant density of incompressible flows, the continuity equation has been modified as Eq. 2 [11].

$$\frac{\partial \rho}{\partial t} + \frac{\partial}{\partial_{x_i}}(\rho u_i) = 0 \qquad (1)$$

$$\frac{\partial}{\partial_{x_i}}(\rho u_i) = 0 \qquad (2)$$

Newton's 2nd law has been applied in Finite Volume Method to a model of the fluid flow. When the fluid element moving, the net force on the fluid element equals its mass

times the acceleration of the element. Therefore, the global Navier-Stokes equation applied the principle of the linear momentum conservation to solve the problem. Here, the momentum conservation equation expressed as Eq. 3.

$$\frac{\partial}{\partial t}(\rho u_i) + \frac{\partial}{\partial x_j}(\rho u_j u_i)$$
$$= -\frac{\partial p}{\partial x_i} + \frac{\partial \tau_{ij}}{\partial x_j} + \rho g_i + F_i \qquad (3)$$

where p = static pressure, g_i = gravitational acceleration, F_i = external body force in an averaged Cartesian component of the velocity-vector in ith direction (i=1,2,3) and δ_{ij} = Kroneker delta and is equal to unity $i = j$ and zero when $i \neq j$ [12]. Finally, τ_{ij} defined Reynolds-stress tensor presented below as Eq. 4, where μ being the dynamics viscosity [3].

$$\tau ij = \left[\mu \left(\frac{\partial u_i}{\partial x_j} + \frac{\partial u_j}{\partial x_i} \right) - \frac{2}{3} \mu \frac{\partial u_i}{\partial x_j} \delta_{ij} \right] \qquad (4)$$

2.3. Turbulent model

During the simulation, a simple one-equation model has relatively applied to compute rotating motions of propeller. Deck [24], Kostic [25], Hejlesen [26] and Lorin [27], reported that the Spalart-Allmaras transports equation model made for eddy viscosity and not required finer grid resolution to capture the velocity field gradients with algebraic models. For internal flow (turbomachinery) application, the kinematic turbulent v_t (m^2/s) in this model can be specified and estimate based on the assumptions, $\frac{vt}{v} = 1$ to 5 [28]. Here, the transport model for the working variable is shown in Eq. 5:

$$\frac{\partial \rho \tilde{v}}{\partial t} + \frac{\partial \rho u_j \tilde{v}}{\partial x_j} = \frac{\partial}{\partial x_j}\left[\left(\mu + \frac{\mu_\tau}{\sigma} \right) \frac{\partial \tilde{v}}{\partial x_j} \right]$$
$$+ c_{b2} \frac{\partial \tilde{v}}{\partial x_j} \frac{\partial \rho \tilde{v}}{\partial x_j} + c_{b1} \rho \tilde{W} \tilde{v} - c_{w1} f_w \rho \left(\frac{\tilde{v}}{y} \right) \qquad (5)$$

The eddy viscosity and damping function are defined as Eqs. 6 and 7, respectively. Where, $x = \frac{\tilde{v}}{v}$ and the kinematic viscosity $v = \mu/\rho$.

$$\mu_\tau = f_{v1} \rho \tilde{v} \qquad (6)$$

$$f_{v1} = \frac{X^3}{X^3 + c_{v1}{}^3} \qquad (7)$$

It should be noted here that the best practice in turbulence modeling quantities by considering an appropriate grid to estimate the cell meshing size, y_{wall}. Referring to the transport model discussed above, the viscosity has been taken into account that presents the high gradients near solid wall layers. Therefore, it is very important to have a sufficient amount the number of grid points in the boundary layers to properly capture the high gradient [21]. Here, an appropriate estimation of cell meshing size, y_{wall} for Navier-Strokes simulation, depends on the wall variable y^+ to measure the viscosity effect region as written in Eq. (8) [29].

$$y_1^+ = \frac{\rho u_\tau y_{wall}}{\mu} \qquad (8)$$

where u_τ is the friction velocity, $u_\tau = \sqrt{\frac{\tau_{wall}}{\rho}} - -\sqrt{\frac{1}{2}\left(V_{ref}\right)^2 C_f}$.

It is clear that the value of y_{wall} depends on the value of y_1^+.

In addition, the estimation for y_{wall} as a function of the desired value is obtained using a truncated series solution of the Blasius equation as expressed in Eq. (9).

$$y_{wall} = 6\left(\frac{V_{ref}}{v}\right)^{\frac{-7}{8}}\left(\frac{L_{ref}}{2}\right)^{\frac{1}{8}} y_1^+ \qquad (9)$$

Note that the reference velocity, V_{ref}, can be taken from the body velocity. The reference length, L_{ref}, should be based on the body length since an estimation of the boundary layer thickness is implied in this calculation. For instance, in the case of a propeller simulation, one could use the propeller diameter, as reference length. This is approximate, of course, as the thickness of the boundary layer will vary widely within the computational domain. Fortunately, it is only necessary to place within a range and not at a specific value.

2.4. Hydrodynamics theory of propeller

In CFD computation, the rotational surface is utilized to compute the force and torque of the system, where the axial thrust projected by the global force on the rotational axis and the torque was exerted by the global force calculated at (0,0,0). Nevertheless, these quantities are computed from the pressure and the velocity fields of the fluid acting on the blade surfaces. The axial thrust is computed based on Eq. 12 [28];

$$\sum_S \vec{F} \cdot \vec{n}_z \qquad (10)$$

The projection of the torque along a given direction $\vec{z}$ is given by

$$\left[\sum_S \vec{r} \times \vec{F}\right] \cdot \vec{z} \qquad (11)$$

The propeller model has been tested in open water test to determine the intrinsic propeller performance without distributed by the ship when it moved forward. The computed result from CFD usually refers to thrust (T), torque (Q) and efficiency (η). Thus, the performance data are given as form dimensionless thrust coefficient (K_T) and torque coefficient (K_Q) to be plotted against the advance ratio (J). The dimensionless quantities are defined as

$$J = \frac{V_a}{n \cdot D} \qquad (12)$$

$$K_T = \frac{T}{\rho n^2 D^4} \qquad (13)$$

$$K_Q = \frac{Q}{\rho n^2 D^5} \qquad (14)$$

$$\eta = \frac{J}{2\pi}\frac{K_T}{K_Q} \qquad (15)$$

where ρ is the water density, n the number of propeller rotations per second (RPS), D the propeller diameter and v_a represents for water advance velocity (m/s).

3. Simulation Condition

3.1. Hydrodynamics theory of propeller

In this paper, different rotational speeds were used to investigates. The principal dimension of the propeller, which composes with four number of blades is clearly presented in Table 1 and Fig. 1.

Table 1. Principle dimensions of propeller

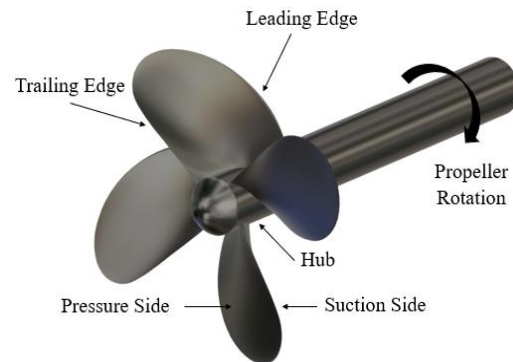| Geometrical parameters	Full Scale	Model Scale
Diameter (mm)	3650	119.25
AE/AO	0.695	0.695
P/D	1.013	1.013
Pitch (mm)	3697.45	120.83
Scale	1:30.6	
Propeller Orientation	Right-hand rotation	

Figure 1. 3D view of propeller geometry

Table 2. The simulation conditions

Rotational Speed (RPM)	Number of blades (Z)
1048	
1200	4
1340	

3.2. Simulation condition

In this study, there are parametric studies to be focused to achieve the objectives. The parametric studies were based on Table 2.

3.3. Computational domain and grid generation

The numerical simulation of propeller performance in various configurations was developed from the commercial software NUMECA Fine^{TM}/Turbo. Here, a single propeller blades geometry needs to define the trailing edge, leading edge, pressure side, suction side, and the hub of the propeller to generate an automatic grid. This simulation only considered a single blade of the propeller and another blades are performed by using a rotational periodicity (number of blades) which is the block of the blades and boundary are repeated in a given axis by a specified angle to save the computational time (for all simulation condition) [30].
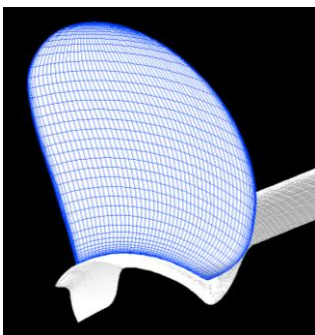

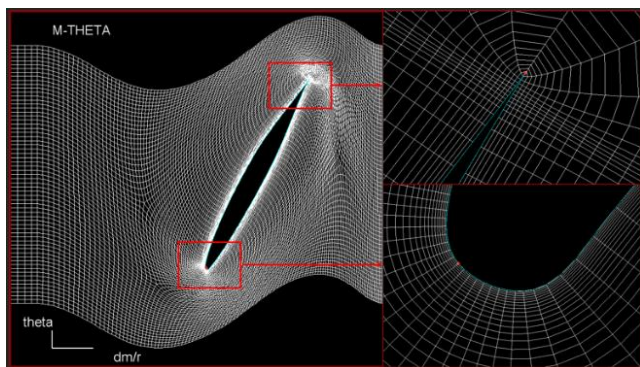Figure 2. 3D surface mesh for single blade associated with Z=4 mesh model

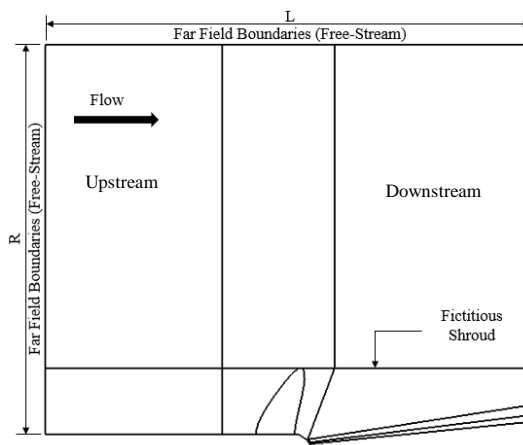Figure 3. Local refinement of the block structured grid in Blade-to-Blade view

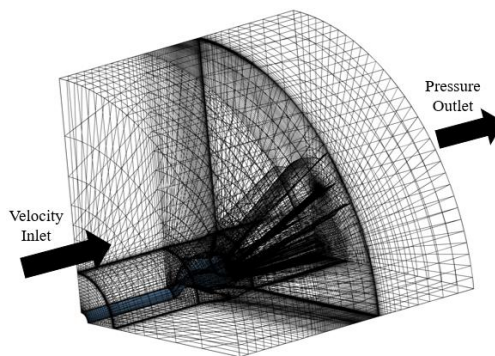Figure 4. Upstream and downstream location in the domain

Figure 5. Upstream and downstream location in the domain

Referring to Figure 4, the far-field boundary extends radially at five times (5R) the rear rotor radius at rotation center, while the axial length was located at three times radius (3R) for inlet and outlet boundary from the center as well. The inlet was specified as having a constant velocity of the flow model and a static pressure has been imposed at outlet boundary as shown in Fig. 5.

Table 3. Mesh Independent study on propeller geometry

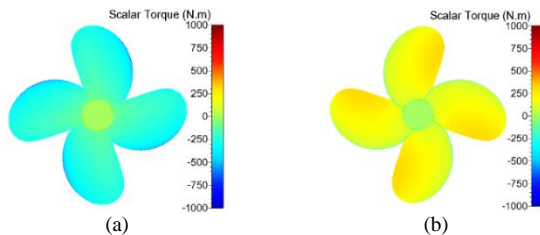| Case	Total Number of Cell Meshing	K_T	$10K_Q$	η
A	1,789,042	0.3679	0.5541	0.1057
B	2,559,546	0.3719	0.5563	0.1064
C	2,817,090	0.3727	0.5571	0.1065
D	4,000,666	0.3744	0.5551	0.1073

Figure 6. Scalar torque contour for (a) pressure and (b) suction side at J=0.1 with 1048 RPM

The value for the rotational speed of the solid boundary condition types (blades and hub) was set as a positive value to indicates a propeller rotational in positive θ-direction according to a right-handed propeller orientation [28]. Since this computational have a complex fluid problem, the Merkle preconditioner has been selected to increase the convergence rate and computation efficiency at very low flow speed [32, 30]. Besides, to overcome an insufficient calculation due to low relative edge cell size, a double solver precision has been selected to solve this computation and has led to increasing the required memory. The average duration of every simulation was about 4 to 7 hours (double solver precision) on a HP Z820 Workstation PC with processor Intel® Xeon® CPU ES-2690 v2 @ 3.0GHz (2 processor) associated with the installed memory RAM of 32.0 GB and 64-bit operating system

The meshing generation of the propeller was created in AutoGrid5 v12.2 software. It should note that an adequate number of mesh is very important for proper and accurate simulation. Hence, a mesh independent study may need to be performed for four different total number of cell meshing. Referring to mesh independent study result, the case C with 2.8 million total number of cell meshing was selected in all computed simulation of the propeller model accuracy of the CFD solution. This can be explained by the fact the 4.0 million total number of cell meshing were unnecessary due to its insignificant influence on the computational result of the thrust coefficient, torque coefficient, and efficiency. In the final stage of the CFD simulation, a package software in CFView was used to visualize the scalar torque for pressure and suction side for all various configurations of the propeller as displayed in Fig. 6.

4. Results and Discussions

The analysis for thrust coefficient, torque coefficient, and efficiency of the propeller in various rotational speed (RPM) was analyzed in the steady-state have been presented and appropriately discussed. In this study, the Computational Fluid Dynamics (CFD) approach was utilized to obtain the propeller performance.
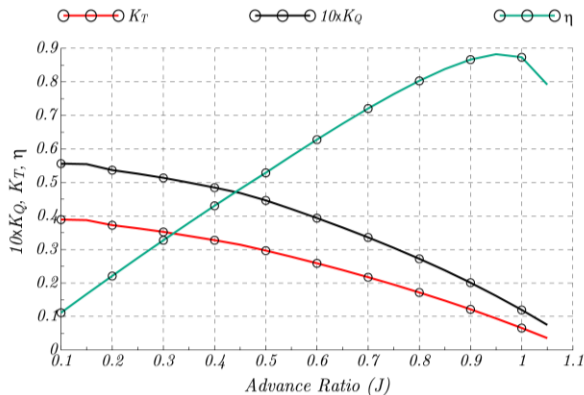

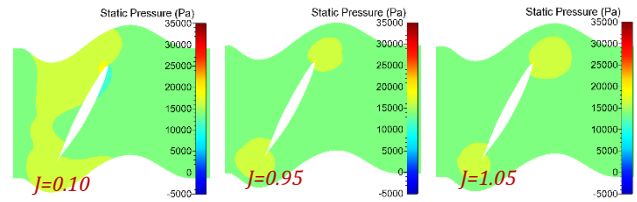Figure 7. Thrust coefficient, torque coefficient, and efficiency for 1048 RPM
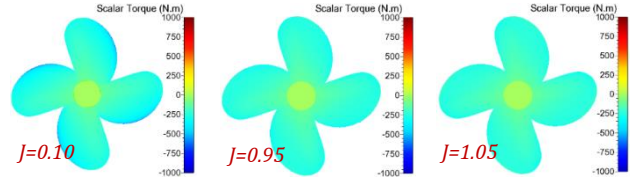

Figure 8. 2D static pressure contour for 1048 RPM

Figure 9. Scalar torque contour at pressure side for 1048 RPM

4.1. Propeller performance in various rotational speed

Referring to the Fig. 7, the K_T and $10K_Q$ decreases by increasing the advance ratio, J. Besides, the η increase steadily at lower advance ratio (J = 0.10) up to propeller optimum value (J = 0.95) and decreased at higher advance ratio (J = 1.00 and 1.05) as showed in Fig. 7 and detailed value in Table 4. The effect to the K_T occurs due to low axial velocity, the water surrounding the propeller will be accelerated from a low velocity. While at the higher advance ratio, the water surrounds the propeller already moving at high velocity and makes less change to the water velocity [33]. Besides that, the effect of $10K_Q$ due to the decreasing drag force on the blade surface. According to [33], the water pressure surrounding the blade was high when the water condition at a low velocity and directly contributes to pressure drag on the blade surface. While at high water velocity, the water pressure surrounding the blades will drop slowly and the pressure drag also drops as shown in Figure 8. This can be explained by the fact that the lowest pressure drags at leading edge (light blue color) resulted in lower scalar torque value as presented in Fig. 9.

The result of testing the propeller model on the various rotational speed of 1048, 1200 and 1340 RPM are represented in Fig. 10. The results showed that the $10K_Q$, K_T and η value obviously had a similar trend with the results at 1048 rpm from J=0.10 up to 1.05. Generally, the comparison between these three numbers of rpm shows that increasing the rpm results in decreasing $10K_Q$, K_T and η of the propeller. The propeller optimum, for 1048 rpm at about J= 0.95 was achieved at η=88.25% with $10K_Q$=0.1614 and K_T=0.0942. Besides, the optimum efficiency of the propeller for 1200 RPM occurs at J=0.90 with η=73.93%, $10K_Q$=0.2318, and K_T=0.1021. While, the optimum J value for 1340 rpm at about J= 0.85 with 67.41%, $10K_Q$=0.2318, and K_T = 0.1298. As compared with various rotational speeds, the propeller with 1048 RPM obtains better efficiency that can be explained by the fact that the propeller with low RPM will absorb less power to achieve requested RPM. According to [34] and [35], the propeller rotation speed greatly influences the blades pressure distribution where the higher rpm resulting in the lower pressure at the

blade surface; where blue color indicates low pressure area increase as higher propeller revolution (see Fig. 11). Meanwhile, the negative pressure magnitude direction being against the propeller continued to increase and expand in the back region. In this situation, the hydrodynamics performance of the 1340 RPM shows that the propeller with high rpm will produce lower pressure at suction side.
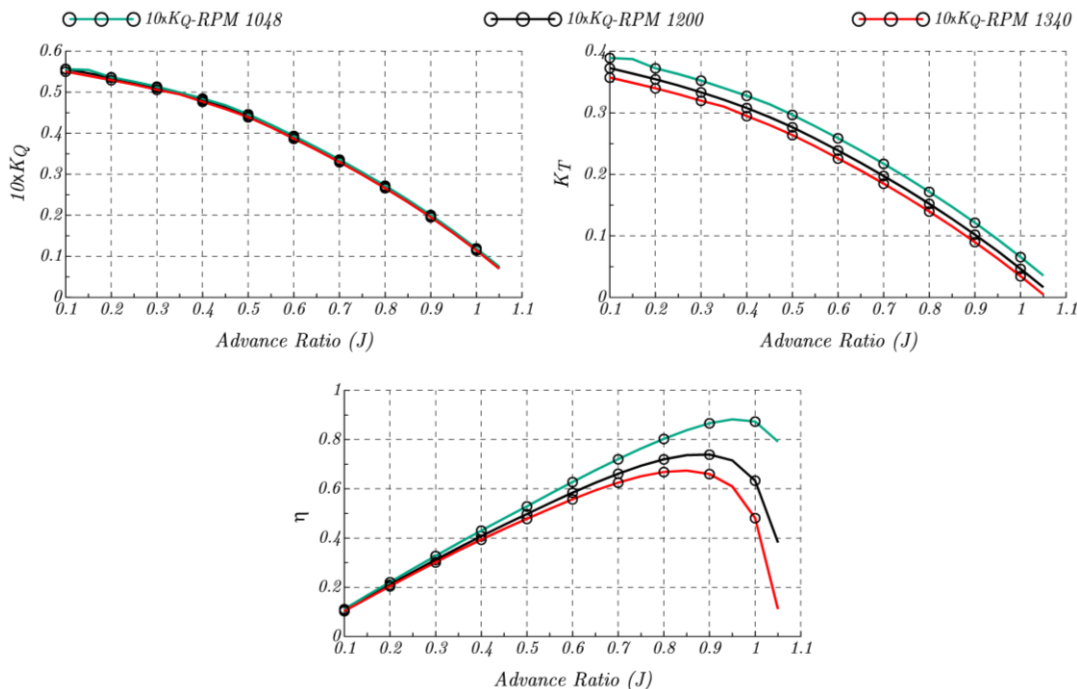

Figure 10. Thrust coefficient, torque coefficient, and efficiency for various rotational speeds

Table 4. Thrust coefficient, torque coefficient, and efficiency for various rotational speeds

| J	1048 RPM			1200 RPM			1340 RPM		
	$10K_Q$	K_T	η	$10K_Q$	K_T	η	$10K_Q$	K_T	η
0.10	0.5562	0.3892	0.1114	0.5571	0.3727	0.1065	0.5505	0.3573	0.1033
0.15	0.5545	0.3873	0.1668	0.5464	0.3638	0.1590	0.5401	0.3488	0.1542
0.20	0.5367	0.3725	0.2209	0.5355	0.3546	0.2108	0.5296	0.3399	0.2043
0.25	0.5258	0.3630	0.2747	0.5238	0.3445	0.2617	0.5184	0.3303	0.2535
0.30	0.5137	0.3524	0.3276	0.5109	0.3334	0.3116	0.5061	0.3197	0.3016
0.35	0.4993	0.3401	0.3794	0.4968	0.3213	0.3603	0.4949	0.3100	0.3490
0.40	0.4846	0.3277	0.4305	0.4808	0.3079	0.4077	0.4768	0.2948	0.3936
0.45	0.4684	0.3141	0.4802	0.4628	0.2930	0.4534	0.4593	0.2802	0.4370
0.50	0.4464	0.2967	0.5288	0.4425	0.2766	0.4974	0.4391	0.2639	0.4782
0.55	0.4206	0.2781	0.5788	0.4174	0.2583	0.5416	0.4144	0.2455	0.5187
0.60	0.3936	0.2588	0.6278	0.3903	0.2389	0.5845	0.3866	0.2258	0.5577
0.65	0.3654	0.2385	0.6752	0.3619	0.2186	0.6248	0.3590	0.2061	0.5938
0.70	0.3359	0.2173	0.7206	0.3325	0.1975	0.6616	0.3296	0.1850	0.6254
0.75	0.3049	0.1950	0.7635	0.3017	0.1754	0.6940	0.2986	0.1629	0.6510
0.80	0.2722	0.1717	0.8031	0.2691	0.1522	0.7201	0.2662	0.1398	0.6686
0.85	0.2376	0.1472	0.8383	0.2344	0.1277	0.7368	0.2318	0.1155	0.6741
0.90	0.2009	0.1215	0.8665	0.1978	0.1021	0.7393	0.1952	0.0900	0.6602
0.95	0.1614	0.0942	0.8825	0.1587	0.0751	0.7155	0.1560	0.0629	0.6099
1.00	0.1196	0.0656	0.8735	0.1168	0.0465	0.6336	0.1144	0.0346	0.4813
1.05	0.0750	0.3892	0.7917	0.0722	0.0165	0.3822	0.0698	0.0047	0.1117
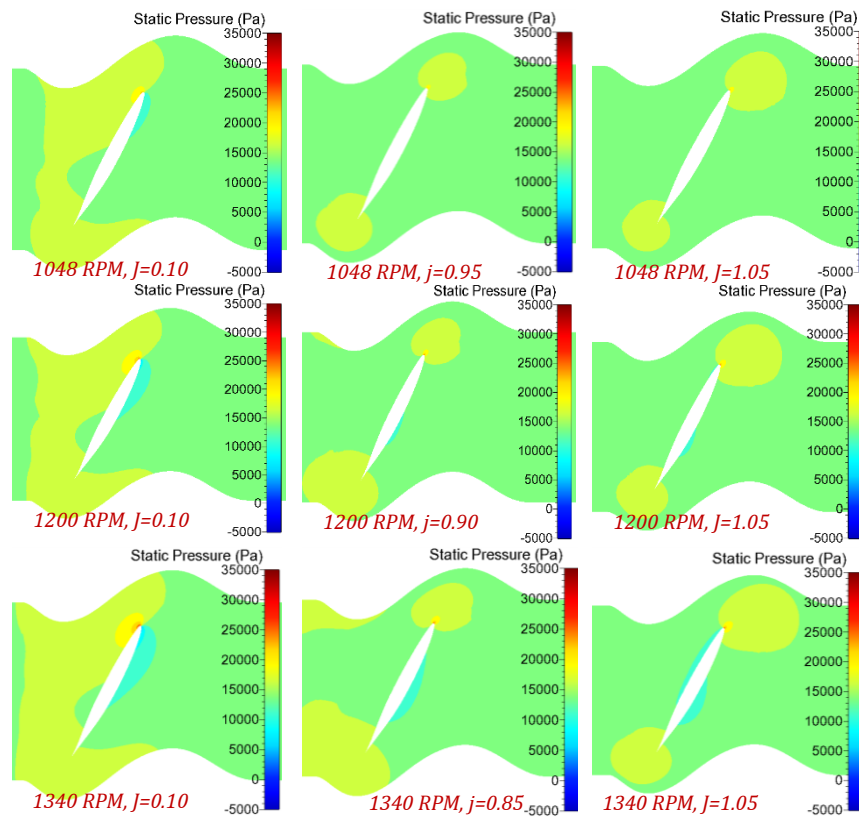
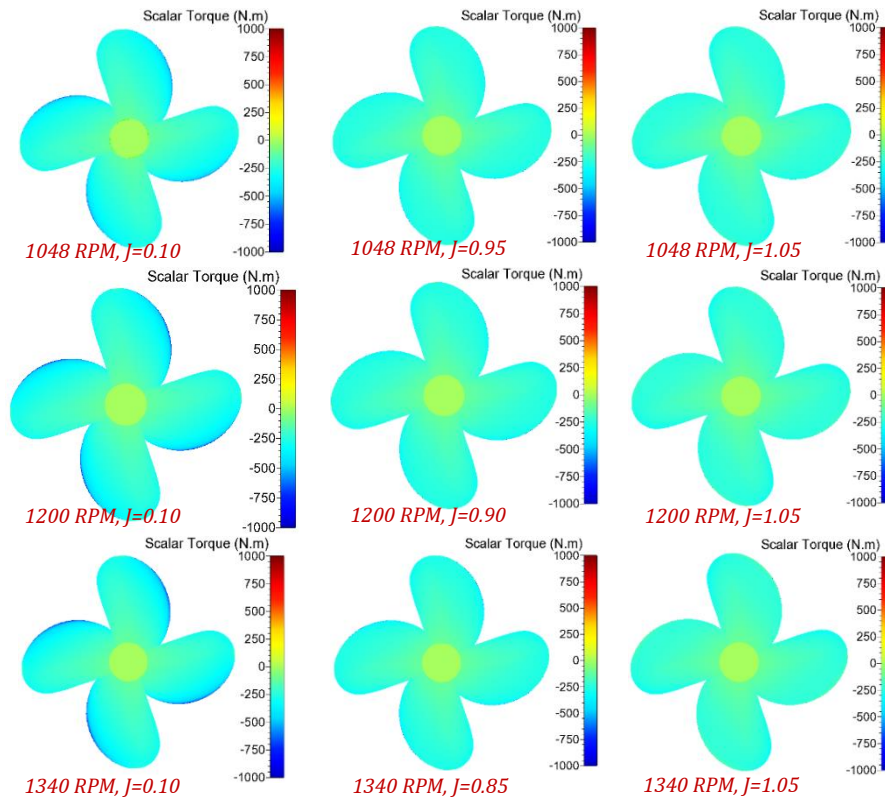Figure 11. 2D static pressure contour for various rotational speed

Figure 12. Scalar torque contour at pressure side for various rotational speed

5. Conclusion

The Computational Fluid Dynamics (CFD) simulation on hydrodynamic analysis of propeller is performed using NUMECA Fine^{TM}/Turbo v.12.2 software. The analysis of propeller performance was summarized as follow:

- The higher value of J lead to decrease $10K_Q$, K_T, and η due to low axial velocity and pressure drag surrounding the propeller.
- The increasing number of rotational speed (RPM), will decrease the propeller performance ($10K_Q$, K_T and η).
- As compared with various numbers of rpm, the optimum efficiency of the propeller with 1048 RPM at J = 0.95 with η = 88.25%, $10K_Q$ = 0.1614 and K_T = 0.0942 produce a better efficiency.

In general, the effect of various rotational speeds has a positive influence on the open water characteristics of the marine propeller. Therefore, these CFD results are useful as a preliminary prediction of propeller performance.

Acknowledgments

References

[1] Das, H. and S. Kapuria, *On the use of bend–twist coupling in full-scale composite marine propellers for improving hydrodynamic performance.* Journal of Fluids and Structures, 2016. **61**: p. 132-153.

[2] Husaini, M., Z. Samad, and M.R. Arshad. *Optimum Design of URRG-AUV Propeller Using PVL.* in *2nd Technical Seminar on Underwater System Technology: Breaking New Frontiers.* 2008.

[3] Mizzi, K., et al., *Design optimisation of Propeller Boss Cap Fins for enhanced propeller performance.* Applied Ocean Research, 2017. **62**: p. 210-222.

[4] Zhu, Z.-f. and S.-l. Fang, *Numerical investigation of cavitation performance of ship propellers.* Journal of Hydrodynamics, Ser. B, 2012. **24**(3): p. 347-353.

[5] Rahman, A., M.R. Ullah, and M.M. Karim, *Marine Propeller Design Method based on Lifting Line Theory and Lifting Surface Correction Factors.* Procedia engineering, 2017. **194**: p. 174-181.

[6] Epps, B., J. Ketcham, and C. Chryssostomidis. *Propeller blade stress estimates using lifting line theory.* in *Proceedings of the 2010 Conference on Grand Challenges in Modeling & Simulation.* 2010. Society for Modeling & Simulation International.

[7] Ekinci, S., *A practical approach for design of marine propellers with systematic propeller series.* Brodogradnja: Teorija i praksa brodogradnje i pomorske tehnike, 2011. **62**(2): p. 123-129.

[8] Taheri, R. and K. Mazaheri, *Hydrodynamic Optimization of Marine Propeller Using Gradient and Non-Gradient-based Algorithms.* Acta Polytechnica Hungarica, 2013. **10**(3): p. 221-237.

[9] Elghorab, M., et al. *Experimental Study of Open Water Non-Series Marine Propeller Performance.* in *Proceedings of World Academy of Science, Engineering and Technology.* 2013. World Academy of Science, Engineering and Technology (WASET).

[10] Arazgaldi, R., A. Hajilouei, and B. Farhanieh, *Experimental and numerical investigation of marine propeller cavitation.* 2009.

[11] Prakash, S. and D.R. Nath, *A computational method for determination of open water performance of a marine propeller.* International Journal of Computer Applications, 2012. **58**(12).

[12] Maghareh, M. and H. Ghassemi, *Propeller Efficiency Enhancement by the Blade's Tip Reformation.* American Journal of Mechanical Engineering, 2017. **5**(3): p. 70-75.

[13] Ting, F.Y., et al., *Development of Seakeeping Test and Data Processing System.* International Journal of Computational Engineering Research (IJCER), 2015: p. 33-39.

[14] Fitriadhy, A., et al., *Computational fluid dynamics investigation on total resistance coefficient of a high-speed" deep-V" catamaran in shallow water.* International Journal of Automotive and Mechanical Engineering, 2017. **14**: p. 4369-4382.

[15] Fitriadhy, A., et al., *Computational fluid dynamics analysis on the course stability of a towed ship.* Journal of Mechanical Engineering and Sciences, 2017. **11**(3): p. 2919-2929.

[16] Colley, E., *Analysis of Flow around a Ship Propeller using OpenFOAM.* 2012, Thesis, Curtin University.

[17] Turunen, T., et al. *Open-water computations of a marine propeller using openfoam.* in *ECFD VI-6th European Congress on Computational Fluid Dynamics, Barcelona, Spain, 20-25 July 2014.* 2014.

[18] Felicjancik, J., et al., *Numerical simulations of hydrodynamic open-water characteristics of a ship propeller.* Polish Maritime Research, 2016. **23**(4): p. 16-22.

[19] Sun, H., et al., *Motion prediction of catamaran with a semisubmersible bow in wave.* Polish Maritime Research, 2016. **23**(1): p. 37-44.

[20] Shamsi, R., S. Soheili, and A. Hamooni. *Hydrodynamic analysis of marine propellers using computational fluid dynamics.* in *Proceedings of the 17th international conference on mechanical engineering.*

[21] Fitriadhy, A., N. Razali, and N. AqilahMansor, *Seakeeping performance of a rounded hull catamaran in waves using CFD approach.* Journal of Mechanical Engineering and Sciences 2017. **11**(2): p. 2601-2614.

[22] Fitriadhy, A. and N.A. Adam, *Heave and pitch motions performance of a monotricat ship in head-seas.* International Journal of Automotive and Mechanical Engineering, 2017. **14**: p. 4243-4258.

[23] Baek, D.-G., et al., *Effects of the advance ratio on the evolution of a propeller wake.* Computers & Fluids, 2015. **118**: p. 32-43.

[24] Deck, S., et al., *Development and application of Spalart–Allmaras one equation turbulence model to three-dimensional supersonic complex configurations.*

Aerospace Science and Technology, 2002. **6**(3): p. 171-183.

[25] Kostić, Č., *Review of the Spalart-Allmaras turbulence model and its modifications to three-dimensional supersonic configurations.* Scientific Technical Review, 2015. **65**(1): p. 43-49.

[26] Hejlesen, M.M., et al. *Implementation of the Spalart-Allmaras turbulence model in the two-dimensional vortex-in-cell method.* in *6th European Congress on Computational Methods in Applied Sciences and Engineering.* 2012. Vienna University of Technology.

[27] Lorin, E., A. Ben Haj Ali, and A. Soulaimani. *An accurate positivity preserving scheme for the Spalart-Allmaras turbulence model. Application to aerodynamics.* in *36th AIAA Fluid Dynamics Conference and Exhibit.* 2006.

[28] International, N., *FINE/Turbo v8. 7, user manual.* 2009, NUMECA International Brussels.

[29] Salim, S.M. and S. Cheah. *Wall Y strategy for dealing with wall-bounded turbulent flows.* in *Proceedings of the international multiconference of engineers and computer scientists.* 2009. Citeseer.

[30] Martinez, J., et al., *Aerodynamic analysis of wind turbine rotor blades.* Task Q, 2015. **19**(2): p. 129-140.

[31] Kamal, I.M. and T.M.A.T.M. Yusof, *A CFD RANS Cavitation Prediction for Propellers.* 2017.

[32] Folkner, D., *Improvement in computational fluid dynamics through boundary verification and preconditioning.* 2013.

[33] Husaini, M., Z. Samad, and M.R. Arshad, *Autonomous underwater vehicle propeller simulation using computational fluid dynamic*, in *Computational Fluid Dynamics Technologies and Applications.* 2011, InTech.

[34] Yeo, K.B. and W.Y. Hau, *Fundamentals of Marine Propeller Analysis.* Journal of Applied Sciences, 2014. **14**(10): p. 1078-1082.

[35] Yeo, K.B., W.H. Choong, and W.Y. Hau, *Prediction of propeller blade stress distribution through FEA.* Journal of Applied Sciences, 2014. **14**(22): p. 3046-3054.

Polya Counting Theory Applied to Combination of Edge Conditions for Generally Shaped Isotropic Plates

Yoshihiro Narita [a]*

[a]Hokkaido University (Professor Emeritus), C-BEST Project, Center of Technology, UNHAS. Email: ynarita@eng.hokudai.ac.jp

Abstract

Structural behaviors of plate components, such as internal stress, deflection, buckling and dynamic response, are important in the structural design of aerospace, mechanical, civil and other industries. These behaviors are known to be affected not only by plate shapes and material properties but also by edge conditions. Any one of the three classical edge conditions in bending, namely free, simply supported and clamped edges, may be used to model the constraint along an edge of plates. Along the entre boundary with plural edges, there exist a wide variety of combinations in the entire plate boundary, each giving different values of structural responses. For counting the total number of possible combinations, the present paper considers Polya counting theory in combinatorial mathematics. For various plate shapes, formulas are derived for counting exact numbers in combination. In some examples, such combinations are confirmed in the figures by a trial and error approach.

Keywords: Counting problem; combinatory mathematics; plate shape; Polya counting theory; structural response

1. Introduction

Many structural panels are found and can be modelled in the form of flat plates in the fields of mechanical, civil, aeronautical, ocean and other industries. Technical publications are therefore numerous on mechanics of flat plates. For example, a monograph "Vibration of Plates" was compiled by Leissa [1] in 1969 to cover the topic from vibrational viewpoint. He also listed up the natural frequencies of isotropic rectangular plates for all the possible combinations of classical edge conditions [2].

Apart from vibrational aspect, it is important to know in design process the mechanical behaviors, such as stress and strain, deflection and critical buckling loads. These values are influenced significantly by edge conditions (The edge conditions are stated as boundary conditions in mathematics, but in the present paper, the terminology "edge condition" is used throughout the paper from mechanics viewpoint), and should be summarized as sets of design data in comprehensive fashion. To the present, however, little efforts have been made to clarify even the number of combinations in terms of edge conditions. For this purpose, an attempt is made in this paper to count all possible combinations of edge conditions. Mathematically, it is interpreted as combinatorics problem of counting different

classes (combinations) that give different sets of results on stress and so on, as the values mentioned above.

As for methodology, Polya counting theory is used. Polya made fundamental contributions to combinatorics, number theory, numerical analysis and probability theory. The theory is also known as Polya enumeration theorem and Redfield–Polya theorem. It is a theorem in combinatorics that generalizes Burnside's lemma on the number of orbits of a group action on a set. After the first publication by Redfield in 1927 [3], Polya developed the theory [4] as a powerful tool in combinatorics and graph theory (for example, refer to textbook [5]), and popularized by applying it to many counting problems. Particularly, it has a wide range of applications to enumeration of chemical compounds. For example, Haigh and Baker [6] applied it to enumeration of the isomers in chemistry.

In the present paper, the theory is used to count the number of combinations of edge conditions that yield different mechanical behaviours. Such behaviours include stress distribution, deflection, natural frequencies and critical buckling loads found in isotropic flat plates with general shapes. After the method is outlined for counting the present cases, cyclic polynomials are derived and used to calculate eighteen examples with different edge numbers when the number of each edge condition is given for 1, 2, 3

---

*Corresponding author.
Kita-13, Nishi-8, Kita-ku, Sapporo, Japan 060-8628

and 4. The total number of sets of edge conditions is listed for eighteen different plate shapes. For showing validity of these results, actual combinations are listed for rhombic, symmetric trapezoidal, equilateral and isosceles triangular and regular pentagonal plates in the case of two edge conditions (free edge and clamped edge) by a trial and error approach.

2. Polya Counting Theory

The combinatorics approach is outlined here as used in [7]. In Group theory, a permutation is defined as a one-to-one mapping from a set D onto D. For example, when there is a set D composed of four elements {1,2,3,4}, i.e., D={1,2,3,4}, a permutation of transposing $1\rightarrow2$, $2\rightarrow4$, $3\rightarrow3$, $4\rightarrow1$ can be written as

$$P = \begin{pmatrix} 1 & 2 & 3 & 4 \\ 2 & 4 & 3 & 1 \end{pmatrix} \qquad (1)$$

or more simply, a cyclic notation

$$P = \left\{ (124)(3) \right\} \qquad (2)$$

can be used as used in this paper. For such two permutations, it is clear that a product $P_1 P_2$ of P_1 and P_2 also becomes a permutation. In Group theory, a set G of all permutations acting on a set D can be considered as a finite group. The reason is that the associative law exists with a unit and inverse elements in G. In the present problem, a set composed of all possible rotation and flipping of a plate shape becomes such a permutation group.

The next important notation is "class" in counting problem. In this paper, this can be explained next by using a case of square plate. Figure 1 presents a square isotropic plate (i.e, plate made of no material anisotropy), and four edges are numbered as Edge 1 (left-hand edge), Edge 2 (lower edge), Edge 3 (right-hand edge) and Edge 4 (upper edge) in counter-clock wise. When one of classical edge conditions of free (denoted by F), simply-supported (S) and clamped (C) in bending is applied to each of the four edges, the notation of entire edges is given by four capital letters, for example, CSFF is the plate with calmed (C) at Edge 1, simply supported (S) at Edge 2 and free (F) at Edge 3 and 4.

The square plate in Fig.1 now has four edges under three different boundary conditions (F,S,C), and when the four edges are fixed in the space, the number of edge conditions is fixed by 3^4=81. However, when this combination problem is looked from mechanical behaviors such as stress distribution, deflection, vibration frequencies, and critical buckling loads, two cases of CSFF and FCSF are identical because one case FCSF is obtained by rotating CSFF with 90 degree in counter-clockwise. These two cases are said to belong to the same class. In contrast, other cases of CSFF and CFSF (the same number of C,S,F exist) cannot be in the same class, because one case cannot be realized either by rotation or flipping. This paper considers counting the number of classes when a cyclic permutation group G acts on a set D.
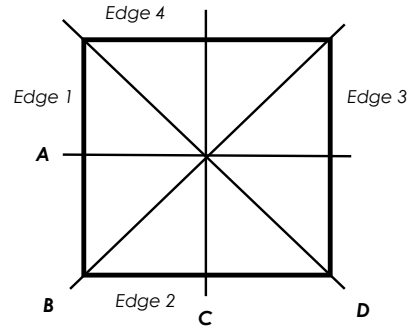

Figure 1. Square plate and symmetry axes (Ex.1)

Polya counting theory [4, 5] derives a kind of polynomial "cyclic polynomial" in order to calculate the number of essentially different cases (i.e, number of different "classes"). When a cyclic group, acting on a finite group, is denoted by G and $C_k(G)$ is a number of elements in G with the cyclic number k, the cyclic polynomial for a group G acting on D is given by

$$Z_G(x) = \frac{1}{|G|} \sum_{k=1}^{|G|} C_k(G) x^k \qquad (3)$$

3. Application of the Theory and Cyclic Polynomials

3.1. Plates with four straight edges

3.1.1. Square plate (Ex.1)

As shown in Fig.1, a square plate has four edges of equal length and four symmetrical axes. Two axes are parallel to the edges (labeled as A and C in the figure), and remaining two axes are diagonal axes labelled as B and D.

For rotation around the central point, it has four possible rotational motions in counter-clockwise as

$$G_r = \left\{ (1)(2)(3)(4), (1234), (13)(24), (1432) \right\} \qquad (4)$$

with rotating angles 0°, 90°, 180° and 270°, respectively.

For flipping, it has four possible flipping motions as

$$G_f = \left\{ (1)(3)(24), (12)(34), (2)(4)(13), (14)(23) \right\} \qquad (5)$$

by flipping with respect to the symmetric axes A, B, C and D, respectively. By adding two sets of motions, one gets

$$G = G_r + G_f, \quad |G| = 8 \qquad (6)$$

and number of elements in Eqs.(4) and (5) are given for each cyclic number k as

$$C_4 = 1, \quad C_3 = 2, \quad C_2 = 3, \quad C_1 = 2 \qquad (7)$$

From (6) and (7), a cyclic polynomial in this example is

$$Z_G(x) = \frac{1}{8} \left(x^4 + 2x^3 + 3x^2 + 2x \right) \qquad (8)$$

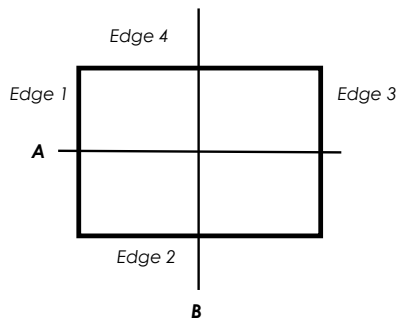This case was already obtained in Ref. [7] written by the present author.

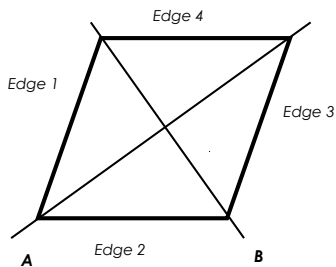Figure 2. Rectangular plate and symmetry axes (Ex.2)

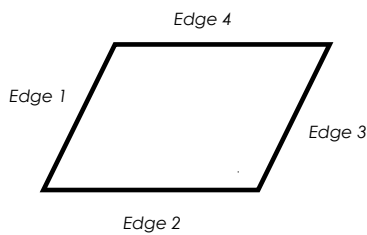Figure 3. Rhombic plate and symmetry axes (Ex.3)
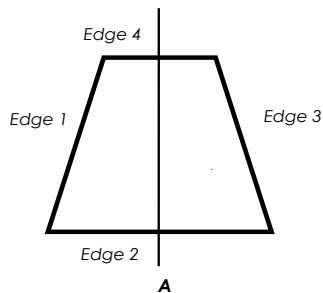

Figure 4. Parallelogram plate (Ex.4)

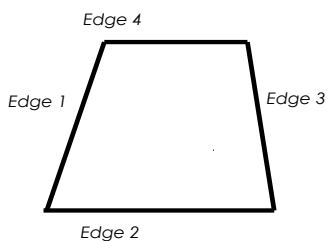Figure 5. Symmetric trapezoidal plate (Ex.5)

Figure 6. Asymmetric trapezoidal plate (Ex.6)

3.1.2. Rectangular plate (Ex.2)

A rectangular plate is generalization of a square plate, and diagonal symmetric axes do not exist, leaving only two symmetric axes parallel to the edges (labelled as A and B) as shown in Fig. 2. For rotation around the central point, it has four possible rotational motions in counter-clockwise as

$$G_r = \left\{ (1)(2)(3)(4), (13)(24) \right\} \tag{9}$$

with angles 0° and 180°, respectively. It has two flipping motions as

$$G_f = \left\{ (1)(3)(24), (2)(4)(13) \right\} \tag{10}$$

by flipping with respect to the symmetric axes A and B, respectively. By adding two sets of motions, one gets a number of elements in Eqs.(9) and (10), totally, as

$$C_4 = 1, \quad C_3 = 2, \quad C_2 = 1, \quad C_1 = 0 \tag{11}$$

A cyclic polynomial in this example is

$$Z_G(x) = \frac{1}{4}\left(x^4 + 2x^3 + x^2 \right) \tag{12}$$

This case is also obtained in Ref. [7].

3.1.3. Rhombic plate (Ex.3)

A rhombus is composed of four edges of equal length, but the corners are no longer perpendicular. There are two symmetric axes connecting opposite corners as shown in Fig.3. For rotation and flipping, the motions are described as motions

$$G_r = \left\{ (1)(2)(3)(4), (13)(24) \right\} \tag{13}$$

and

$$G_f = \left\{ (12)(34), (14)(23) \right\} \tag{14}$$

by flipping with respect to the symmetric axes A and B, respectively. By following the same process, a cyclic polynomial is

$$Z_G(x) = \frac{1}{4}\left(x^4 + 3x^2 \right) \tag{15}$$

3.1.4. Parallelogram plate (Ex.4)

As shown in Fig.4, a parallelogram is a geometry where two pairs of parallel straight lines intersect each other. The length of two sets of edges are generally not equal (if they are equal, it becomes a rhombus). There are no symmetry axes in geometry. For rotation and flipping, the motions are

$$G_r = \left\{ (1)(2)(3)(4), (13)(24) \right\} \tag{16}$$

and $G_f = \{0\}$. A cyclic polynomial is

$$Z_G(x) = \frac{1}{2}\left(x^4 + x^2 \right) \tag{17}$$

3.1.5. Symmetric trapezoidal plate (Ex.5)

As shown in Fig. 5, a symmetric trapezoid is a geometry where one pairs of parallel straight lines is intersected by a pair of lines with the same angle. Only one pair of opposite edges is of equal length. There is only one symmetry axis in geometry. For rotation and flipping, the motions are

$$G_r = \{(1)(2)(3)(4)\}, G_f = \{(13)(2)(4)\} \qquad (18)$$

A cyclic polynomial is

$$Z_G(x) = \frac{1}{2}\left(x^4 + x^3\right) \qquad (19)$$

3.1.6. Asymmetric trapezoidal plate (Ex.6)

An asymmetric trapezoid is a geometry with a pair of two parallel lines but the other two opposite straight lines have different intersecting angles to the parallel lines. This geometry has no symmetric axis as seen in Fig. 6, and has only unit element,

$$G_r = \{(1)(2)(3)(4)\} \qquad (20)$$

and $G_f = \{0\}$. A cyclic polynomial is

$$Z_G(x) = x^4 \qquad (21)$$

3.2. Triangular Plates

3.2.1. Equilateral triangular plate (Ex.7)

An equilateral triangle is a triangle where all three sides are equal in length, and is also equiangular. All three internal angles are 60° each. It is also a regular polygon and can be called as a regular triangle. As shown in Fig.7, it has three symmetric axes, labelled as A, B and C. For rotation around the central point, it has three rotational motions in counter-clockwise as

$$G_r = \{(1)(2)(3),(123),(132)\} \qquad (22)$$

with 0°, 120° and 240°, respectively. It has two flipping motions as

$$G_f = \{(1)(23),(2)(13),(3)(12)\} \qquad (23)$$

by flipping with respect to the symmetric axes *A, B* and *C*, respectively. A cyclic polynomial in this example is

$$Z_G(x) = \frac{1}{6}\left(x^3 + 3x^2 + 2x\right) \qquad (24)$$

3.2.2. Isosceles triangular plate (Ex.8)

An isosceles triangle in Fig. 8 has only one axis of symmetry, and has only one action for each of rotation and flipping. Therefore, a cyclic polynomial is
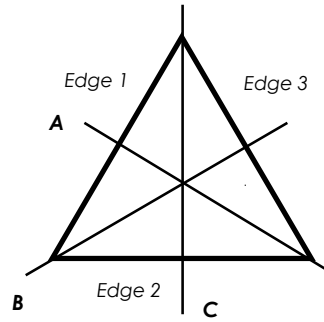

Figure 7. Equilateral triangular plate (Ex.7)

$$Z_G(x) = \frac{1}{2}\left(x^3 + x^2\right) \qquad (25)$$

3.2.3. Right-angled triangular plate (Ex.9)

A right-angled triangle has no axis in symmetry, and can be an isosceles triangle when length of two edges is equal. But in this section as shown in Fig.9, all three edges are assumed to be different length, then, there is only an unit action. A cyclic polynomial is

$$Z_G(x) = x^3 \qquad (26)$$

3.2.4. General triangular plate (Ex.10)

For most general case of triangle in Fig.10, there are no edges of equal length. Because it has only unit element,

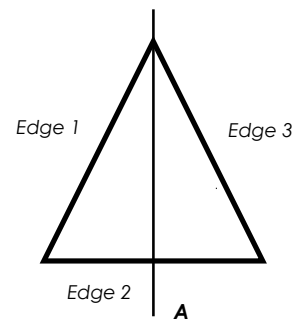$$Z_G(x) = x^3 \qquad (27)$$

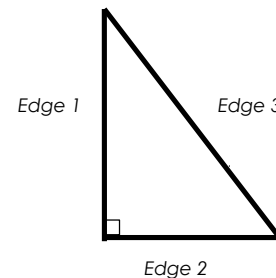Figure 8. Isosceles triangular plate (Ex.8)
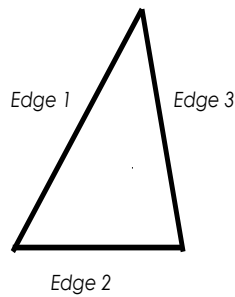

Figure 9. Right-angled triangular plate (Ex.9)
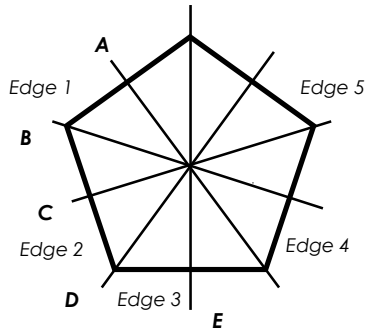
Figure 10. General triangular plate (Ex.10)

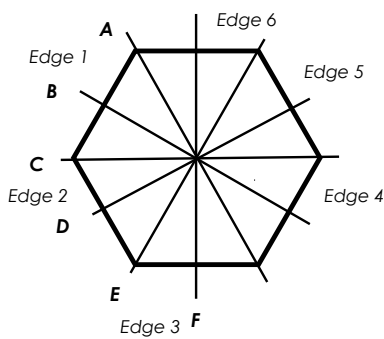Figure 11. Regular pentagonal plate (Ex.11)

Figure 12. Regular hexagonal plate (Ex.12)

3.3. Polygonal Plates

3.3.1. Regular pentagonal plate (Ex.11)

A pentagon is a five-sided polygon and the sum of the internal angles is 540°. A self-intersecting regular pentagon is called a pentagram. As shown in Fig. 11, it has five symmetric axes, labelled as *A, B, C, D* and *E*. For rotation around the central point, it has five rotational motions in counter-clockwise as

$$G_r = \{(1)(2)(3)(4)(5),(12345),(13524),$$
$$(14253),(15432)\} \tag{28}$$

with 0°, 72°, 144°, 216° and 288°, respectively. It has five flipping motions as

$$G_f = \{(1)(25)(34),(2)(13)(45),(3)(24)(15),$$
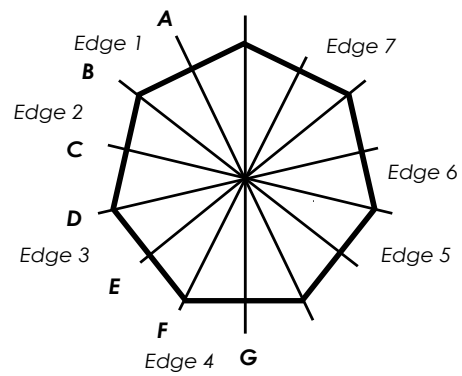$$(4)(12)(35),(5)(23)(14)\} \tag{29}$$

Figure 13. Regular septagonal plate (Ex.13)
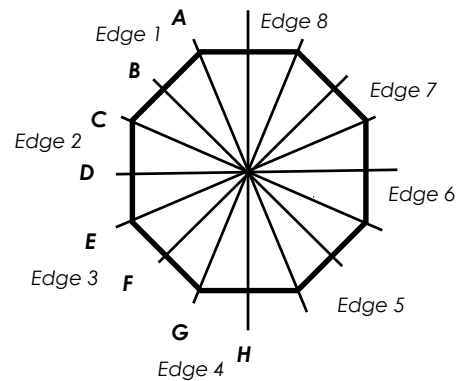

Figure 14. Regular octagonal plate (Ex.14)

by flipping with respect to the symmetric axes *A, B, C, D* and *E*, respectively. So, a cyclic polynomial in this case is

$$Z_G(x) = \frac{1}{10}\left(x^5 + 5x^3 + 4x\right) \tag{30}$$

3.3.2. Regular hexagonal plate (Ex.12)

A regular hexagonal plate has six symmetric axes (*A, B, C, D, E* and *F*) as shown in Fig. 12. For rotations,

$$G_r = \{(1)(2)(3)(4)(5)(6),(123456),(135)(246),$$
$$(14)(25)(36),(153)(264),(165432)\} \tag{31}$$

with 0°, 60°, 120°, 180°, 240° and 300°, respectively. It has two flipping motions as

$$G_f = \{(12)(36)(45),(23)(14)(56),$$
$$(34)(25)(16),(3)(6)(24)(15),$$
$$(1)(4)(26)(35),(2)(5)(14)(46)\} \tag{32}$$

Then, a cyclic polynomial is

$$Z_G(x) = \frac{1}{12}\left(x^6 + 3x^4 + 4x^3 + 2x^2 + 2x\right) \tag{33}$$

3.3.3. Regular septagonal plate (Ex.13)

A septagon (or heptagon) is a seven seven-sided polygon, as sown in Fig. 13, it has seven symmetric axes. For rotation around the central point, it has seven rotational motions.

$$G_r = \{(1)(2)(3)(4)(5)(6)(7),(1234567),(1357246),$$
$$(1473625),(1526374),(1642753),(1765432)\}$$

$$(34)$$

with $0°$, α, 2α, 3α, 4α, 5α and 6α ($\alpha=360/7°$), respectively. It has seven flipping motions as

$$G_f = \{(1)(27)(36)(45),(2)(13)(47)(56),$$
$$(3)(24)(15)(67),(4)(35)(26)(17),$$
$$(5)(46)(37)(12),(6)(14)(23)(57)$$
$$(7)(16)(25)(34)\}$$

$$(35)$$

Therefore, a cyclic polynomial in this case is

$$Z_G(x) = \frac{1}{14}\left(x^7 + 7x^4 + 6x\right) \qquad (36)$$

3.3.4. Regular octagonal plate (Ex.14)

An octagon is an eight-sided polygon, as sown in Fig. 14, it has eight symmetric axes. For rotation around the central point, it has eight rotational motions.

$$G_r = \{(1)(2)(3)(4)(5)(6)(7)(8),(12345678),$$
$$,(1357)(2468),(14725836),(15)(26)(37)(48),\quad (37)$$
$$(16385274),(1753)(2864),(18765432)\}$$

with $0°$, $45°$, $90°$, $135°$, $180°$, $225°$, $270°$ and $315°$, respectively. It has seven flipping motions as

$$G_f = \{(1)(5)(28)(37)(46),(2)(6)(13)(48)(57),$$
$$(3)(7)(24)(15)(68),(4)(8)(35)(26)(17),$$
$$(12)(38)(47)(56),(23)(14)(58)(67),\qquad (38)$$
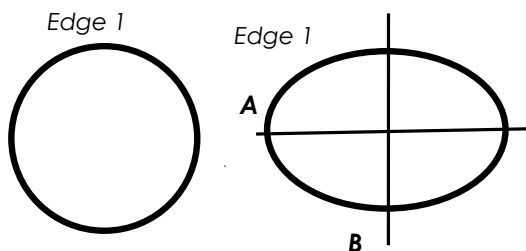$$(34)(25)(16)(78),(18)(27)(36)(45)\}$$

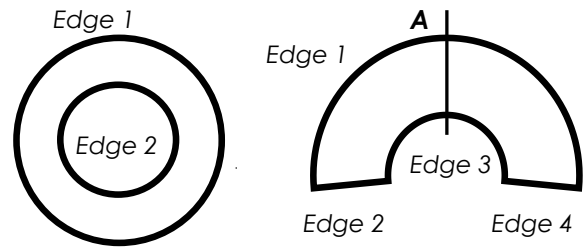
Figure 15. Circular and Elliptical plate (Ex.15 & 16)

Figure 16. Annular and Sectorial plate (Ex.17 & 18)

Therefore, a cyclic polynomial in this case is

$$Z_G(x) = \frac{1}{16}\left(x^8 + 4x^5 + 5x^4 + 2x^2 + 4x\right)$$

3.4. Plates with Circular Edges

3.4.1. Solid circular plate (Ex.15)

Except for cases considering mixed edge conditions, circular plate in Fig. 15 has only one edge condition, and so

$$Z_G(x) = x \qquad (39)$$

3.4.2. Solid elliptical plate (Ex.16)

Again, except for cases with mixed edge conditions, solid elliptical plate in Fig.15 has only one edge, and so

$$Z_G(x) = x \qquad (40)$$

3.4.3. Annular circular plate (Ex.17)

An annular circular plate in Fig.16 has two edges, and

$$Z_G(x) = x^2 \qquad (41)$$

3.4.4. Annular circular sectorial plate (Ex.18)

As shown in Fig.16, the present plate has two circular and two straight edges, and one axis of symmetry. There is no rotation but one flipping with the axis, i.e.,

$$G_r = \{(1)(2)(3)(4)\} \qquad (42)$$

and

$$G_f = \{(1)(3)(24)\} \qquad (43)$$

Therefore, a cyclic polynomial is

$$Z_G(x) = \frac{1}{2}\left(x^4 + x^3\right) \qquad (44)$$

Table 1. Different classes (combinations) of plates (Ex.1-18) versus number of edge conditions applied along each edge

	Number of conditions x per edge			
	1	2	3	4
Plates with four straight edges				
Ex.1	1	6	21	55
Ex.2	1	9	36	100
Ex.3	1	7	27	76
Ex.4	1	10	45	136
Ex.5	1	12	54	160
Ex.6	1	16	81	256
Triangular plates				
Ex.7	1	4	10	20
Ex.8	1	6	18	40
Ex.9	1	8	27	64
Ex.10	1	8	27	64
Polygonal plates				
Ex.11	1	8	39	136
Ex.12	1	13	92	430
Ex.13	1	18	198	1300
Ex.14	1	30	498	4435
Plates with circular edges				
Ex.15	1	2	3	4
Ex.16	1	2	3	4
Ex.17	1	4	9	16
Ex.18	1	12	54	160

4. Numerical Examples and Discussions

The cyclic polynomials are derived for eighteen plate shapes (Ex.1-18) to calculate number of different combinations in edge conditions. Table 1 presents a list of numbers of different combinations, when one, two, three and four edge conditions are applied along each edge. For typical plate bending problem, there considered three classical conditions, such as free edge (F), simply supported (S) and clamped (C) edges. In this table, the number of conditions 1, 2, and 3 per edge indicates any choices of one edge condition, two conditions and three conditions, respectively, chosen from (F,S,C). A case of four conditions implies, say, including another condition of elastic support, or a little unrealistic sliding edge (slope and shear force both being zero).

As seen (Ex.6) in the table, the maximum number of different combinations are 16, 81 and 256 versus Number of conditions x=2, 3 and 4 at each edge, for Asymmetric trapezoid among examples of "Plates with four straight edges".

Similarly, the maximum number is 8, 27 and 64 for (Ex.10) in "Triangular plates", and for most complicated case of "Polygonal plates", it is 30, 498 and 4435 of (Ex.14) (regular) Octagonal plate. In contrast, "Plates with circular edges" provide smaller number of combinations due to no

corners (i.e., small number of distinct edges) along curved edges except for (Ex.18).

In previous report [7] dealing with square and rectangular plates only, the number of different combinations was numerically demonstrated to be exact. This was possible by using a software to accommodate any sets of edge conditions for calculating natural frequencies of rectangular plates. Such software, however, is not available to the cases of plates with general shapes discussed in this paper.

An attempt was made next by a trial and error approach to figure out different number of combinations for the two conditions along each edge, and the two edge conditions are represented by F and C in the examples.

Figure 17 presents seven different combinations (as listed in Table 1) of a rhombic plate. As expected, in addition to FFFF and CCCC, there is only one case of one C and three F (also one F and three C) due to four edges of equal length, while CCFF and CFCF are regarded as different since CCFF cannot be made from CFCF by any rotation and flipping.

The next example is taken from (Ex.5) Symmetric trapezoid, where only symmetry axis exists. There are twelve (as given in the table) possible combinations, as shown in Fig.18. When this symmetry is broken as in (Ex.6) Asymmetric trapezoid, there are no duplication and the number of combinations becomes 2^4=16, which is the same as general quadrilateral plate.

For (Ex.7) Equilateral triangular plate, there are three symmetric axes and the number of combinations is reduced significantly by the symmetry to only four, as shown in Fig.19. Figure 20 presents the combinations of F and C for (Ex.8) Equilateral triangle and only one symmetry axis exists. The loss of symmetry from three to one causes the combination being increased to six, as observed in the figure.
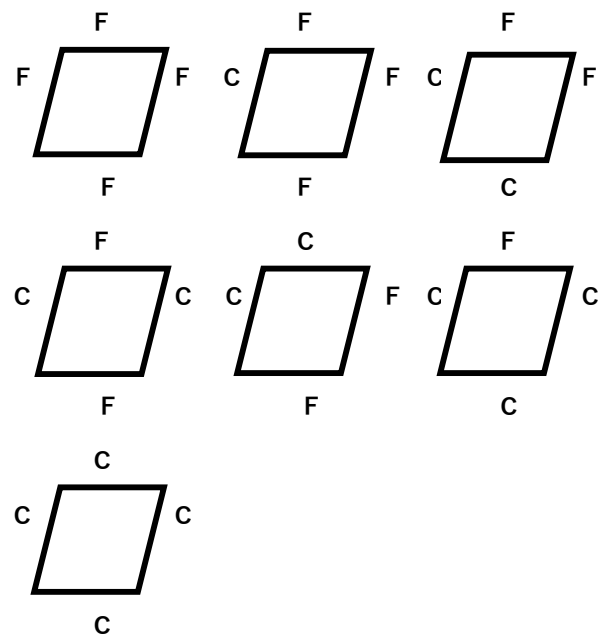

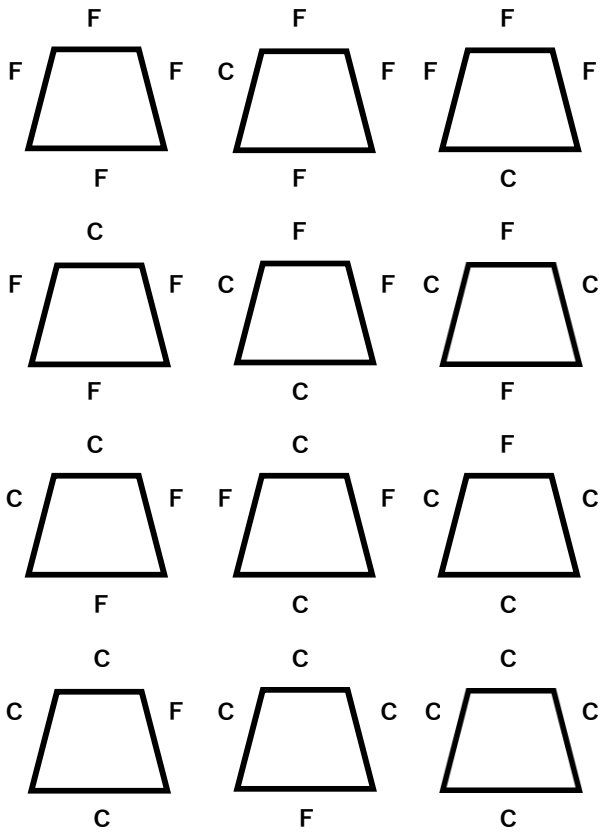Figure 17. Combination of two edge conditions (F, C) for rhombic plate (Ex.3)

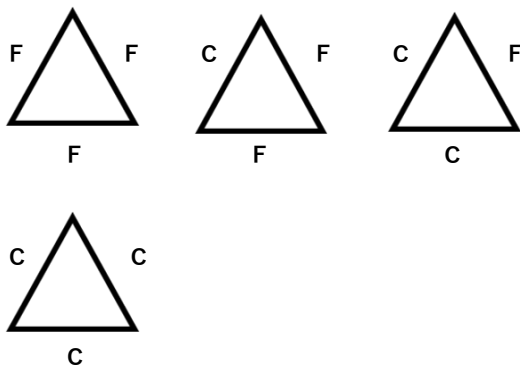Figure 18. Combination of two edge conditions (F, C) for symmetric trapezoidal plate (Ex.5)

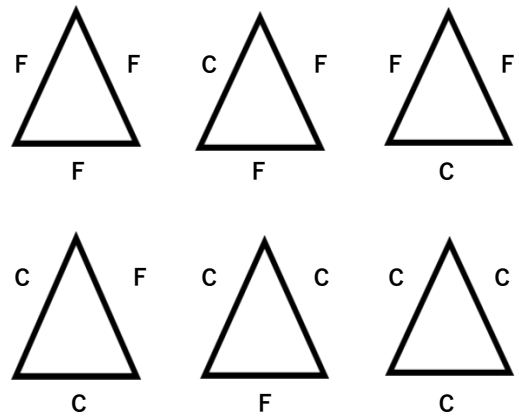Figure 19. Combination of two edge conditions (F, C) for equilateral triangular plate (Ex.7)

Figure 20. Combination of two edge conditions (F, C) for isosceles triangular plate (Ex.8)
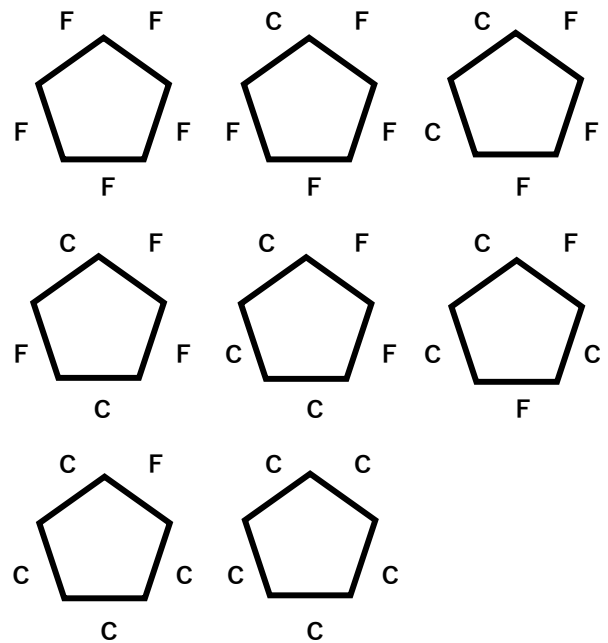
Figure 21. Combination of two edge conditions (F, C) for regular pentagonal plate (Ex.11)

Figure 21 presents eight combinations of a regular pentagonal plate. For complicated cases of regular polygonal plates, it is interesting to observe the balance between the increase of edges (increasing the number of combinations) and the increase of symmetry axes (decreasing the number). It is observed that the increase of edges is more dominant than that of symmetry, and in the case of (Ex.14) regular octagonal plates, the number of combinations become significantly large as 30, 498 and 4435 for x=2,3 and 4, respectively. For such large number of combinations, it is impossible to figure out all the possible combinations by a trial and error approach.

5. Conclusions

Polya counting theory was developed in the 1930's, and has been applied to a wide range of combinatorial problems in mathematics and chemistry. The present paper extended use of the theory to combination of edge (boundary) conditions that yield different sets of mechanical characteristics, such as stress distribution, deflection, natural frequencies and critical buckling loads, that are found in isotropic flat plates with various geometry.

First, a method for counting was outlined for a case of a rectangular plate. Secondly, eighteen examples of different plate shapes are introduced, and for each of plate shape, a cyclic polynomial was derived. When the number of each edge condition is given for 1, 2, 3 and 4, the total number of sets of edge conditions is listed for eighteen examples. Validity of these results is partially established by showing

actual combinations for rhombic, symmetric trapezoidal, equilateral and isosceles triangular, and regular pentagonal plates in the case of two edge conditions (free edge and clamped edge) applied along each edge. These examples collaborated the validity of the present method. It is hoped that this combinatorics approach will help in summarizing design data books and monographs.

References

[1] Leissa, A.W., 1993, Vibration of Plates, Acoustical Society of America, (previously, 1969 NASA SP-160, U.S. Government Printing Office, Washington D.C.).

[2] Leissa, A.W. 1973, The free vibration of rectangular plates, J. Sound Vib., vol.31, pp.257-293.

[3] Redfield, J.H., 1927, The theory of group-reduced distributions, American Journal of Mathematics, vol.49, no.3, pp.433–455.

[4] Pólya, G. and Read, R.C., 1987, *Combinatorial Enumeration of Groups, Graphs, and Chemical Compounds*, Springer-Velag.

[5] Harris, J.M., Hirst, J.L., Mossinghoff, M.J., 2000, *Combinatorics and Graph Theory,* Springer.

[6] Haigh, C.W., Baker, P.K., 1994, Use of Polya's theorem to enumerate the isomers of seven-coordinate complexes with capped octahedral geometry, Polyhedron, vol. 13, no. 3, pp. 417-433.

[7] Narita, Y., 2000, Combinations for the free-vibration behaviors of anisotropic rectangular plates under general edge conditions, Trans. ASME Journal of Applied Mechanics, vol.67, pp.568-573.